

TECHNISCHE UNIVERSITÄT MÜNCHEN  
Fakultät für Physik

# Highly doubly excited states of two-electron atoms: spectra, cross sections and localization properties

Johannes Eiglsperger

Vollständiger Abdruck der von der Fakultät für Physik der Technischen Universität München  
zur Erlangung des akademischen Grades eines

Doktors der Naturwissenschaften (Dr. rer. nat.)

genehmigten Dissertation.

Vorsitzender: Univ.-Prof. Dr. Lothar Oberauer

Prüfer der Dissertation: 1. Univ.-Prof. Dr. Harald Friedrich

2. Univ.-Prof. Dr. Manfred Kleber

Die Dissertation wurde am 30.03.2010 bei der Technischen Universität München  
eingereicht und durch die Fakultät für Physik am 01.06.2010 angenommen.



# Contents

<b>Introduction</b>	<b>5</b>
<b>1 Generalities</b>	<b>9</b>
1.1 Hamiltonian . . . . .	9
1.2 Wave function . . . . .	10
1.3 Basic spectral properties . . . . .	11
1.3.1 Influence of the electron-electron interaction . . . . .	11
1.3.2 Herrick classification . . . . .	13
1.4 Complex Rotation . . . . .	14
<b>2 Planar two-electron atom model</b>	<b>16</b>
2.1 Why consider a planar two-electron atom model? . . . . .	16
2.2 Planar approach . . . . .	17
2.2.1 Transformation to parabolic coordinates . . . . .	17
2.2.2 Stationary Schrödinger equation . . . . .	18
2.2.3 Harmonic oscillator representation . . . . .	19
2.2.4 Selection rules . . . . .	19
2.2.5 Remaining symmetries . . . . .	20
2.2.6 Cross section . . . . .	21
2.2.7 Expectation value of $\cos(\theta_{12})$ . . . . .	21
2.2.8 Electronic densities . . . . .	22
2.3 Spectral structure . . . . .	23
2.4 Numerical treatment . . . . .	24
2.4.1 Matrix representation . . . . .	24
2.4.2 Lanczos algorithm . . . . .	26
2.4.3 Numerical implementation . . . . .	27
<b>3 Three-dimensional treatment of a two-electron atom</b>	<b>31</b>
3.1 Spectral method . . . . .	31
3.1.1 Expectation value of $\cos(\theta_{12})$ . . . . .	34
3.1.2 Electronic densities . . . . .	35
3.2 Matrix representation . . . . .	35
3.2.1 Linearization of the product of two Coulomb-Sturmian functions . . . . .	36
3.2.2 Recurrence relation for the coefficients $(\nu_i, \lambda_i, \kappa_i, n_i, l_i, k_i   N_i)$ . . . . .	37
3.2.3 Recurrence relations for the integrals $\mathcal{G}_{N_i, N_j}^{L_i, L_j, q}(\xi_i, \xi_j)$ . . . . .	37
3.3 Numerical treatment . . . . .	38
3.3.1 Computation of the matrix representation of the generalized eigenvalue problem . . . . .	38
3.3.2 Solution of the eigenvalue problem . . . . .	40

<b>4</b>	<b>Spectral properties of helium</b>	<b>41</b>
4.1	Natural parity states . . . . .	41
4.1.1	Ground state . . . . .	42
4.1.2	Resonances . . . . .	44
4.2	Unnatural parity states . . . . .	53
4.2.1	Non-autoionizing states . . . . .	53
4.2.2	Resonances . . . . .	56
4.3	Summary . . . . .	61
<b>5</b>	<b>Frozen planet states of helium for non-zero angular momentum</b>	<b>62</b>
5.1	The classical frozen planet configuration . . . . .	63
5.1.1	Identification criteria of frozen planet states . . . . .	64
5.2	Frozen planet states with total angular momentum $L = 1$ . . . . .	65
5.3	Frozen planet states with total angular momentum $L = 2$ . . . . .	69
5.3.1	Identification of $L = 2$ frozen planet states for three-dimensional helium . . . . .	69
5.3.2	Comparison of $L = 2$ frozen planet states for planar and three-dimensional helium . . . . .	71
5.4	Summary . . . . .	74
<b>6</b>	<b>Fluctuations in photoionization cross sections of planar two-electron atoms</b>	<b>75</b>
6.1	Computation of the fluctuations in photoionization cross sections . . . . .	76
6.2	Photoionization cross section for singlet helium . . . . .	78
6.3	Photoionization cross section for singlet ionic lithium . . . . .	82
6.4	Photoionization cross section for triplet helium . . . . .	85
6.5	Summary . . . . .	90
	<b>Conclusions and Outlook</b>	<b>91</b>
<b>A</b>	<b>Planar two-electron atom supplement</b>	<b>94</b>
A.1	Parabolic transformation . . . . .	94
A.2	Some integrable two-dimensional systems . . . . .	95
A.2.1	Eigenfunctions of the two-dimensional harmonic oscillator . . . . .	95
A.2.2	Planar hydrogenic atoms . . . . .	96
A.2.3	Planar two-electron atom without electron-electron interaction . . . . .	99
<b>B</b>	<b>Three dimensional treatment of a two-electron atom supplement</b>	<b>101</b>
B.1	Coulomb-Sturmian functions . . . . .	101
B.2	Matrix Formulation of the Schrödinger equation . . . . .	102
B.2.1	Matrix elements of $\cos(\theta_{12})$ . . . . .	105
B.3	Gauß-Laguerre integration . . . . .	105
B.3.1	Matrix elements of the electron-electron interaction . . . . .	106
<b>C</b>	<b>Spectral properties of helium supplement</b>	<b>108</b>
C.1	Natural parity . . . . .	108
C.1.1	$^1P^o$ resonance data . . . . .	108
C.1.2	$^3P^o$ resonance data . . . . .	113
C.1.3	$^1D^e$ resonance data . . . . .	117
C.1.4	$^3D^e$ resonance data . . . . .	121
C.2	Unnatural parity . . . . .	125
C.2.1	$^1P^e$ resonance data . . . . .	125
	<b>Bibliography</b>	<b>128</b>

# Introduction

Three-body problems are defined to be systems of three particles with non-negligible interactions between each pair. As first noticed by Poincaré [1], while studying the system *Moon-Earth-Sun* (see also [2] for a comprehensive review), the classical dynamics of the three-body problem with  $1/r^2$  forces is non-integrable. This remains true when gravitational forces are substituted by attractive and repulsive Coulomb forces, such as define the three-body Coulomb problem. Indeed, the electron-electron interaction term in the Hamiltonian of an unperturbed two-electron atom – which otherwise is just the sum of two hydrogenic Hamiltonians – renders the two-electron dynamics in general irregular and chaotic with only small regions of regular motion in the classical phase space [3]. The loss of integrability, due to the electron-electron interaction, caused the failure of first quantization attempts on the basis of Niels Bohr’s quantum postulates [4]. Only with the development of modern semiclassical theory [5, 6] and the subsequent semiclassical quantization of helium [7, 8] could the non-integrability of the quantum system be understood as the direct counterpart of the corresponding classical mixed regular-chaotic dynamics [3]. The failure of the Bohr-Sommerfeld quantization to reproduce the ground state energy of helium (see, e.g., [9]) lead, among other reasons, to the formulation of quantum wave mechanics by Heisenberg [10] and Schrödinger [11]. Starting with the first quantization attempts, it took more than four decades until the ground-breaking work by Pekeris [12, 13] which provided a satisfactory description of bound states. Up to date, various approaches have been proposed for the treatment of bound states of two-electron atoms ranging from semiclassical (see [3] and references therein) to quantum mechanical including relativistic corrections [14, 15]. As was first realized through the seminal experiment by Madden and Codling [16], doubly excited states of two-electron atoms are highly correlated states and therefore, they cannot be in general described by a simple model based on independent-particle quantum numbers. This experiment drew the interest of theoreticians and experimentalists to doubly excited states, and particularly to the regime near the double ionization threshold, which since then represents a paradigm for electronic correlations in atomic physics. This regime is in fact the semiclassical one in two-electron atoms. Consequently, the underlying classical chaotic dynamics should influence the quantum spectrum of highly doubly excited states and signatures of quantum chaos such as Ericson fluctuations [17, 18] or semiclassical scaling laws for the fluctuations of excitation cross sections [19], are expected to become observable [20].

Direct manifestations of electronic correlations are found for instance in certain highly asymmetrically doubly excited states which are associated to highly correlated classical configurations, such as the frozen planet configuration [21, 22]. Studies for one-dimensional [23, 24] and planar helium [25, 26] suggest that these states form, under near resonant driving, non-dispersive two-electron wave packets [27], i.e., very robust quantum objects, which propagate along the frozen planet classical trajectory. However, the existence of these highly correlated wave packets still awaits its confirmation in full three-dimensional calculations and its experimental verification. Manifestations of electronic correlations have also been observed in double ionization of helium from the ground state by strong laser fields [28, 29]. An enhancement by several orders of magnitude for the production of doubly charged ions is observed compared to the yield expected on

basis of a single active electron approximation [30, 31], in which the electron-electron interaction is neglected. This is interpreted as a fingerprint of correlated electronic ionization processes (manifesting in *non-sequential* ionization, as opposed to *sequential* ionization in the independent particle picture), where one electron is “knocked out” by the other one in a laser-induced recollision process. The geometry of the fragmentation process observed in more refined experiments [32, 33] also suggests a strong dependence of the ionization process on the electronic structure [34] of helium-like atoms. Highly doubly excited states are expected to play an important role in the ionization by low frequency intense laser pulses [35, 36]. However, an accurate theoretical treatment of such a problem defines a formidable theoretical and numerical challenge due to the field induced coupling of several total angular momenta and the dimensions of the matrices associated to single total angular momenta. Note, however, that a three-dimensional ab initio fully numerical treatment of the ionization of helium in the low frequency regime is available [37] and has already been used to give a rather qualitative description of the correlations in the ionization process of helium from the ground state by a 780 nm laser pulse of peak intensity  $(0.275 - 14.4) \times 10^{14} \text{ W/cm}^2$ . However, due to the difficulty to extract physical information from this grid approach and its high requirements concerning computational resources, an accurate spectral approach to this problem becomes even more desirable. Further correlation effects have been observed in two-photon double ionization by strong XUV pulses where almost no experimental data is available and theoretical predictions [38–46] for the two-photon double ionization cross section among themselves deviate by orders of magnitude.

The understanding of each of these issues requires an accurate description of (highly) doubly excited states for various values of the total angular momentum  $L$ . Unlike in the case of the hydrogen atom exact eigenfunctions cannot be found. The non-integrability of the three-body problem forces us to recur to numerical and approximation methods, which include, e.g., variational approaches, grid methods and spectral methods. Probably the most successful approaches for the description of spectral properties of two-electron atoms are spectral methods, of which two basis types can be considered: the so-called explicitly correlated [12, 13, 47–56] bases, in which the basis functions depend explicitly on the interelectronic distance  $r_{12}$ , and the configuration interaction bases [57–64], in which the wave function is written as a linear combination of (antisymmetrized) products of one-electron wave functions. Explicitly correlated bases allow for a very accurate description of two-electron atoms, however, the computation of the matrix elements either involves coupled three-dimensional radial integrals or is based on an analytic computation and selection rules, the number of which grows rapidly with increasing total angular momentum  $L$ . Moreover, rather large bases are needed for the description of highly asymmetrically excited states. Note, however, that due to the resulting analytic computation of matrix elements combined with selection rules, the explicitly correlated expansion in terms of Coulomb-Sturmian functions of the perimetric coordinates [12, 13] is probably the most successful method for the treatment of highly doubly excited states with  $L = 0, 1$  [51–54, 65]. Configuration interaction bases have been widely used due to their simplicity and flexibility, however, they are plagued with slow convergence for symmetrically excited states and most severely for the ground state. This is due to the fact that the basis expansion does not satisfy the Kato cusp condition associated with the coalescence of the two electrons [57, 66, 67]. Moreover, the standard configuration interaction approach requires large basis sizes for the description of highly asymmetrically excited states. However, the computation of matrix elements in these bases involves at most two-dimensional coupled radial integrals and the computation of states with high total angular momentum  $L$  does not pose any additional difficulties; these bases are frequently used for the description of few-photon ionization processes [39, 40, 45, 68–71] where highly doubly excited states do not play a fundamental role. Up to now, methods of this type have not been applied to the computation of highly doubly excited states.

In the present thesis we are going to lay the foundations for the treatment of multiphoton processes, in which highly double excited states play an important role, and we will explore photoionization cross sections in the regime of highly doubly excited states of two-electron atoms in order to look for signatures of quantum chaos.

To treat multiphoton processes, e.g., the formation of non-dispersive two-electron wave packets, a description of the regime of doubly excited states is needed for various values of total angular momenta  $L$ . In order to describe these spectra, a non-standard configuration interaction approach is applied to their computation. In particular, the frozen planet states, which seem to be essential for the formation of two-electron non-dispersive wave packets, for non-zero total angular momentum  $L$  are investigated. Moreover, they are compared to their planar counterparts in order to obtain a feeling for the value of computations for non-dispersive wave packets in a planar approach [25, 26].

The treatment of photoionization cross sections of helium in a three-dimensional approach is so far restricted to energies below the 17th single ionization threshold [65]. In order to explore cross sections at energies closer to the total fragmentation threshold, a planar approach, which is proven to contain the relevant degrees of freedom for the description of these cross sections, is applied to their computation. Photoionization cross sections for the helium atom and the positively charged lithium ion are computed within this approach.

## Structure of the thesis

In chapter 1 the complex rotation method for the treatment of resonances and general aspects of two-electron atoms are discussed. This includes a description of the Hamiltonian and the properties of wave functions and spectra.

Chapter 2 motivates and describes our approach to planar helium. To regularize the Coulomb singularities in the planar three-body Coulomb problem the Hamiltonian is transformed into parabolic coordinates. This facilitates a representation in creation and annihilation operators, which leads in an appropriate basis set to analytic expressions for the matrix elements of the Hamiltonian. The numerical implementation of this approach and the computation of the quantities needed in chapters 5 and 6 are described.

In chapter 3 our spectral method for the treatment of two-electron atoms in three dimensions is presented. The matrix representation of the problem and its numerical implementation is discussed. In particular, a newly developed, highly efficient method for the computation of matrix elements of the electron-electron repulsion is described in detail.

Chapter 4 presents spectral data for states and resonances of helium for natural and unnatural parity. For natural parity, the energy regime up to the tenth single ionization threshold is explored for  $^1S^e$  and  $^3S^e$  resonances of helium. In case of unnatural parity, we treat non-autoionizing states below the second threshold for  $L = 1$  to  $L = 9$ . In addition, results for  $^3P^e$  resonance states for energies up to the eighth threshold are presented.

In chapter 5 a brief introduction to the classical frozen planet configuration is given and results for quantum mechanical states with total angular momentum  $L = 1$  and  $L = 2$  localized along this configuration are presented and compared for both planar and three-dimensional treatment.

In chapter 6 we study the spectrum of two-electron atoms close to the double ionization threshold with the help of our planar approach. Photoionization cross sections of singlet planar helium are compared to experimental data. We investigate the semiclassical scaling law [19] for the fluctuations in the photoionization cross sections and also the implications of the existence of an approximate quantum number in the discussion about Ericson fluctuations.

The thesis is concluded with a short summary, and a brief outlook for future applications of both the planar and the three-dimensional approach. In addition, three appendices are included

in this work. In appendix A, the technical details of the parabolic coordinate transformation are outlined. Moreover, appendix A is used to illustrate the most relevant features of simple integrable systems for the planar approach of chapter 2. Appendix B is a supplement to chapter 3. Coulomb-Sturmian functions are introduced in this appendix, together, with the matrix formulation of the Schrödinger equation and a standard method for the computation of the matrix elements. In appendix C additional spectral data for three-dimensional helium is presented in order to complement chapters 4 and 5.

Unless stated otherwise, atomic units (a. u.) defined by  $e = m_e = \hbar = 1$  are used throughout this document. For conversion of energy the relation  $1 \text{ a. u.} = 27.2113895 \text{ eV}$  is used.

# Chapter 1

## Generalities

General aspects of two-electron atoms and a method which is widely used to extract information about resonances are outlined in this chapter. Following a description of the two-electron atom Hamiltonian (Sec. 1.1) the properties of the wave function of two-electron atom states are discussed (Sec. 1.2). Section 1.3 is concerned with the spectral properties of two-electron atoms and the classification of their states. Finally, section 1.4 is dedicated to the description of the complex rotation method, which is used in the following to treat the resonances of two-electron atoms.

### 1.1 Hamiltonian

Two-electron atoms consist of a nucleus with mass  $M$  containing  $Z$  protons and two electrons of mass  $m$  interacting through Coulomb forces. Here, as depicted in figure 1.1, the positions of the electrons with respect to the nucleus are given by  $\vec{r}_1$  and  $\vec{r}_2$ , respectively, the conjugated momenta are denoted by  $\vec{p}_1$  and  $\vec{p}_2$ , and  $r_{12} = |\vec{r}_1 - \vec{r}_2|$  is the interelectronic distance. Within the framework of non-relativistic quantum mechanics the Hamiltonian of this system – in atomic units – reads,

$$H = \frac{\vec{p}_1^2}{2\mu} + \frac{\vec{p}_2^2}{2\mu} + \frac{\vec{p}_1 \cdot \vec{p}_2}{M} - \frac{Z}{r_1} - \frac{Z}{r_2} + \frac{1}{r_{12}}, \quad (1.1)$$

where  $\mu$  is the reduced mass of the electron-nucleus subsystem defined by

$$\mu = \frac{mM}{m + M}. \quad (1.2)$$

The first two terms of the Hamiltonian (1.1) are associated to the kinetic energy of the two electrons. The third one is a mass polarization term. The potential energy is given by the rest of the terms of (1.1), where

$$V = -\frac{Z}{r_1} - \frac{Z}{r_2}, \quad (1.3)$$

describes the interaction between the nucleus and the electrons and

$$U = \frac{1}{r_{12}}, \quad (1.4)$$

the electron-electron repulsion.

As the mass of the nucleus is by orders of magnitude larger than that of the electrons, one usually employs the approximation of an infinitely heavy nucleus. In this approximation

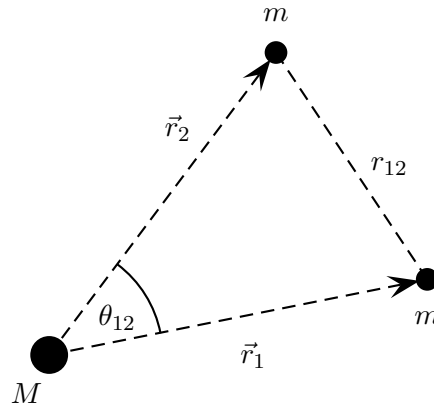


Figure 1.1: Two-electron atom: a nucleus with mass  $M$  and charge  $Z$ , and two electrons of mass  $m$  interacting through Coulomb forces.  $\vec{r}_1$  and  $\vec{r}_2$  are the positions of electron one and two with respect to the nucleus,  $r_{12}$  the interelectronic distance and  $\theta_{12}$  the mutual angle between the position vectors of the electrons.

the mass polarization term vanishes, the reduced mass is substituted by the electron mass and using the center of mass system the nucleus is fixed at the origin. Thus, the non-relativistic Hamiltonian for two-electron atoms, assuming an infinitely heavy nucleus, is given by

$$H = \frac{\vec{p}_1^2}{2} + \frac{\vec{p}_2^2}{2} - \frac{Z}{r_1} - \frac{Z}{r_2} + \frac{1}{r_{12}}. \quad (1.5)$$

## 1.2 Wave function

The Hamiltonian (1.5) is independent of the spin of the electrons. Consequently, the wave function  $\Phi(q_1, q_2)$  of the system can be written as a product of the spatial wave function  $\Psi(\vec{r}_1, \vec{r}_2)$  and the spin wave function  $\chi(1, 2)$ :

$$\Phi(q_1, q_2) = \Psi(\vec{r}_1, \vec{r}_2)\chi(1, 2), \quad (1.6)$$

which has to be anti-symmetric due to the Pauli principle. For two-electron atoms spatial and spin parts of the wave function (1.6) possess a well defined symmetry. The spatially symmetric wave functions – denoted by  $\Psi^+(\vec{r}_1, \vec{r}_2)$  – are defined by the relation,

$$\Psi(\vec{r}_1, \vec{r}_2) = +\Psi(\vec{r}_2, \vec{r}_1), \quad (1.7)$$

while the spatially antisymmetric wave functions  $\Psi^-(\vec{r}_1, \vec{r}_2)$  obey

$$\Psi(\vec{r}_1, \vec{r}_2) = -\Psi(\vec{r}_2, \vec{r}_1). \quad (1.8)$$

The possible spin states  $|S, M_S\rangle$ , where  $S$  denotes the total spin and  $M_S$  its projection on the quantization axis, are given by the antisymmetric singlet state

$$|0, 0\rangle = \frac{1}{\sqrt{2}}(|\uparrow\downarrow\rangle - |\downarrow\uparrow\rangle), \quad (1.9)$$

and the symmetric triplet states

$$\begin{aligned} |1, 1\rangle &= |\uparrow\uparrow\rangle, \\ |1, 0\rangle &= \frac{1}{\sqrt{2}}(|\uparrow\downarrow\rangle + |\downarrow\uparrow\rangle), \\ |1, -1\rangle &= |\downarrow\downarrow\rangle. \end{aligned} \quad (1.10)$$

Thus, there are four physical combinations obeying the Pauli principle, which are commonly labeled after their spin properties, denoting

$$\Psi_1(\vec{r}_1, \vec{r}_2) = \Psi^+(\vec{r}_1, \vec{r}_2)|0, 0\rangle \quad (1.11)$$

a singlet state, and

$$\begin{aligned} \Psi_2(\vec{r}_1, \vec{r}_2) &= \Psi^-(\vec{r}_1, \vec{r}_2)|1, 1\rangle \\ \Psi_3(\vec{r}_1, \vec{r}_2) &= \Psi^-(\vec{r}_1, \vec{r}_2)|1, 0\rangle \\ \Psi_4(\vec{r}_1, \vec{r}_2) &= \Psi^-(\vec{r}_1, \vec{r}_2)|1, -1\rangle \end{aligned} \quad (1.12)$$

triplet states.

### 1.3 Basic spectral properties

Altogether there are, including spin, eight degrees of freedom for two-electron atoms described by (1.5). Thus, for a full classification of a given state eight quantum numbers are needed. The classification of the quantum states of (1.5) can be achieved at least partly through exact symmetries of the three-body Coulomb problem. The overall rotational symmetry, related to conservation of the total orbital angular momentum  $\vec{L}$  and its projection, and the fact that (1.5) commutes with the spin  $\vec{S}$  give rise to  $L$ ,  $M$ ,  $S$  and  $M_S$  as good quantum numbers. The quantum numbers of the total spin  $S$  and its  $z$  component are linked to electron exchange  $\vec{r}_1 \leftrightarrow \vec{r}_2$  through the antisymmetry of the total wave function as already discussed in section 1.2. This leads to the distinction between singlet ( $S = 0$ ) and triplet ( $S = 1$ ) states. The four remaining degrees of freedom are nonseparable and are usually described by approximate quantum numbers, e.g., independent particle quantum numbers  $(N, n, l_1, l_2)$ .

Commonly, the spectral notation of  $^{2S+1}L^\pi$  is used. This notation makes use of the fact that the reflection symmetry infers that the wave function of the electron pair are eigenfunctions of the parity operator  $\Pi : (\vec{r}_1, \vec{r}_2) \rightarrow (-\vec{r}_1, -\vec{r}_2)$  with eigenvalue  $\pi = +1$  or  $\pi = -1$  describing even (e) and odd (o) states, respectively. Note, that  $\pi$  is, e.g., connected to the independent particle quantum numbers by  $\pi = (-1)^{l_1+l_2}$ . The quantum numbers  $M$  and  $M_S$  are omitted as the states associated to different values of these quantum numbers are degenerate in a non-relativistic treatment.

#### 1.3.1 Influence of the electron-electron interaction

Let us briefly consider the Hamiltonian (1.5) without the electron-electron repulsion term (1.4). In this case the Hamiltonian

$$H_0 = \frac{\vec{p}_1^2}{2} + \frac{\vec{p}_2^2}{2} - \frac{Z}{r_1} - \frac{Z}{r_2}, \quad (1.13)$$

consists of two independent hydrogenic atom Hamiltonians. The spectrum of  $H_0$  is given through bound states with energies

$$E_{N,n,l_1,l_2}^{L,M} = -\frac{Z^2}{2N^2} - \frac{Z^2}{2n^2}, \quad N \leq n, \quad (1.14)$$

and continua above the single ionization thresholds (SIT), with  $N$  and  $n$  excitation, and  $l_1$  and  $l_2$  angular momentum of the inner and outer electron, respectively. In figure 1.2 a part of the spectrum of  $H_0$  for helium ( $Z = 2$ ) is depicted. The energy levels are organized in an infinite number of Rydberg series, labeled by the principal quantum number  $N$ , each of which converges to single ionization thresholds,  $I_N = -Z^2/(2N^2)$ , of the remaining ion. The series of the single

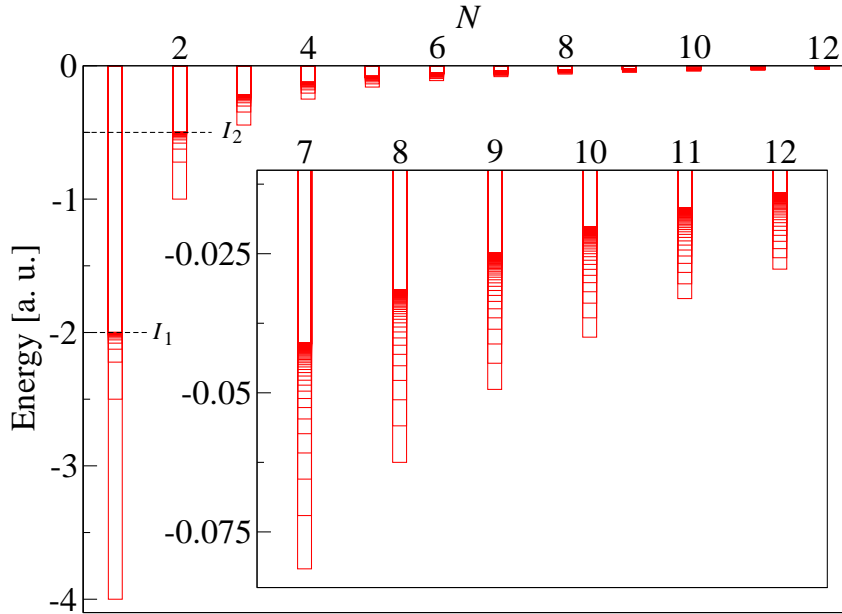


Figure 1.2: Spectrum of helium for  $L = 0$  without electron-electron interaction (independent particle model). The energy levels (horizontal bars) are organized in series labeled by the principal quantum number  $N$  of the inner electron. The first two single ionization thresholds are represented by dashed lines.

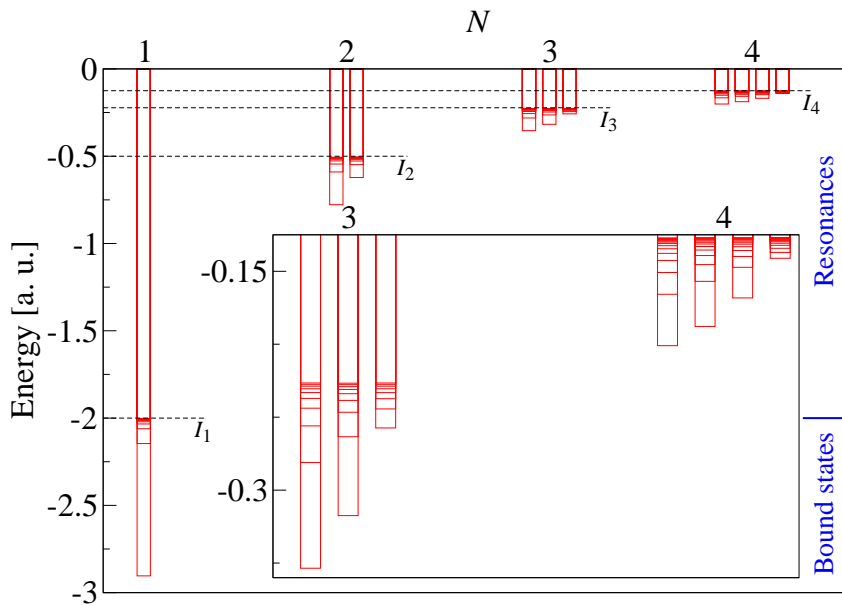


Figure 1.3: Spectrum of helium for  $1S^e$  states (data taken from [51]). The energy levels (horizontal bars) are organized in series labeled by the principal quantum number  $N$  of the inner electron. The separation into subseries is done on the basis of the Herrick classification [72–74]. Single ionization thresholds are represented by dashed lines.

ionization thresholds  $I_N$  converges to the double ionization or total fragmentation threshold (DIT).

The model roughly describes the structure of the spectrum of two-electron atoms. However,

there are two essential qualitative discrepancies to the spectrum of (1.5) which includes the  $1/r_{12}$ -term. Firstly, the electron-electron interaction couples different channels of the noninteracting two-electron dynamics and gives rise to autoionizing resonance states embedded in the continua above the first single ionization threshold. Secondly, the electron-electron interaction introduces a mixing of states with different values of  $N$ ,  $n$ ,  $l_1$  and  $l_2$ . If  $\Delta N = 0$  and  $\Delta n = 0$ , the mixing of  $l_1$  and  $l_2$  is particularly strong, leaving no dominant independent-particle configuration  $(l_1, l_2)$  to be assigned to an individual state as these configurations are degenerate in the independent particle picture.

In figure 1.3 a part of the spectrum for  $1S^e$  states of helium is presented to illustrate the influence of  $1/r_{12}$ . Note, that for states with  $\pi = (-1)^{l_1+l_2} = (-1)^{L+1}$ , bound states lie below  $I_2$  and resonances above  $I_2$ . Therefore, there are no bound states below the first single ionization threshold and no continuum emerges from this threshold (see Sec. 4.2). Apart from  $H^-$  ( $Z = 1$ ), which possesses only two bound states [75], one for  $1S^e$  and one for  $3P^e$ , all two-electron atoms exhibit similar spectral structures.

The fact, that the independent-particle angular momentum quantum numbers  $l_1, l_2$  are inappropriate to characterize a series of doubly excited states if the electrons can occupy a number of quasidegenerate (individual electron) configurations was already revealed in the first experimental observation of doubly excited states of helium [16] and its theoretical interpretation [76]. The inherent strongly correlated nature of double excited states of two-electron atoms requires therefore the introduction of new classification schemes based on approximate quantum numbers, e.g., [72–74, 77–81]. In the following, the (probably) most widely used of these classification schemes is briefly reviewed.

### 1.3.2 Herrick classification

In order to describe doubly excited states, Herrick *et al.* [72–74] utilized the properties of the symmetry group  $SO(4)$ . The group can be used to describe the Stark effect in hydrogen and is represented by the angular momentum of the electron  $\vec{l}$  and the vector  $\vec{b}$  which is connected to the Runge-Lenz vector,

$$\vec{a} = \frac{1}{2} (\vec{l} \times \vec{p} - \vec{p} \times \vec{l}) + \frac{\vec{r}}{r}, \quad (1.15)$$

by the relation  $\vec{b} = n\vec{a}$ . The idea of Herrick was to take into account the Stark effect induced by the outer electron onto the inner one. He constructed, based on  $SO(4)_1 \otimes SO(4)_2$ , a new basis of doubly excited states  $|NnKT; LMSM_S\rangle$ , which is connected by

$$|NnKT; LMSM_S\rangle = \sum_{l_1, l_2} |Nl_1nl_2; LMSM_S\rangle D_{Nl_1nl_2}^{KTL}, \quad (1.16)$$

to the independent particle basis, where  $D_{Nl_1nl_2}^{KTL}$  is an expression including a Wigner  $9j$  symbol [82]. The numbers  $K$  and  $T$  result from diagonalization of an operator  $\vec{B} = \vec{b}_1 - \vec{b}_2$ . The  $9j$  symbol imposes conditions on  $T$  and  $K$  for which  $D_{Nl_1nl_2}^{KTL}$  is non-zero for given  $N$  and  $L$ :

$$\begin{aligned} T &= 0, 1, \dots, \min(L, N-1), \\ K &= -N+1+T, -N+3+T, \dots, N-3-T, N-1-T. \end{aligned} \quad (1.17)$$

Note, that for  $\pi = (-1)^{L+1}$ ,  $T = 0$  is not allowed.

The two integer numbers  $K$  and  $T$  are convenient indices for labeling angular correlations. In terms of asymptotic properties of the two electrons,  $K$  is proportional to the average value of  $r_1 \cos \theta_{12}$  and  $T$  describes the magnitude of the overlap  $\vec{l}_1 \cdot \hat{r}_2$ , or roughly speaking, the relative

orientation between the orbitals of the two electrons. If the two electron orbits are in the same plane, then  $T = 0$  [78]. Note, that in the limit  $n \rightarrow \infty$ , [54, 65, 74]

$$\langle \cos \theta_{12} \rangle \xrightarrow{n \rightarrow \infty} -\frac{K}{N}. \quad (1.18)$$

## 1.4 Complex Rotation

The electron-electron interaction in helium couples different channels of the non-interacting two-electron dynamics, and gives rise to resonance states embedded in the continua above the first single ionization threshold. To extract the energies and decay rates of resonance states we use complex rotation (or “dilation”) [83–87], which was shown to be applicable for the Coulomb potential in [88].

The complex dilation of any operator by an angle  $\theta$  is mediated by the non-unitary complex rotation operator

$$R(\theta) = \exp \left( -\theta \frac{\vec{r} \cdot \vec{p} + \vec{p} \cdot \vec{r}}{2} \right), \quad (1.19)$$

where  $\vec{r}$  and  $\vec{p}$  represent the  $2N$  component vector made up of  $\vec{r}_1, \vec{r}_2$  and  $\vec{p}_1, \vec{p}_2$ , respectively, with  $N$  the dimension of the treated system. The transformation of the position and momentum operators consists of a rotation by  $\theta$  in the complex plane,

$$\begin{aligned} \vec{r} &\rightarrow R(\theta) \vec{r} R(-\theta) = \vec{r} e^{i\theta}, \\ \vec{p} &\rightarrow R(\theta) \vec{p} R(-\theta) = \vec{p} e^{-i\theta}. \end{aligned} \quad (1.20)$$

Thus, the Hamiltonian (1.5) transforms into,

$$H(\theta) = R(\theta) H R(-\theta) = \left( \frac{\vec{p}_1^2 + \vec{p}_2^2}{2} \right) e^{-2i\theta} - \left( \frac{Z}{r_1} + \frac{Z}{r_2} - \frac{1}{r_{12}} \right) e^{-i\theta}. \quad (1.21)$$

This operator is no longer Hermitean and, therefore, its eigenvalues are in general complex. However, the spectrum of the rotated Hamiltonian is related to the spectrum of the unrotated operator according to (see Fig. 1.4) [84, 86, 88]:

1. The bound spectrum of  $H$  is invariant under the complex rotation.
2. The continuum states are located on half lines, rotated by an angle  $-2\theta$  around the ionization thresholds of the unrotated Hamiltonian into the lower half of the complex plane.
3. There are isolated complex eigenvalues  $E_{i,\theta} = E_i - i\Gamma_i/2$  in the lower half plane, corresponding to resonance states. These are stationary under changes of  $\theta$ , provided the dilation angle is large enough to uncover their positions on the Riemannian sheets of the associated resolvent [89, 90]. The associated resonance eigenfunctions are square integrable [87], in contrast to the resonance eigenfunctions of the unrotated Hamiltonian.

The eigenstates of  $H(\theta)$ ,

$$H(\theta) |\Psi_{i,\theta}\rangle = E_{i,\theta} |\Psi_{i,\theta}\rangle, \quad (1.22)$$

are normalized for the scalar product

$$\langle \Psi_{j,-\theta} | \Psi_{i,\theta} \rangle = \delta_{ij}, \quad (1.23)$$

and satisfy the closure relation:

$$\sum_i |\Psi_{i,\theta}\rangle \langle \Psi_{i,-\theta}| = 1. \quad (1.24)$$

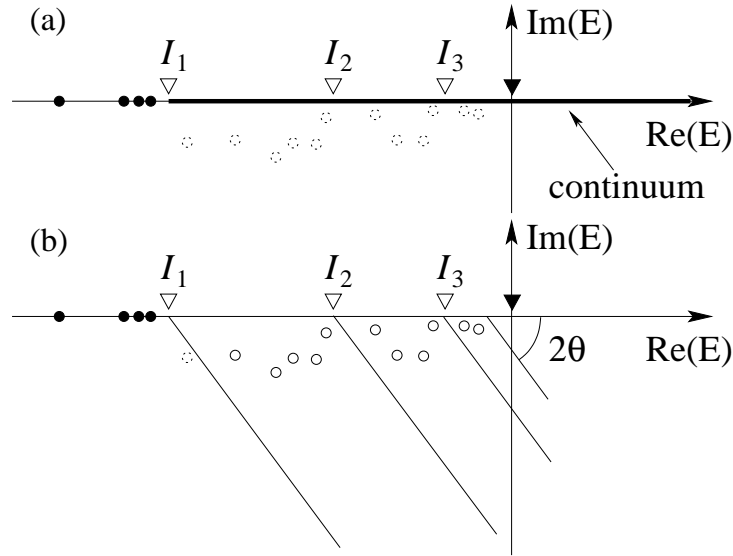


Figure 1.4: (a) Spectrum of the unrotated Hamiltonian. Bound states are denoted by black filled circles. Continuum cuts (solid black lines) starting from the ionization thresholds on the real axis and the resonances remain hidden (dotted circles). Triangles indicate the single ( $\nabla$ ) and double ( $\blacktriangledown$ ) ionization thresholds. (b) Spectrum of the complex rotated Hamiltonian  $H(\theta)$ . The continua are rotated by an angle  $-2\theta$  around the ionization thresholds in the lower half plane, uncovering resonances (continuous circles) if  $\theta$  is large enough.

Following [91], the Green function of the rotated Hamiltonian reads:

$$G_\theta = \frac{1}{E - H(\theta)} = \sum_i \frac{|\Psi_{i,\theta}\rangle\langle\Psi_{i,-\theta}|}{E - E_{i,\theta}}, \quad (1.25)$$

while the relation between the Green function of the unrotated Hamiltonian and Eq. (1.25) has been shown [92] to be:

$$G(E) = \frac{1}{E - H} = R(-\theta)G_\theta(E)R(\theta). \quad (1.26)$$

The projection operator on a real energy eigenstate is related to the Green function through

$$|\phi_E\rangle\langle\phi_E| = \frac{1}{2i\pi} (G^-(E) - G^+(E)), \quad (1.27)$$

with

$$G^\pm(E) = \frac{1}{E \pm i\eta - H}, \quad \eta \rightarrow 0^+. \quad (1.28)$$

Using Eq. (1.25) and Eq. (1.26) gives for the projection operator on a real energy eigenstate, in terms of the eigenstates of the rotated Hamiltonian,

$$|\phi_E\rangle\langle\phi_E| = \frac{1}{2i\pi} \sum_i \left[ \frac{R(-\theta)|\Psi_{i,\theta}\rangle\langle\Psi_{i,-\theta}|R(\theta)}{E_{i,\theta} - E} - \frac{R(\theta)|\Psi_{i,-\theta}\rangle\langle\Psi_{i,\theta}|R(-\theta)}{E_{i,-\theta} - E} \right]. \quad (1.29)$$

## Chapter 2

# Planar two-electron atom model

This chapter gives a brief review of our treatment of a planar two-electron atom [25, 26, 93–95]. After a justification of the planar model using semiclassical arguments (Sec. 2.1), a set of parabolic coordinates is introduced, which induces a representation in terms of creation and annihilation operators of four harmonic oscillators (Sec. 2.2). The key features of this representation are given, including the computation of photoionization cross sections, probability densities and the expectation value of  $\cos(\theta_{12})$ , which will be needed in chapters 5 and 6. Section 2.3 is concerned with a brief description of the spectral properties of the planar model. Finally, a brief description of the numerical implementation is presented in section 2.4.

### 2.1 Why consider a planar two-electron atom model?

In the planar two-electron atom model we confine the dynamics to two dimensions of the configuration space, with Cartesian positions  $(x_1, y_1)$  and  $(x_2, y_2)$  of the electrons. The planar two-electron atom dynamics thus has four degrees of freedom which span an eight-dimensional phase space. While such a confinement of the dynamics to a plane in configuration space certainly restricts the generality of our model, semiclassical scaling arguments – presented in the following – suggest, that the three-body dynamics is essentially planar at high electronic excitations and at small to moderate total angular momenta [25].

Both the classical and the quantum mechanical dynamics of a two-electron atom with a fixed nucleus in non-relativistic treatment are governed by the Hamiltonian (1.5). The classical dynamics is invariant under scaling transformations [96]:

$$\begin{aligned} H &\mapsto |E|^{-1} H \\ \vec{r}_i &\mapsto |E| \vec{r}_i, & (i = 1, 2), \\ \vec{p}_i &\mapsto |E|^{-1/2} \vec{p}_i, & (i = 1, 2), \\ t &\mapsto \lambda^{3/2} t, \end{aligned} \tag{2.1}$$

where  $E$  is the energy of the two-electron system. The angular momentum thus scales as  $L^{\text{sc}} = |E|^{1/2} L$ . Therefore, for moderate values of  $L$  and highly doubly excited states ( $E \simeq 0$ ), the scaled angular momentum is close to zero, tantamount to an almost planar three-body configuration. Precisely this is the semiclassical energy regime where one expects the classical and quantum mechanical dynamics to be similar.

The planar model comes with essentially two advantages. Firstly, it has a reduced complexity compared to the full three-dimensional treatment paired with an at least good qualitative description [97]. Secondly, similar to the description of the three-dimensional system in perimeteric coordinates [12] with Coulomb-Sturmian functions [98, 99] the approach leads to selection rules and allows an exact analytic computation of the matrix elements [53, 54]. However, the

number of selection rules is independent of the total angular momentum in the planar model and thus bears no additional difficulty for the description of states for larger values of the total angular momentum.

## 2.2 Planar approach

The computation and discussion of the spectrum, localization properties and photoionization cross sections of two-electron atoms demand – apart from the confinement of the dynamics to a plane in configuration space – a description of the system with a minimum of approximations. In particular the description of resonances plays a key role. To extract the resonance states and their decay rates the complex rotation method (see Sec. 1.4) is used. All the relevant physical information is contained in the spectrum of the rotated Hamiltonian, and can be obtained by a subsequent diagonalization. However, one of the main difficulties to actually perform this diagonalization are the Coulomb singularities in the Hamiltonian (1.5). Nevertheless, choosing an appropriate representation in parabolic coordinates [93], the singularities are rigorously regularized.

### 2.2.1 Transformation to parabolic coordinates

The appropriate set of parabolic coordinates is obtained after three subsequent coordinate transformations (see also appendix A.1). Starting with the Cartesian coordinates of both electrons  $(x_1, y_1)$  and  $(x_2, y_2)$ , respectively, the first transformation leads to polynomial expressions in the new coordinates  $\mu_i, \nu_i$  ( $i = 1, 2$ ) only for  $r_1$  and  $r_2$ ,

$$\begin{aligned} x_i &= \frac{1}{2}(\mu_i^2 - \nu_i^2), & \mu_i &= \sqrt{r_i + x_i}, \\ y_i &= \mu_i \nu_i, & \nu_i &= \sqrt{r_i - x_i}, \\ r_i &= \sqrt{x_i^2 + y_i^2} = \frac{1}{2}(\mu_i^2 + \nu_i^2), & i &= 1, 2, \end{aligned} \quad (2.2)$$

while  $r_{12}$  still involves square root functions of  $\mu_i$  and  $\nu_i$ .

The second transformation consists in a rotation by  $\pi/4$  of each pair  $(\mu_1, \mu_2)$  and  $(\nu_1, \nu_2)$  of the new coordinates

$$\begin{aligned} \mu_p &= (\mu_1 + \mu_2)/\sqrt{2}, & \mu_1 &= (\mu_p + \mu_m)/\sqrt{2}, \\ \mu_m &= (\mu_1 - \mu_2)/\sqrt{2}, & \mu_2 &= (\mu_p - \mu_m)/\sqrt{2}, \\ \nu_p &= (\nu_1 + \nu_2)/\sqrt{2}, & \nu_1 &= (\nu_p + \nu_m)/\sqrt{2}, \\ \nu_m &= (\nu_1 - \nu_2)/\sqrt{2}, & \nu_2 &= (\nu_p - \nu_m)/\sqrt{2}. \end{aligned} \quad (2.3)$$

resulting for the interelectronic separation in  $r_{12} = \sqrt{(\mu_p^2 + \nu_p^2)(\mu_m^2 + \nu_m^2)}$ .

After another parabolic transformation,  $r_{12}$  will also be a polynomial function of the coordinates. The final coordinate set is defined as

$$\begin{aligned} \mu_p &= (x_p^2 - y_p^2)/2, & x_p &= \sqrt{r_p + \mu_p}, \\ \nu_p &= x_p y_p, & y_p &= \sqrt{r_p - \mu_p}, \\ \mu_m &= (x_m^2 - y_m^2)/2, & x_m &= \sqrt{r_m + \mu_m}, \\ \nu_m &= x_m y_m, & y_m &= \sqrt{r_m - \mu_m}, \\ r_p &= \sqrt{\mu_p^2 + \nu_p^2} = (x_p^2 + y_p^2)/2, \\ r_m &= \sqrt{\mu_m^2 + \nu_m^2} = (x_m^2 + y_m^2)/2, \end{aligned} \quad (2.4)$$

leading to the following representation of  $r_1$ ,  $r_2$  and  $r_{12}$  in terms of  $x_p$ ,  $y_p$ ,  $x_m$  and  $y_m$ :

$$\begin{aligned} r_1 &= \frac{1}{16} [(x_p - y_m)^2 + (x_m + y_p)^2] [(x_p + y_m)^2 + (x_m - y_p)^2] \\ r_2 &= \frac{1}{16} [(x_p - x_m)^2 + (y_p - y_m)^2] [(x_p + x_m)^2 + (y_p + y_m)^2] \\ r_{12} &= \frac{1}{4} (x_p^2 + y_p^2) (x_m^2 + y_m^2). \end{aligned} \quad (2.5)$$

The Jacobian of each parabolic transformation in (2.2) is  $\mu_i + \nu_i = 2r_i$ . Thus, the Jacobian of the first transformation is  $J_1 = 4r_1r_2$ . The second transformation corresponds to two rotations, hence  $J_2 = 1$ . The third transformation is again composed of two parabolic transformations, therefore  $J_3 = (x_p^2 + y_p^2)(x_m^2 + y_m^2) = 4r_{12}$ . The Jacobian of the complete transformation reads

$$B = J_1J_2J_3 = 16r_1r_2r_{12}. \quad (2.6)$$

### 2.2.2 Stationary Schrödinger equation

The stationary Schrödinger equation  $H|\Psi\rangle = E|\Psi\rangle$  of the planar two-electron atom is regularized by multiplication with the Jacobian (2.6). The eigenvalue equation then takes the form of a generalized eigenvalue problem:

$$\left(-\frac{1}{2}\tilde{T} + \tilde{V}\right)|\Psi\rangle = EB|\Psi\rangle, \quad (2.7)$$

where the kinetic and potential operators,  $\tilde{T}$  and  $\tilde{V}$ , are given by

$$\begin{aligned} \tilde{T} &= 16r_1r_2r_{12}(\nabla_1^2 + \nabla_2^2), \\ \tilde{V} &= -16Zr_2r_{12} - 16Zr_1r_{12} + 16r_1r_2. \end{aligned} \quad (2.8)$$

The explicit expression for the potential term  $\tilde{V}$  in terms of parabolic coordinates follows upon substitution of Eq. (2.5). The expression for the kinetic term  $\tilde{T}$  is a bit more complicated,

$$\begin{aligned} \tilde{T} &= (r_1 + r_2) \left\{ (x_p^2 + y_p^2) \left( \frac{\partial^2}{\partial x_m^2} + \frac{\partial^2}{\partial y_m^2} \right) + (x_m^2 + y_m^2) \left( \frac{\partial^2}{\partial x_p^2} + \frac{\partial^2}{\partial y_p^2} \right) \right\} \\ &+ 2(r_2 - r_1) \left\{ (x_mx_p + y_my_p) \left( \frac{\partial^2}{\partial x_m \partial x_p} + \frac{\partial^2}{\partial y_m \partial y_p} \right) \right. \\ &\quad \left. + (y_mx_p - x_my_p) \left( \frac{\partial^2}{\partial x_m \partial y_p} - \frac{\partial^2}{\partial y_m \partial x_p} \right) \right\}. \end{aligned} \quad (2.9)$$

$\tilde{T}$  and  $\tilde{V}$  are polynomial functions of eighth degree in the parabolic coordinates  $x_p$ ,  $y_p$ ,  $x_m$ ,  $y_m$  and their partial derivatives  $\partial_{x_p}$ ,  $\partial_{y_p}$ ,  $\partial_{x_m}$ ,  $\partial_{y_m}$ . The Jacobian  $B$  has a polynomial expression of degree twelve.

### Angular momentum

The angular momentum  $L_z$  – an important quantity in our further treatment – has a particularly simple polynomial expression in terms of the parabolic coordinates (2.5). Note, that it preserves its original differential form except for a prefactor:

$$\begin{aligned} L_z &= -i \left( x_1 \frac{\partial}{\partial y_1} - y_1 \frac{\partial}{\partial x_1} + x_2 \frac{\partial}{\partial y_2} - y_2 \frac{\partial}{\partial x_2} \right) \\ &= -\frac{i}{4} \left( x_p \frac{\partial}{\partial y_p} - y_p \frac{\partial}{\partial x_p} + x_m \frac{\partial}{\partial y_m} - y_m \frac{\partial}{\partial x_m} \right). \end{aligned} \quad (2.10)$$

### 2.2.3 Harmonic oscillator representation

The various terms of the general eigenvalue problem (2.7) are polynomials in the coordinates and conjugate momenta, and can therefore be expressed using the corresponding creation and annihilation operators:

$$\begin{aligned}
a_{x_p} &= (x_p + ip_{x_p})/\sqrt{2}, & a_{x_p}^\dagger &= (x_p - ip_{x_p})/\sqrt{2}, \\
a_{x_m} &= (x_m + ip_{x_m})/\sqrt{2}, & a_{x_m}^\dagger &= (x_m - ip_{x_m})/\sqrt{2}, \\
a_{y_p} &= (y_p + ip_{y_p})/\sqrt{2}, & a_{y_p}^\dagger &= (y_p - ip_{y_p})/\sqrt{2}, \\
a_{y_m} &= (y_m + ip_{y_m})/\sqrt{2}, & a_{y_m}^\dagger &= (y_m - ip_{y_m})/\sqrt{2}.
\end{aligned} \tag{2.11}$$

From these expressions we deduce the right and left circular operators in the planes  $(x_p, y_p)$  and  $(x_m, y_m)$  defined by

$$\begin{aligned}
a_1 &= (a_{x_p} - ia_{y_p})/\sqrt{2}, \\
a_2 &= (a_{x_p} + ia_{y_p})/\sqrt{2}, \\
a_3 &= (a_{x_m} - ia_{y_m})/\sqrt{2}, \\
a_4 &= (a_{x_m} + ia_{y_m})/\sqrt{2}.
\end{aligned} \tag{2.12}$$

The full expressions for the operators  $\tilde{T}$ ,  $\tilde{V}$  and  $B$  in normal ordered circular operators (creation operators on the left) have 335, 357 and 1463 terms, respectively. The expressions have been obtained using a home-made MATHEMATICA code (for details see [25]). A much simpler expression is available for the angular momentum  $L_z$ :

$$L_z = \frac{1}{4} (a_1^\dagger a_1 - a_2^\dagger a_2 + a_3^\dagger a_3 - a_4^\dagger a_4) = \frac{1}{4} (N_1 - N_2 + N_3 - N_4), \tag{2.13}$$

where the  $N_i = a_i^\dagger a_i$ , ( $i = 1, 2, 3, 4$ ) are the corresponding number operators.

### 2.2.4 Selection rules

Since the circular operators satisfy the usual commutation relations,

$$[a_i, a_j] = 0, \quad [a_i^\dagger, a_j^\dagger] = 0, \quad [a_i, a_j^\dagger] = \delta_{ij}, \tag{2.14}$$

for  $i, j = 1, 2, 3, 4$ , we can associate a harmonic oscillator with each pair of circular operators  $a_i^\dagger$  and  $a_i$ . This induces a natural basis set composed of tensor products of harmonic oscillator Fock states:

$$|n_1 n_2 n_3 n_4\rangle = |n_1\rangle \otimes |n_2\rangle \otimes |n_3\rangle \otimes |n_4\rangle. \tag{2.15}$$

Due to the strictly polynomial form of (2.7) in the circular operators, each basis state couples to a limited number of states. Whether two states are coupled or not by some operator  $A$  is determined by a *selection rule* defined in the following way: Two elements  $|n_1 n_2 n_3 n_4\rangle$  and  $|n'_1 n'_2 n'_3 n'_4\rangle$  of the basis set (2.15) are coupled or satisfy the selection rule  $\{\Delta n_1, \Delta n_2, \Delta n_3, \Delta n_4\}$ , with  $\Delta n_i = n_i - n'_i$ , if  $\langle n_1 n_2 n_3 n_4 | A | n'_1 n'_2 n'_3 n'_4 \rangle \neq 0$ . It is found that the Jacobian  $B$  and the sum of the kinetic and potential operators  $-\frac{1}{2}\tilde{T} + \tilde{V}$  have 155 and 91 selection rules, respectively [25]. For a given selection rule  $\Delta \mathbf{n} = \{\Delta n_1, \Delta n_2, \Delta n_3, \Delta n_4\}$ , the matrix elements  $\langle \mathbf{n} + \Delta \mathbf{n} | -\frac{1}{2}\tilde{T} + \tilde{V} | \mathbf{n} \rangle$  and  $\langle \mathbf{n} + \Delta \mathbf{n} | B | \mathbf{n} \rangle$ , with  $|\mathbf{n}\rangle = |n_1 n_2 n_3 n_4\rangle$  and  $|\mathbf{n} + \Delta \mathbf{n}\rangle = |n_1 + \Delta n_1 \ n_2 + \Delta n_2 \ n_3 + \Delta n_3 \ n_4 + \Delta n_4\rangle$ , involve square roots of integer numbers and depend only on  $n_1, n_2, n_3$  and  $n_4$ . For example, the matrix element of the operator  $-\frac{1}{2}\tilde{T} + \tilde{V}$  for the selection rule  $\Delta \mathbf{n} = \{-2, -2, 0, 0\}$  reads

$$\begin{aligned}
\langle \mathbf{n} + \Delta \mathbf{n} | -\frac{1}{2}\tilde{T} + \tilde{V} | \mathbf{n} \rangle &= \frac{1}{8} \sqrt{n_1(n_1-1)n_2(n_2-1)} \left( 8 + 3n_1^2 - 7n_2 + 3n_2^2 \right. \\
&\quad \left. + n_1(8n_2 - 7) - (n_1 + n_2 - 1)(n_3 + n_4 + 1)(12Z - 1) \right). \tag{2.16}
\end{aligned}$$

This and all other matrix elements were calculated with the help of symbolic calculus [25].

In addition to the selection rules for the atomic quantum numbers  $n_i$ , there are also selection rules for the angular momentum. For an unperturbed planar two-electron atom, the angular momentum is a conserved quantity,  $\Delta l = 0$ . Therefore, with (2.13), each selection rule  $\{\Delta n_1, \Delta n_2, \Delta n_3, \Delta n_4\}$  satisfies  $\Delta n_1 - \Delta n_2 + \Delta n_3 - \Delta n_4 = 0$ .

### 2.2.5 Remaining symmetries

The basis set (2.15) does not yet account for the symmetries of the system, and, therefore, must be appropriately symmetrized. The Hamiltonian commutes with the angular momentum  $L_z$ , and is invariant under rotations around a perpendicular axis  $z$ , under the exchange operation  $P_{12}$  and under the parity operation  $\Pi$  ( $\vec{r} \rightarrow -\vec{r}$ ). In two dimensions, the latter coincides with a rotation of  $180^\circ$  around  $z$ , so that  $\Pi$  and the angular momentum  $L_z$  are related by

$$\Pi = e^{-i\pi L_z} = (-1)^{L_z} . \quad (2.17)$$

In addition, the Hamiltonian commutes with the reflections  $\Pi_x$  and  $\Pi_y$  with respect to the coordinate axes  $x$  and  $y$ , respectively, which are connected via

$$\Pi = \Pi_x \Pi_y = \Pi_y \Pi_x , \quad (2.18)$$

to the total parity, with which both  $\Pi_x$  and  $\Pi_y$  commute. However, the symmetries  $\Pi_x$  and  $\Pi_y$  do not commute with the angular momentum, since

$$\Pi_x L_z = -L_z \Pi_x , \quad (2.19)$$

but do commute with  $L_z^2$ . The representation in parabolic coordinates introduces nonphysical symmetries induced by the two-fold coordinate transformation [Eq. (2.2) and (2.3)] [25, 93]. The basis elements need to be properly symmetrized in order to get rid of these. Considering the symmetries mentioned beforehand, there are two alternatives to label the eigenstates of planar two-electron atoms. On the one hand, one can use the eigenvalues  $l = 0, \pm 1, \pm 2, \dots$  of angular momentum  $L_z$  and the exchange symmetry  $P_{12} = \pm 1$ , in which case the spectra corresponding to  $l$  and  $-l$  are identical, as a consequence of the time reversal invariance of the problem [100]. On the other hand, the eigenstates can be labeled by the absolute value  $|l|$  of the angular momentum  $L_z$ , the exchange symmetry, and the symmetry  $\Pi_x = \pm 1$ .

The symmetrized basis adapted for  $P_{12}$  and  $L_z$  is defined by [25, 93]

$$|n_1 n_2 n_3 n_4\rangle^+ = |n_1 n_2 n_3 n_4\rangle + |n_3 n_4 n_1 n_2\rangle , \quad (2.20)$$

with  $n_1 - n_2 + n_3 - n_4 = 4L_z$  and  $n_1 - n_2 \equiv n_3 - n_4 \equiv c_{12} \pmod{4}$  ( $c_{12} = 0$  for singlet states, and  $c_{12} = 2$  for triplet states).

Since  $\Pi_x L_z = -L_z \Pi_x$  the basis elements (2.20) are not eigenstates of  $\Pi_x$ . However, the basis elements

$$|n_1 n_2 n_3 n_4\rangle^{+\epsilon_x} = |n_1 n_2 n_3 n_4\rangle^+ + \epsilon_x |n_2 n_1 n_4 n_3\rangle^+ , \quad (2.21)$$

where  $\epsilon_x = \pm 1$ , are properly symmetrized with respect to  $L_z^2$ ,  $P_{12}$  and  $\Pi_x$  [25, 26]. Note, that this choice can also be used for the case when the atom is exposed to an electromagnetic field polarized along the  $x$  direction, where the Hamiltonian is not invariant under the parity operation  $\Pi$ .

For the description of resonances this approach is combined with the complex rotation method described in section 1.4.

### 2.2.6 Cross section

Fermi's Golden rule results for the photoionization cross section in (see e.g. [101]):

$$\sigma(\omega) = \frac{4\pi^2\omega}{c} |\langle \phi_E | D | \phi_E^{\text{in}} \rangle|^2, \quad (2.22)$$

where  $|\phi_E^{\text{in}}\rangle$  denotes the initial state with energy  $E_{\text{in}}$ ,  $|\phi_E\rangle$  a state with energy  $E = E_{\text{in}} + \omega$ , and  $D = \vec{e} \cdot \vec{r}$  the dipole operator with the light polarization  $\vec{e}$ . Combining Eq. (1.29) and Eq. (2.22) leads to

$$\sigma(\omega) = \frac{2\pi\omega}{ic} \sum_i \left[ \frac{\langle \phi_E^{\text{in}} | DR(-\theta) | \Psi_{i,\theta} \rangle \langle \Psi_{i,-\theta} | R(\theta) D | \phi_E^{\text{in}} \rangle}{E_{i,\theta} - E} - \frac{\langle \phi_E^{\text{in}} | DR(\theta) | \Psi_{i,-\theta} \rangle \langle \Psi_{i,\theta} | R(-\theta) D | \phi_E^{\text{in}} \rangle}{E_{i,-\theta} - E} \right]. \quad (2.23)$$

Substitution of  $\theta$  by  $-\theta$  is, for a real representation of the unrotated Hamiltonian, equivalent to changing  $H(\theta)$  into its complex conjugate, resulting in

$$\begin{aligned} E_{i,-\theta} &= \overline{E_{i,\theta}}, \\ |\Psi_{i,-\theta}\rangle &= \overline{|\Psi_{i,\theta}\rangle}, \end{aligned} \quad (2.24)$$

where  $\overline{E_{i,\theta}}$  and  $\overline{|\Psi_{i,\theta}\rangle}$  are the complex conjugate of  $E_{i,\theta}$  and  $|\Psi_{i,\theta}\rangle$ , respectively. As has been stated in [91], Eq. (2.23) is somewhat formal, as  $R(-\theta)|\Psi_{i,\theta}\rangle$  is not a well defined state, and  $\langle \phi_E^{\text{in}} | DR(-\theta) | \Psi_{i,\theta} \rangle$  has to be understood as  $\langle \overline{\Psi_{i,\theta}} | R(\theta) D | \phi_E^{\text{in}} \rangle$ . The last expression coincides, for an initial state with a real radial wavefunction, with  $\langle \overline{\Psi_{i,\theta}} | R(\theta) D | \phi_E^{\text{in}} \rangle$ . The second term of Eq. (2.23) has to be understood and translated in an analogous manner. Together with Eq. (2.24) this leads to the final result:

$$\sigma(\omega) = \frac{4\pi\omega}{c} \text{Im} \left[ \sum_i \frac{\langle \overline{\Psi_{i,\theta}} | R(\theta) D | \phi_E^{\text{in}} \rangle^2}{E_{i,\theta} - E_{\text{in}} - \omega} \right]. \quad (2.25)$$

Transformation into the appropriate coordinates allows one to represent the matrix elements of the dipole operator in the creation and annihilation operators,  $a_j, a_j^\dagger$ ,  $j = 1, 2, 3, 4$ . In practice light polarized along the  $x$  axis is used, leading to  $D = x_1 + x_2$ .

### 2.2.7 Expectation value of $\cos(\theta_{12})$

The expectation value of  $\cos(\theta_{12})$  for a given state  $\phi_E$  of energy  $E$  is obtained, up to normalization of  $|\phi_E\rangle$ , by

$$\begin{aligned} \langle \phi_E | \cos(\theta_{12}) | \phi_E \rangle &= \frac{1}{2\pi i} \sum_i \left[ \frac{\langle \Psi_{i,-\theta} | \cos(\theta_{12}) | \Psi_{i,\theta} \rangle}{E_{i,\theta} - E} - \frac{\langle \Psi_{i,\theta} | \cos(\theta_{12}) | \Psi_{i,-\theta} \rangle}{E_{i,-\theta} - E} \right] \\ &= \frac{1}{\pi} \text{Im} \left[ \sum_i \frac{\langle \overline{\Psi_{i,\theta}} | \cos(\theta_{12}) | \Psi_{i,\theta} \rangle}{E_{i,\theta} - E} \right], \end{aligned} \quad (2.26)$$

where we have used the projector (1.29). Similarly, the square of the norm of  $|\phi_E\rangle$  reads as

$$\begin{aligned} \langle \phi_E | \phi_E \rangle &= \frac{1}{2\pi i} \sum_i \left[ \frac{\langle \Psi_{i,-\theta} | \Psi_{i,\theta} \rangle}{E_{i,\theta} - E} - \frac{\langle \Psi_{i,\theta} | \Psi_{i,-\theta} \rangle}{E_{i,-\theta} - E} \right] \\ &= \frac{1}{\pi} \text{Im} \left[ \sum_i \frac{1}{E_{i,\theta} - E} \right], \end{aligned} \quad (2.27)$$

where the normalization (1.23) of  $|\Psi_{i,\theta}\rangle$  has been taken into account in the last step. The expectation value is thus given by

$$\langle \cos(\theta_{12}) \rangle = \frac{\langle \phi_E | \cos(\theta_{12}) | \phi_E \rangle}{\langle \phi_E | \phi_E \rangle} = \frac{\text{Im} \left[ \sum_i \frac{\langle \overline{\Psi}_{i,\theta} | \cos(\theta_{12}) | \Psi_{i,\theta} \rangle}{E_{i,\theta} - E} \right]}{\text{Im} \left[ \sum_i \frac{1}{E_{i,\theta} - E} \right]}. \quad (2.28)$$

A well isolated resonance  $|\Psi_{j,\theta}\rangle$  with  $E_{j,\theta} \simeq E$  and  $|\text{Re}(E_{j,\theta}) - \text{Re}(E_{i,\theta})| \gg |E_{j,\theta} - E|$ ,  $\forall i \neq j$ , gives the dominant contribution to the above sum, and justifies the *single pole approximation* [91]

$$\langle \phi_E | \cos(\theta_{12}) | \phi_E \rangle \simeq \frac{1}{\pi |\text{Im}(E_{i,\theta})|} \text{Re} \langle \overline{\Psi}_{i,\theta} | \cos(\theta_{12}) | \Psi_{i,\theta} \rangle, \quad (2.29)$$

$$\langle \phi_E | \phi_E \rangle \simeq \frac{1}{\pi |\text{Im}(E_{i,\theta})|}, \quad (2.30)$$

leading to

$$\langle \cos(\theta_{12}) \rangle \simeq \text{Re} \langle \overline{\Psi}_{i,\theta} | \cos(\theta_{12}) | \Psi_{i,\theta} \rangle. \quad (2.31)$$

After transformation to appropriate parabolic coordinates the matrix elements of  $\cos(\theta_{12})$  can be expressed as polynomials in the coordinates and thus be represented through the creation and annihilation operators,  $a_j, a_j^\dagger$ ,  $j = 1, 2, 3, 4$  resulting in 2088 monomial terms associated with 171 selection rules in the Fock basis.

### 2.2.8 Electronic densities

The electronic density of a given state  $|\phi_E\rangle$  can be obtained from the projection operator (1.29) on the given state [54, 91, 102]. The electronic probability density in configuration space reads [91] up to normalization,<sup>1</sup>

$$\begin{aligned} |\widetilde{\phi_E(\vec{r})}|^2 &= \langle \vec{r} | \phi_E \rangle \langle \phi_E | \vec{r} \rangle \\ &= \frac{1}{\pi} \text{Im} \sum_j \frac{\langle \vec{r} | R(-\theta) | \Psi_{j,\theta} \rangle \langle \overline{\Psi}_{j,\theta} | R(\theta) | \vec{r} \rangle}{E_{j,\theta} - E} \\ &= \frac{1}{\pi} \text{Im} \sum_j \frac{\langle \vec{r} | R(-\theta) | \Psi_{j,\theta} \rangle^2}{E_{j,\theta} - E}. \end{aligned} \quad (2.32)$$

In the single pole approximation the density is given by,

$$|\phi_E(\vec{r})|^2 \simeq \text{Re} \langle \vec{r} | R(-\theta) | \Psi_{j,\theta} \rangle^2, \quad (2.33)$$

where the correct normalization (2.30) has already been included. In terms of the basis set (2.21)  $\langle \vec{r} | R(-\theta) | \Psi_{j,\theta} \rangle$  reads

$$\langle \vec{r} | R(-\theta) | \Psi_{j,\theta} \rangle = \sum_{\mathbf{n}} \langle \vec{r} | \mathbf{n} \rangle^{+\epsilon_x} \langle \mathbf{n} | R(-\theta) | \Psi_{j,\theta} \rangle, \quad (2.34)$$

where  $\mathbf{n}$  denotes the set of quantum numbers  $n_1, n_2, n_3$  and  $n_4$ . Therefore, we need an expression for the basis states  $|n_1 n_2 n_3 n_4\rangle^{+\epsilon_x}$  in the coordinate representation, together with a matrix

---

<sup>1</sup> $|\widetilde{\phi_E(\vec{r})}|^2$  stands for the unnormalized density.

representation of the operator  $R(-\theta)$ . In both cases, it is sufficient to derive this for the product states  $|n_1 n_2 n_3 n_4\rangle$ , by virtue of (2.20) and (2.21).

Since the circular operators given by (2.12) are independently defined for the pairs  $(x_p, y_p)$  and  $(x_m, y_m)$  of parabolic coordinates,  $\langle \vec{r} | n_1 n_2 n_3 n_4 \rangle$ , if written in parabolic coordinates, can be expressed as a product of two functions depending on  $(x_p, y_p)$  and  $(x_m, y_m)$ , respectively, i.e.,  $\langle \vec{r} | n_1 n_2 n_3 n_4 \rangle = \langle x_p, y_p | n_1 n_2 \rangle \langle x_m, y_m | n_3 n_4 \rangle$ , where

$$\langle x_p, y_p | n_1 n_2 \rangle = \sqrt{\frac{1}{\pi}} \sqrt{\frac{n_p!}{(n_p + |m_p|)!}} e^{im_p \phi_p} r_p^{|m_p|} e^{-r_p^2/2} L_{n_p}^{(|m_p|)}(r_p^2), \quad (2.35)$$

with  $n_p = \min\{n_1, n_2\}$ ,  $m_p = n_1 - n_2$ ;  $L_{n_p}^{(|m_p|)}(r)$  is the generalized Laguerre polynomial [103]. By analogy, the expression for  $\langle r_m, \phi_m | n_3 n_4 \rangle$  has precisely the same form. The functions (2.35) are often termed Darwin-Fock states [104, 105]. Note, that the coordinate representation of  $|n_1 n_2 n_3 n_4\rangle$  contains a factor  $e^{-(r_p^2 + r_m^2)/2} = e^{-(x_p^2 + y_p^2 + x_m^2 + y_m^2)/2}$ , and therefore, from (2.5), the product state  $\langle \vec{r} | n_1 n_2 n_3 n_4 \rangle$  decays roughly as  $e^{-\sqrt{r_1 + r_2}}$ .

For the calculation of the matrix elements of  $R(-\theta)$ , we note that this operator can be expressed as a product of two rotation operators  $R_p(-\theta)$  and  $R_m(-\theta)$ , acting on the spaces  $(x_p, y_p)$  and  $(x_m, y_m)$ , respectively, and thus, as before:

$$\langle n_1 n_2 n_3 n_4 | R(-\theta) | n'_1 n'_2 n'_3 n'_4 \rangle = \langle n_1 n_2 | R_p(-\theta) | n'_1 n'_2 \rangle \langle n_3 n_4 | R_m(-\theta) | n'_3 n'_4 \rangle. \quad (2.36)$$

The matrix elements of  $R_p(-\theta)$  in the representation given by the product states  $|n_1 n_2\rangle$  read [106]

$$\begin{aligned} \langle n_1 n_2 | R_p(-\theta) | n'_1 n'_2 \rangle &= (-1)^{n'_p} \sqrt{\binom{n_p + |m_p|}{n_p} \binom{n'_p + |m_p|}{n'_p}} i^{n_p + n'_p} (\sin \theta)^{n_p + n'_p} \\ &\times (\cos \theta)^{-(n_p + n'_p + |m_p| + 1)} F\left(-n_p, -n'_p, |m_p| + 1; -\frac{1}{\sin^2 \theta}\right) \delta_{m_p m'_p}, \end{aligned} \quad (2.37)$$

where  $n_p = \min\{n_1, n_2\}$ ,  $m_p = n_1 - n_2$ ,  $n'_p = \min\{n'_1, n'_2\}$ ,  $m'_p = n'_1 - n'_2$ , and  $F(a, b, c; x)$  is the hypergeometric function [103] (which reduces to a polynomial here). Analogously, we obtain the expression for the matrix elements of  $R_m(-\theta)$ , with a formally identical result.

Combining (2.37) and (2.35) in (2.33), we obtain the electronic density in configuration space.

## 2.3 Spectral structure

Before coming to the numerical treatment let us have a brief look at the spectral structure of planar two-electron atoms. The general spectral structure of a planar two-electron atom is similar to the one described in section 1.3 for the real atom, however, there are some important differences.

The ionization thresholds are given by the energy levels of the one-electron system remaining after ionization. These energy levels are given by (see appendix A.2.2) [25, 93]

$$I_N^{2D} = -\frac{Z^2}{2(N - \frac{1}{2})^2}, \quad (2.38)$$

instead of

$$I_N^{3D} = -\frac{Z^2}{2N^2}, \quad (2.39)$$

for the three-dimensional system.

As already shown in section 2.2.5, planar two-electron atoms are restricted to the description of states with parity  $\pi = (-1)^{|l|}$ . However, for the classification of states the parity  $\pi_x$  with respect to reflection by the  $x$ -axis is used. For  $|l| = 0$  the spectrum consists for  $\Pi_x = 1$  and  $\Pi_x = -1$  of bound states below first and second ionization threshold, respectively, with resonances starting to appear above these threshold. For  $|l| > 0$  the spectra for  $\Pi_x = 1$  and  $\Pi_x = -1$  are degenerate. This is a consequence of the degeneracy of the energy levels for  $l$  and  $-l$  ( $l > 0$ ). Bound states and resonances occur below and above the first single ionization threshold, respectively.

The Herrick classification can be applied to the planar model of two-electron atoms by remembering, that if the two electron orbits are on the same plane, then  $T = 0$  [78, 97]. A consequence of this is, there are, for total angular momentum  $|l| > 0$ , fewer series converging to individual single ionization thresholds than for the three-dimensional system with  $L = |l|$ .

## 2.4 Numerical treatment

### 2.4.1 Matrix representation

Representing the stationary Schrödinger equation for a planar two-electron atom in the basis set (2.21) leads to the generalized eigenvalue problem

$$\tilde{\mathbf{H}}_{\theta}^{\alpha} \Psi_{i,\theta} = E_{i,\theta} \mathbf{B} \Psi_{i,\theta}, \quad (2.40)$$

where  $\Psi_{i,\theta}$  is the vector representation of  $|\Psi_{i,\theta}\rangle$ ,  $\tilde{\mathbf{H}}_{\theta}^{\alpha}$  and  $\mathbf{B}$  are the matrices associated with the complex rotated (Coulomb singularity regularized) Hamiltonian and the Jacobian. Together with the rotation of configuration space by an angle  $\theta$  into the complex plane, a dilation by a positive real number  $\alpha$  is used, such that the (Cartesian) coordinates and momenta transform according to

$$\vec{r} \rightarrow \alpha \vec{r} e^{i\theta}, \quad \vec{p} \rightarrow \frac{1}{\alpha} \vec{p} e^{-i\theta}. \quad (2.41)$$

As the dilation by a factor  $\alpha$  is a unitary transformation [90, 100, 106] described by the unitary operator

$$D_{\alpha} = \exp \left[ i \log(\alpha) \frac{\vec{r} \cdot \vec{p} + \vec{p} \cdot \vec{r}}{2} \right], \quad (2.42)$$

the spectra of a Hamiltonian  $H$  and of the dilated Hamiltonian  $H^{\alpha} = D_{\alpha} H D_{\alpha}^{\dagger}$  are identical. However, if the basis is truncated, the spectrum *does* depend on the parameter  $\alpha$  in case that the basis set is not large enough. Thus,  $\alpha$  can be used as a variational parameter that has to be optimized.

The selection rules for the Hamiltonian and Jacobian (Sec. 2.2.4) couple only a finite number of basis elements, which can readily be computed by exact analytical expressions. Together with the necessity of a truncation of the basis for the numerical implementation this leads to a finite number of non-zero matrix elements. The complex rotation method leads to a matrix representation of the Hamiltonian as a complex symmetric matrix. Altogether,  $\tilde{\mathbf{H}}_{\theta}^{\alpha}$  and  $\mathbf{B}$  are represented by sparse banded symmetric matrices with complex and real entries, respectively.

### Construction of the basis

As described in section 2.2.5 the basis  $|n_1 n_2 n_3 n_4\rangle^{+\epsilon_x}$  decomposes for a given value of  $|l|$  into the subspace of singlet and triplet states, and of even or odd states with respect to the symmetry

$\Pi_x$ , with the following identification:

$$\left\{ \begin{array}{ll} \epsilon_x = \pm 1 & \text{even or odd states with respect to } \Pi_x, \\ n_1 - n_2 \equiv n_3 - n_4 \equiv 0 \pmod{4} & \text{singlet states,} \\ n_1 - n_2 \equiv n_3 - n_4 \equiv 2 \pmod{4} & \text{triplet states.} \end{array} \right. \quad (2.43)$$

However, due to twofold symmetrization of the basis [Eq. (2.20) and Eq. (2.21)], each element of the symmetrized basis can be represented by four quadruplets  $(n_1, n_2, n_3, n_4)$ ,  $(n_2, n_1, n_4, n_3)$ ,  $(n_3, n_4, n_1, n_2)$  and  $(n_4, n_3, n_2, n_1)$ . The basis must only contain one of these quadruplets and is unambiguously defined for  $\epsilon_x = 1$ , if each quadruplet  $(n_1, n_2, n_3, n_4)$  satisfies one of the following conditions:

$$\left\{ \begin{array}{l} |l| > 0 \quad \text{and} \quad n_1 \geq n_3, \\ |l| = 0 \quad \text{and} \quad n_1 > n_3 \quad \text{and} \quad n_1 \geq n_4 > n_2, \\ \quad \quad \quad n_1 > n_3 \quad \text{and} \quad n_1 > n_2 > n_4, \\ \quad \quad \quad n_1 > n_3 \quad \text{and} \quad n_1 = n_2, \\ \quad \quad \quad n_1 = n_3 \quad \text{and} \quad n_2 > n_4, \\ \quad \quad \quad n_1 = n_3 = n_2 = n_4. \end{array} \right. \quad (2.44)$$

The basis spanning the subspace for odd symmetry with respect to the  $x$  axis ( $\epsilon_x = -1$ ) is defined by the same conditions, however, with basis states  $n_1 = n_3 = n_2 = n_4$  forbidden [see Eq. (2.21)].

For the numerical implementation, the infinite symmetrized basis set also needs to be truncated. For a given angular momentum  $|l|$  the basis is truncated according to

$$n_1 + n_2 + n_3 + n_4 \leq n_{\text{base}}, \quad (2.45)$$

with  $n_{\text{base}}$  a given positive integer.

### Dimensions of matrices

The dimensions of the matrices which give well converged eigenvalues and eigenvectors are rather large: the number of elements along the diagonal, denoted by  $n_{\text{tot}}$ , scales as  $n_{\text{tot}} \simeq n_{\text{base}}^3/360$  and  $n_{\text{tot}} \simeq n_{\text{base}}^3/180$  for angular momentum  $|l| = 0$  and  $|l| > 0$ , respectively. E.g., for an accurate description of the spectrum of triplet planar helium for total angular momentum  $|l| = 1$  and  $\Pi_x = 1$  below the 25th single ionization threshold a basis size of  $n_{\text{tot}} = 586760$  ( $n_{\text{base}} = 480$ ) is needed. The rather slow convergence of eigenstates and eigenvectors with respect to the basis size can be understood considering the asymptotics of the basis and wavefunction. As explained in section 2.2.8 the asymptotic behaviour of the coordinate representation of the basis functions is given by  $e^{-\sqrt{r_1+r_2}}$ . However, since the Coulomb interaction vanishes at large distances, the asymptotics of planar two-electron wave functions are expected to decay exponentially, i.e., as  $e^{-(r_1+r_2)}$  [25] (see appendix A.2.3). Therefore, a large number of basis functions is needed in order to describe the asymptotic behaviour of eigenstates of the planar two-electron atom correctly.

As stated earlier, the matrices representing the generalized eigenvalue problem (2.40) are banded. Both the required memory as well as the number of floating point operations necessary to diagonalize such matrices depends heavily on the bandwidth. However, the bandwidth of the matrices depends on the ordering of the basis. Finding the optimal permutation of the basis that yields the minimum value of  $n_{\text{larg}}$ , which denotes the bandwidth, in limited time is a particular case of an open problem of graph partitioning, and several heuristic algorithms have been developed for this purpose [107–109]. The code uses a recursive method developed by Benoît Grémaud which reduces the bandwidth of the matrices considerably, e.g., for the case of triplet planar helium of total angular momentum  $|l| = 1$  and  $\Pi_x = 1$  with  $n_{\text{base}} = 480$  the

bandwidth is reduced from  $n_{\text{larg}} = 36165$  with hierarchical ordering to  $n_{\text{larg}} = 24102$ . For the description of the algorithm the interested reader is referred to [25] where an outline of the algorithm is given.

### 2.4.2 Lanczos algorithm

In this work the spectral structure as well as the localization properties of certain quantum states of planar two-electron atoms will be of interest, requiring specific eigenvalues and eigenstates of the generalized eigenvalue problem (2.7). The dimensions of the involved matrices become typically rather large in the spectral range of highly excited states. However, it is not necessary to extract all the eigenvalues and eigenstates, but only those in a given spectral region of interest, which is defined by either specific target states, e.g., to analyse the localization properties, or energy regimes to be probed, e.g., to obtain a scan of a suitably defined cross section.

The Lanczos algorithm is precisely suitable for this task, and finds a few eigenvalues and eigenvectors of a huge eigenvalue problem in the vicinity of some predefined position of the energy axis. More specifically, the algorithm was originally developed to find a few extremal eigenvalues of a large symmetric matrix, along with the associated eigenvectors [110, 111]. Later it was adapted for generalized symmetric eigenvalue problems  $\mathcal{A}\mathbf{x} = \epsilon\mathcal{B}\mathbf{x}$  [112]. In this case, the generalized eigenvalue problem is equivalent to an eigenvalue problem obtained by multiplication from the left with  $\mathcal{A}^{-1}$ ,

$$\mathcal{A}^{-1}\mathcal{B}\mathbf{x} = \mu\mathbf{x}, \quad (2.46)$$

where  $\mu = 1/\epsilon$ . The Lanczos algorithm finds the largest values of  $\mu$  (i.e.,  $\epsilon \simeq 0$ ). By shifting the matrix  $\mathcal{A}$  by  $E_s$ ,

$$\mathcal{A} \rightarrow \mathcal{A} - E_s\mathcal{B}, \quad (2.47)$$

before diagonalization, eigenvalues and eigenstates in the vicinity of  $E_s$  can be obtained.

In the Lanczos algorithm a set  $\mathbf{q}_1, \mathbf{q}_2, \dots, \mathbf{q}_{n_{\text{Lanczos}}}$  ( $n_{\text{Lanczos}} \leq n_{\text{tot}}$ ) of orthogonal column vectors of dimension  $n_{\text{tot}}$  is iteratively constructed in such a way, that the matrix  $\mathcal{Q} = \mathbf{q}_1, \mathbf{q}_2, \dots, \mathbf{q}_{n_{\text{Lanczos}}}$  is an orthogonal matrix with respect to  $\mathcal{B}$  (i.e.,  $\mathcal{Q}^T\mathcal{B}\mathcal{Q} = 1$ , where  $\mathcal{Q}^T$  is the transpose matrix of  $\mathcal{Q}$ ), which transforms the matrix  $\mathcal{A}^{-1}\mathcal{B}$  into the tridiagonal matrix  $\mathcal{A}^{-1}\mathcal{B}\mathcal{Q} = \mathcal{Q}\mathcal{T}$ , where

$$\mathcal{T} = \begin{pmatrix} \alpha_1 & \beta_1 & 0 & \dots & 0 & 0 \\ \beta_1 & \alpha_2 & \beta_2 & \dots & 0 & 0 \\ 0 & \beta_2 & \alpha_3 & \dots & 0 & 0 \\ \vdots & \vdots & \vdots & \ddots & \vdots & \vdots \\ 0 & 0 & 0 & \dots & \alpha_{n_{\text{Lanczos}}-1} & \beta_{n_{\text{Lanczos}}-1} \\ 0 & 0 & 0 & \dots & \beta_{n_{\text{Lanczos}}-1} & \alpha_{n_{\text{Lanczos}}} \end{pmatrix}. \quad (2.48)$$

The largest eigenvalues  $\mu_i$  of (2.46) are then given by the eigenvalues of  $\mathcal{T}$ .

The  $j$ th matrix elements  $\alpha_j$  and  $\beta_j$  of  $\mathcal{T}$  are obtained from the  $j$ th column of  $\mathcal{A}^{-1}\mathcal{B}\mathcal{Q} = \mathcal{Q}\mathcal{T}$ , taking into account that the vectors  $\mathbf{q}_j$  are orthonormal with respect to  $\mathcal{B}$ . Choosing an arbitrary normalized initial vector  $\mathbf{q}_1$ , the iterative formulae read [111, 113]

$$\begin{cases} \alpha_j &= \mathbf{q}_j^T \mathcal{B} \mathcal{A}^{-1} \mathcal{B} \mathbf{q}_j, \\ \beta_j &= \|\mathbf{t}_{j+1}^T \mathcal{B} \mathbf{t}_{j+1}\|, \text{ with } \mathbf{t}_{j+1} = \mathcal{A}^{-1} \mathcal{B} \mathbf{q}_j - \alpha_j \mathbf{q}_j - \beta_{j-1} \mathbf{q}_{j-1}, \\ \mathbf{q}_{j+1} &= \frac{1}{\beta_j} \mathbf{t}_{j+1}. \end{cases} \quad (2.49)$$

Note, that in the relations  $\mathcal{A}^{-1}$  is never used explicitly, but only products of type  $\mathcal{A}^{-1}\mathcal{B}\mathbf{x}$ , which makes it unnecessary to invert  $\mathcal{A}$ . Instead, using the  $LL^T$  factorization of  $\mathcal{A}$  [114] the vector  $\mathbf{x} = \mathcal{A}^{-1}\mathcal{B}\mathbf{x}$  can be found solving the linear system of equations  $\mathcal{A}\mathbf{x} = \mathcal{B}\mathbf{x}$  by backward substitution [114].

The Lanczos algorithm is thus composed of three fundamental steps:

1. The  $LL^T$  factorization of  $\mathcal{A}$ .
2.  $n_{\text{Lanczos}}$  iterations of the recursive expressions (2.49) in order to find  $\mathcal{T}$ .
3. Diagonalization of  $\mathcal{T}$ , which can be achieved by standard diagonalization routines like  $QR$ -decomposition [114].

### 2.4.3 Numerical implementation

The typical dimension of the matrices to diagonalize was discussed in section 2.4.1. Such matrices cannot be stored in the main memory of a standard PC, and the corresponding eigenvalue problem cannot be solved numerically using them. Moreover, the number of operations needed for the diagonalization of these matrices is huge and leads on a single processor to extremely long computation times. Instead, such eigenvalue problems can be solved on parallel computers, where all processing elements work simultaneously on different parts of the problem. This requires special techniques of parallel programming. In the following, some features of the parallel implementation of our code are discussed.

#### Basic notions of parallel programming

In a parallel program different parts of the problem are distributed on several processing elements of a given parallel computer. The program speeds up by some factor which is not bigger than the number of processing elements.<sup>2</sup> There are two basic concepts for memory management: *shared memory* computers, where each processing element has access to the entire memory, and *distributed memory* computers, where the memory is distributed over different processing elements. Besides these basic memory architectures some supercomputers use or enable a mixture of both concepts, called *hybrid architecture*, where subgroups of processing elements form nodes with either shared memory or a low latency high band width interconnect that emulates actual shared memory. These nodes are then organized as distributed memory machines.

There are special libraries available for the programming of these parallel computers. The two probably most widely used are the MPI (Message Passing Interface) [115, 116] and OpenMP (Open Multi-Processing) [117] programming schemes. OpenMP is an application programming interface that supports multi-platform shared memory multiprocessing programming using multithreading. It is usually employed for shared memory computers with a small to medium number of processors (e.g., 32). MPI is a language-independent communications protocol which provides means for the communication between different processing elements. In particular, it provides communication routines to program distributed memory computers with any number of processing elements.

MPI has been chosen for the implementation of our code. The matrices  $\mathcal{A}$  and  $\mathcal{B}$  are split into smaller matrices, which are treated locally on the processing units. Therefore, an optimization of the interaction between single processing elements is crucial, besides, of course, an efficient sequential computation. In MPI, there are basically two forms of communication:

- Point-to-point communication: a single processing element sends or receives a message from another processing element.

---

<sup>2</sup>Cache memory effects, which are not considered here, might in some cases lead to a speed-up larger than the number of processing elements.

- Collective communication: in this case several processing elements are involved, i.e., a single processing element sends or receives a message from all other processing elements, all processing elements are synchronized at some point, or global reduction operation (maximum, minimum, sum, etc.) of data distributed over all processing elements are performed.

Using these communication elements of MPI an existing scalar code can be transformed into a parallel code. However, one needs to choose carefully where to place the communication directives, and whether communication with a single or with all processing elements is preferable, in order to achieve optimal efficiency of the code. Beyond these decisions many fine details, which are deliberately ignored here, will influence the efficiency of the code in the actual MPI implementation.

The speed-up  $S(p)$  of a code running on  $p$  processing elements is defined as [113]

$$S(p) = \frac{T(1)}{T(p)}, \quad (2.50)$$

where  $T(p)$  is the execution time on  $p$  processing elements. Thus the efficiency  $E(p)$  is given by

$$E(p) = \frac{S(p)}{p} = \frac{T(1)}{pT(p)}. \quad (2.51)$$

In an efficient parallel code the time required for communication is short compared with the time spent for purely local operations, i.e.,  $E(p) \rightarrow 1$ . However, since there is always a fraction of the calculation that has to be solved sequentially, it is impossible to achieve efficiency  $E(p) = 1$  (a superscalar speed-up  $E(p) > 1$  due to cache effects is not considered here).

### Storage of matrices

As described in section 2.4.1, the matrices  $\tilde{\mathbf{H}}_0^\alpha$  and  $\mathbf{B}$ , which coincide with  $\mathcal{A}$  and  $\mathcal{B}$  of section 2.4.2, respectively, are complex or real symmetric banded sparse matrices. Therefore, all information is contained in the lower triangular band. In the course of the  $LL^T$  decomposition of  $\mathcal{A}$  the sparse character of  $\mathcal{A}$  is lost and  $L$  is given by a full banded matrix. In contrast, the matrix  $\mathcal{B}$  is, in the recursion relations (2.49), only needed to calculate products with vectors  $\mathbf{x}$  of type  $\mathcal{B}\mathbf{x}$  and it would be sufficient to store only the non-zero matrix elements of which the number per row is at most the number of selection rules [25]. The implementation does not make use of this fact and uses band structure matrices for both  $\mathcal{A}$  and  $\mathcal{B}$ , which are distributed over  $n_{\text{procs}}$  processing elements. The memory needed to store one complex (double precision) array of  $n_{\text{tot}} \times n_{\text{larg}}$  is  $(16 \times n_{\text{tot}} \times n_{\text{larg}}/2^{30})\text{GB}$  and the number of processing elements needed is approximately given by

$$n_{\text{procs}} = \frac{16 \times n_{\text{tot}} \times n_{\text{larg}}}{M}, \quad (2.52)$$

where  $M$  is the accessible memory per processing element given in bytes which can be used for the storage of this array.<sup>3</sup>

For the distribution on different processors the matrix  $\mathcal{A}$  ( $\mathcal{B}$ ) is partitioned into  $n_{\text{sizg}} \times n_{\text{sizg}}$  blocks as sketched in figure 2.1, such that

$$n_{\text{larg}} = n_{\text{r}} \times n_{\text{procs}} \times n_{\text{sizg}}, \quad (2.53)$$

---

<sup>3</sup>Note, that for the determination of the available memory  $M$  one has to take into account both matrices  $\mathcal{A}$  and  $\mathcal{B}$  and their data type.

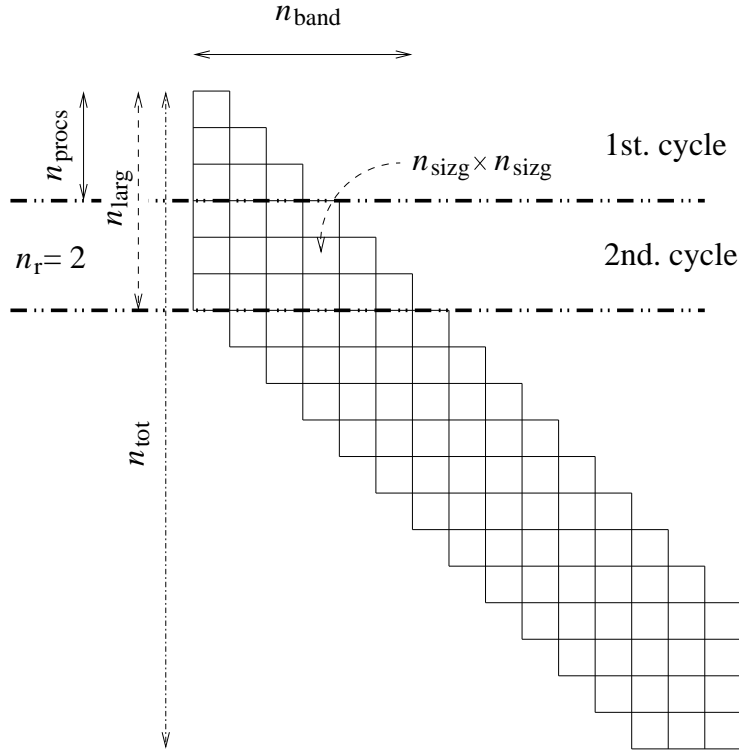


Figure 2.1: Partitioning of the matrices:  $n_{\text{larg}}$  and  $n_{\text{tot}}$  are the bandwidth and the total dimension, respectively;  $n_{\text{sizg}}$  is the dimension of the subblocks;  $n_{\text{band}}$  is the number of subblocks in a line, and  $n_r$  is the number of such lines per processing element that are contained in the bandwidth.

where  $n_r$  is an integer number which represents the number of lines of  $n_{\text{band}} = n_r \times n_{\text{procs}}$  of the  $n_{\text{sizg}} \times n_{\text{sizg}}$  blocks that each processing element has to process until a  $n_{\text{larg}} \times n_{\text{larg}}$  block of the matrix is completed. To complete an operation through the whole matrix requires to process  $n_{\text{cycle}}$  lines, where

$$n_{\text{cycle}} = \frac{n_{\text{tot}}}{n_{\text{larg}} \times n_{\text{procs}}} . \quad (2.54)$$

Any vector is stored in the same way, since it can be seen as a banded matrix of bandwidth one.

Most of the local calculations on the  $n_{\text{sizg}} \times n_{\text{sizg}}$  blocks are carried out using BLAS (Basic Linear Algebra Subprograms). These subroutines are standardized and optimized on most computers.

### Implementation of the Lanczos algorithm

After filling the matrices  $\mathcal{A}$  and  $\mathcal{B}$  as described in the preceding section, the generalized eigenvalue problem is diagonalized using the Lanczos algorithm (2.49) described in section 2.4.2. To perform these iterations, routines performing the following operations are needed: scalar products between two vectors, products between the matrix  $\mathcal{B}$  and a vector, and products of the form  $\mathcal{A}^{-1}\mathcal{B}\mathbf{x}$  using  $LL^T$  decomposition and backward substitution (here  $\mathbf{x}$  is a vector). The first and second operation can be easily implemented using BLAS, however the situation is more complicated for the third operation. A detailed description of the implementation of the  $LL^T$  decomposition and of the backward substitution is given in [113].

### Performance of the code

The speed of a computer is characterized by the performance of the CPU (central processor unit), which is measured by the number of floating point operations per second (Flops). The performance of a parallel code can be measured in terms of Flops achieved per processing element. In addition, a well performing parallel code should be scalable, i.e., the solution of a large problem should achieve about the same performance per processing element as the solution of a smaller problem. As mentioned above, we use BLAS to achieve a good single processing element performance.

Calculations have been carried out on the SGI Altix 3700xB and the SGI Altix 4700 of the Linux Cluster of the Leibniz-Rechenzentrum [118] and the SGI Altix 4700 of the Höchstleistungsrechner Bayern II [119]. The single processing element peak performance of these systems is 6.4 GFlops. For jobs scaling from 16 to 128 processing elements the performance typically achieved on both systems was 1.5 GFlops to 2.0 GFlops (the job performance is influenced by the relative separation of the individual processing elements on the computing grid). A top performance in the range of 2.3 GFlops to 2.4 GFlops, which is more than 35% of the peak performance, could be achieved for 16 up to 128 processing elements.

## Chapter 3

# Three-dimensional treatment of a two-electron atom

In this chapter our approach for the full three-dimensional treatment of a two-electron atom is presented [45, 68, 120–122]. After describing the spectral method, in which the basis is expanded in Coulomb-Sturmian functions with independent dilation parameters for both electrons and bipolar spherical harmonics for radial and angular coordinates, respectively, the matrix representation of the problem and its numerical implementation is discussed (see also appendix B). In particular, a newly developed, highly efficient method for the computation of matrix elements of the electron-electron repulsion is presented in detail.

### 3.1 Spectral method

The nonrelativistic Hamiltonian  $H$  for a two-electron atom with an infinitely heavy, pointlike nucleus of charge  $Z$  is, as in Eq. (1.5), given by

$$H = \frac{\vec{p}_1^2}{2} + \frac{\vec{p}_2^2}{2} - \frac{Z}{r_1} - \frac{Z}{r_2} + \frac{1}{r_{12}}, \quad (3.1)$$

with the interelectronic distance

$$\frac{1}{r_{12}} = \frac{1}{|\vec{r}_1 - \vec{r}_2|}, \quad (3.2)$$

and  $\vec{r}_1$ ,  $\vec{r}_2$ ,  $\vec{p}_1$  and  $\vec{p}_2$  the position and momentum vectors of particle one and two, respectively. The eigenstate wavefunction of a two-electron atom with total energy  $E$  satisfies the time independent Schrödinger equation

$$(H - E)\Psi(\vec{r}_1, \vec{r}_2) = 0. \quad (3.3)$$

Unlike in hydrogen, exact eigenfunctions of the Hamiltonian (3.1) cannot be found. Here, in order to solve the time independent Schrödinger equation (3.3) a spectral method, which consists of an expansion of the spatial wave function in terms of suitably chosen basis functions, is used. As discussed in the Introduction to this work many different choices for these basis functions, each with individual benefits and drawbacks, can be found in the literature. Basically all of them can be assigned to the group of either *explicitly correlated* (EC) bases [12, 13, 47–56], in which the basis functions explicitly depend on the interelectronic distance  $r_{12}$ , or *configuration interaction* (CI) bases [57–64], in which the basis functions are given by properly symmetrized combinations of two single particle functions.

The choice of basis functions substantially depends on the actual problem to be investigated, e.g. on the necessity of describing states with high angular momentum or of a highly accurate

description of the ground state. Apart from the treatment of highly doubly excited states itself, the aim here is to lay the foundation for the description of multiphoton processes in two-electron atoms, e.g., investigation of a possible formation of non-dispersive two-electron wave packets in helium [24, 26] or of multiphoton ionization processes [29, 38, 40–46, 71, 123], which requires an accurate description of (asymmetrically) doubly excited states for various values of the total angular momentum  $L$ . In addition, an accurate description of eigenstates in a given energy regime should be achievable within a matrix representation of the problem of small size as several angular momenta have to be treated simultaneously in the treatment of multiphoton processes, and the matrix elements should be easily accessible. EC bases allow for a very accurate description of two-electron atoms, however, the computation of the matrix elements either involves coupled three-dimensional radial integrals or is based on an analytic computation and selection rules, the number of which grows rapidly with increasing total angular momentum  $L$ . Moreover, rather large bases are needed for the description of highly asymmetrically excited states. Within CI bases the description of states with a large value of the total angular momentum  $L$  does not pose any additional difficulty and the computation of matrix elements involves at most two-dimensional coupled radial integrals. However, the CI approach has always been plagued with slow convergence in terms of the number of radial functions and of angular configurations used, which is particularly severe for the ground state and is essentially due to the fact that the CI expansion does not satisfy the Kato cusp condition associated with the coalescence of the two electrons [57, 66, 67]. As in EC bases the description of highly asymmetrically excited states requires a large basis within the standard CI approach. This is due to the fact that two distinct regions of space are associated with the electron probability distributions: a region close to the nucleus for the inner electron and a region far from the core for the highly excited outer electron. An efficient description of such states requires the basis to adequately span these two regions.

As one of our main goals is the treatment of two-electron atoms with an arbitrary value of the total angular momentum  $L$ , a basis expansion of CI type is considered for the spatial part of the wave function. In our approach [45, 68, 120–122] the solutions to Eq. (3.3) are expanded as follows:

$$\Psi(\vec{r}_1, \vec{r}_2) = \sum_{L,M} \sum_{\epsilon_{12}, \pi} \sum_{l_1, l_2}^{\pi} \sum_s \sum_{n_1, n_2} \psi_{k_{1s}, k_{2s}, n_1, n_2}^{l_1, l_2, L, M, \epsilon_{12}} \beta_{n_1, n_2}^{l_1, l_2} \mathcal{A} \frac{S_{n_1, l_1}^{(k_{1s})}(r_1)}{r_1} \frac{S_{n_2, l_2}^{(k_{2s})}(r_2)}{r_2} \Lambda_{l_1, l_2}^{L, M}(\hat{r}_1, \hat{r}_2), \quad (3.4)$$

where  $\psi_{k_{1s}, k_{2s}, n_1, n_2}^{l_1, l_2, L, M, \epsilon_{12}}$  is the expansion coefficient and

$$\beta_{n_1, n_2}^{l_1, l_2} = 1 + \left( \frac{1}{\sqrt{2}} - 1 \right) \delta_{n_1, n_2} \delta_{l_1, l_2}, \quad (3.5)$$

controls the redundancy that occurs within the basis due to symmetrization for basis states with equal quantum numbers for particle one and two. The symbol  $\sum^{\pi}$  indicates that these sums depend on the parity  $\pi$ . The symmetry or antisymmetry of the spatial wave function, as required by the Pauli principle, is ensured by a projection onto either singlet or triplet states via the operator

$$\mathcal{A} = \frac{1 + \epsilon_{12} P_{12}}{\sqrt{2}}, \quad (3.6)$$

where the operator  $P_{12}$  exchanges the coordinates of both electrons and  $\epsilon_{12}$  takes values of  $+1$  or  $-1$ . The radial one-electron functions  $S_{n, l}^{(k)}(r)$  are Coulomb-Sturmian functions [98, 99] (see appendix B.1) defined for a given angular momentum  $l$  and radial index  $n$  by

$$S_{n, l}^{(k)}(r) = N_{n, l}^{(k)} e^{-kr} (2kr)^{l+1} L_{n-l-1}^{(2l+1)}(2kr), \quad (3.7)$$

where  $k$  is a dilation parameter,  $L_{n-l-1}^{(2l+1)}(2kr)$  is an associated Laguerre polynomial and  $N_{n,l}^{(k)}$  the normalization constant given by

$$N_{n,l}^{(k)} = \sqrt{\frac{k}{n}} \left( \frac{(n-l-1)!}{(n+l)!} \right)^{1/2}. \quad (3.8)$$

The orthogonality relation for the Coulomb-Sturmian functions reads

$$\int_0^\infty dr S_{n,l}^{(k)}(r) \frac{1}{r} S_{n',l}^{(k)}(r) = \frac{k}{n} \delta_{nn'}. \quad (3.9)$$

The radial index  $n$  of the Sturmian functions is a positive integer satisfying  $n \geq l+1$ . The angular part of the expansion (3.4) is expressed in terms of bipolar spherical harmonics [82],

$$\Lambda_{l_1, l_2}^{L, M}(\hat{r}_1, \hat{r}_2) = \sum_{m_1, m_2} \langle l_1, m_1, l_2, m_2 | L, M \rangle Y_{l_1, m_1}(\hat{r}_1) Y_{l_2, m_2}(\hat{r}_2), \quad (3.10)$$

which couple the two individual angular momenta  $l_1$  and  $l_2$  in the  $L-S$  scheme.  $Y_{l,m}$  denotes the spherical harmonics and  $\langle l_1, m_1, l_2, m_2 | L, M \rangle$  is a Clebsch-Gordan coefficient. The relevant angular configurations  $(l_1, l_2)$  for the description of states with total angular momentum  $L$  are determined by the triangle relation for the addition of angular momenta

$$|l_1 - l_2| \leq L \leq l_1 + l_2. \quad (3.11)$$

In order to preserve parity  $\pi$ , which is a good quantum number, the  $L-S$  coupled individual angular momenta of the electrons must satisfy  $\pi = (-1)^{l_1+l_2}$ . This is also reflected in  $\sum^\pi$ , which stands for the sum over individual angular momenta  $l_1, l_2$  for a given parity  $\pi$ . Note, that states with  $\pi = (-1)^L$  are usually denoted as natural parity states, while those with  $\pi = (-1)^{L+1}$  are labeled as unnatural parity states. The associated spin symmetry is determined by the exchange symmetry, with  $\epsilon_{12} = +1$  and  $\epsilon_{12} = -1$  defining singlet and triplet symmetry for  $S = 0$  and  $S = 1$ , respectively. In total this allows us to target eigenstates classified by  $^{2S+1}L^\pi$  and total angular momentum projection  $M$  (see Sec. 1.3) by fixing  $L, M, \pi$  and  $\epsilon_{12}$  in expansion (3.4).

Note, that the operator  $\mathcal{A}$  can also be written as<sup>1</sup>

$$\mathcal{A} = \frac{1 + \epsilon P}{\sqrt{2}}, \quad (3.12)$$

where  $P$  is the operator which simultaneously exchanges  $k_{1,s}, n_1, l_1, m_1$  for electron one and  $k_{2,s}, n_2, l_2, m_2$  for electron two, with

$$\epsilon = (-1)^{l_1+l_2-L} \epsilon_{12}. \quad (3.13)$$

The factor that relates the quantities  $\epsilon_{12}$  and  $\epsilon$  is due to the symmetry properties of the Clebsch-Gordan coefficient in (3.10):

$$\langle l_2, m_2, l_1, m_1 | L, M \rangle = (-1)^{l_1+l_2-L} \langle l_1, m_1, l_2, m_2 | L, M \rangle. \quad (3.14)$$

Within a CI approach the interelectronic distance  $r_{12}$  is not an explicit coordinate and therefore not accessible directly. To obtain an expression for  $1/r_{12}$  in the Hamiltonian (3.1) one has to exploit the multipole expansion of the electron-electron repulsion:

$$\frac{1}{r_{12}} = \sum_{q=0}^{\infty} \sum_{p=-q}^q \frac{4\pi}{2q+1} \frac{r_{<}^q}{r_{>}^{q+1}} Y_{q,p}^*(\hat{r}_1) Y_{q,p}(\hat{r}_2), \quad (3.15)$$

---

<sup>1</sup>This form is more convenient for the computation of the matrix representation of the Schrödinger equation (see appendix B.2).

with  $r_< = \min(r_1, r_2)$  and  $r_> = \max(r_1, r_2)$ .

In general the CI expansions involving Coulomb-Sturmian functions use the same dilation parameter  $k$  for all Coulomb-Sturmian functions, which is equivalent to setting  $k_{1s} = k_{2s} \equiv k$  and  $s = 1$  in our expansion (3.4). Furthermore, for each pair of  $(l_1, l_2)$ , the same number  $N$  of Coulomb-Sturmian functions  $S_{n_1, l_1}^{(k)}(r_1)$  with  $l_1 + 1 \leq n_1 \leq l_1 + N$  and  $S_{n_2, l_2}^{(k)}(r_2)$  with  $l_2 + 1 \leq n_2 \leq l_2 + N$  is chosen for the representation. In contrast, our approach is constructed in order to allow the dilation parameter and the number of Coulomb-Sturmian functions associated to one electron to be different from those attributed to the other electron. This leads to the introduction of a set of Coulomb-Sturmian functions  $\{S_{n_1, l_1}^{(k_{1s})}(r_1), S_{n_2, l_2}^{(k_{2s})}(r_2)\}$  associated to electron one and two, which is characterized by the combination  $[k_{1s}, N_{1s}^{\min}, N_{1s}^{\max}, k_{2s}, N_{2s}^{\min}, N_{2s}^{\max}]$  with  $l_1 + N_{1s}^{\min} \leq n_1 \leq l_1 + N_{1s}^{\max}$  and  $l_2 + N_{2s}^{\min} \leq n_2 \leq l_2 + N_{2s}^{\max}$ . Moreover, more than one and different sets – labeled by the subscript  $s$  – may be selected for any angular configuration  $(l_1, l_2)$ . To avoid redundancies in expansion (3.4), the orbital angular momenta are restricted to  $l_1 \leq l_2$ , and if  $l_1 = l_2$  and  $k_{1s} = k_{2s}$  to  $n_1 \leq n_2$ . Be aware of the fact, that due to the restriction to  $l_1 \leq l_2$ , each set of Coulomb-Sturmian functions  $[k_{1,s}, N_{1,s}^{\min}, N_{1,s}^{\max}, k_{2,s}, N_{2,s}^{\min}, N_{2,s}^{\max}]$  should be accompanied by  $[k_{2,s}, N_{2,s}^{\min}, N_{2,s}^{\max}, k_{1,s}, N_{1,s}^{\min}, N_{1,s}^{\max}]$  in the case of  $k_{1,s} \neq k_{2,s}$  and  $l_1 \neq l_2$ . The reason for this is that, e.g., sets with  $k_{1,s} > k_{2,s}$  would explicitly favour a smaller extent of the  $l_1$ -orbital than of the  $l_2$ -orbital. This would limit the descriptive power of the basis after truncation. To illustrate the importance of this kind of symmetrization let us consider states of  $L = 1$  below the second single ionization threshold. In the independent particle model (see Sec. 1.3.1) the spectrum consists of  $2snp$ ,  $2pns$  and  $2pnd$  states. Using only sets with  $k_{1,s} > k_{2,s}$  would allow a good representation of  $2snp$  and  $2pnd$  states, however, the description of the  $2pns$  would be very poor in a truncated basis. As already realized by the first experiment on doubly excited states [16] and its theoretical interpretation [76] the electron-electron interaction mixes the different configurations of the independent particle model. Consequently, the exclusive use of sets with  $k_{1,s} > k_{2,s}$  requires a huge basis to get converged results, which is not the case if the mirrored set of Coulomb-Sturmian functions  $[k_{2,s}, N_{2,s}^{\min}, N_{2,s}^{\max}, k_{1,s}, N_{1,s}^{\min}, N_{1,s}^{\max}]$  is included.

Combined with the complex rotation method presented in section 1.4 the approach allows the description of resonance states. By choosing appropriate sets of Coulomb-Sturmian functions the description of a given energy regime, i.e., below a certain ionization threshold, is possible with a rather small number of basis functions. This is in particular true for highly asymmetrically excited states.

### 3.1.1 Expectation value of $\cos(\theta_{12})$

As already shown in section 2.2.7 the expectation value of  $\cos(\theta_{12})$  (in single pole approximation) is given by

$$\langle \cos(\theta_{12}) \rangle \simeq \text{Re}(\langle \overline{\Psi_{i,\theta}} | \cos(\theta_{12}) | \Psi_{i,\theta} \rangle). \quad (3.16)$$

Rewriting  $\cos(\theta_{12})$  in terms of spherical harmonics  $Y_{l,m}(\hat{r})$ ,

$$\cos(\theta_{12}) = \frac{\vec{r}_1 \cdot \vec{r}_2}{r_1 r_2} = \frac{4\pi}{3} \sum_{q_1} \sum_{q_2} \mathcal{C}_{1,q_1,1,q_2}^{1,0} Y_{1,q_1}(\hat{r}_1) Y_{1,q_2}(\hat{r}_2), \quad (3.17)$$

with Clebsch-Gordan coefficients  $\mathcal{C}_{1,q_1,1,q_2}^{1,0}$ , leads to an easily accessible matrix representation of  $\cos(\theta_{12})$  – the details of which are given in appendix B.2.1 – in terms of overlap integrals of Coulomb-Sturmian functions and Wigner  $3jm$  and  $6j$  symbols [82].

### 3.1.2 Electronic densities

As described in section 2.2.8 the density of a well isolated resonance (in single pole approximation) is given by

$$|\phi_E(\vec{r})|^2 \simeq \text{Re} (\langle \vec{r} | R(-\theta) | \Psi_{j,\theta} \rangle^2) . \quad (3.18)$$

To compute  $\langle \vec{r} | R(-\theta) | \Psi_{j,\theta} \rangle$  in the basis given through (3.4) complex backscaling is used, in which the complex rotation operator acts on the basis. The evaluation of the involved Coulomb-Sturmian functions with complex arguments is achieved through a stable implementation of the recursion formula

$$\begin{aligned} \sqrt{n(n+l-1)(n+l)} S_{n,l}^{(k)}(r) - 2\sqrt{n-1}(n-1-kr) S_{n-1,l}^{(k)}(r) \\ + \sqrt{(n-2)(n-l-2)(n+l-1)} S_{n-2,l}^{(k)}(r) = 0 , \end{aligned} \quad (3.19)$$

which is based on a recurrence relation for Kummer's functions [103, 120].<sup>2</sup>

## 3.2 Matrix representation

After substituting  $\Psi$  in Eq. (3.3) by its expansion (3.4) and using the complex rotation method described in section 1.4, the following generalized eigenvalue problem is obtained (see appendix B.2):

$$\mathbf{H}_\theta \Psi_{i,\theta} = E_{i,\theta} \mathbf{S} \Psi_{i,\theta} , \quad (3.20)$$

where  $\Psi_{i,\theta}$  is the vector representation of the wavefunction  $|\Psi_{i,\theta}\rangle$ ,  $\mathbf{S}$  is the matrix representing the overlap and  $\mathbf{H}_\theta$  is the matrix associated with the rotated Hamiltonian. The calculation of matrix elements of  $\mathbf{S}$  and  $\mathbf{H}_\theta$  may be performed analytically, which becomes, however, cumbersome as soon as various sets of Coulomb-Sturmian functions with different dilation parameters are introduced. Alternatively, Gauss-Laguerre (GL) integration [103, 120], as described in appendix B.3, provides extremely accurate results for the matrix elements in (3.20) since the GL quadrature formula is exact in our case where all integrals to calculate involve products of polynomials and decreasing exponentials. In addition the matrix elements of the overlap matrix  $\mathbf{S}$ , of the kinetic energy, and of the Coulomb interaction of the electrons with the nucleus can be computed efficiently with GL integration. The situation for the electron-electron repulsion is different: The computation of matrix elements associated with the  $1/r_{12}$  term (3.15) involves the following radial double integral:

$$\mathcal{R} = \int_0^\infty dr_1 \int_0^\infty dr_2 S_{\nu_1,\lambda_1}^{(\kappa_1)}(r_1) S_{\nu_2,\lambda_2}^{(\kappa_2)}(r_2) \left( \frac{r_1^q}{r_2^{q+1}} \right) S_{n_1,l_1}^{(k_1)}(r_1) S_{n_2,l_2}^{(k_2)}(r_2) , \quad (3.21)$$

which can be decomposed into

$$\begin{aligned} \mathcal{R} = & \int_0^\infty dr_1 S_{\nu_1,\lambda_1}^{(\kappa_1)}(r_1) S_{n_1,l_1}^{(k_1)}(r_1) r_1^q \int_{r_1}^\infty dr_2 S_{\nu_2,\lambda_2}^{(\kappa_2)}(r_2) S_{n_2,l_2}^{(k_2)}(r_2) \frac{1}{r_2^{q+1}} \\ & + \int_0^\infty dr_2 S_{\nu_2,\lambda_2}^{(\kappa_2)}(r_2) S_{n_2,l_2}^{(k_2)}(r_2) r_2^q \int_{r_2}^\infty dr_1 S_{\nu_1,\lambda_1}^{(\kappa_1)}(r_1) S_{n_1,l_1}^{(k_1)}(r_1) \frac{1}{r_1^{q+1}} . \end{aligned} \quad (3.22)$$

The GL quadrature formula for these integrals involves double sums over a number of integration points which are determined by the degree of the polynomial part of the subintegral

<sup>2</sup>The relation between the Coulomb-Sturmian and the Kummer's function is given in appendix B.1.

functions (for details see appendix B.3.1). If the maximum degree of the polynomial part of the subintegral functions involved in the whole basis is given by  $N^{\max}$ , then the length of the double sums in the GL integration, which allows a computation of all matrix elements, scales quadratically with  $N^{\max}$ . With this choice all double sums have the same length and one set of weights and abscissae can be used for the computation of all matrix elements. Note, that this allows a simultaneous computation of all matrix elements corresponding to a given pair of dilation parameters and angular configurations. The description of highly excited states requires rather large values for the radial indices of the Coulomb-Sturmian functions, resulting in a high value of  $N^{\max}$  for which the choice of a uniform length for the double sums turns out to be rather inefficient. Alternatively, one might adjust the number of integration points to each of the integrals (3.22), which would imply calculating the integrations points (zeros of Laguerre polynomials) several times. However, this is even less efficient.

To reduce the number of operations needed to compute the matrix representation of  $1/r_{12}$  we adopt a method, recently developed by Zamastil *et al.* [124, 125], based on the generalized Wigner-Eckart theorem and recurrence relations. In the following the method is reviewed and adjusted to our definition of Coulomb-Sturmian functions  $S_{n,l}^{(k)}(r)$ , which are connected to the Sturmian functions  $R_{n,l}(kr)$  used in [125] by

$$R_{n,l}(kr) = C_n^{(k)} \frac{S_{n,l}^{(k)}(r)}{r}, \quad \text{with} \quad C_n^{(k)} = \sqrt{\frac{n}{k}}. \quad (3.23)$$

### 3.2.1 Linearization of the product of two Coulomb-Sturmian functions

The Wigner-Eckhart theorem for Coulomb-Sturmian functions (Eq. (49) of [125]) reads<sup>3</sup>

$$S_{n_i, l_i}^{(k_i)}(r) S_{\nu_i, \lambda_i}^{(\kappa_i)}(r) = \sum_{N_i=L_i+1}^{\nu_i+n_i} (\nu_i, \lambda_i, \kappa_i, n_i, l_i, k_i | N_i) S_{N_i, L_i}^{(\xi_i)}(r), \quad (3.24)$$

with  $\xi_i = \kappa_i + k_i$ , and  $L_i = \lambda_i + l_i$ . The orthogonality relation (3.9) for the Coulomb-Sturmian functions leads to

$$(\nu_i, \lambda_i, \kappa_i, n_i, l_i, k_i | N_i) = \frac{N_i}{\xi_i} \int_0^\infty dr S_{n_i, l_i}^{(k_i)}(r) S_{\nu_i, \lambda_i}^{(\kappa_i)}(r) \frac{1}{r} S_{N_i, L_i}^{(\xi_i)}(r). \quad (3.25)$$

After substitution of the products of two Coulomb-Sturmian functions in the radial integrals of the  $1/r_{12}$  matrix elements (3.22) by the corresponding expansions (3.24) we obtain

$$\begin{aligned} \mathcal{R} &= \sum_{N_1=L_1+1}^{\nu_1+n_1} \sum_{N_2=L_2+1}^{\nu_2+n_2} \left( \mathcal{G}_{N_1, N_2}^{L_1, L_2, q}(\xi_1, \xi_2) + \mathcal{G}_{N_2, N_1}^{L_2, L_1, q}(\xi_2, \xi_1) \right) \\ &\quad \times (\nu_1, \lambda_1, \kappa_1, n_1, l_1, k_1 | N_1) (\nu_2, \lambda_2, \kappa_2, n_2, l_2, k_2 | N_2), \end{aligned} \quad (3.26)$$

where  $\mathcal{G}_{N_i, N_j}^{L_i, L_j, q}$  are the integrals defined by

$$\mathcal{G}_{N_i, N_j}^{L_i, L_j, q}(\xi_i, \xi_j) = \int_0^\infty dr_i S_{N_i, L_i}^{(\xi_i)}(r_i) r_i^q \int_{r_i}^\infty dr_j S_{N_j, L_j}^{(\xi_j)}(r_j) \frac{1}{r_j^{q+1}}. \quad (3.27)$$

The advantage of the transcription of Eq. (3.22) in terms of coefficients (3.25) and integrals (3.27) is given through the possibility of a recursive computation of the coefficients involved, as well as of the integrals.

<sup>3</sup>The coefficients for our Sturmian functions are accordingly related to the coefficients  $(\nu_i, \lambda_i, \kappa_i, n_i, l_i, k_i | N_i)_{p=1}$  of [125] through the relation  $(\nu_i, \lambda_i, \kappa_i, n_i, l_i, k_i | N_i) = \sqrt{\frac{\kappa_i k_i}{\xi_i}} \sqrt{\frac{N_i}{\nu_i n_i}} (\nu_i, \lambda_i, \kappa_i, n_i, l_i, k_i | N_i)_{p=1}$ .

### 3.2.2 Recurrence relation for the coefficients $(\nu_i, \lambda_i, \kappa_i, n_i, l_i, k_i|N_i)$

In case of fixed values for  $\lambda_i, \kappa_i, l_i$  and  $k_i$  within an equation, we employ the shorthand notation

$$(\nu_i, n_i|N_i) = \sqrt{\frac{\xi_i}{\kappa_i k_i}} \sqrt{\frac{\nu_i n_i}{N_i}} (\nu_i, \lambda_i, \kappa_i, n_i, l_i, k_i|N_i). \quad (3.28)$$

The coefficients satisfy the recurrence relation [125]

$$\begin{aligned} \sqrt{(\nu_i - \lambda_i - 1)(\nu_i + \lambda_i)} (\nu_i, n_i|N_i) &= 2 \left( \nu_i - 1 - \frac{\kappa_i N_i}{\xi_i} \right) (\nu_i - 1, n_i|N_i) \\ &\quad - \sqrt{(\nu_i + \lambda_i - 1)(\nu_i - \lambda_i - 2)} (\nu_i - 2, n_i|N_i) \\ &\quad + \frac{\kappa_i}{\xi_i} \sqrt{(N_i + L_i)(N_i - L_i - 1)} (\nu_i - 1, n_i|N_i - 1) \\ &\quad + \frac{\kappa_i}{\xi_i} \sqrt{(N_i - L_i)(N_i + L_i + 1)} (\nu_i - 1, n_i|N_i + 1). \end{aligned} \quad (3.29)$$

This equation can be used to lower the quantum number  $\nu_i$  to  $\lambda_i + 1$ . Taking into account that

$$(\nu_i, \lambda_i, \kappa_i, n_i, l_i, k_i|N_i) = (n_i, l_i, k_i, \nu_i, \lambda_i, \kappa_i|N_i) \quad (3.30)$$

provides the means to lower the quantum number  $n_i$  to  $l_i + 1$ . The initial conditions for the recursion (3.29) are  $(\nu_i^{(0)}, n_i^{(0)}|N_i^{(0)})$  and  $(\nu_i^{(0)}, n_i^{(0)}|N_i^{(0)} + 1)$ , with  $\nu_i^{(0)} = \lambda_i + 1$ ,  $n_i^{(0)} = l_i + 1$  and  $N_i^{(0)} = \lambda_i + l_i + 1$ . These have simple analytical expressions given by [125]

$$\begin{aligned} (\nu_i^{(0)}, n_i^{(0)}|N_i^{(0)}) &= 2(\lambda_i + l_i + 1) \frac{\kappa_i^{\lambda_i+1} k_i^{l_i+1}}{(\kappa_i + k_i)^{\lambda_i+l_i+2}} \sqrt{\frac{(2\lambda_i + 2l_i + 1)!}{(2\lambda_i + 1)!(2l_i + 1)!}}, \\ (\nu_i^{(0)}, n_i^{(0)}|N_i^{(0)} + 1) &= -\sqrt{2(\lambda_i + l_i + 1)} \frac{\kappa_i^{\lambda_i+1} k_i^{l_i+1}}{(\kappa_i + k_i)^{\lambda_i+l_i+2}} \sqrt{\frac{(2\lambda_i + 2l_i + 1)!}{(2\lambda_i + 1)!(2l_i + 1)!}}. \end{aligned} \quad (3.31)$$

In addition,

$$(\nu_i^{(0)}, n_i^{(0)}|N_i) = 0, \quad N_i > \lambda_i + l_i + 2. \quad (3.32)$$

### 3.2.3 Recurrence relations for the integrals $\mathcal{G}_{N_i, N_j}^{L_i, L_j, q}(\xi_i, \xi_j)$

Equations (67) and (72) of [125] provide recurrence relations for the  $\mathcal{G}_{N_i, N_j}^{L_i, L_j, q}(\xi_i, \xi_j)$  which keep the indices  $L_i, L_j$  and  $q$ , and the parameters  $\xi_1$  and  $\xi_2$  constant.<sup>4</sup> After transforming these according to (3.23) we obtain

$$\begin{aligned} \langle N_1, L_1, \xi_1 | N_2, L_2, \xi_2 \rangle &= q \mathcal{G}_{N_1, N_2} + \frac{(N_2 + L_2)}{2} \sqrt{\frac{(N_2 - 1)(N_2 - L_2 - 1)}{N_2(N_2 + L_2)}} \mathcal{G}_{N_1, N_2 - 1} \\ &\quad - \frac{(N_2 - L_2)}{2} \sqrt{\frac{(N_2 + 1)(N_2 + L_2 + 1)}{N_2(N_2 - L_2)}} \mathcal{G}_{N_1, N_2 + 1}, \end{aligned} \quad (3.33)$$

and

$$\begin{aligned} \langle N_1, L_1, \xi_1 | N_2, L_2, \xi_2 \rangle &= (q + 1) \mathcal{G}_{N_1, N_2} + \frac{(N_1 - L_1)}{2} \sqrt{\frac{(N_1 + 1)(N_1 + L_1 + 1)}{N_1(N_1 - L_1)}} \mathcal{G}_{N_1 + 1, N_2} \\ &\quad - \frac{(N_1 + L_1)}{2} \sqrt{\frac{(N_1 - 1)(N_1 - L_1 - 1)}{N_1(N_1 + L_1)}} \mathcal{G}_{N_1 - 1, N_2}, \end{aligned} \quad (3.34)$$

<sup>4</sup>The integrals  $\mathcal{G}_{N_i, N_j}^{L_i, L_j, q}(\xi_i, \xi_j)$  are accordingly related to integrals  $\mathcal{P}_{N_i, N_j}^{L_i, L_j, q}(\xi_i, \xi_j)$  of [125] through the relation  $\mathcal{G}_{N_i, N_j}^{L_i, L_j, q}(\xi_i, \xi_j) = \sqrt{\frac{\xi_i}{N_i}} \sqrt{\frac{\xi_j}{N_j}} \sqrt{\frac{(N_i - L_i - 1)!}{(N_i + L_i)!}} \sqrt{\frac{(N_j - L_j - 1)!}{(N_j + L_j)!}} \mathcal{P}_{N_i, N_j}^{L_i, L_j, q}(\xi_i, \xi_j)$ .

respectively. Here we have employed – under the condition of a fixed set of parameters  $L_1, L_2, q, \xi_1, \xi_2$  – the shorthand notation:

$$\mathcal{G}_{N_1, N_2} = \mathcal{G}_{N_1, N_2}^{L_1, L_2, q}(\xi_1, \xi_2). \quad (3.35)$$

The left hand side of equations (3.33) and (3.34) refer to the overlap integral

$$\langle N_1, L_1, \xi_1 | N_2, L_2, \xi_2 \rangle = \int_0^\infty dr S_{N_1, L_1}^{(\xi_1)}(r) S_{N_2, L_2}^{(\xi_2)}(r). \quad (3.36)$$

These overlaps and the initial conditions for the recursions (3.33) and (3.34) are calculated with GL integration. Notice that for  $\xi_1 = \xi_2$  the overlaps have simple analytical expressions [126] which are implemented in our computations.

### 3.3 Numerical treatment

#### 3.3.1 Computation of the matrix representation of the generalized eigenvalue problem

The matrix elements of the kinetic term and the electron-nucleus interaction of  $\mathbf{H}_\theta$ , and of the overlap matrix  $\mathbf{S}$  are calculated using GL integration which guarantees an accuracy of the order of the machine precision (in double and quadruple precision). The matrix elements of  $1/r_{12}$  can also be computed very accurately with GL integration, but Eq. (3.26) combined with the recursive relations (3.29), (3.33) and (3.34) provides a much more efficient method. However, its implementation is delicate. The recursions (3.29), (3.33) and (3.34)<sup>5</sup> are not numerically stable even for rather small values of  $N_i$  and  $L_i$  (e.g.  $N_i - L_i > 15, L_i > 10$ ). Typically one observes a slow decay in precision at each recursion step up to a certain point, which is then followed by a rather rapid total breakdown of precision. Consequently, a computation of matrix elements of  $1/r_{12}$  using purely the recursive method described in section 3.2 seems not to be feasible. To overcome the instability issues we limit the length of the recursions and restart the recursion process. The implementation is described in detail in the following.

To compute the coefficients  $(\nu_i, n_i | N_i)$  the three dimensional coefficient matrix is initialized to zero and decomposed into two-dimensional slices with fixed  $\nu_i$ . Using Eq. (3.31) the two initial values for the slice with  $\nu_i = \lambda_i + 1$  are then evaluated. Looking at Eq. (3.29) it is easy to spot that for  $\nu_i = \lambda_i + 1$  the non-zero coefficients are situated in the upper right triangle, the diagonal and the first lower subdiagonal. These matrix elements are then computed columnwise, starting with the element of the first lower subdiagonal (see Fig. 3.1 (left)). Analogously we compute the auxiliary matrix for  $n_i = l_i + 1$ . From Eq. (3.30) follows that the coefficients with  $n_i = l_i + 1$  correspond to the initial conditions for the matrix slices with  $\nu_i \neq \lambda_i + 1$  (see Fig. 3.1 (center and right)). The slices with  $\nu_i \neq \lambda_i + 1$  are computed in a similar way. The major difference in their computation is that after a number ‘**reclength**’ of columns computed via the recursion formula we compute two columns by using GL integration techniques and then restart the recursion for another ‘**reclength**’ columns (see Fig. 3.1 (right)). In doing so we ensure that we are able to contain the loss of precision.

The matrix  $\mathcal{G}_{N_i, N_j}$  is divided into blocks of dimension ‘**blocklength**’ (see Fig. 3.2). Displaced by two rows downwards with respect to the center of the block, a set of four initial values is calculated by using GL integration methods. The displacement of the starting values is done

---

<sup>5</sup>Ref. [125] contains further recurrence relations for the integrals  $\mathcal{P}_{N_i, N_j}^{L_i, L_j, q}(\xi_i, \xi_j)$  which connect integrals with different values of  $N_i, L_i$  and  $N_j, L_j$ , respectively. We have not investigated the stability properties of these recursions.

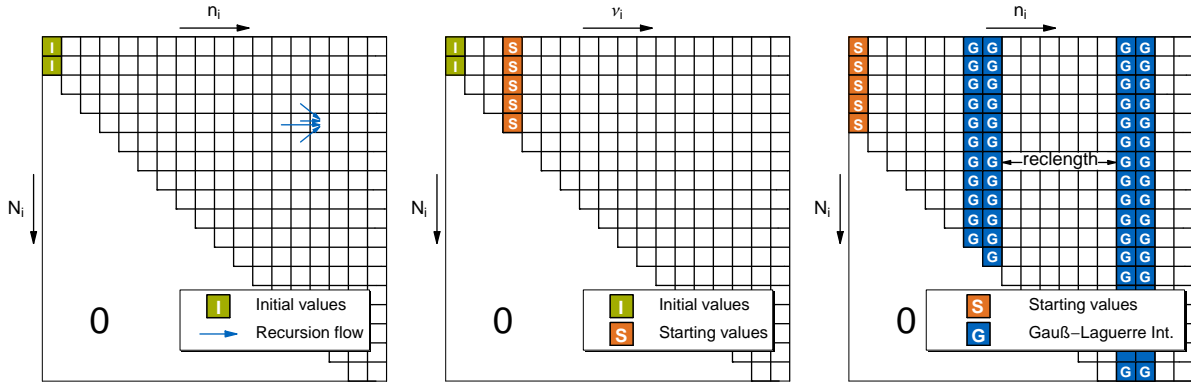


Figure 3.1: (left) Coefficients for  $\nu_i = \lambda_i + 1$ : Initial values computed via Eq. (3.31) are marked by the letter I. Representative for all coefficients, the recursion flow for the computation of one matrix element is indicated with arrows. (center) Coefficients for  $n_i = l_i + 1$ : Initial values computed via Eq. (3.31) are marked by the letter I. The starting values for the coefficients with  $\nu_i = \lambda_i + 4$  are marked by the letter S. (right) Coefficients for  $\nu_i \neq \lambda_i + 1$ : As a representative the coefficients with  $\nu_i = \lambda_i + 4$  are pictured. The starting values characterized by the letter S correspond to the values marked by an S in the center picture of this figure. The values for the restart of the recursion are highlighted by G. All coefficients  $(\nu_i, n_i | N_i)$  with  $N_i > \nu_i + n_i$  are equal to zero.

as to be able to compute efficiently zero values for integrals with  $N_i > N_j$  in the case of equal dilation parameters  $\xi_i = \xi_j$ . Starting from these the rest of the block is computed by employing the recursion formulas Eq. (3.33) and Eq. (3.34). In doing so we are able to shorten the length of the recursion and ensure a certain level of precision.

The computations of the coefficients  $(\nu_i, n_i | N_i)$  and the integrals  $\mathcal{G}_{N_i, N_j}$  are performed in 128-bit arithmetic, if necessary converted to other precision, and then used to compute matrix elements of  $1/r_{12}$  as given by Eq. (3.26) and Eq. (3.15). The parameters ‘reclength’, ‘blocklength’ are optimized to yield the desired precision by as few GL integrated elements as possible, e.g. to ensure 26 digits of accuracy ‘reclength’=6, ‘blocklength’=10 are sufficient, while ‘reclength’=18, ‘blocklength’=26 provide at least 15 digits of accuracy for coefficients and integrals ( $L_i, L_j < 50$ ,  $N_i - L_i, N_j - L_j < 100$ ,  $0.02 \leq \xi_i, \xi_j \leq 4.00$ ).<sup>6</sup>

The computation time for the matrix representation of  $1/r_{12}$  suitable to treat doubly excited states as in section 4.1.2 is, on a Dual Core AMD Opteron 8222SE/3GHz, of the order of one day for pure Gauß-Laguerre integration. A computation of matrices for other values of the total angular momentum, different energy regimes or simply higher precision results often need significantly more computation time. The computation of the matrix associated to  $1/r_{12}$  with the method presented beforehand results in a tremendous performance gain compared to pure Gauß-Laguerre integration. The speed-up of the calculation mainly depends on the number of integration points needed for the Gauß-Laguerre integration and the size of the auxiliary matrices for coefficients and integrals (the number of restarts of the recursions and how many elements remain to be computed after the last restart play a role here). If the matrix elements of  $1/r_{12}$  are to be computed in double precision typical performance gains of a factor between 10 to 130 are observed. The speed-up by a factor of 130 was observed using one set of Coulomb-Sturmian functions ([2.0, 1, 70, 2.0, 1, 70]) and 26 angular configurations (1,1) for the computation of the helium ground state. For matrices used for the description of highly doubly excited states of

<sup>6</sup> ‘reclength’=20, ‘blocklength’=20 provide at least 15 digits of accuracy for coefficients and integrals with  $L_i, L_j < 50$ ,  $N_i - L_i, N_j - L_j < 140$ ,  $\xi_i = \xi_j = 4.00$ .

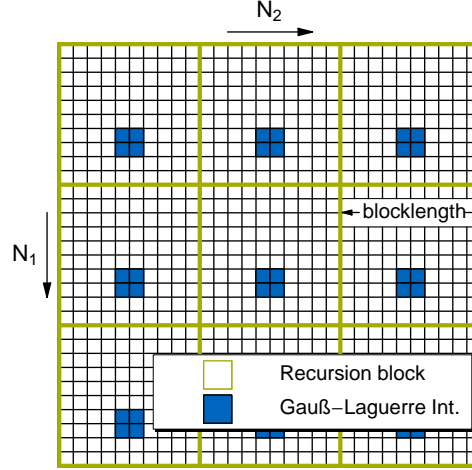


Figure 3.2:  $\mathcal{G}_{N_1, N_2}$ : A schematic depiction for the computation of matrix  $\mathcal{G}$ . The matrix is decomposed in subblocks of dimension ‘blocklength’. Within each of these subblocks a set of four initial values is computed using GL integration from which the rest of the matrix elements can be calculated employing Eq. (3.33) and Eq. (3.34).

helium the computation is faster by a factor of 10 to 30.

### 3.3.2 Solution of the eigenvalue problem

The inclusion of many sets of Coulomb-Sturmian functions with different dilation parameters in our basis makes it numerically overcomplete, which means that some eigenvalues of the overlap matrix (which must be positive definite) can be numerically zero. This results from a loss of numerical independence due to finite precision arithmetic. In order to solve this problem we proceed as follows. Let  $\mathbf{H}_\theta$  and  $\mathbf{S}$  be  $(n \times n)$  matrices, and let us consider the  $(n \times n)$  orthogonal matrix  $\mathbf{T}$  that diagonalizes  $\mathbf{S}$ . Therefore,  $\mathbf{T}^T \mathbf{S} \mathbf{T} = \mathbf{s}$  where  $\mathbf{s}$  is the diagonal matrix containing the eigenvalues of  $\mathbf{S}$  of which the associated eigenvectors are stored in columns of  $\mathbf{T}$ . We define a small cutoff  $\epsilon$  (of the order of  $10^{-12}$ ) and reject all eigenvalues of  $\mathbf{S}$  that are smaller than this cutoff. We denote by  $p$  the number of overlap eigenvalues that are greater than or equal to the cutoff. By rejecting the  $n - p$  overlap eigenvalues and their corresponding eigenvectors, the sizes of  $\mathbf{T}$  and  $\mathbf{s}$  are reduced to  $(n \times p)$  and  $(p \times p)$ , respectively. Using basic matrix algebra, one can show that Eq. (3.20) can be transformed into the ordinary eigenvalue problem

$$\tilde{\mathbf{H}}_\theta \tilde{\Psi}_{i,\theta} = E_{i,\theta} \tilde{\Psi}_{i,\theta}, \quad (3.37)$$

with

$$\begin{aligned} \tilde{\mathbf{H}}_\theta &= \mathbf{V}^T \mathbf{H} \mathbf{V}, \\ \tilde{\Psi}_{i,\theta} &= \mathbf{V}^T \Psi_{i,\theta}, \end{aligned} \quad (3.38)$$

where  $\tilde{\mathbf{H}}_\theta$  is a  $(p \times p)$  matrix,  $\tilde{\Psi}_{i,\theta}$  is a  $(p \times 1)$  vector, and  $\mathbf{V}$  is a  $(n \times p)$  matrix given by

$$\mathbf{V} = \mathbf{T} \mathbf{s}^{-1/2}. \quad (3.39)$$

If only one set of Coulomb-Sturmian functions is used per angular configuration no such procedure is needed. The numerical diagonalization of the eigenvalue problem (3.37) or the generalized eigenvalue problem (3.20) is performed by an efficient scalar implementation of the Lanczos algorithm presented in section 2.4.2.

## Chapter 4

# Spectral properties of helium

Since the failure of the Bohr-Sommerfeld quantization to reproduce the ground state energy of helium, which among other reasons led to the formulation of quantum wave mechanics by Heisenberg [10] and Schrödinger [11], the ground state and singly excited states of helium have attracted the interest of many theoreticians. Various approaches have been proposed for the treatment of this system ranging from semiclassical (see [3] and references therein) to quantum mechanical including relativistic corrections [14, 15]. Doubly excited states drew continuous attention of theoreticians and experimentalists after the experiment by Madden and Codling [16], through which the highly correlated nature of doubly excited states was shown. Most of the attention was directed towards natural parity states ( $\pi = (-1)^L$ ), i.e., states and resonances which are accessible through dipole transitions from the ground state. In particular, resonances for total angular momentum  $L = 0$  and  $L = 1$  have been subject to extensive studies of spectral nature, e.g., [51, 52], and through photoionization cross sections [53, 65, 127–129]. States of unnatural parity ( $\pi = (-1)^{L+1}$ ) have drawn a lot less attention. These states are all doubly excited, i.e., there are no bound states below the first ionization threshold and no continuum starts from this threshold. In fact, the spectrum consists of non-autoionizing doubly excited states below and resonances above the second ionization threshold. Indeed, the non-autoionizing states have already been observed experimentally [130–132] and their identification confirmed theoretically [133] in the late 1920's and early 1930's. The theoretical treatment of complex physical processes like, e.g., electron impact ionization or multiphoton processes with circular polarized light, requires an accurate description of states and resonances of both parities. Note also, that accurate values of the energy and radiative lifetime of non-autoionizing doubly excited states of helium are important in various fields like for instance, astrophysics [134, 135] and plasma physics [136–140].

In the following, spectral data for states and resonances of helium are presented. After a study on the convergence of the ground state, our approach is applied to the computation of  $^1S^e$  and  $^3S^e$  resonances of helium for energies up to the tenth ionization threshold. Following this, non-autoionizing doubly excited states of unnatural parity with angular momentum ranging from  $L = 1$  to  $L = 9$  are treated within our approach. Finally, we present results for  $^3P^e$  resonance states.

### 4.1 Natural parity states

The approach presented in chapter 3 has already been shown to perform excellently for the description of singly excited states of helium [45, 68, 120, 121], in particular, for non-zero total angular momentum. Therefore, we will, concerning bound states, only discuss the convergence of the helium ground state. Following that, we will demonstrate that our configuration interaction approach, in combination with the complex rotation method, is able to accurately describe

$(l_1^{\max}, l_2^{\max})$	$E_0$ [a. u.]		
	$N_i^{\max} = 30$	$N_i^{\max} = 40$	$N_i^{\max} = 50$
(5, 5)	-2.90358924628349	-2.90359778723568	-2.90360124209599
(10, 10)	-2.90366394376605	-2.90368261011208	-2.90369154406158
(15, 15)	-2.90366571552177	-2.90368612752801	-2.90369679541358
(20, 20)	-2.90366573200293	-2.90368620213144	-2.90369699088231
(25, 25)	-2.90366573205997	-2.90368620279737	-2.90369699428155
value of [51]: $E_0 = -2.903724377034119589$			

Table 4.1: Energy values for the ground state (without analysis of converged digits); the basis is given through the used set of Coulomb-Sturmian functions defined by  $[k_1, N_1^{\min}, N_1^{\max}, k_2, N_2^{\min}, N_2^{\max}] = [2.0, 1, N_i^{\max}, 2.0, 1, N_i^{\max}]$  and the angular configurations  $(l_1, l_2)$  included (see Sec. 3.1).

resonance states within bases of rather small size. For this purpose we focus on singlet and triplet states of helium with  $L = 0$ . Results for other values for the total angular momentum  $L$  can be found in appendix C.1.

#### 4.1.1 Ground state

Within our configuration interaction approach [45, 68, 120–122] the convergence of the ground state to its exact value is rather slow. As already mentioned in section 3.1 the reason for this is that the Kato cusp [66, 67], which is a discontinuity in the derivative of the wavefunction at  $r_{12} = 0$ , is not satisfied within the CI approach and not resolvable with a finite number of basis functions. Effectively, the basis expansion within our approach is truncated in two very different ways. On the one hand, the basis is truncated through a maximum value for the radial excitation of the Coulomb-Sturmian functions for each electron, and on the other hand, the multipole expansion for the computation of  $1/r_{12}$  includes only a finite number of angular configurations  $(l_1, l_2)$ .

In this context, it is not clear how large the quantitative influence of the Kato cusp on the ground state energy is and whether one has to include more Coulomb-Sturmian functions for each electron, more angular configurations or both in order to improve the resolution of the cusp and therefore to obtain a ground state energy as close as possible to its true value.

In table 4.1 we present the energy of the ground state computed for various basis expansions, differing in the number of Coulomb-Sturmian functions and angular configurations included. Obviously, the deviation of the eigenvalue from the true value of the ground state energy decreases with an increasing number of Coulomb-Sturmian functions included for each electron. The data of table 4.1, however, shows that there is, depending on  $N_i^{\max}$ , a minimal number of angular configurations for which the energy value obtained exhibits only small variations under the inclusion of additional angular configurations. Thus, the data reveals that the number of Coulomb-Sturmian functions plays the key-role for the energy value, while the number of angular configurations – as long as a certain minimal number of them is included – plays only a minor role. Considering this, a calculation including 26 angular configurations ( $l_1^{\max} = 25, l_2^{\max} = 25$ ) and 70 Coulomb-Sturmian functions per electron ( $[2.0, 1, 70, 2.0, 1, 70]$ ) has been performed, resulting in the eigenvalue

$$E_0 = -2.90370777337547 \text{ a. u. .} \quad (4.1)$$

Note, that the matrices associated to the generalized eigenvalue problem are of dimension

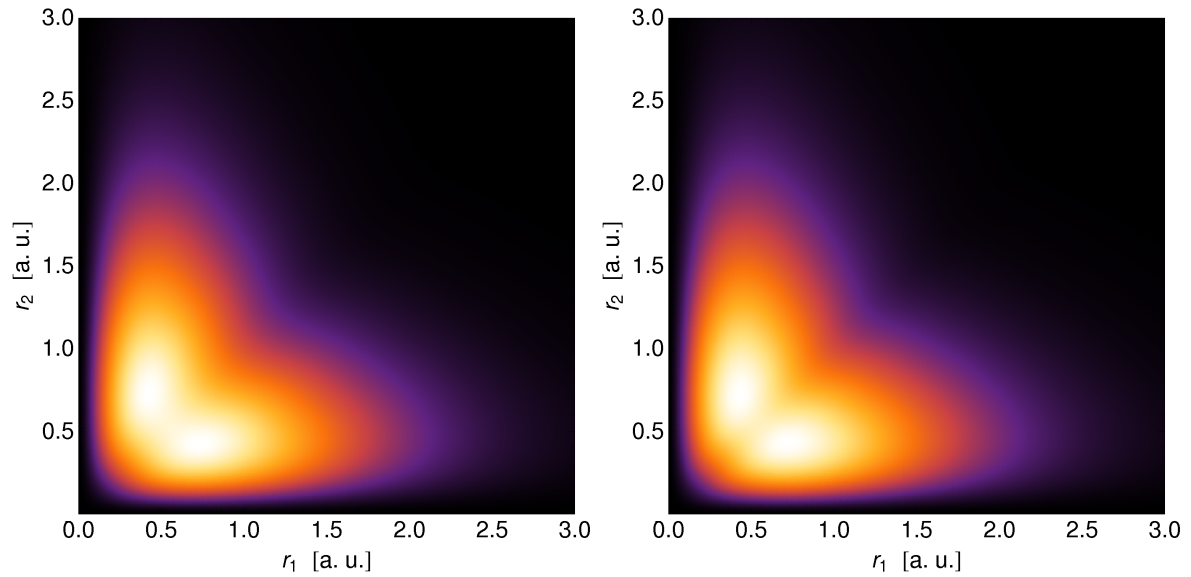


Figure 4.1: Density distribution of the ground state projected onto the subspace with  $\theta_{12} = 0$ . The basis expansions consist of 26 angular configurations with 30 and 70 Coulomb-Sturmian functions per electron for left and right plot, respectively. Note, that in the figures  $|r_1 r_2 \Psi_0(\vec{r}_1, \vec{r}_2)|_{\theta_{12}=0}^2$  is displayed. Areas of low and high density are represented by black and white color, respectively.

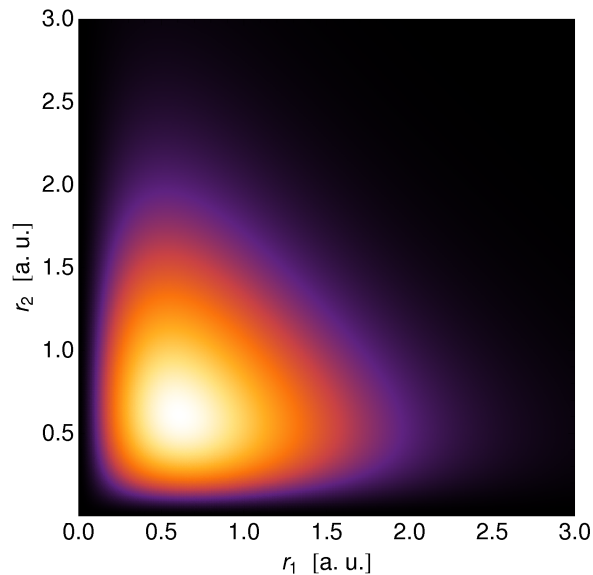


Figure 4.2: Probability density after integration over the angular coordinates ( $\int d\Omega_1 d\Omega_2 r_1^2 r_2^2 |\Psi_i(\vec{r}_1, \vec{r}_2)|^2$ ) of the  $1S^e$  helium ground state. Areas of low and high density are represented by black and white color, respectively.

$n = 64610$ .<sup>1</sup> Though this eigenvalue represents a significant improvement compared to those of table 4.1 it still only agrees to five digits with the reference value by Bürgers *et al.* [51].

The effect of the inclusion of more Coulomb-Sturmian functions on the resemblance of the cusp can also be traced in the density distribution of the ground state. In figure 4.1 projections of the densities of computed eigenstates on the subspace with  $\theta_{12} = 0$  are displayed. Under this condition,  $r_{12} = 0$  is equivalent to  $r_1 = r_2$ , and the density should be zero along this line due to the Coulomb repulsion. For both plots this is not the case, however, the inclusion of more Coulomb-Sturmian functions in the basis leads to a density along this line which is significantly reduced compared to the one containing fewer Coulomb-Sturmian functions. Figure 4.2 present the density of the ground state after integration of the angular coordinates. Note, that the effect of the Kato cusp cannot be spotted in this plot.

### 4.1.2 Resonances

The spectral method described in chapter 3 and the computation of matrix elements of  $1/r_{12}$  via the restarted recursion method have been used to compute highly doubly excited states of helium for singlet and triplet symmetry. We have chosen to compute resonances for  $L = 0$  as these states contain the highest degree of symmetry, which makes them converge slower in this CI approach. The method is applicable to any value of the total angular momentum and should give better convergence for higher values of  $L$ , which has already been illustrated for singly excited states [45, 68].

In order to compute the spectra up to the 10th SIT we have used one choice of parameter sets for each regime between two SITs and for each symmetry. Each basis expansion consists of an expansion into 16 angular configurations and five sets  $[k_{1s}, N_{1s}^{\min}, N_{1s}^{\max}, k_{2s}, N_{2s}^{\min}, N_{2s}^{\max}]$  for each angular configuration. Up to the 5th ionization threshold the dilation parameters are, by a rule of thumb, chosen to be  $k_{1s} \approx 2/N$  and  $k_{2s} \approx 2/n_s$ , where  $N$  and  $n_s$  are the excitations of the inner and the outer electron of the resonance, respectively. The  $n_s$  are taken as such that they account for different excitation of the outer electron in order to allow a description of a whole energy regime. The values of  $N_{is}^{\min}, N_{is}^{\max}$  ( $i = 1, 2$ ) are then chosen to provide an interval around  $N$  and  $n_s$ , respectively, i.e.  $N_{1s}^{\min} < N < N_{1s}^{\max}$  and  $N_{2s}^{\min} < n_s < N_{2s}^{\max}$ . In general the number of Coulomb-Sturmian functions used for the inner electron is larger for symmetric excitation of both electrons than in the case of a very asymmetric configuration. For the higher lying thresholds the choice of the dilation parameters has to be amended as they have to account for different series and screening effects.

To take care of the numerical overcompleteness of the basis the  $(n \times n)$  matrices  $\mathbf{H}_\theta$  and  $\mathbf{S}$  are transformed into the basis where the overlap is diagonal. The transformation matrix consists of the eigenvectors of the overlap matrix associated to eigenvalues larger than the cutoff  $\epsilon = 10^{-12}$ , resulting in an effective reduction of the Hamiltonian matrix into an  $(p \times p)$  matrix (see Sec. 3.3.2) which then has to be diagonalized.

The computation of matrix elements of  $1/r_{12}$  with GL integration techniques is rather cumbersome and renders the optimization of the basis for an energy regime extremely time-consuming and therefore limits the described approach. The implementation of the computation of  $1/r_{12}$  via the restarted recursion method reduces computation time tremendously and allows an application of this spectral method to the computation of highly doubly excited states of helium. Several performance tests have been done. For instance, we have computed the matrix representation of  $1/r_{12}$  for a matrix designed to describe the resonance spectrum below

---

<sup>1</sup>For this choice of the basis the computation of  $1/r_{12}$  with the restarted recursion method (Sec. 3.3.1) lasts 90 hours on a single core of a Dual Core AMD Opteron 8222SE/3GHz. The computation via the Gauß-Laguerre integration exceeds all computation time limits, however, by the fraction of the matrix computed after 20 days a total computation time of 490 days could be estimated. This corresponds to a speed-up of 130 for the restarted recursion method.

$-\text{Re}(E_{i,\theta})$ this work	$-\text{Im}(E_{i,\theta})$	$-\text{Re}(E_{i,\theta})$ Bürgers <i>et al.</i> [51]	$-\text{Im}(E_{i,\theta})$	$-\text{Re}(E_{i,\theta})$ this work	$-\text{Im}(E_{i,\theta})$ (continued)
0.77787	0.00227	0.777867636	0.002270653	0.5046973	0.0000072
0.6219	0.0001	0.621927254	0.000107818	0.5039403	0.0000021
0.589895	0.000681	0.589894682	0.000681239	0.5039040	0.0000054
0.54808	0.00004	0.548085535	0.000037392	0.5033238	0.0000016
0.544882	0.000246	0.544881618	0.000246030	0.5032958	0.0000042
0.527715	0.000023	0.527716640	0.000023101	0.5028415	0.0000013
0.526687	0.000109	0.526686857	0.000109335	0.5028196	0.0000033
0.518103	0.000015	0.518104252	0.000014894	0.5024570	0.0000011
0.517641	0.000057	0.517641112	0.000056795	0.5024395	0.0000026
0.512763	0.000010	0.512763242	0.000009970	0.5021456	0.0000009
0.5125135	0.0000330	0.512513488	0.000032992	0.5021314	0.0000021
0.5094833	0.0000069	0.509483569	0.000006918	0.5018898	0.0000007
0.5093327	0.0000208	0.509332686	0.000020795	0.5018782	0.0000018
0.507324	0.000005	0.507324340	0.000004959	0.5016675	0.0000015
0.5072258	0.0000139	0.507225835	0.000013936		
0.505827	0.000004	0.505827143	0.000003657		
0.5057591	0.0000098	0.505759104	0.000009790		
0.5047463	0.0000028	0.504746388	0.000002766		

Table 4.2:  $^1S^e$  resonances below  $I_2$ : our results compared with the results of [51]. The dimension of the matrices used to obtain the data was  $n = 11472$  and  $p = 8304$ , respectively. The data presented was subject to a stability analysis with respect to varying values of the complex rotation angle  $\theta$ . By increasing the excitation of the outer electron the convergence improves.

$-\text{Re}(E_{i,\theta})$ this work	$-\text{Im}(E_{i,\theta})$	$-\text{Re}(E_{i,\theta})$ Bürgers <i>et al.</i> [51]	$-\text{Im}(E_{i,\theta})$	$-\text{Re}(E_{i,\theta})$ this work	$-\text{Im}(E_{i,\theta})$ (continued)
0.60257751	0.00000332	0.602577505	0.000003325	0.504817014	0.000000061
0.55974655	0.00000010	0.559746626	0.000000130	0.50399459	0.00000005
0.54884086	0.00000155	0.548840858	0.000001547	0.503366094	0.000000035
0.53250532	0.00000006	0.532505349	0.000000072	0.502875028	0.000000027
0.528413972	0.000000772	0.528413972	0.000000771	0.502484067	0.000000022
0.52054918	0.00000004	0.520549199	0.000000041	0.502167743	0.000000018
0.518546375	0.000000429	0.518546375	0.000000428	0.501902040	0.000000015
0.51418035	0.00000002	0.514180356	0.000000025		
0.513046496	0.000000260	0.513046496	0.000000260		
0.510378167	0.000000017	0.510378174	0.000000016		
0.509672798	0.000000169	0.509672798	0.000000169		
0.50792515	0.00000001	0.507925149	0.000000011		
0.507456056	0.000000116	0.507456056	0.000000116		
0.506250076	0.000000007	0.506250079	0.000000008		
0.505922151	0.000000083	0.505922151	0.000000082		
0.505055338	0.000000005	0.505055341	0.000000006		

Table 4.3:  $^3S^e$  resonances below  $I_2$ : our results compared with the results of [51]. The dimension of the matrices used to obtain the data was  $n = 11472$  and  $p = 7936$ , respectively. The data presented was subject to a stability analysis with respect to varying values of the complex rotation angle  $\theta$ . The last few resonances are exclusively members of the  $K = 1$  series, which typically have the largest widths.

$-\text{Re}(E_{i,\theta})$ this work	$-\text{Im}(E_{i,\theta})$	$-\text{Re}(E_{i,\theta})$ Bürgers <i>et al.</i> [51]	$-\text{Im}(E_{i,\theta})$	$-\text{Re}(E_{i,\theta})$ this work (continued)	$-\text{Im}(E_{i,\theta})$
0.353538	0.001505	0.353538536	0.001504906	0.225971	0.000037
0.31745	0.00333	0.317457836	0.003329920	0.225848	0.000012
0.281073	0.000751	0.281072703	0.000750733	0.2258390	0.0000026
0.263388	0.001209	0.263388312	0.001209354	0.225397	0.000029
0.25737	0.00001	0.257371610	0.000010564	0.2253023	0.0000092
0.25597	0.00035	0.255972114	0.000350036	0.2252943	0.0000020
0.246635	0.000566	0.246634603	0.000565481	0.224945	0.000023
0.244324	0.000021	0.244324739	0.000021400	0.2248710	0.0000073
0.243824	0.000180	0.238524104	0.000318437	0.2248640	0.0000016
0.23853	0.00032	0.243824049	0.000179910	0.224584	0.000018
0.237310	0.000016	0.237311202	0.000017021	0.2245242	0.0000059
0.23715	0.00010	0.237147099	0.000102160	0.2245181	0.0000013
0.233900	0.000196	0.233898812	0.000196262	0.2242898	0.0000152
0.233172	0.000012	0.233173689	0.000012347	0.2242413	0.0000049
0.233122	0.000062	0.233121363	0.000062881	0.22423593	0.00000110
0.231002	0.000129	0.231001524	0.000129185	0.2240475	0.0000126
0.230531	0.000009	0.230531347	0.000008810	0.2240074	0.0000040
0.230520	0.000041	0.230519146	0.000041369	0.22400277	0.00000092
0.229065	0.000090	0.229064586	0.000089418	0.223845	0.000010
0.228744	0.000028	0.228744234	0.000028755	0.223811	0.000003
0.228741	0.000006	0.228741812	0.000006247	0.2238080	0.0000008
0.227706	0.000065	0.227705232	0.000064398		
0.227482	0.000021	0.227481269	0.000020794		
0.227474	0.000004	0.227473958	0.000004545		
0.226715	0.000048	0.22671442	0.00004789		
0.226552	0.000015	0.226551500	0.000015492		
0.2265427	0.0000033	0.22654299	0.00000342		

Table 4.4:  $^1S^e$  resonances below  $I_3$ : our results compared with the results of [51]. The dimension of the matrices used to obtain the data was  $n = 11744$  and  $p = 6951$ , respectively. The data presented was subject to a stability analysis with respect to varying values of the complex rotation angle  $\theta$ .

the 6th SIT with both methods on an Itanium2 processor at the Linux Cluster of the Leibniz-Rechenzentrum of the Bayerische Akademie der Wissenschaften. The computation time reduces from 22.5 hours for pure GL integration to 1.75 hours for the method described in section 3.3.1. Moreover, the speedup of this method compared to GL integration increases with increasing maximum radial and angular indices of the Coulomb-Sturmian functions included.

Tables 4.2 to 4.7 display the real and imaginary part of resonances up to below  $I_4$ . Only converged digits are shown. In Tables 4.2, 4.4 and 4.6 our results for the singlet symmetry spectra below  $I_2$  to below  $I_4$  are compared to reference data from [51], while in Tables 4.3, 4.5 and 4.7 our results for triplet symmetry are again presented together with data from [51]. The data has been tested for convergence with respect to variation of the complex rotation angle  $\theta$ , the dilation parameters, and the number of angular configurations. For a given choice of the parameters  $[k_{1s}, N_{1s}^{\min}, N_{1s}^{\max}, k_{2s}, N_{2s}^{\min}, N_{2s}^{\max}]$  several values of  $\theta$  in the interval  $[0.085, 0.2]$  have been chosen. Note, that the data presented in Tab. 4.2 to 4.7 have each been obtained with one optimized basis choice with an effective dimension of the resulting matrix of  $p < 8500$  for singlet and  $p < 8000$  for triplet symmetry. In contrast, the results in [51] were obtained using perimetric coordinates and the typical basis dimensions were three times larger for the

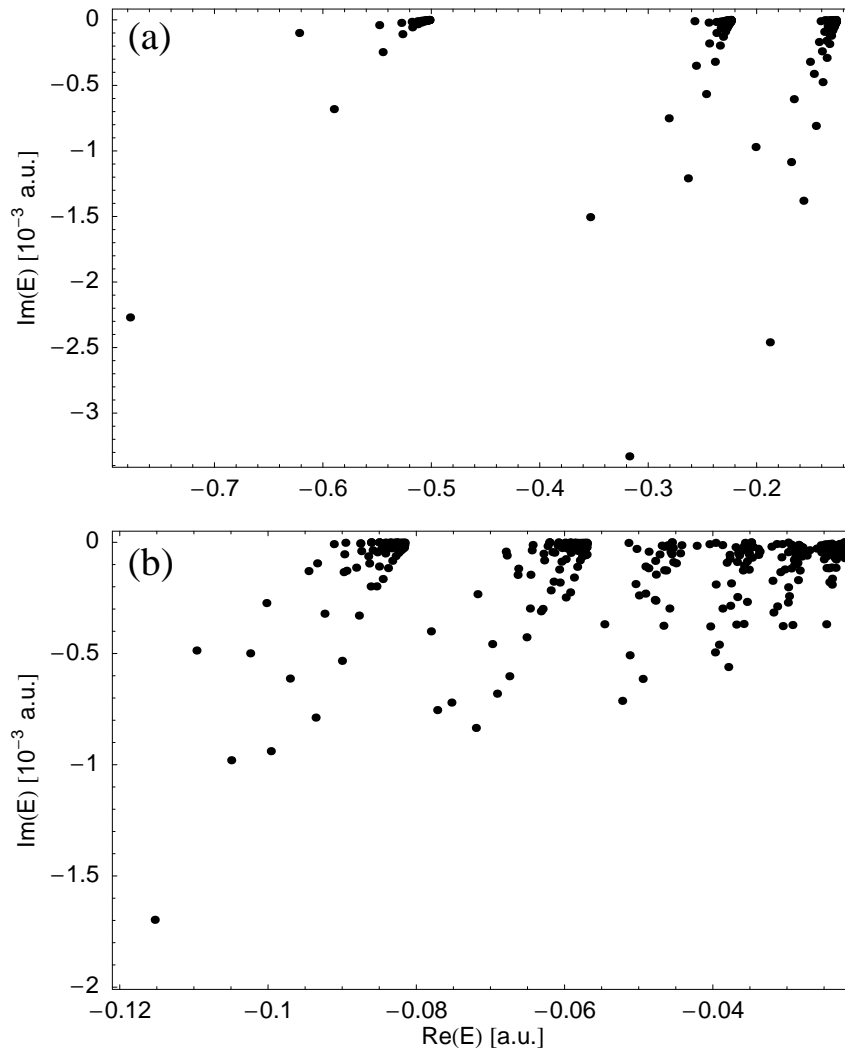


Figure 4.3: Resonance spectrum for singlet symmetry  $L = 0$  states. (a) shows the data presented in Tables 4.2, 4.4 and 4.6. In (b) the converged resonances from above  $I_4$  to below  $I_{10}$  are displayed. The criterion of convergence used was maximum relative deviation of the real part of  $10^{-4}$  and maximum relative deviation of the imaginary part of  $10^{-2}$  for at least three values of  $\theta$ . The spectra have been obtained with matrices smaller than or equal to  $n = 12240$  and  $p = 8778$ , respectively.

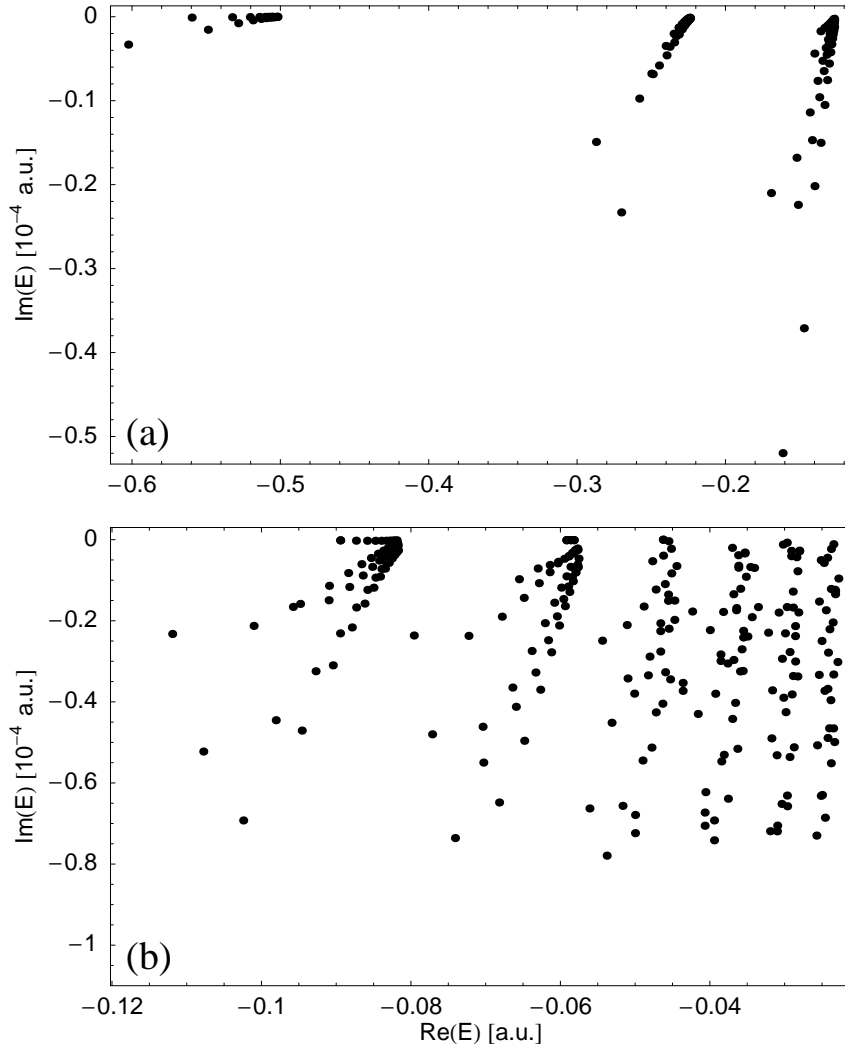


Figure 4.4: Resonance spectrum for triplet symmetry  $L = 0$  states. (a) shows the data presented in Tables 4.3, 4.5 and 4.7. In (b) the converged resonances from above  $I_4$  to below  $I_{10}$  are displayed. The criterion of convergence used was maximum relative deviation of the real part of  $10^{-4}$  and maximum relative deviation of the imaginary part of  $10^{-2}$  for at least three values of  $\theta$ . The spectra have been obtained with matrices smaller than or equal to  $n = 12240$  and  $p = 8278$ , respectively. For the energy regime above  $I_5$  the convergence of narrow resonances ( $K = -N + 1$ ) is limited, due to the smallness of the imaginary part of the eigenvalues in comparison with the real part.

$-\text{Re}(E_{i,\theta})$ this work	$-\text{Im}(E_{i,\theta})$	$-\text{Re}(E_{i,\theta})$ Bürgers <i>et al.</i> [51]	$-\text{Im}(E_{i,\theta})$	$-\text{Re}(E_{i,\theta})$ this work (continued)	$-\text{Im}(E_{i,\theta})$
0.28727713833	0.00001491439	0.287277138	0.000014914	0.22662254	0.00000061
0.270283613	0.000023307	0.270283614	0.000023308	0.22615767	0.00000034
0.258133977	0.000009749	0.258133976	0.000009748	0.22607865	0.00000064
0.24996463	0.00000678	0.249964616	0.000006789	0.225901438	0.000000473
0.249000427	0.000006842	0.249000418	0.000006848	0.225542108	0.000000264
0.24480749	0.00000581	0.244807489	0.000005801	0.225480290	0.000000496
0.24031449	0.00000348	0.240314494	0.000003490	0.225343862	0.000000371
0.23969689	0.00000460	0.239696887	0.000004600	0.225060490	0.000000209
0.23767221	0.00000358	0.237672213	0.000003578	0.225011251	0.000000400
0.23496955	0.00000203	0.234969582	0.000002042	0.224903928	0.000000297
0.23456903	0.00000306	0.234569038	0.000003061	0.224676582	0.000000169
0.23343332	0.00000233	0.233433327	0.000002322	0.224636744	0.000000323
0.231692091	0.000001298	0.231692116	0.000001300	0.224550762	0.000000241
0.23142164	0.00000211	0.231421646	0.000002100	0.224365627	0.000000137
0.23071908	0.00000158	0.230719088	0.000001578	0.224332952	0.000000265
0.229535681	0.000000880	0.229535701	0.000000880	0.224262980	0.000000198
0.229345777	0.000001492	0.229345782	0.000001491	0.224110242	0.000000113
0.228880000	0.000001117	0.228880000	0.000001117	0.224083116	0.000000221
0.228040858	0.000000620	0.228040873	0.000000623	0.22387516	0.000000017
0.227902911	0.000001092	0.227902914	0.000001091		
0.22757745	0.00000082	0.2275778	0.0000008		
0.226961937	0.000000455	0.226962	0.0000001		
0.226858802	0.000000823	0.226859	0.0000001		

Table 4.5:  ${}^3S^e$  resonances below  $I_3$ : our results compared with the results of [51]. The dimension of the matrices used to obtain the data was  $n = 11744$  and  $p = 6760$ , respectively. The data presented was subject to a stability analysis with respect to varying values of the complex rotation angle  $\theta$ .

results presented up to the 4th SIT and about a factor 5 larger for convergence around the 9th ionization threshold [54].

In the case of singlet symmetry the data in Tables 4.2, 4.4 and 4.6 show a precision of five to eight significant digits for the real part and around two significant digits for the imaginary part of the resonance energies. For triplet symmetry (see Tables 4.3, 4.5 and 4.7) the accuracy is around nine significant digits for the real and two significant digits for the imaginary part, respectively. The discrepancy between the precision for singlet and triplet symmetry is due to the influence of the Kato cusp [66, 67], which is a discontinuity of the derivative of the wavefunction at  $r_{12} = 0$  which is not resolvable within our approach. In the case of triplet symmetry the influence of the Kato cusp is softened by the Pauli principle. With increasing excitation of the outer electron the number of converged digits rises in general in contrast to the EC approach in [51]. This is due to the fact that the Kato cusp is more important for symmetrically excited configurations. Along the tables 4.2 to 4.7 some resonances converge better than others, which is a signature that the chosen basis parameters are better suited for the description of such resonances. Indeed, the convergence of a single state depends significantly on the basis used, a clear example for this is the triplet  $I_3$  ground state, which converges better than anticipated from the above argument, and which is most probably a consequence of an almost ideal basis for the description of this state. The precision for a particular resonance can be vastly improved by optimizing the basis for this state instead of optimizing the basis for an energy regime.

$-\text{Re}(E_{i,\theta})$ this work	$-\text{Im}(E_{i,\theta})$	$-\text{Re}(E_{i,\theta})$ Bürgers <i>et al.</i> [51]	$-\text{Im}(E_{i,\theta})$	$-\text{Re}(E_{i,\theta})$ this work (continued)	$-\text{Im}(E_{i,\theta})$	$-\text{Re}(E_{i,\theta})$ Bürgers <i>et al.</i> [51] (cont.)	$-\text{Im}(E_{i,\theta})$
0.200990	0.000970	0.200989572	0.000969178	0.1299935	0.0000027	0.129993447	0.000002704
0.18783	0.00246	0.187834626	0.002458380	0.1297182	0.0000028	0.129717890	0.000002986
0.168261	0.001085	0.168261328	0.001086186	0.129251	0.000046	0.129251251	0.000046022
0.165734	0.000605	0.165734021	0.000605047	0.129323	0.000033	0.129322969	0.000033799
0.15691	0.00138	0.156904051	0.001377256	0.129225	0.000058	0.129224756	0.000057660
0.15083	0.00032	0.150824382	0.000320293	0.1289253	0.0000025	0.128925097	0.000002597
0.147267	0.000412	0.147266965	0.000416449	0.128777	0.000053	0.128776594	0.000054043
0.145400	0.000809	0.145397764	0.000808943	0.1285627	0.0000361	0.128562811	0.000036493
0.142603	0.000169	0.142602474	0.000169806	0.128552	0.000041	0.128551852	0.000041001
0.141066	0.000010	0.141064156	0.000011739	0.12831547	0.00000213	0.128315304	0.000002218
0.1398403	0.0002400	0.139840342	0.000239815	0.1282625	0.0000396	0.128262189	0.000039756
0.139190	0.000475	0.139189490	0.000475268	0.1280296	0.0000312	0.128029833	0.000031311
0.137686	0.000091	0.137685346	0.000092512	0.1280257	0.0000274	0.128025335	0.000027559
0.137088	0.000002	0.137088229	0.000002490	0.1278368	0.0000018	0.127836684	0.000001881
0.135728	0.000160	0.135728512	0.000160253	0.1278159	0.0000270	0.12781573	0.00002743
0.135439	0.000290	0.135437398	0.000289889	0.1276101	0.0000257	0.127610012	0.000025737
0.134551	0.000049	0.134551108	0.000049711	0.1276056	0.0000198	0.127605478	0.000019886
0.134229	0.000003	0.134228598	0.000002711	0.12745445	0.00000154	0.127454353	0.000001595
0.133141	0.000110	0.133141846	0.000111361	0.1274462	0.0000196	0.1274461	0.0000200
0.132997	0.000184	0.132996200	0.000183914	0.1272715	0.0000206	0.127271404	0.000020669
0.1324519	0.0000233	0.132451935	0.000023393	0.1272676	0.0000153	0.127267459	0.000015312
0.1322133	0.0000030	0.132212660	0.000003293	0.1271443	0.0000013	0.127144218	0.000001356
0.131396	0.000080	0.131396547	0.000080331	0.1271418	0.0000148	0.1271415	0.0000152
0.131320	0.000121	0.131319807	0.000120624	0.1269945	0.0000164	0.1269944	0.0000166
0.1309991	0.0000058	0.130999124	0.000005799	0.1269913	0.0000123	0.1269912	0.0000123
0.1307731	0.0000031	0.130772717	0.000003289	0.1268895	0.0000116		
0.130160	0.000059	0.130160039	0.000059877	0.12688930	0.00000112	0.12688926	0.00000118
0.130121	0.000080	0.130120051	0.000080068	0.1267651	0.0000131		

Table 4.6:  $^1S^e$  resonances below  $I_4$ : our results compared with the results of [51]. The dimension of the matrices used to obtain the data was  $n = 11744$  and  $p = 6576$ , respectively. The data presented was subject to a stability analysis with respect to varying values of the complex rotation angle  $\theta$ . Some more converged resonances have been obtained which are not displayed here.

$-\text{Re}(E_{i,\theta})$ this work	$-\text{Im}(E_{i,\theta})$	$-\text{Re}(E_{i,\theta})$ Bürgers <i>et al.</i> [51]	$-\text{Im}(E_{i,\theta})$	$-\text{Re}(E_{i,\theta})$ this work (continued)	$-\text{Im}(E_{i,\theta})$	$-\text{Re}(E_{i,\theta})$ Bürgers <i>et al.</i> [51] (cont.)	$-\text{Im}(E_{i,\theta})$
0.169306634	0.000021005	0.169306635	0.000021006	0.129327408	0.000000718	0.129327395	0.000000724
0.161480663	0.000051983	0.161480663	0.000051980	0.129281535	0.000004229	0.129281436	0.000004228
0.15212204	0.00001680	0.152122029	0.000016799	0.129028519	0.000001558	0.129028519	0.000001559
0.15117642	0.00002241	0.151176420	0.000022408	0.128742045	0.000001860	0.128742039	0.000001867
0.14716881	0.00003711	0.147168813	0.000037116	0.128621741	0.000000588	0.128621731	0.000000593
0.14317600	0.00001140	0.143175987	0.000011381	0.128585657	0.000003277	0.128585657	0.000003276
0.14169136	0.00001470	0.141691356	0.000014696	0.128395405	0.000001218	0.128395405	0.000001219
0.14008854	0.00000439	0.140088484	0.000004409	0.128168621	0.000001452	0.128168616	0.000001457
0.13999805	0.00002018	0.139998046	0.000020176	0.128075628	0.000000487	0.128075620	0.000000489
0.13796132	0.00000764	0.137961324	0.000007642	0.128046837	0.000002588	0.128046838	0.000002588
0.13678714	0.00000959	0.136787119	0.000009622	0.127900092	0.000000969	0.127900092	0.000000970
0.13597556	0.00000173	0.135975513	0.000001752	0.127717811	0.000001154	0.127717807	0.000001158
0.13585741	0.00001502	0.135857413	0.000015013	0.127644357	0.000000404	0.127644351	0.000000407
0.13467953	0.00000525	0.134679533	0.000005256	0.127621072	0.000002079	0.127621073	0.000002078
0.13381173	0.00000647	0.133811711	0.000006493	0.127505445	0.000000783	0.12750544	0.00000079
0.133329281	0.000001326	0.133329246	0.000001340	0.127356921	0.000000932	0.127356918	0.000000935
0.13323044	0.00001051	0.133230435	0.000010505	0.127297848	0.000000338	0.127297839	0.000000341
0.13249065	0.00000372	0.132490651	0.000003725	0.127278774	0.000001694	0.127278774	0.000001694
0.13184923	0.00000452	0.131849211	0.000004540	0.127186005	0.000000641	0.1271860	0.0000006
0.131533756	0.000001077	0.131533731	0.000001087	0.127063496	0.000000763	0.12706350	0.00000077
0.13145699	0.00000755	0.131456986	0.000007547	0.127015248	0.000000285	0.12701524	0.00000029
0.130962374	0.000002716	0.130962374	0.000002717	0.126999448	0.000001398	0.1269993	0.0000014
0.13048099	0.00000327	0.130480976	0.000003283	0.126923855	0.000000532		
0.130261387	0.000000879	0.130261370	0.000000886	0.126821690	0.000000634		
0.130202294	0.000005580	0.130202295	0.000005577	0.126781760	0.000000243		
0.129855236	0.000002034	0.129855236	0.000002035	0.12676853	0.00000117		
0.129487234	0.000002436	0.129487225	0.000002444	0.1267061	0.0000004		

Table 4.7:  ${}^3S^e$  resonances below  $I_4$ : our results compared with the results of [51]. The dimension of the matrices used to obtain the data was  $n = 11744$  and  $p = 6386$ , respectively. The data presented was subject to a stability analysis with respect to varying values of the complex rotation angle  $\theta$ .

$-\text{Re}(E_{i,\theta})$	$-\text{Im}(E_{i,\theta})$	$-\text{Re}(E_{i,\theta})$	$-\text{Im}(E_{i,\theta})$	$-\text{Re}(E_{i,\theta})$	$-\text{Im}(E_{i,\theta})$
0.07803	0.00040	0.061377	0.000047	0.058214	0.000019
0.077179	0.000755	0.0609470	0.0000141	0.05815259	0.00000639
0.075259	0.000724	0.06084037	0.00000096	0.0579425	0.0000813
0.07197	0.00083	0.060732	0.000123	0.0579212	0.0000024
0.071751	0.000233	0.060650	0.000181	0.0579127	0.0000421
0.069767	0.000456	0.0604259	0.0000869	0.0578718	0.0000108
0.069113	0.000680	0.060350	0.000026	0.05782639	0.00000857
0.067934	0.000042	0.0599835	0.0000140	0.0576439	0.0000640
0.067803	0.000059	0.05993838	0.00000137	0.05763370	0.00000235
0.067454	0.000601	0.0598501	0.0000758	0.05755575	0.00000868
0.066339	0.000146	0.059850	0.000248	0.0574577	0.0000197
0.066252	0.000119	0.0596356	0.0000284	0.0573948	0.0000022
0.065135	0.000427	0.0595730	0.0000115	0.0573938	0.0000378
0.0646766	0.0002976	0.0592650	0.0000218	0.0573937	0.0000580
0.0646037	0.0001459	0.0592493	0.0002250	0.05732928	0.00000769
0.0644329	0.0000361	0.05924720	0.00000099	0.0572486	0.0000144
0.0643087	0.0000122	0.0591693	0.0000474	0.05719414	0.00000207
0.063202	0.000310	0.05903087	0.00000400	0.0571939	0.0000285
0.062962	0.000300	0.058739	0.000158	0.0571928	0.0000580
0.0628546	0.0000515	0.0587098	0.0000314	0.05713818	0.00000645
0.0627563	0.0000814	0.05870388	0.00000155	0.0570707	0.0000108
0.06229723	0.00001692	0.0586368	0.0000295	0.0570269	0.0000552
0.06205363	0.00000056	0.0585482	0.0000027	0.05702415	0.00000195
0.061872	0.000216	0.0583035	0.0001101	0.0570228	0.0000220
0.0616514	0.0000441	0.0582713	0.0000023	0.05697575	0.00000537
0.061491	0.000177	0.0582679	0.0000382		

Table 4.8:  $^1S^e$  resonances below  $I_6$  and actual precision; the dimension of the matrices used to obtain the data was  $n = 11808$  and  $p = 6193$ , respectively. The used criterion of convergence was maximum relative deviation of the real part of  $10^{-4}$  and maximum relative deviation of the imaginary part of  $10^{-2}$  for at least three values of  $\theta$ .

$-\text{Re}(E_{i,\theta})$	$-\text{Im}(E_{i,\theta})$	$-\text{Re}(E_{i,\theta})$	$-\text{Im}(E_{i,\theta})$
0.0239821	0.0000061	0.0233936	0.0000775
0.023951	0.000190	0.023265	0.000062
0.023929	0.000163	0.0231951	0.0000558
0.0238002	0.0000345	0.0230812	0.0000105
0.0236262	0.0000606	0.0229936	0.0000248
0.023619	0.000025	0.022926	0.000062
0.0235660	0.0000303	0.0228979	0.0000073
0.0235573	0.0000713	0.0228237	0.0000075
0.023441	0.000116	0.022682	0.000051
0.0233989	0.0000122	0.022672	0.000042

Table 4.9: Real and imaginary part of a few selected  $^1S^e$  resonances below  $I_{10}$ . The dimension of the matrices used to obtain the data was  $n = 12240$  and  $p = 8548$ , respectively. The used criterion of convergence was maximum relative deviation of the real part of  $10^{-4}$  and maximum relative deviation of the imaginary part of  $10^{-2}$  for at least three values of  $\theta$ .

In Fig. 4.3 and 4.4 the spectra up to  $I_{10}$  are displayed for singlet and triplet symmetry, respectively. For resonances above the 4th SIT the criterion of convergence is given through a coincidence of eigenenergies for at least three different values of the complex rotation angle  $\theta$  with a maximum relative deviation of  $10^{-4}$  of the real and  $10^{-2}$  of the imaginary part. The criterion is designed to exclude the discretized continuum states, numerical artefacts and non-converged resonances in an efficient manner and does not reflect the actual accuracy of the computed resonances, which is in most cases significantly higher. To show the actual precision of our results we give apart from the graphical data in Fig. 4.3 and 4.4 the energy and half width for converged resonances below the 6th and 10th threshold in Tables 4.8 and 4.9 (only converged digits are displayed), respectively. In Table 4.9 we present the resonances in a narrow energy window; these are by far not all converged resonances found.<sup>2</sup> Triplet state resonances with extremely narrow width, which are usually members of the  $K = -N + 1$  series, do often not fulfill the above mentioned criterion as for these resonances we usually obtain only one to two significant digits for the imaginary part. This is clearly visible in Fig. 4.4, where for the energy regime above the 5th SIT only few members of these series are visible. Note, that the largest matrices to diagonalize in order to obtain these spectra were of dimension  $p = 8778$  for singlet and  $p = 8278$  for triplet symmetry; these are thus significantly smaller than the typical dimensions in alternative state-of-the-art methods [51, 54].

## 4.2 Unnatural parity states

In the following, spectral data for unnatural parity states and resonances is presented. The data is compared to available reference data. In case of  $^3P^e$  resonances a significant disagreement is found with recently published results by Saha *et al.* [141], calculated using the stabilization method based on the Ritz variational method. Spectral data for  $^1P^e$  resonances can be found in appendix C.2.1.

### 4.2.1 Non-autoionizing states

For total angular momentum  $L$ , individual angular momenta of the electrons satisfy the relation  $(-1)^{L+1} = (-1)^{l_1+l_2}$  for unnatural parity states. As a consequence of this and of the triangular condition for the addition of angular momenta, the single particle angular momenta cannot be zero ( $l_i \neq 0$ ,  $i = 1, 2$ ), the total angular momentum is at least 1, and the lower electron excitation must be at least  $n_i = 2$ . Therefore, the series of non-autoionizing states of unnatural parity states converge to the second ionization threshold. Energies of singlet and triplet non-autoionizing helium doubly excited states of unnatural parity for  $L = 1, \dots, 9$  are presented in Tables 4.10 and 4.11. These have been obtained after diagonalization of the matrix representation of (3.3) in the basis described in chapter 3. We have used up to 26 angular configurations  $(l_1, l_2)$  which lead to matrix dimensions up to  $p = 16000$  (most of the results presented here converge with a ten-times smaller basis). The data presented has been tested for convergence with respect to variation of the complex rotation angle  $\theta$ , the dilation parameters, and the number of angular configurations. In particular, these energies are invariant with respect to  $\theta$  in an exact representation. The variations of the eigenvalues with respect to  $\theta$  induced by the truncation of the basis are used to find the converged digits. In our calculations we have used the values of the rotation angle  $\theta \in \{0.0, 0.005, 0.01, 0.025, 0.05\}$ . Only converged digits are shown in Tables 4.10 and 4.11.

Low-lying  $P$ ,  $D$  and  $F$  unnatural parity states have been calculated by other groups within different approaches [142–146]. In Table 4.10 we reproduce the energies of these states and present more benchmark results for further excited states. Table 4.11 displays energies of states

---

<sup>2</sup>Roughly 110 well converged resonances could be identified.

$^1P^e$		$^3P^e$		$^1D^o$		$^3D^o$	
$n$	present work	Ref. data	present work	Ref. data	$n$	present work	Ref. data
2			0.7104998	0.7105001556783 <sup>a</sup> 0.7105001556567833 <sup>b</sup> 0.71050015565678 <sup>c</sup>	3	0.563800418	0.563800420462 <sup>a</sup> 0.56380042 <sup>d</sup>
3	0.5802464715	0.580246472594 <sup>a</sup> 0.58024647259438 <sup>b</sup>	0.56781281	0.567812898724 <sup>a</sup> 0.567812898725152 <sup>b</sup>	4	0.5345763848	0.534576385556 <sup>a</sup> 0.53457638 <sup>d</sup>
4	0.5400415905	0.54004159009 <sup>a</sup> 0.54004159093851 <sup>b</sup>	0.53586715	0.5358671887 <sup>a</sup> 0.53586718876821 <sup>b</sup>	5	0.5216590151	0.521659015466 <sup>a</sup> 0.52165901 <sup>d</sup>
5	0.5241789816	0.5241790 <sup>a</sup> 0.52417898181141 <sup>b</sup>	0.52225456	0.52225457 <sup>a</sup> 0.52225457570723 <sup>b</sup>	6	0.5148335930	0.51483359321 <sup>a</sup> 0.51483359 <sup>d</sup>
6	0.5162086103	0.51620861046818 <sup>b</sup>	0.515160194	0.51516020385435 <sup>b</sup>	7	0.5107926190	0.5107926191 <sup>a</sup> 0.51078723 <sup>d</sup>
7	0.51162653629	0.51162653637782 <sup>b</sup>	0.510991685	0.51099169120713 <sup>b</sup>	8	0.50820376391	0.50820375 <sup>a</sup> 0.50801548 <sup>d</sup>
8	0.50874801146	0.50874801151596 <sup>b</sup>	0.508334233	0.50833423750462 <sup>b</sup>	9	0.50644607146	0.506445 <sup>a</sup>
9	0.50682104438	0.50682104441578 <sup>b</sup>	0.506536276	0.50653627909544 <sup>b</sup>	10	0.50519830878	0.5062884965 0.5050840140
10	0.50546767514	0.50546767516722 <sup>b</sup>	0.505263296	0.50526329773772 <sup>b</sup>	11	0.50428070170	0.5041951822 0.5035206081
11	0.50448074392	0.50448074393511 <sup>b</sup>	0.5043290797		12	0.50358625606	0.5029965724 0.5025813973
12	0.50373889704		0.5036232454		13	0.50304805849	0.5022468913 0.50197343200
13	0.50316718527		0.5030769762		14	0.50262251928	0.50174701984 0.501557450
14	0.50271727806		0.5026455559		15	0.50228025461	0.5013971 0.5013921
15	0.50235686959		0.5022989044		16	0.502000872000	
16	0.50206369874		0.50201618273		17	0.501769859819	
17	0.501822020527		0.50178258397		18	0.501576663	
18	0.501620444		0.501587352		19	0.501413	
19	0.5014506		0.5014224				

$^1F^e$		$^3F^e$		$^1F^e$ (continued)		$^3F^e$ (continued)	
$n$	present work	Ref. data	present work	Ref. data	$n$	present work	present work
4	0.53199543671	0.5319954369509 <sup>a</sup>	0.5319913251	0.5319913263465 <sup>a</sup>	12	0.503500444342	0.50350020079
5	0.52038567086	0.5203856710486 <sup>a</sup>	0.5203828583	0.5203828592839 <sup>a</sup>	13	0.502980780358	0.50298058847
6	0.51411321805	0.5141132181781 <sup>a</sup>	0.5141114284	0.5141114291180 <sup>a</sup>	14	0.502568796718	0.50256864290
7	0.51034573795	0.510345738040 <sup>a</sup>	0.51034456422	0.510344564686 <sup>a</sup>	15	0.5022366755580	0.50223655040
8	0.50790754830	0.5079075482 <sup>a</sup>	0.50790674595	0.5079067461 <sup>a</sup>	16	0.5019650343034	0.50196493112
9	0.50623965811	0.506239653 <sup>a</sup>	0.50623908834	0.506239088 <sup>a</sup>	17	0.501740032588	0.50173994653
10	0.50504873915		0.50504832108		18	0.5015515739	0.5015515014
11	0.504168863147		0.50416854777		19	0.501392	0.5013921

<sup>a</sup> Reference [142]; <sup>b</sup> Reference [143]; <sup>c</sup> Reference [144]; <sup>d</sup> Reference [145];

Table 4.10: Absolute values of the energies ( $-E$  [a. u.]) of non-autoionizing doubly excited  $^1P^e$ ,  $^3P^e$ ,  $^1D^o$ ,  $^3D^o$ ,  $^1F^e$ , and  $^3F^e$  states of helium in comparison with reference data.

$n$	${}^1G^{\circ}$	${}^3G^{\circ}$	${}^1H^e$	${}^3H^e$	${}^1I^{\circ}$	${}^3I^{\circ}$
5	0.520159333525	0.52015932019				
6	0.513982240486	0.51398222681	0.513936277123	0.513936277088		
7	0.510263292891	0.51026328169	0.5102342063486	0.5102342063021	0.5102215045173	0.51022150452
8	0.507852347306	0.50785233860	0.5078328026556	0.5078328026105	0.5078242511171	0.507824251117
9	0.506200910578	0.506200903864	0.5061871566018	0.5061871565623	0.5061811305642	0.50618113056407
10	0.505020507250	0.505020502034	0.5050104670730	0.5050104670397	0.5050060638226	0.5050060638225
11	0.5041476624683	0.504147658368	0.50414011195527	0.5041401119275	0.50413679810896	0.5041367981088
12	0.5034841216571	0.5034841183916	0.50347830182959	0.50347830180655	0.5034757460826	0.5034757460825
13	0.5029679472607	0.502967944626	0.50296336747273	0.50296336745355	0.5029613553543	0.5029613553542
14	0.5025585255313	0.5025585233796	0.50255485728707	0.50255485727102	0.5025532450494	0.5025532450493
15	0.5022283274272	0.5022283256500	0.50222534413265	0.50222534411914	0.5022240325335	0.5022240325335
16	0.5019581576888	0.5019581562056	0.5019556989716	0.5019556989601	0.50195461772224	0.5019546177222
17	0.5017343010499	0.501734299800	0.5017322508379	0.5017322508281	0.5017313490360	0.5017313490360
18	0.5015467467	0.5015467457	0.50154501935	0.50154501934	0.501544259403	0.501544259403
19	0.50138805	0.5013880	0.50138658	0.50138658	0.501385934	0.501385934
20	0.50125	0.501252	0.501251	0.501251	0.501251	0.501251
$n$	${}^1K^e$	${}^3K^e$	${}^1L^{\circ}$	${}^3L^{\circ}$	${}^1M^e$	${}^3M^e$
8	0.50781992488219	0.5078199248822				
9	0.50617807968861	0.50617807968861	0.50617636756478	0.50617636756478		
10	0.50500383331558	0.50500383331558	0.505002581178723	0.505002581178723	0.505001822851975	0.505001822851975
11	0.50413511875810	0.50413511875810	0.50413417579851	0.50413417579851	0.504133604634452	0.504133604634452
12	0.50347445049881	0.50347445049881	0.50347372289118	0.50347372289118	0.50347328211932	0.50347328211932
13	0.50296033509375	0.50296033509375	0.50295976202569	0.50295976202569	0.5029594148402	0.5029594148402
14	0.50255242738438	0.50255242738438	0.50255196805760	0.50255196805760	0.5025516897607	0.5025516897607
15	0.502223367228905	0.50222336722891	0.50222299345507	0.50222299345507	0.5022227669796	0.5022227669796
16	0.50195406918493	0.50195406918493	0.5019537609871	0.50195376098707	0.50195357423604	0.50195357423603
17	0.50173089148147	0.50173089148147	0.5017306343852	0.5017306343852	0.5017304785924	0.5017304785924
18	0.5015438737845	0.5015438737845	0.5015436570959	0.501543657096	0.5015435257843	0.5015435257843
19	0.5013856063	0.5013856063	0.50138542198	0.50138542198	0.5013853102875	0.5013853102874
20	0.5012505	0.5012505	0.50125033	0.50125033	0.5012502305023	0.5012502305023
21					0.501133986035	0.501133986035

Table 4.11: Absolute values of the energies ( $-E$  [a. u.]) of non-autoionizing doubly excited helium states of unnatural parity and total angular momentum  $L = 4, \dots, 9$ .

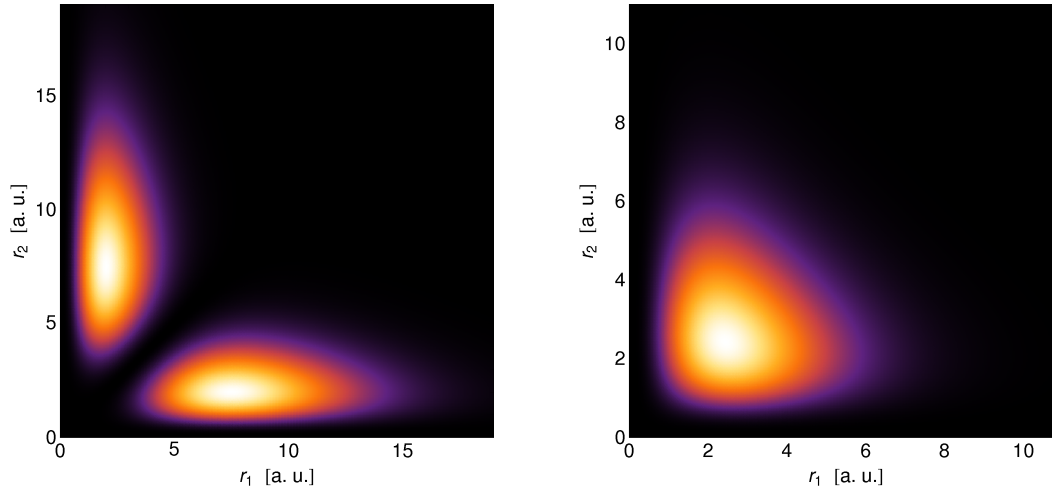


Figure 4.5: Probability density after integration over the angular coordinates ( $\int d\Omega_1 d\Omega_2 r_1^2 r_2^2 |\Psi_i(\vec{r}_1, \vec{r}_2)|^2$ ) of the lowest lying  $^1P^e$ -state (left) and of the lowest  $^3P^e$ -state (right). In contrast to the states of natural parity (see Fig. 4.2), the singlet state exhibits a vanishing radial density along  $r_1 = r_2$ , while the density of the triplet state has a maximum along this line. This apparent contradiction is an artifact of the angular integration. Areas of low and high density are represented by black and white color, respectively.

with total angular momentum  $L = 4, \dots, 9$ <sup>3</sup>. As in the case of natural parity states [147], exchange effects can be neglected for sufficiently large values of  $L$ . For instance, the singlet-triplet splitting for  $n = 10$  goes exponentially fast to zero as  $\exp(-4.9L)$ .

As in the case of natural parity states our approach suffers from the influence of the Kato cusp [66, 67] for symmetric excitation of both electrons. The effect can easily be spotted in our tables as the precision of our results increases with increasing excitation of the outer electron.

Figure 4.5 shows the radial density integrated over the angles of the lowest lying  $^1P^e$  and  $^3P^e$  state, respectively. The density plot for the triplet state shows the same behaviour as helium ground state, i.e., the density plot exhibits a maximum along the axis  $r_1 = r_2$ . However, this behaviour would be expected for singlet states. This apparent contradiction is a consequence of the integration over the angular coordinates which introduces a sign change for the exchange term. This can be understood from the properties of the projector  $\mathcal{A}$  of Eq. (3.4) and of the Clebsch-Gordan coefficients (3.14). From the relation  $\langle l_2 m_2 l_1 m_1 | L M \rangle = (-1)^{l_1+l_2-L} \langle l_1 m_1 l_2 m_2 | L M \rangle$  it follows that the wave function (3.4) is symmetric (antisymmetric) for  $\epsilon_{12} = \epsilon(-1)^{l_1+l_2-L} = 1$  ( $\epsilon_{12} = \epsilon(-1)^{l_1+l_2-L} = -1$ ). On the one hand, as can be seen from (3.13), single (triplet) unnatural parity states are characterized by  $\epsilon = -1$  ( $\epsilon = +1$ ), i.e., exactly the opposite situation as for natural parity states. On the other hand, integration over the angle coordinates of  $\Psi$  eliminates the sign  $(-1)^{l_1+l_2-L}$ . Thus, the structure of the density plots depends exclusively on  $\epsilon$ , which finally explains the apparent contradiction in figure 4.5.

#### 4.2.2 Resonances

In the following we present energies and widths for  $^3P^e$  resonances below the 3rd to 8th SIT. Data for  $^1P^e$  resonances is presented in appendix C.2.1. The data for the 3rd up to the 7th threshold of  $^3P^e$  resonances is compared to existing data [141, 148]. The results have been computed

<sup>3</sup>Some results for these states, obtained within a similar approach, have already been presented in [146]. The results are, however, given without analysing the convergence of the energies obtained. The results agree with our data for five to nine digits.

$N = 3$							
This work		Saha <i>et al.</i> [141]		Ho <i>et al.</i> [148]		This work (continued)	
$-\text{Re}(E_{i,\theta})$	$-\text{Im}(E_{i,\theta})$	$-\text{Re}(E_{i,\theta})$	$-\text{Im}(E_{i,\theta})$	$-\text{Re}(E_{i,\theta})$	$-\text{Im}(E_{i,\theta})$	$-\text{Re}(E_{i,\theta})$	$-\text{Im}(E_{i,\theta})$
0.33609	0.00225	0.33607	0.00227	0.3360879	0.00224435	0.22511389	0.00001330
0.2911579	0.0000369	0.29116	0.0000350	0.291158225	0.0000370	0.224750367	0.0000004740
0.271557	0.000894	0.27156	0.000885	0.27155715	0.00089435	0.22471977	0.00001065
0.25357458	0.00001174	0.25357	0.0000100	0.25357465	0.0000117615	0.224425756	0.000000389
0.250932	0.000428	0.25093	0.000425	0.2509315	0.0004275	0.22440104	0.00000866
0.24195825	0.00000721	0.24196	0.0000050	0.2419583	0.0000072	0.2241598887	0.0000003224
0.2409603	0.0002276	0.24096	0.000225	0.24096	0.000225	0.22413963	0.00000714
0.23589422	0.00000469	0.23589	0.00000467	0.2358935	0.0000040	0.2239292977	0.0000002704
0.2353963	0.0001336	0.23539	0.000135			0.22392258	0.00000596
0.23227095	0.00000318	0.23227	0.00000316			0.223754513	0.000000229
0.2319828	0.0000846	0.23198	0.000085			0.22374040	0.00000502
0.22992382	0.00000225	0.22992	0.000002245			0.2235979593	0.0000001955
0.2297407	0.0000568	0.22974	0.0000550			0.22358599	0.00000427
0.22831428	0.00000164	0.22831	0.000001625			0.22346430	0.00000017
0.2281902	0.0000400	0.22819	0.0000400			0.22345399	0.00000366
0.22716196	0.00000123	0.22716	0.000001205			0.2233491	0.00000002
0.2270737	0.0000292	0.22707	0.0000350			0.223340	0.000003
0.226308471	0.000000940	0.22631	0.000000825				
0.22624335	0.00002192	0.22624	0.0000250				
0.225658634	0.000000736	0.22565	0.00000393				
0.22560915	0.00001690	0.22561	0.0000200				
0.225152407	0.000000586	0.22514	0.00001				

Table 4.12:  ${}^3P^e$  resonances of helium below the third ( $N=3$ ) SIT: our results are compared with data from [141] and [148]. Only converged digits are displayed for our results. The results of [148] have been converted from Ry to a. u.. The data of [141] is presented without comment on the actual precision.

using up to 21 angular configurations and up to 7 sets of Coulomb-Sturmian functions for each angular configuration. In choosing these sets properly we are able to describe a rather large energy regime [122]. Our results have been tested for convergence with respect to variation of the basis size – including the number of angular configurations and Coulomb-Sturmian functions used –, variation of the real dilation parameters and variation of the complex rotation angle  $\theta$ , with  $\theta \in \{0.1, 0.12, 0.14, 0.16, 0.18, 0.2\}$ . Tables 4.12, 4.13 and 4.14 contain the data for  ${}^3P^e$  resonances. The tables are limited to at most 50 entries even if more converged resonances have been identified.

Once more the Kato cusp [66, 67] leads to a lower precision for states with symmetric excitation of both electrons and is easily traceable in our tables, as the precision of our results increases with increasing excitation of the outer electron.

The agreement with the results for  ${}^3P^e$  (Tabs. 4.12, 4.13) of [148], where an explicitly correlated approach together with complex rotation has been used to extract energy and width of resonances, is in general excellent. Nevertheless, we obtain a significantly larger amount of additional converged resonances and are able to provide a high accuracy for asymmetrically excited states.

In contrast, the comparison with the recently published results for  ${}^3P^e$  resonances obtained within the stabilization technique [141] yields significant disagreements. Already the data for resonances below the third SIT (Tab. 4.12) shows significant differences for  $\text{Im}(E_{i,\theta})$  of higher excited resonances. Below the fourth SIT (Tab. 4.13) the approach by [141] seems not to be able to resolve the two close lying resonances  $E_{i,\theta} = -0.1423413 - i0.0001641$  and  $E_{i,\theta} = -0.1423411 - i0.0004192$ . Moreover, the part of the spectrum lying closer to the fourth SIT is not completely resolved. Table 4.13, which presents the data for the fourth and fifth SIT, shows for the data below the fifth SIT pronounced deviations already for the first two

$N = 4$							
This work		Saha <i>et al.</i> [141]		Ho <i>et al.</i> [148]		This work (continued)	
$-\text{Re}(E_{i,\theta})$	$-\text{Im}(E_{i,\theta})$	$-\text{Re}(E_{i,\theta})$	$-\text{Im}(E_{i,\theta})$	$-\text{Re}(E_{i,\theta})$	$-\text{Im}(E_{i,\theta})$	$-\text{Re}(E_{i,\theta})$	$-\text{Im}(E_{i,\theta})$
0.194442	0.001653	0.19738	0.001685	0.194442	0.0016525	0.128821702	0.000004491
0.178257	0.002402	0.17878	0.002295	0.178257	0.0024035	0.12880368	0.00001041(*)
0.1612297	0.0009514	0.16136	0.000945	0.161223	0.0009515	0.128274538	0.000047145
0.1551767	0.0001291	0.15520	0.000135	0.1551768	0.00012925	0.128234933	0.000004126
0.151550	0.000883	0.15154	0.00077	0.1515495	0.000883	0.128229787	0.000004085
0.1480323	0.0005245	0.14808	0.00058	0.1480315	0.000525	0.12780435	0.00003655
0.1423413	0.0001641	0.14235	0.000255	0.1423415	0.00016425	0.127783669	0.000002192
0.1423411	0.0004192	0.14207	0.000370	0.142341	0.00041895	0.127768101	0.000002356
0.1408404	0.0002882	0.14090	0.000400	0.14084	0.000235	0.127428137	0.000028487(*)
0.1372933	0.0003112	0.13742	0.000290	0.137295	0.000306	0.1274227601	0.0000012725
0.13715311	0.00005671	0.13716	0.000055	0.13715	0.000055	0.127398134	0.000001730
0.1365225	0.0001640	0.13655	0.000240			0.1271290799	0.0000012063
0.13418294	0.00021526					0.127122185	0.000022666
0.13406130	0.00002841	0.13405	0.0000200			0.127097627	0.000001314
0.1337445	0.0000962	0.13375	0.000090			0.1268886070	0.0000013974
0.1321266	0.0001517	0.13202	0.0001345			0.126870516	0.000018768
0.132028688	0.000016275					0.1268502500	0.0000010212
0.13185858	0.00005724	0.13182	0.000089			0.126682106	0.000002031
0.13069296	0.00010968	0.13077	0.0001205			0.1266612876	0.0000158575
0.130614425	0.000010054	0.13062	0.000135			0.1266441818	0.0000008083
0.13052259	0.00003386	0.13047	0.0000515			0.126509105	0.000001939
0.129652551	0.000081231					0.1264853783	0.0000135071
0.129589107	0.000006557					0.1264707128	0.0000006502
0.12954291	0.00001942	0.12952	0.00002405			0.126361036	0.000003841
0.128873334	0.000061402					0.1263360130	0.0000115748

$N = 5$							
This work		Saha <i>et al.</i> [141]		Ho <i>et al.</i> [148]		This work (continued)	
$-\text{Re}(E_{i,\theta})$	$-\text{Im}(E_{i,\theta})$	$-\text{Re}(E_{i,\theta})$	$-\text{Im}(E_{i,\theta})$	$-\text{Re}(E_{i,\theta})$	$-\text{Im}(E_{i,\theta})$	$-\text{Re}(E_{i,\theta})$	$-\text{Im}(E_{i,\theta})$
0.11930	0.00177	0.11937	0.000985	0.11930	0.00177	0.0849144	0.0000887(*)
0.109463	0.001561	0.10996	0.000925	0.109463	0.001561	0.08467477	0.00001360
0.107265	0.000765	0.10765	0.00050	0.107265	0.000765	0.0844635	0.0001449
0.102096	0.001134	0.10299	0.00102	0.102096	0.0011345	0.08424956	0.00000624
0.0986031	0.0004517	0.09828	0.000414	0.098602	0.000453	0.0840879	0.0000603
0.096641	0.000687	0.09656	0.000453	0.0966405	0.000687	0.08396429	0.00005412
0.0952542	0.0000442	0.09526	0.000201	0.09525385	0.00004425	0.08374283	0.00011013
0.095136	0.000744			0.095143	0.00074	0.08356441	0.00000423
0.0934409	0.0002212	0.09365	0.0002265	0.093435	0.000205	0.0834489	0.0000430
0.0915093	0.0004702	0.09166	0.000327	0.09151	0.00047	0.0833809	0.0000792
0.091108	0.000435	0.09112	0.0003685	0.091105	0.000425	0.0831841	0.0000827
0.09072496	0.00002125	0.09072	0.00001725	0.0907245	0.000021	0.08303258	0.00000281
0.0902365	0.0000532	0.09026	0.000127			0.0829466	0.0000322
0.088632	0.000340	0.08908	0.0002995			0.0829094	0.0000856
0.0885032	0.0002189	0.08850	0.00000995			0.0827411	0.0000615
0.0885015	0.0000583					0.08261147	0.00000183
0.08812097	0.00001786	0.08810	0.000067			0.0825452	0.0000248
0.087296	0.000209	0.08744	0.0000110			0.0825278	0.0000819
0.0867708	0.0000967	0.08696	0.0001015			0.0823837	0.0000455
0.0867355	0.0002446	0.08602	0.0001795			0.08227232	0.00000119
0.08638263	0.00001308					0.08221996	0.00001955
0.0859899	0.0001392	0.08593	0.0000775			0.0822152	0.0000737
0.0855889	0.0000130					0.08209119	0.00003370
0.0854195	0.0001889	0.08543	0.000112			0.08199515	0.00000077
0.08515358	0.00000908					0.0819559	0.0000641

Table 4.13:  $^3P^e$  resonances of helium below the fourth ( $N=4$ ) and fifth ( $N=5$ ) SIT: our results are compared with data from [141] and [148]. Only converged digits are displayed for our results. The results of [148] have been converted from Ry to a. u.. The data of [141] is presented without comment on the actual precision. The states marked with (\*) can also be identified with states given in [141].

$N = 6$							
This work		Saha <i>et al.</i> [141]		This work (continued)		This work (continued)	
$-\text{Re}(E_{i,\theta})$	$-\text{Im}(E_{i,\theta})$	$-\text{Re}(E_{i,\theta})$	$-\text{Im}(E_{i,\theta})$	$-\text{Re}(E_{i,\theta})$	$-\text{Im}(E_{i,\theta})$	$-\text{Re}(E_{i,\theta})$	$-\text{Im}(E_{i,\theta})$
0.076443	0.000596	0.07721	0.000369	0.0621389	0.0001555	0.0588219	0.0001051
0.073661	0.000871	0.07079	0.000483	0.0618691	0.0002110	0.05879852	0.00001422
0.0733870	0.0007392	0.06825	0.000735	0.06130050	0.00000546	0.05863624	0.00008777
0.0707545	0.0003581	0.06704	0.000275	0.061275	0.000329	0.0584702	0.0000579
0.070218	0.000841	0.06665	0.000149	0.0610510	0.0000826	0.058390002	0.000007444
0.0686312	0.0005865	0.06545	0.0002745	0.06097248	0.00001812	0.0583546	0.0001234
0.0670725	0.0001050	0.06522	0.0000705	0.0606669	0.0001813	0.05835248	0.00000517
0.0665272	0.0003683	0.06449	0.0000051	0.0603619	0.0002213	0.05822598	0.00005642
0.066190	0.000655	0.06383	0.000152	0.06025692	0.00000681	0.05807616	0.00003978
0.0655169	0.000234	0.06358	0.000003425	0.06011466	0.00002553	0.05801162	0.00000471
0.0652949	0.0000941	0.06272	0.0000003365	0.0600951	0.0000488	0.0579979178	0.0000005803
0.06449512	0.00000892	0.06187	0.0001735	0.0597971	0.0001538	0.0579794	0.0001421
0.063937	0.000256	0.06115	0.00001255	0.0595825	0.0001349		
0.0638142	0.0003889	0.06075	0.000092	0.059470995	0.000012354		
0.0636138	0.0002572	0.06028	0.000163	0.0594026	0.0000739		
0.063594605	0.000004761	0.05973	0.0002345	0.0593652	0.0000279		
0.06272169	0.00000340	0.05913	0.000267	0.0591449	0.0001225		
0.0623372	0.0002073	0.05774	0.0001685	0.0589620	0.0000865		
0.062326	0.000145	0.05632	0.000127	0.05886415	0.00001062		

$N = 7$							
This work		Saha <i>et al.</i> [141]		This work (continued)		This work (continued)	
$-\text{Re}(E_{i,\theta})$	$-\text{Im}(E_{i,\theta})$	$-\text{Re}(E_{i,\theta})$	$-\text{Im}(E_{i,\theta})$	$-\text{Re}(E_{i,\theta})$	$-\text{Im}(E_{i,\theta})$	$-\text{Re}(E_{i,\theta})$	$-\text{Im}(E_{i,\theta})$
0.05347	0.00070	0.05363	0.000125	0.0468818	0.0000893	0.0445696	0.0000784
0.0534029	0.0002803	0.05190	0.000280	0.0467502	0.0001037	0.04452085	0.00003366
0.0522288	0.0003677	0.05085	0.0000450	0.04657657	0.00001232	0.04438100	0.00000408
0.052015	0.000430	0.04965	0.0000200	0.0462402	0.0001862	0.044188	0.000116
0.051024	0.0000482	0.04860	0.000105	0.0461108	0.0002040	0.0441801	0.0001084
0.05084780	0.00001202	0.04752	0.000295	0.0459701	0.0000966	0.0441677	0.0000956
0.050394	0.000530	0.04655	0.0000150	0.0458268	0.0000314	0.04405193	0.00000679
0.049773	0.000241	0.04573	0.000075	0.04581448	0.00000527	0.04397197	0.00006718
0.0497026	0.0000623	0.04519	0.0000250	0.0455806	0.0000931	0.04385962	0.00000615
0.048578	0.000458	0.04484	0.000110	0.0453482	0.0003857	0.0437622	0.0000627
0.0484611	0.0001567	0.04409	0.000275	0.0453137	0.0000873	0.0437050	0.0000958
0.0484048	0.0001576	0.04337	0.000165	0.04516912	0.00000814	0.0436928	0.0000567
0.048397	0.000174			0.04507011	0.00000094	0.04362921	0.00000448
0.048275	0.000193			0.04503307	0.00000180	0.0435225	0.0000908
0.047323	0.000366			0.0447859	0.0002184	0.04344286	0.00000769
0.04715483	0.00001855			0.0447759	0.0000974	0.0433770	0.0000368
0.0470707	0.0002854			0.0446000	0.0000344		

$N = 8$							
This work		This work (continued)		This work (continued)		This work (continued)	
$-\text{Re}(E_{i,\theta})$	$-\text{Im}(E_{i,\theta})$	$-\text{Re}(E_{i,\theta})$	$-\text{Im}(E_{i,\theta})$	$-\text{Re}(E_{i,\theta})$	$-\text{Im}(E_{i,\theta})$	$-\text{Re}(E_{i,\theta})$	$-\text{Im}(E_{i,\theta})$
0.04086	0.00032	0.0371688	0.0001793	0.035428934	0.000010562	0.034435779	0.000012427
0.04000562	0.00000504	0.0370676	0.0003178	0.035407698	0.000000352	0.03440853	0.00003555
0.039768	0.000413	0.03673341	0.00006163	0.0353413	0.0000808	0.03440112	0.00002060
0.039188412	0.000003812	0.03670367	0.00003908	0.03497965	0.00005916	0.034267095	0.000022262
0.0391736	0.0002594	0.0363853	0.0004327	0.0349791	0.0000845	0.03419595	0.00012631
0.0389917	0.0003175	0.03627663	0.00002418	0.0349681	0.0000435	0.03407729	0.00007149
0.03855256	0.00016179	0.03620860	0.00008645	0.03486608	0.00003274	0.03403227	0.00001104
0.0384843	0.0005025	0.0360819	0.0002314	0.034847195	0.000001719	0.03401928	0.00000455
0.03823994	0.00003134	0.03593187	0.00001334	0.034820	0.000497	0.034015479	0.000006518
0.0382008	0.0003181	0.03569253	0.00004820	0.03476450	0.00001178	0.03394773	0.00006212
0.0378439	0.0001367	0.0356900	0.0001755	0.0345951	0.0001651	0.03385377	0.00003512
0.0372215	0.0001213	0.0354842	0.0001532	0.0344563	0.0000368		
0.0372087	0.0002426	0.0354361	0.0001282	0.0344384	0.0002023		

Table 4.14:  $^3P^e$  resonances of helium below the sixth ( $N = 6$ ), seventh ( $N = 7$ ) and eighth ( $N = 8$ ) SIT: our results on the left are compared with data from [141]. Only converged digits are displayed for our results. The data of [141] is presented without comment on the actual precision.

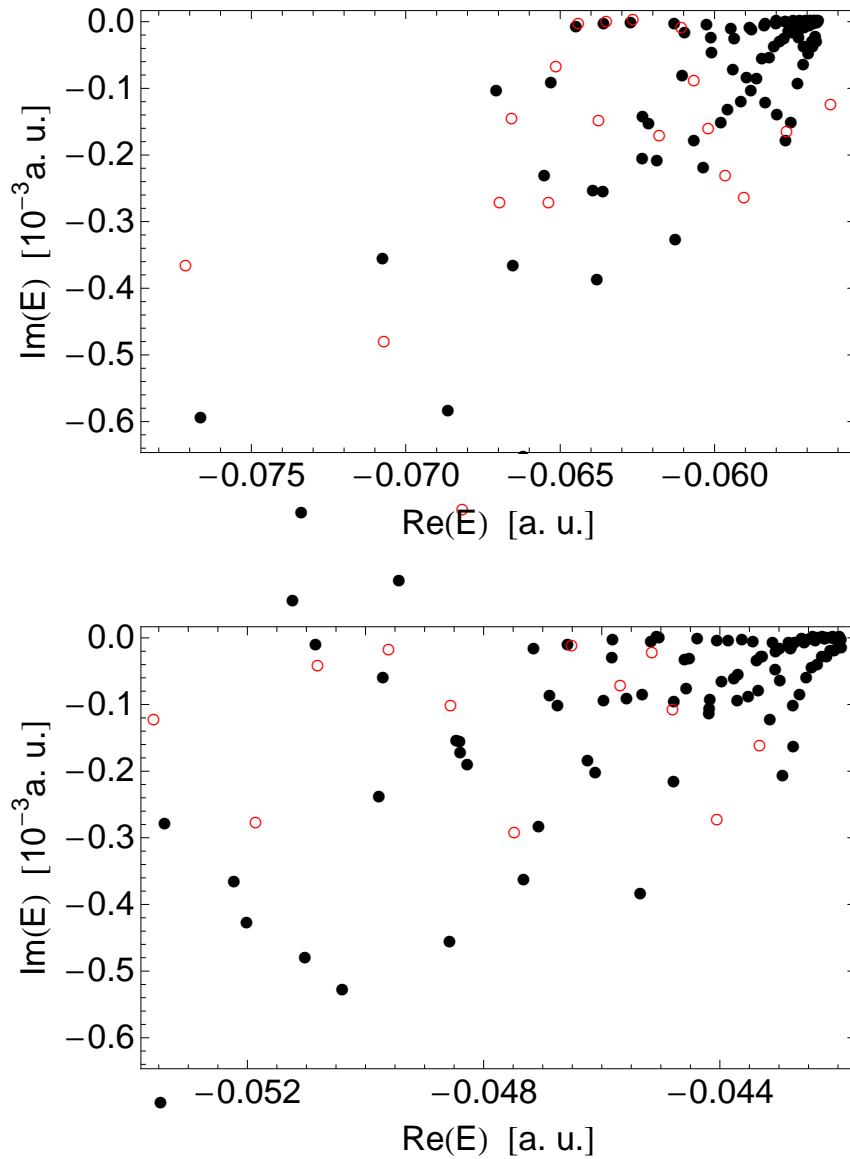


Figure 4.6: Energies and half-widths of  ${}^3P^e$ -states of helium below the sixth (top) and seventh (bottom) SIT. As expected, the complex energies calculated with the help of the spectral approach described in chapter 3 ( $\bullet$ ) are organized in Rydberg-like series converging to the respective SITs. In contrast, the data obtained with the stabilization method ( $\circ$ ) [141] exhibit a scattered pattern and no agreement with our results can be seen.

states of the table and again the spectrum for higher excited states misses some resonances. The disagreement for the two close lying resonances  $E_{i,\theta} = -0.0952542 - i0.0000442$  and  $E_{i,\theta} = -0.095136 - i0.000744$  has already been addressed by Saha *et al.* in [141]. However, we do not agree with their interpretation that the sudden decrease in the gap between resonances favours their results over [148]. Instead, we speculate that the stabilization method does have problems resolving resonances lying close to each other (see Tab. 4.12 and 4.13). Moreover, the statement of Saha *et al.* that the stabilization method allows them to obtain more results than the complex rotation method is not true: the large number of states that they missed below the fourth and fifth SIT clearly contradicts this claim. Table 4.14 presents a comparison of the data by Saha *et al.* [141] with our results obtained below the sixth and seventh SIT. We are unable to associate any result of [141] with our results as there is no agreement at all.

For moderate excitation of the inner electron – which is the case here – resonances are organized in Rydberg-like series converging to the SIT. Figure 4.6 displays the energies and half-widths of  $^3P^e$  states of unnatural parity below the sixth (top) and seventh (bottom) SIT. Our data is compared with the results by Saha *et al.*. Note, that these plots contain all our converged results for the sixth and seventh SIT (around 100 for each threshold, even though only 50 entries are given in Table 4.14). Besides the small number of states given by Saha *et al.* [141], their results are organized in an unexpectedly irregular pattern which does not coincide at all with our calculations and the expected structure.

Table 4.14 also presents our results for  $^3P^e$  resonances below the eighth SIT, which have been calculated by us for the first time. Considering the huge difficulties of Saha *et al.* [141] to resolve close lying resonances in general and the non-existent series structure for their data below the sixth and seventh SIT for  $^3P^e$  resonances our results should be viewed as benchmark results below the sixth, seventh and eighth SIT.

### 4.3 Summary

The configuration interaction approach described in chapter 3 has been used to compute bound states and resonances of helium. In section 4.1.1 the slow convergence of the ground state in our configuration interaction approach, which is due to the Kato cusp, has been studied. The convergence of the computed energies depends dominantly on the number of Coulomb-Sturmian functions, and to a lesser extent on the number of angular configurations included. Moreover, the issues with the resolution of the Kato cusp have been illustrated by projections of the ground state electronic density on the subspace with  $\theta_{12} = 0$ . Note, that the Kato cusp essentially limits our approach only for the ground state. Our approach has successfully been applied to the computation of  $^{1,3}S^e$  resonances up to the tenth threshold and compared to available reference data in section 4.1.2. The computation of these doubly excited states has been achieved within a basis size not exceeding 9000 which is three to five times smaller than the basis size needed in other state-of-the-art approaches. In section 4.2.1 results for non-autoionizing doubly excited states of helium with  $L = 1, \dots, 9$  have been presented. In addition, an apparent contradiction in the structure of density plots for unnatural parity states has been explained. Finally, results for  $^3P^e$  resonances up to below the eighth single ionization threshold have been presented in section 4.2.2 (data for  $^1P^e$  is presented in appendix C.2.1). The data shows perfect agreement with the few available results by Ho *et al.* [148], however, disagrees strongly with recent results by Saha *et al.* [141], which have been obtained using a stabilization method.

## Chapter 5

# Frozen planet states of helium for non-zero angular momentum

The frozen planet configuration and its quantum mechanical counterpart were first described by Richter and Wintgen [21, 22] at the beginning of the 1990's. So far the studies have mostly been concerned with helium frozen planet states (FPS) for zero angular momentum, where frozen planet states have been identified in calculations for one-dimensional [24, 149], planar (2D) [25, 26, 97] and three-dimensional (3D) helium [22]. Our motivation to investigate helium frozen planet states for non-zero total angular momentum is, apart from the interest in their spectral and dynamical properties, the potentially high relevance of these states in the context of coherent control [150–152] in the electronic dynamics of Rydberg systems in the presence of electron-electron interactions [153]: During the last decade, it has been realized that near-resonant electromagnetic driving of atomic electrons in one-electron Rydberg systems allows the creation of *non-dispersive electronic wave packets* [102, 154, 155] (in a quantum system with a *non-harmonic* spectrum!) which propagate along Kepler trajectories of essentially arbitrary eccentricity and orientation for very long times [27, 102, 156]. This field has by now been investigated theoretically in much detail and is well understood, and first experimental realizations of such long living quantum objects have been reported very recently [157–159]. An immediate question is of course whether such a localization and stabilization effect is also to be expected in Rydberg systems with additional electron-electron interaction, e.g., in helium. Since the unperturbed frozen planet configuration has a well defined associated eigenfrequency, the external field can be tuned such as to drive that frequency near resonantly, and, as a matter of fact, it was already shown that non-dispersive two-electron wave packets which propagate along the frozen planet trajectory *do exist* in a one-dimensional model of helium [23, 24], and there is strong evidence for their existence in the planar helium model [25, 26]. Note, however, that in one-dimensional models the lifetime of frozen planet states is, compared to the full three-dimensional treatment, dramatically overestimated [97]. Moreover, it is not entirely clear how well the planar model performs in the description of non-zero angular momentum frozen planet states, in particular, with moderate excitation of the inner electron. The full three-dimensional treatment of frozen planet states of helium under near resonant driving requires a description of the relevant energy regime, defined by the energy of the initial state, the driving frequency and the number of transitions considered, for multiple values of the total angular momentum. Apart from the description of the initial frozen planet state the description of frozen planet states with non-zero total angular momenta in the same energy regime is expected to be important. Note, that spectra for  $1,3P^o$  and  $1,3D^e$  states, including frozen planet states, can be found in appendix C.1.

In this chapter, we will give a brief introduction to the relevant properties of the classical frozen planet configuration and the identification of its quantum mechanical counterpart, fol-

lowed by results for helium frozen planet states with  $L = 1$  and  $L = 2$ . In particular, the performance of the planar approach and differences to the  $L = 0$  frozen planet states are discussed.

## 5.1 The classical frozen planet configuration

In the classical frozen planet configuration both electrons are located on the same side of the nucleus, with asymmetric excitation (see Fig. 5.1). Classical studies show that these configurations are stable [8, 21, 23, 160]. The outer electron is dynamically stabilized due to the fast oscillation of the inner electron along highly eccentric elliptic trajectories around the nucleus. This generates a rapidly oscillating potential for the outer electron as a result of the competition between electron-electron repulsion and the Coulomb attraction exerted on the outer electron by the screened Coulomb potential of the nucleus. Upon averaging [161] over the characteristic time scale of the inner electron's motion, the outer electron experiences an effective, time-independent, attractive potential [162]. This effective potential is attractive Coulombic for large distances, and strongly repulsive for positions close to the nucleus, with a minimum which precisely defines the equilibrium position of the frozen planet configuration (see Fig. 5.2). The outer electron is (almost) “frozen” in this equilibrium position. This together with the Kepler-like motion of the inner electron lead to the term frozen planet state. Due to the invariance of the Hamiltonian (1.5), which governs classical and quantum dynamics of a two-electron atom, under the scaling transformations (2.1), the position  $x_{\min}$  of the minimum of the effective potential and the minimum energy  $E_{\min}$  depend only [24] on the action integral  $S = (1/2\pi) \oint p_2 dx_2$  over one cycle of the Kepler oscillation of the inner electron,

$$\begin{aligned} x_{\min} &= 2.6 S^2, \\ E_{\min} &= -2.22 S^{-2}. \end{aligned} \tag{5.1}$$

Due to the large phase space volume occupied by the stability region of the frozen planet configuration, it is possible to identify eigenstates in the spectrum which are localized along the frozen planet orbit. Indeed, the existence of such states (with  $N \geq 3$ ) for zero total angular momentum has been demonstrated by several approaches [22, 24–26, 97]. For each  $N$ , the FPS form a Rydberg series characterized by the long life time of its constituents and large expectation values of the cosine of the angle  $\theta_{12}$  between the electron radii  $\vec{r}_1$  and  $\vec{r}_2$  ( $\langle \cos(\theta_{12}) \rangle \approx 1$ ). Thus, the frozen planet configurations are well-defined configurations of the classical three body Coulomb problem, with unambiguous quantum correspondence.

In a quantum description, the action  $S$  is replaced by the effective quantum number of the inner electron, which is in the one- and three-dimensional case given by  $N$ , while it is  $N - 1/2$

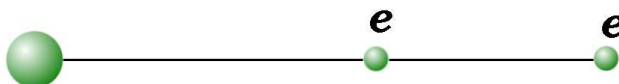


Figure 5.1: Collinear frozen planet configuration [21] of a two-electron atom: the three particles of the atom are aligned in one line with both electrons located on the same side of the nucleus.

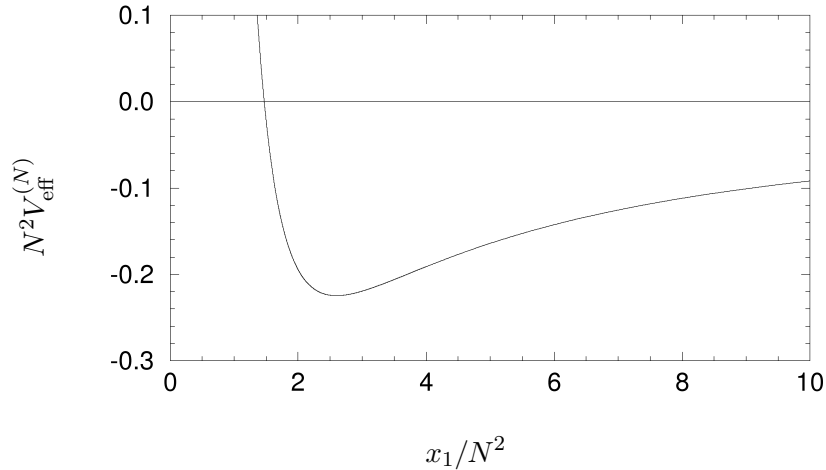


Figure 5.2: Effective adiabatic potential for the outer electron of the collinear frozen planet configuration [23].

in the planar case [25]. Thus, the scaled quantities (5.1) take the form

$$x_{\min}^{3D} = 2.6 N^2 \text{ a. u.}, \quad x_{\min}^{2D} = 2.6 (N - 0.5)^2 \text{ a. u.}, \quad (5.2)$$

$$E_N^{3D} = -2.22 N^{-2} \text{ a. u.}, \quad E_N^{2D} = -2.22 (N - 0.5)^{-2} \text{ a. u.} \quad (5.3)$$

Apart from the frozen planet ground state for a given  $N$  a whole series of frozen planet states exists. Members of the frozen planet series for a given value of  $N$  are labeled by an integer number  $n_F$ , accounting for the excitation of outer electron in the frozen planet states, starting with  $n_F = 1$  for the ground state.

In contrast to available theoretical results, FPS have so far not been unambiguously identified in experiments, though sequential multiphoton excitation schemes [163–165] have successfully been used for the creation of planetary states [166], i.e., two-electron atoms<sup>1</sup> where both electrons are highly excited and are moving in different regions of space ( $\langle r_2 \rangle \ll \langle r_1 \rangle$ ).

### 5.1.1 Identification criteria of frozen planet states

Frozen planet states are characterized by the localization of both electrons on the same side of the nucleus along the collinear  $Zee$  configuration and by their long lifetime compared to other resonances in the same energy regime. The expectation value of  $\cos(\theta_{12})$  is, for these states, close to unity. The decay rates and the expectation value of  $\cos(\theta_{12})$  can be used as indicators for frozen planet states which are for instance sufficient for the identification of frozen planet states in helium with  $L = 0$ . However, frozen planet states can be identified unambiguously by their localization properties in configuration space, i.e., by analysing probability density distributions.<sup>2</sup> Because of the dimension of the configuration space (four-dimensional for planar and six-dimensional for full three-dimensional treatment of two-electron atoms) a complete visualization of the wave function within one plot is not possible. Therefore, two alternative projections of the electronic densities in configuration space are used in the following: conditional probability distributions for  $\theta_{12} = 0$  and one-electron probability densities where the position of one of the electrons is fixed.

<sup>1</sup>This includes also helium-like atoms with two valence electrons.

<sup>2</sup>A further additional tool is the analysis of the phase space of frozen planet states, e.g., through Husimi distributions.

The conditional probability distributions relies on the fact, that two-electron atoms are invariant under rotations and that therefore the probability distributions depend only on the relative position of the electrons, i.e., for a given angle  $\theta_{12}$ , the wave function depends only on radii  $r_1$  and  $r_2$ . For  $\theta_{12} = 0$  the conditional density distribution represents the projection of the density onto the subspace of the collinear frozen planet configuration.

The frozen planet configuration and states are characterized by an asymmetric excitation of both electrons and therefore a disjoint area of high density for electron one and two. To analyse these properties one-electron probability densities are used, in which the position of one of the two electrons of the system is fixed in the respective maximum of the conditional probability distribution.<sup>3</sup>

Note, that in the density plots  $r_1 r_2 r_{12} |\Psi_i(\vec{r}_1, \vec{r}_2)|_{\mathcal{C}}^2$  and  $r_1^2 r_2^2 |\Psi_i(\vec{r}_1, \vec{r}_2)|_{\mathcal{C}}^2$  are displayed for planar and three-dimensional treatment of two-electron atoms, respectively, with  $\mathcal{C}$  a condition stating at which value the mutual angle between the electrons or at which position one of the electrons is fixed.

## 5.2 Frozen planet states with total angular momentum $L = 1$

An identification of the helium frozen planet states for  $L = 1$  with  $N \geq 3$  on basis of the electronic probability densities yields, that, as for  $L = 0$  [97], frozen planet states can be identified by a simple criterion, namely by possessing simultaneously a small width and the largest value of  $\langle \cos(\theta_{12}) \rangle$  in the respective energy regime. Members of the frozen planet series can, as for  $L = 0$ , be associated to a state with approximate quantum number  $K = -N + 1$ . Note, that starting with  $N = 6$  the lowest members of the frozen planet series for  $L = 1$  are not the states with the smallest width in the respective energy regime anymore (see [52]), however, they still possess the largest expectation values of  $\cos(\theta_{12})$  and are members of the  $K = -N + 1$  series, which has its series ground state at the highest energy of all  $K$  series. The energies of the ground states of the frozen planet series are close to the semiclassical prediction (5.3). With increasing  $N$  the

$N$	$E_N^{2D}$ [a. u.]	$E^{2D}(^1P^o)$ [a. u.]	$E^{2D}(^3P^o)$ [a. u.]
3	-0.35520	-0.34895078343	-0.34938910
4	-0.18122	-0.17924859425	-0.17942414
5	-0.10963	-0.1087734	-0.108874
6	-0.07339	-0.07304413	-0.0734043
$N$	$E_N^{3D}$ [a. u.]	$E^{3D}(^1P^o)$ [a. u.]	$E^{3D}(^3P^o)$ [a. u.]
3	-0.24666	-0.24551751	-0.24605967
4	-0.13875	-0.13861396	-0.1388839
5	-0.08880	-0.088845297	-0.088990798
6	-0.06167	-0.0617345	-0.061680

Table 5.1: Energies of helium frozen planet ground states;  $E^{2D}$  and  $E^{3D}$  are the numerical values of  $L = 1$  frozen planet ground states for  $N = 3, \dots, 6$ .  $E_N^{2D}$  and  $E_N^{3D}$  are the semiclassical predictions of Eq. (5.3). Energies of planar and three-dimensional treatment do not coincide due to the different effective quantum numbers of the inner electron associated to the planar and three-dimensional configurations. Note, that for three-dimensional calculations the spectra for  $^1P^o$  and  $^3P^o$  are presented in appendix C.1.1 and C.1.2, respectively.

<sup>3</sup>In addition either the  $\theta$  or  $\phi$  coordinate of the electron with varying position needs to be fixed in the three-dimensional case, however, due to the rotational invariance of two-electron atoms this poses no additional restriction.

$N$	$\Gamma/2$ [a. u.]		$\langle \cos(\theta_{12}) \rangle$	
	2D	3D	2D	3D
Singlet				
3	0.0000000873	0.000000006	0.61560397	0.495763
4	0.00000153429	0.000000038	0.692580373	0.5997586
5	0.00000055	0.000002916	0.6904	0.67231
6	0.00000257	0.0000076	0.818376	0.735
Triplet				
3	0.00000010	0.00000015	0.6900023	0.5278342
4	0.00000871	0.0000415	0.7748194	0.592
5	0.000006	0.000001976	0.7760	0.560563
6	0.0000014	0.000001	0.776426	0.606

Table 5.2: Half-widths and  $\langle \cos \theta_{12} \rangle$  of the  $^1P^o$  (upper table) and  $^3P^o$  (lower table) helium frozen planet ground states in planar and three-dimensional treatment.

$n_F$	$-E$ [a. u.]		$\Gamma/2$ [a. u.]		$\langle \cos(\theta_{12}) \rangle$	
	2D	3D	2D	3D	2D	3D
Singlet						
1	0.17924859425	0.13861396	0.00000153429	0.000000038	0.692580373	0.5997586
2	0.17480789	0.13510236	0.00000101	0.00000012	0.691312	0.616777
3	0.171980611	0.13277430	0.000000668	0.00000005	0.6897096	0.624551
4	0.170073966	0.13115996	0.000000462	0.00000003	0.687684858	0.627725
Triplet						
1	0.17942414	0.1388839	0.00000871	0.0000415	0.7748194	0.592
2	0.1749656	0.13533969	0.0000010	0.00000316	0.80120	0.63989
3	0.17210547	0.13295781	0.00000031	0.00000091	0.818417	0.67929
4	0.17017049	0.13130270	0.00000014	0.00000043	0.828598	0.699072

Table 5.3: Energies, half-widths and expectation values of  $\cos(\theta_{12})$  for the four lowest  $L = 1$  helium frozen planet states below  $I_4$  in planar and three-dimensional treatment.

quantum results converge more and more to the semiclassical predictions (see Table 5.1), which is expected as the semiclassical regime of helium lies close to the double ionization threshold. In addition, the semiclassical prediction (5.3) does not consider particle exchange effects leading to the singlet-triplet energy splitting, which, however, decreases exponentially with increasing  $N$ .

Half-widths and expectation values of  $\cos(\theta_{12})$  for  $L = 1$  frozen planet ground states with  $N = 3, \dots, 6$  are displayed in Table 5.2, while Table 5.3 gives energy, half-width and  $\langle \cos(\theta_{12}) \rangle$  for the first four states of the singlet and triplet frozen planet series below the fourth single ionization threshold. As for the  $L = 0$  case, the respective half-widths of frozen planet states coincide within one order of magnitude for planar and three-dimensional treatment. In general  $\langle \cos(\theta_{12}) \rangle$  increases with increasing  $N$  and  $n_F$ , though the first four  $^3P^o$  frozen planet states with  $N = 4$  show a small decrease. The systematically larger values of the expectation value of  $\cos(\theta_{12})$  for the planar case emphasize the restriction to the plane, where transverse deviations in only two directions from the collinear configuration are possible.

In figure 5.3 the conditional ( $\theta_{12} = 0$ ) density distributions for  $^1P^o$  frozen planet states of helium below the fourth single ionization threshold for the planar model and three-dimensional calculations are presented. The coordinates are scaled according to (5.2) to allow for a direct

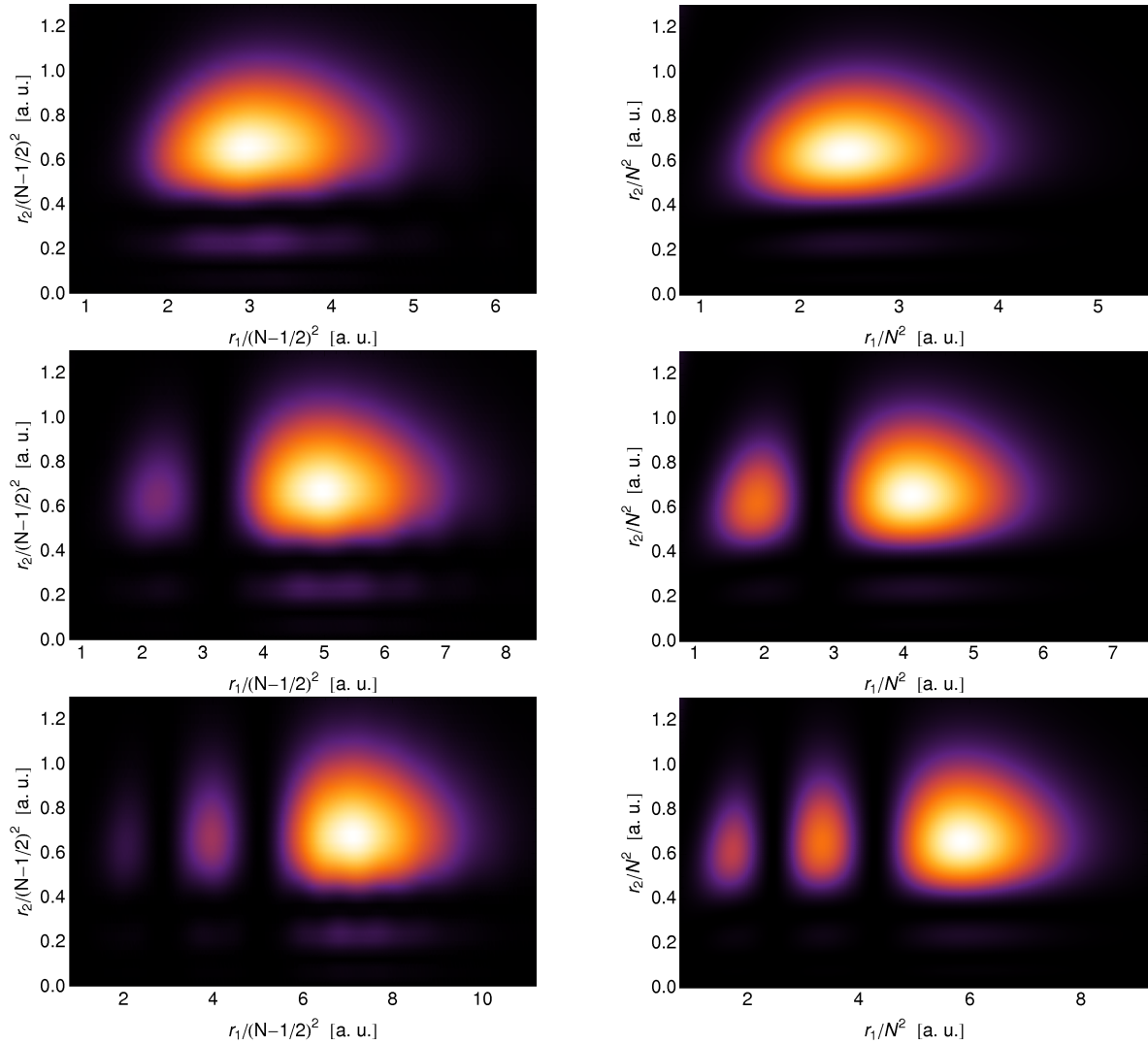


Figure 5.3: Electronic densities of the first three  $^1P^0$  helium frozen planet states in planar (left) and three-dimensional (right) treatment projected onto the subspace with  $\theta_{12} = 0$ . From top to bottom the densities of  $n_F = 1$ ,  $n_F = 2$  and  $n_F = 3$  states are presented.  $r_1 r_2 r_{12} |\Psi_i(\vec{r}_1, \vec{r}_2)|_{\theta_{12}=0}^2$  and  $r_1^2 r_2^2 |\Psi_i(\vec{r}_1, \vec{r}_2)|_{\theta_{12}=0}^2$  are displayed for the planar and three-dimensional case, respectively, with areas of low density represented by black color while those of high density are colored in white. The coordinates are scaled according to (5.2).

comparison of the planar model and three-dimensional calculations. The density plots correspond to planar and three-dimensional helium frozen planet states with an excitation of the outer electron  $n_F = 1, \dots, 3$ . The highly asymmetric character of the frozen planet states are evident in figure 5.3: the inner electron oscillates close to the nucleus while the outer electron remains, far from the nucleus, near the equilibrium position of the frozen planet configuration. Furthermore, the maximum of the probability density of the frozen planet ground state is localized close to the equilibrium position (5.2) for the outer electron of the classical configuration. A close look at these density plots shows that there are  $N - 1 = 3$  maxima along the inner electron axis  $r_2$ , indicating the series of doubly excited states they belong to, while along the  $r_1$  axis, the number of density maxima is given by  $n_F$ . In figures 5.4 and 5.5 one-electron densities of the  $n_F = 3$  state for fixed position of inner and outer electron are displayed, respectively. The

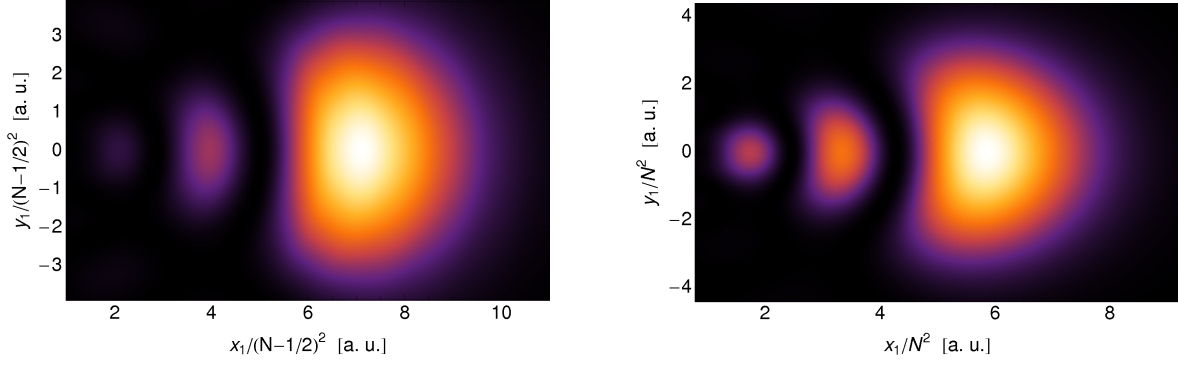


Figure 5.4: One-electron densities for fixed inner electron:  $r_1 r_2 r_{12} |\Psi_i(\vec{r}_1, \vec{r}_2)|_{x_2=x_2^{\max}}^2$  (left) and  $r_1^2 r_2^2 |\Psi_i(\vec{r}_1, \vec{r}_2)|_{x_2=x_2^{\max}}^2$  (right) are displayed for the planar and three-dimensional case, respectively, for the  $^1P^o$ ,  $N = 4$ ,  $n_F = 3$  helium frozen planet state, with areas of low density represented by black color while those of high density are colored in white. The coordinates are scaled according to (5.2).

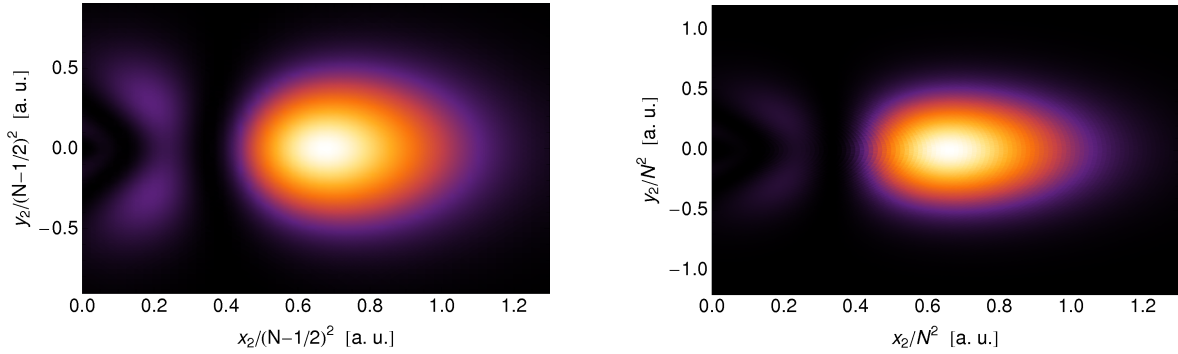


Figure 5.5: One-electron densities for fixed outer electron:  $r_1 r_2 r_{12} |\Psi_i(\vec{r}_1, \vec{r}_2)|_{x_1=x_1^{\max}}^2$  (left) and  $r_1^2 r_2^2 |\Psi_i(\vec{r}_1, \vec{r}_2)|_{x_1=x_1^{\max}}^2$  (right) are displayed for the planar and three-dimensional case, respectively, for the  $^1P^o$ ,  $N = 4$ ,  $n_F = 3$  helium frozen planet state, with areas of low density represented by black color while those of high density are colored in white. The coordinates are scaled according to (5.2).

position  $x_i^{\max}$  of the fixed electron is given by the coordinate of maximum of the conditional density distribution of figure 5.3 for the respective electron. These density plots illustrate even more clearly the main features of frozen planet states: the inner electron rapidly oscillates close to the nucleus (Fig. 5.5) while the outer electron moves slowly along the collinear configuration around its equilibrium position exhibiting only small transverse deviations (Fig. 5.4).

The energies and half-widths in tables 5.1, 5.2 and 5.3 already indicate that the planar model provides an adequate description of frozen planet state even for low values of  $N$ , though the expectation values of  $\cos(\theta_{12})$  are systematically larger than those of the three-dimensional atom. This is corroborated by the comparison of the density distributions in figures 5.3, 5.4 and 5.5 where an excellent qualitative agreement of the localization properties of planar and three-dimensional helium is found. Note, however, the density maximum in the planar case is found at somewhat higher values for the coordinate of the outer electron (see Figs. 5.3, 5.4).

### 5.3 Frozen planet states with total angular momentum $L = 2$

The identification of frozen planet states for  $L = 2$  for full three-dimensional treatment is a lot more difficult than for  $L = 0, 1$ , where frozen planet states can be easily identified by a criterion based on decay rates and the expectation value of  $\cos(\theta_{12})$  (see Sec. 5.2). The issues concerning the identification are given in section 5.3.1, followed by a comparison of data for planar and three-dimensional calculations in section 5.3.2.

#### 5.3.1 Identification of $L = 2$ frozen planet states for three-dimensional helium

States below the fourth ionization threshold will be used to illustrate the difficulties in the identification of frozen planet states for  $L = 2$ . In fact, for  $L = 2$  the states with the longest lifetime do not necessarily coincide with those which exhibit the largest value of  $\langle \cos(\theta_{12}) \rangle$  in the respective energy regime. Indeed, there are two series of resonances which potentially could represent the frozen planet series. This is illustrated in figure 5.6, where  $^1D^e$  and  $^3D^e$  resonance states converging to the fourth ionization threshold are displayed. The two potential frozen planet series  $A$  and  $B$  are highlighted in figure 5.6 by using squares and diamonds as plot symbols, respectively. Energy, half-width, and expectation value of  $\cos(\theta_{12})$  for the first few members of these series are given in table 5.4. The series  $A$  and  $B$  both consist of resonances with small decay rates and rather large values of  $\langle \cos(\theta_{12}) \rangle$ . Series  $A$  starts at lower energies and its states exhibit larger widths than those of series  $B$ . The series ground state exhibits a larger value of  $\langle \cos(\theta_{12}) \rangle$  for series  $B$ , however, for increasing excitation  $\langle \cos(\theta_{12}) \rangle$  stays almost constant or decreases for series  $B$  but increases significantly for series  $A$ . This behaviour is particularly pronounced for triplet states. Considering this, an identification of the frozen planet series on basis of the simple criterion used for  $L = 0, 1$  is not possible. Neither, does the semiclassical prediction (5.3) provide a decisive argument. Consequently, electronic densities have to be used for the identification of frozen planet states.

In figure 5.7 conditional probability densities for the third member of series  $A$  (left) and  $B$  (right) for  $^1D^e$  helium below the fourth ionization threshold are displayed. The mutual angle is set to  $\theta_{12} = 0$  and coordinates have been scaled according to (5.2). It is difficult to denote one of these states as member of the frozen planet series as both density plots resemble a state localized along the collinear frozen planet configuration. In order to obtain more information about the localization properties of these states and to be finally able to discriminate the states more clearly the one-electron densities are used. In figure 5.8 the one-electron density with the position of the inner electron determined by the density maximum in figure 5.7 are presented for same states as before. The density for the state of series  $A$  shows the typical structure expected

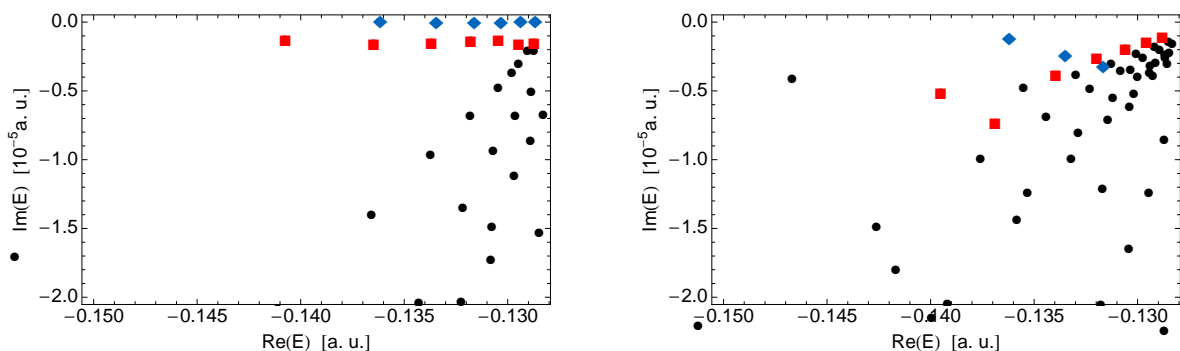


Figure 5.6: Spectra for  $^1D^e$  (left) and  $^3D^e$  (right) states of helium below  $I_4$  (three-dimensional treatment); the two series  $A$  and  $B$ , represented by squares (■) and diamonds (◆), respectively, are characterized by small decay rates and rather large values of  $\langle \cos(\theta_{12}) \rangle$  (see Tab. 5.4).

$n_S$	$-E$ [a. u.]	$\Gamma/2$ [a. u.]	$\langle \cos(\theta_{12}) \rangle$	$-E$ [a. u.]	$\Gamma/2$ [a. u.]	$\langle \cos(\theta_{12}) \rangle$
	Singlet			Triplet		
A1	0.140755520	0.000001401	0.36413	0.13951882	0.00000526	0.19106
A2	0.136481737	0.000001676	0.528905	0.1368997	0.0000075	0.38351
B1	0.136162775	0.000000095	0.394402	0.13620744	0.00000128	0.43960
A3	0.133696493	0.000001607	0.578572	0.13395946	0.00000399	0.47424
B2	0.133454834	0.000000114	0.378325	0.13349784	0.00000251	0.4075
A4	0.131803657	0.000001457	0.58224	0.13198639	0.00000274	0.51297
B3	0.131625024	0.000000110	0.372770	0.13165783	0.00000335	0.3603

Table 5.4: Energy, half-widths and  $\langle \cos(\theta_{12}) \rangle$  for the first few representatives of series  $A$  and  $B$  below  $I_4$ . Data for  $^1D^e$  and  $^3D^e$  calculated within the full three-dimensional approach is given.  $n_S = Xi$  indicates the respective series  $X = A, B$  and excitation  $i = 1, 2, \dots$  of the state within the series, where  $i = 1$  denotes the groundstate of the series.

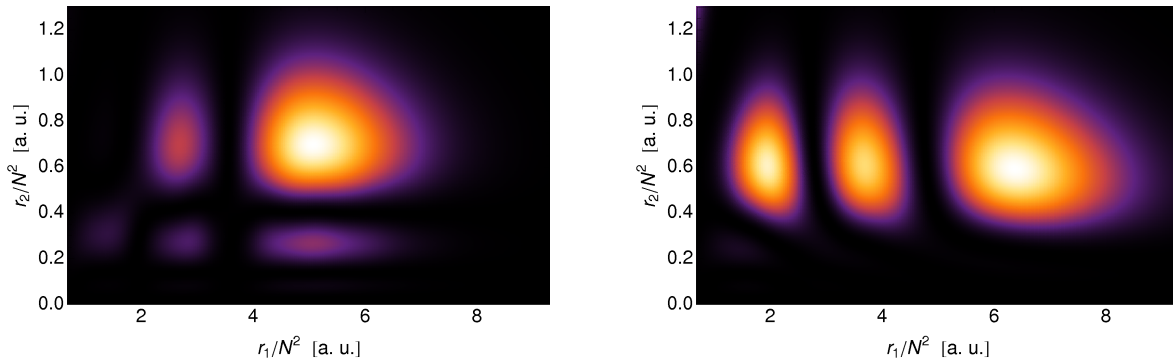


Figure 5.7: Electronic densities of the second excited state of series  $A$  (left) and  $B$  (right) of  $^1D^e$  states below  $I_4$  projected onto the subspace with  $\theta_{12} = 0$ .  $r_1 r_2 r_{12} |\Psi_i(\vec{r}_1, \vec{r}_2)|_{\theta_{12}=0}^2$  are displayed, with areas of low density represented by black color while those of high density are colored in white. The coordinates are scaled according to (5.2). Both plots show a density distribution similar to that of a frozen planet state.

for an excited state localized along the frozen planet configuration, namely, density maxima, of which the number is determined by the excitation, along the collinear configuration with small transverse extension. In contrast, the state of series  $B$  exhibits a density structure spread out over all of the displayed plane. Thus, for this state the outer electron is not necessarily collinear with the inner electron. Densities for  $^3D^e$  states exhibit equivalent behaviours. Consequently, the frozen planet states are given through the members of series  $A$ .

The frozen planet states in helium are thus not anymore the most stable states in the respective energy regime for  $L = 2$ . Moreover, the states of series  $A$ , i.e. the frozen planet states, are systematically located in the spectrum at lower energies than those of series  $B$ , rendering the frozen planet series to be not the last series to start below a given threshold. In addition, the fundamental state of series  $B$  does, besides the smaller width, even have a larger value of  $\langle \cos(\theta_{12}) \rangle$  than the frozen planet ground state for singlet as well as for triplet states.

Preliminary data for  $L = 3, 4$  indicates that these issues in the identification of frozen planet states persist for larger values of the total angular momentum.

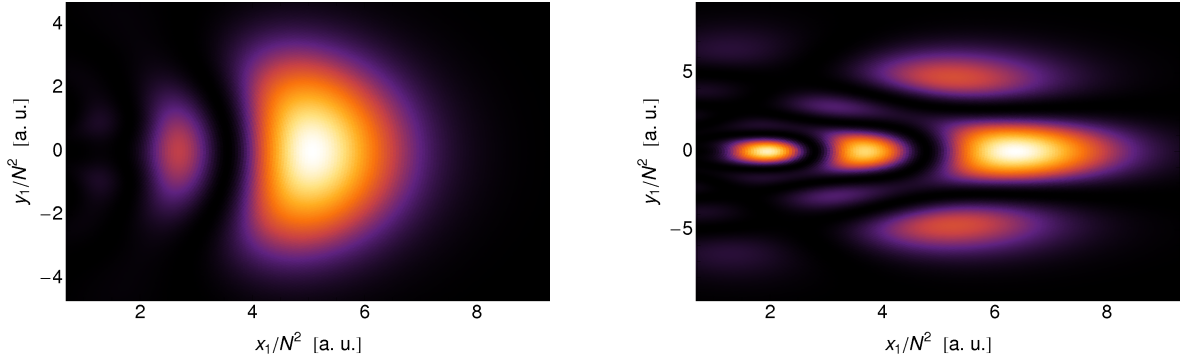


Figure 5.8: One-electron densities for fixed inner electron:  $r_1^2 r_2^2 |\Psi_i(\vec{r}_1, \vec{r}_2)|_{x_2=x_2^{\max}}^2$  is displayed for second excited state of series  $A$  (left) and  $B$  (right) of  $^1D^e$  states below  $I_4$ , respectively, with areas of low density represented by black color while those of high density are colored in white. The coordinates are scaled according to (5.2). While the state of series  $A$  exhibits a density structure expected for a state localized along the frozen planet configuration, the state of series  $B$  shows regions of high density spread out over the displayed plane. Note, that the plot range of the ordinate is large for the right plot.

### 5.3.2 Comparison of $L = 2$ frozen planet states for planar and three-dimensional helium

In table 5.5 energy, half-width and  $\langle \cos(\theta_{12}) \rangle$  is presented for the first four members of the frozen planet series below  $I_4$  for  $^1D^e$  and  $^3D^e$ . Data computed with the planar model as well as with the full three-dimensional approach is given. The half-widths for planar and three-dimensional treatment differ roughly by one order of magnitude. As for the  $L = 0, 1$  case states of the planar model exhibit larger values of  $\langle \cos(\theta_{12}) \rangle$  than the respective ones in three-dimensional calculations, which is a consequence of the restriction to a plane. In contrast to the three-dimensional case (see Sec. 5.3.1) the frozen planet series in the planar model is the series starting closest to the respective ionization threshold. Note, that the planar model is restricted to  $T = 0$  while the classification of states in a three-dimensional setting requires  $T = 0, 1, 2$ . This and the near degeneracy for small  $N$  of the frozen planet configuration with the Langmuir configuration [167–170] might be the reason for the frozen planet states being not the most

$n_F$	$-E$ [a. u.]		$\Gamma/2$ [a. u.]		$\langle \cos(\theta_{12}) \rangle$	
	2D	3D	2D	3D	2D	3D
Singlet						
1	0.1766447	0.140755520	0.0000001	0.000001401	0.6618273	0.36413
2	0.1731883	0.136481737	0.0000002	0.000001676	0.71076235	0.528905
3	0.17090597	0.133696493	0.00000020	0.000001607	0.73844	0.578572
4	0.1693252	0.131803657	0.0000002	0.000001457	0.755629	0.58224
Triplet						
1	0.176654703	0.13951882	0.000000220	0.00000526	0.675776	0.19106
2	0.17319843	0.1368997	0.00000026	0.0000075	0.7316057	0.38351
3	0.17091436	0.13395946	0.00000025	0.00000399	0.7631063	0.47424
4	0.1693265922	0.13198639	0.0000004942	0.00000274	0.77991228	0.51297

Table 5.5: Energies, half-widths and expectation values of  $\cos(\theta_{12})$  for the four lowest  $L = 2$  helium frozen planet states below  $I_4$  in planar and three-dimensional treatment.

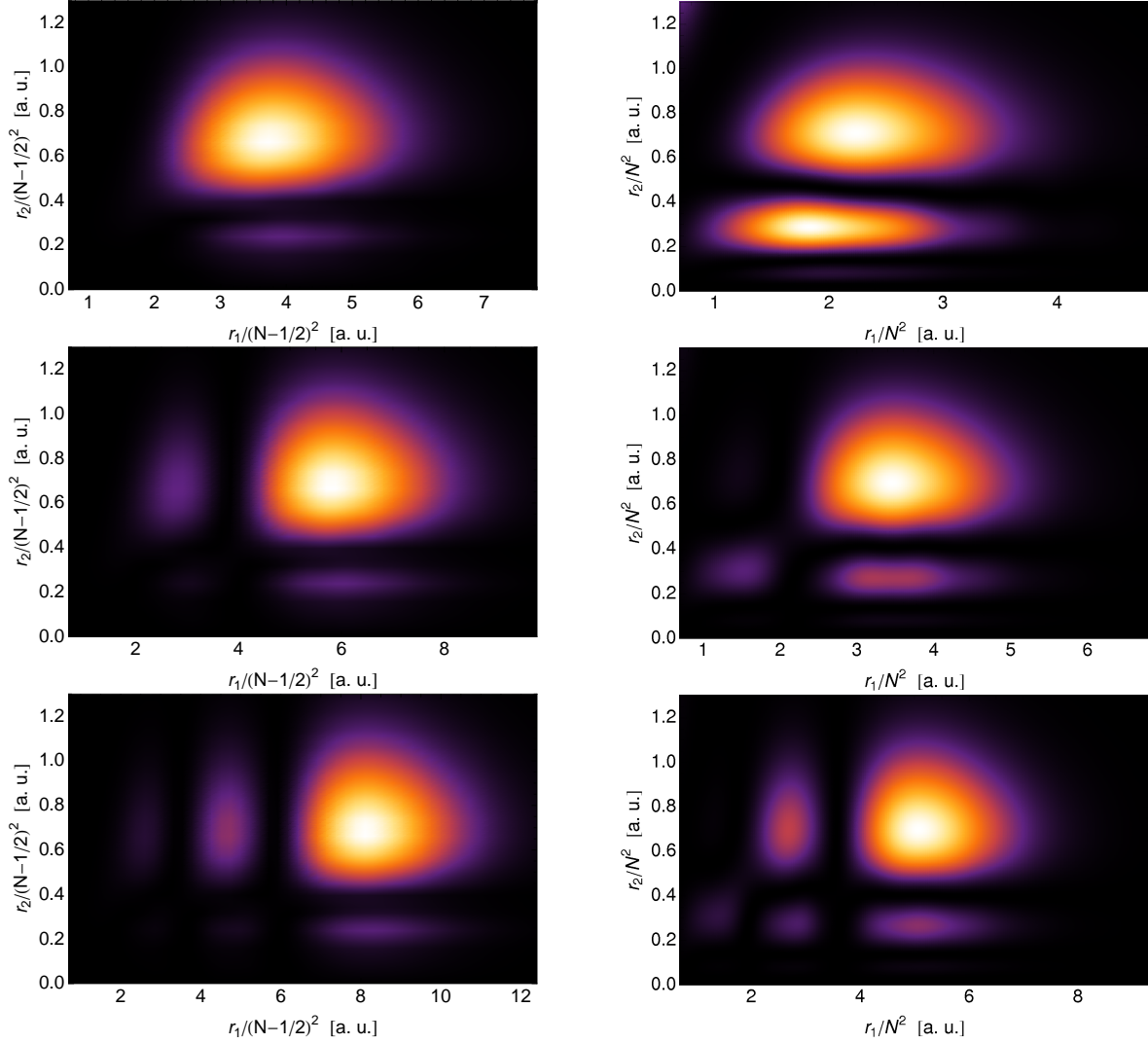


Figure 5.9: Electronic densities of the first three  ${}^1D^e$  helium frozen planet states in planar (left) and three-dimensional (right) treatment projected onto the subspace with  $\theta_{12} = 0$ . From top to bottom the densities of  $n_F = 1$ ,  $n_F = 2$  and  $n_F = 3$  are presented.  $r_1 r_2 r_{12} |\Psi_i(\vec{r}_1, \vec{r}_2)|_{\theta_{12}=0}^2$  and  $r_1^2 r_2^2 |\Psi_i(\vec{r}_1, \vec{r}_2)|_{\theta_{12}=0}^2$  are displayed for the planar and three-dimensional case, respectively, with areas of low density represented by black color while those of high density are colored in white. The coordinates are scaled according to (5.2).

stable ones anymore.

In figure 5.9 conditional probability densities with  $\theta_{12} = 0$  of planar and three-dimensional  ${}^1D^e$  helium are compared. The three lowest members of the frozen planet series below the fourth ionization threshold are displayed. As in  $L = 0$  [25] and  $L = 1$ , the main properties of the classical frozen planet configuration are evident. For both planar and three-dimensional helium the position of the density maximum for inner electron remains invariant as  $n_F$  increases. Again, a closer look at these density plots reveals that there are  $N - 1 = 3$  maxima along the inner electron axis  $r_2$  and  $n_F$  maxima along the axis of the outer electron  $r_1$ , as expected for frozen planet states. For three-dimensional treatment of helium the maximum of the density is localized close to equilibrium position (5.2) for the outer electron of the frozen planet configuration, however, one of the density submaxima (in  $r_2$  direction) is rather pronounced and shifted to slightly lower values of  $r_2$  than anticipated for frozen planet states. Note, that

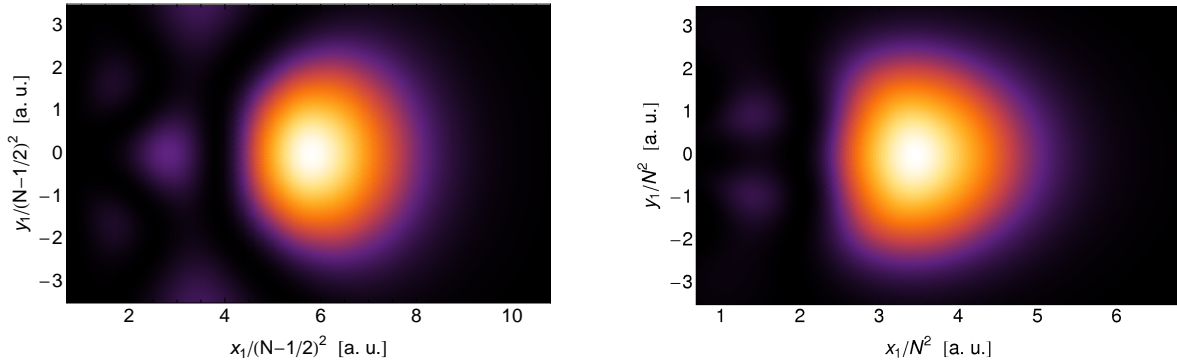


Figure 5.10: One-electron densities for fixed inner electron:  $r_1 r_2 r_{12} |\Psi_i(\vec{r}_1, \vec{r}_2)|_{x_2=x_2^{\max}}^2$  (left) and  $r_1^2 r_2^2 |\Psi_i(\vec{r}_1, \vec{r}_2)|_{x_2=x_2^{\max}}^2$  (right) are displayed for the planar and three-dimensional case, respectively, for the  $^1D^e$ ,  $N = 4$ ,  $n_F = 3$  helium frozen planet state, with areas of low density represented by black color while those of high density are colored in white. The coordinates are scaled according to (5.2).

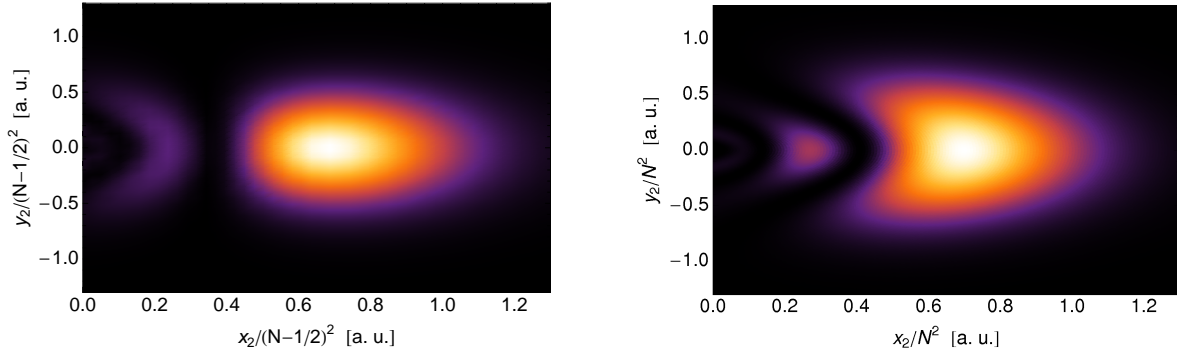


Figure 5.11: One-electron densities for fixed outer electron:  $r_1 r_2 r_{12} |\Psi_i(\vec{r}_1, \vec{r}_2)|_{x_1=x_1^{\max}}^2$  (left) and  $r_1^2 r_2^2 |\Psi_i(\vec{r}_1, \vec{r}_2)|_{x_1=x_1^{\max}}^2$  (right) are displayed for the planar and three-dimensional case, respectively, for the  $^1D^e$ ,  $N = 4$ ,  $n_F = 3$  helium frozen planet state, with areas of low density represented by black color while those of high density are colored in white. The coordinates are scaled according to (5.2).

the respective density plot for the  $^3D^e$  frozen planet ground state below  $I_4$  shows the same features. The densities for planar frozen planet states show a qualitative agreement with the three-dimensional predictions, however, the positions of the density maxima are displaced to larger values of the outer electron coordinate  $r_1$ .

Figures 5.10 and 5.11 show one-electron densities with fixed inner and outer electron, respectively. Densities for the first excited frozen planet state for  $^1D^e$  planar and three-dimensional helium are displayed, where the position of the fixed electron is determined by the density maxima in the respective plot in figure 5.9 (see Sec. 5.2). In the planar model the density for fixed inner electron is localized farther from the core than in three-dimensional calculations, however, apart from deviations in the shape of the density the density for fixed outer electron agrees well within both methods.

The graphical analysis performed so far for singlet states can be extended to the triplet symmetry. Apart from some rather small quantitative differences, triplet states have the same qualitative properties as singlet states.

## 5.4 Summary

Frozen planet states for total angular momenta  $L = 1, 2$  have been calculated for planar and three-dimensional helium. For total angular momentum  $L = 1$ , the frozen planet states possess the largest expectation values of  $\cos(\theta_{12})$  and the smallest widths in the respective energy regime. In particular, the frozen planet series is given by the  $K = -N + 1$  series. Energies, widths and expectation values of  $\cos(\theta_{12})$  for frozen planet ground states with  $N = 3, \dots, 6$  and for the first four states of the frozen planet series with  $N = 4$  have been given. The energies of the series ground states agree well with semiclassical predictions. The widths of the frozen planet states is reproduced by the planar model within one order of magnitude, however, the planar helium model exhibits systematically larger expectation values of  $\cos(\theta_{12})$  than those in three-dimensional calculations. Conditional and one-electron densities for planar and three-dimensional helium have been presented and reveal a good qualitative agreement. The densities for the frozen planet ground states are localized around the equilibrium position of the classical frozen planet configuration. However, the densities of planar helium are located systematically farther from the core than those for three-dimensional calculations. For total angular momentum  $L = 2$ , an identification of frozen planet states in three-dimensional helium on basis of the before mentioned criterion is not possible. Indeed, in three-dimensional calculations the frozen planet states for  $L = 2$  are not the most stable states in the respective energy regime anymore. Conditional and one-electron densities allow for an unambiguous identification of the frozen planet states. As an example the identification has been performed for the state below the fourth ionization threshold. The energies and densities of frozen planet ground state reproduce well the semiclassical predictions. Again the densities of the planar model resemble those of three-dimensional calculations but are located farther from the nucleus.

## Chapter 6

# Fluctuations in photoionization cross sections of planar two-electron atoms

The electron-electron interaction term in the Hamiltonian of the unperturbed helium atom – which otherwise is just the sum of two hydrogen Hamiltonians with amended nuclear charge – renders the two-electron dynamics in general irregular and chaotic with only small regions of regular motion in the classical space [3, 171]. Due to the scaling properties of the helium Hamiltonian the regime of highly doubly excited states can be described semiclassically. As a consequence, the quantum spectrum of highly doubly excited states should be influenced by the underlying classical chaotic dynamics and typical signatures of quantum chaos, such as a Wigner distribution of the energy spacings between nearest-neighbor resonances [172], semiclassical scaling laws for the fluctuations in cross sections close to the double ionization threshold [19] or Ericson fluctuations [17, 18], are expected to become observable [20].

In the 1950's Wannier was able to derive a threshold law for double ionization [173] which was confirmed in [174] for the double-photoionization cross section of helium. Recently, a semiclassical scaling law [19] for fluctuations in the cross section below the double ionization threshold has been derived via closed orbit theory. The scaling law predicts an algebraic decay of the fluctuations in the single photoionization cross section  $\sigma_{\text{fl}}$ ,

$$\begin{aligned}\sigma_{\text{fl}} &\propto |E|^\mu \quad \text{for } E \rightarrow 0^-, \\ \mu &= \mu_{eZe} + 2\mu_{WR} = \frac{1}{4} \left[ \sqrt{\frac{100Z-9}{4Z-1}} + 2\sqrt{\frac{4Z-9}{4Z-1}} \right].\end{aligned}\tag{6.1}$$

The exponent  $\mu$  consists of two components:  $\mu_{eZe}$  is related to the linearized dynamics in the  $eZe$  space and  $\mu_{WR}$  picks up contributions from two equivalent expanding degrees of freedom orthogonal to the  $eZe$  space in the so-called Wannier ridge, which is the invariant subspace of symmetric electron dynamics with  $|r_1| = |r_2|$  at all times [171]. Note, that the Wannier ridge contributes to the decay of the fluctuations for  $Z > 9/4$  where  $\mu_{WR}$  is real [19]. The scaling law has been corroborated for one-dimensional helium restricted to the  $eZe$  configuration [19], where the electrons are located on different sides of the nucleus, and experimental evidence has been found below the 17th ionization threshold [129] for partial photoionization cross sections of helium.

Ericson fluctuations are a universal statistical feature of strongly coupled, fragmenting quantum systems, first predicted [17, 18] and observed [175] in compound nuclear reactions. They manifest themselves in the excitation cross sections into the regime of highly excited resonance states with typical decay widths larger than the average level spacing, such that single maxima in the cross section cannot be identified with single resonances anymore, but are rather due to the interference of several of them. In particular, this implies that the typical scale of fluctuations

induced by interfering decay channels is smaller than the typical width of individual resonances. Later, Ericson fluctuations were studied in quantum billiards [176–178] and could be understood as a hallmark of chaotic scattering [179]. So far the only observation of Ericson fluctuations in an open deterministic quantum system was achieved for alkali atoms in crossed electromagnetic fields [180–182]. However, the rapidly increasing density of states near the double ionization threshold lead to speculations about the existence of Ericson fluctuations in helium and their onset [20, 53, 65, 183, 184]. Note, that in some disordered systems and many-body problems [185–188] with spectra which exhibit erratic fluctuations it is unclear whether these fluctuations are Ericson fluctuations.

In the helium atom members of higher lying series interfere with lower series starting from the fourth single ionization threshold. Above the 8th ionization series the widths of the resonances can be larger than their separation [53, 128]. Whether the overlap of these series and the overlap of the resonances will break down the approximative quantum numbers of Herrick’s algebraic classification [72–74] and will lead to Ericson fluctuations is not clear yet. The understanding of these issues indeed poses a challenge for both experiment and theory. In recent years an improvement of measurement techniques has allowed a detailed examination of the doubly excited states converging up to the  $N = 16$  threshold of helium [65, 128, 189]. Close to the double ionization threshold the number of open channels increases dramatically. Therefore, currently available full three-dimensional approaches require rather large basis sets for the representation of the associated eigenvalue problem. Simplified one-dimensional models or the  $s^2$ -model [190–193] of the three-dimensional atom reduce the calculation difficulties significantly. However, the former models may underestimate the decay rates of the resonances by orders of magnitude [97] and the latter does not resolve all resonances that are important for Ericson fluctuations as observed below. Studies on quantum chaos of the one-dimensional helium atom have predicted Ericson fluctuations in the total photoionization cross sections (TPCS) to be observable above  $I_{34}$  [127, 183] and studies within the  $s^2$ -model find Ericson fluctuations in the partial inelastic cross sections between electrons and  $\text{He}^+$  already around  $I_{16}$  [184]. Currently available full three-dimensional approaches are able to describe the spectrum up to the  $N = 17$  threshold [65]. The analysis of the theoretical and experimental results up to  $I_{17}$  in [65] reveals a clear dominance of principal Rydberg series in the total photoionization cross section. The hierarchy in the intensities of the resonances reveals that  $F = N - K$  is an approximate quantum number for a large fraction of the states. Consequently Ericson fluctuations are absent in this regime and no transition to full chaos is observed, in clear contradiction with the predictions of simplified models [184].

In the following, we use our planar approach described in chapter 2 for the study of the fluctuations of photoionization cross sections. After a brief explanation of how to calculate the fluctuations in the photoionization cross sections, the cross section for singlet planar helium up to  $I_{20}$  is presented. The results are compared to experimental data and the contributions to the cross section are analysed. Photoionization cross sections for the lithium ion  $\text{Li}^+$  up to the 20th threshold are presented and a test for the validity of the semiclassical scaling law is performed with the results of the cross sections for helium and the lithium ion. Finally, the cross sections for triplet planar helium for energies up to the 25th single ionization threshold are given, for which series structure, contributions to the cross sections and the existence of the Ericson fluctuations are investigated.

## 6.1 Computation of the fluctuations in photoionization cross sections

The resolution of the photoionization cross section at high energies close to the double ionization threshold requires the accurate calculation of the spectrum associated to these states. A typical

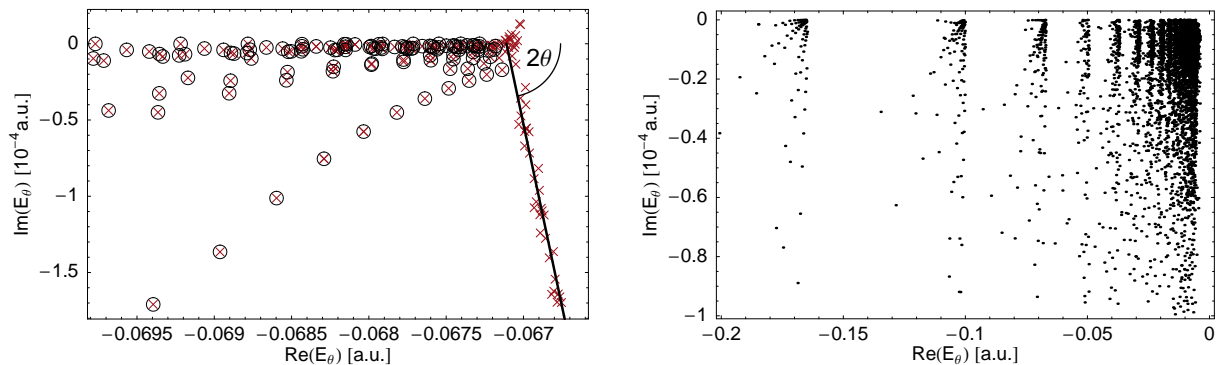


Figure 6.1: (left) Spectrum of complex rotated triplet planar helium below the threshold  $I_6$  with parameters  $\alpha = 0.45$ ,  $\theta = 0.25$  and  $n_{\text{base}} = 395$ . The eigenvalues obtained after numerical diagonalization of Eq. (2.7) (crosses) contain the converged resonances (circles), the discretized continuum spectrum rotated by an angle  $2\theta$ , and some numerical artefacts and non-converged resonances around the ionization threshold due to the truncation of the basis. (right) Spectrum of resonances of triplet planar helium from below  $I_4$  up to below  $I_{23}$ . The data was obtained by several runs of the Lanczos algorithm, choosing the shift parameter [25, 113] to provide a continuous spectrum. Numerical artefacts, discretized continuum states and non-converged resonances have been removed.

spectrum is shown in figure 6.1 (left), which has been obtained after the diagonalization of the eigenvalue problem (2.7) with  $\alpha = 0.45$  and  $\theta = 0.25$ . Besides the discretized continuum states rotated by  $2\theta$  in the complex plane and the resonances there are eigenvalues with positive imaginary part close to  $I_6$  due to the truncation of the basis. In order to exclude these numerical artefacts and non-converged resonances, all data points have to be checked for convergence with data for other parameter sets. The convergence test is based on comparison of  $\text{Re}(E_{i,\theta})$ ,  $\text{Im}(E_{i,\theta})$ ,  $\langle \cos(\theta_{12}) \rangle$  and  $\langle \overline{\Psi}_{i,\theta} | R(\theta) D | \phi_E^{\text{in}} \rangle^2$  for different parameter sets  $(\alpha, \theta, n_{\text{base}})$ . In figure 6.1 (left) the converged resonances are highlighted by circles. Figure 6.1 (right) displays all converged resonances with  $|\text{Im}(E_{i,\theta})| < 10^{-4}$  a. u. converging to  $I_N$ , with  $N = 4, \dots, 23$  for triplet planar helium. The discretized continuum states depend on the value of  $\theta$  and to some extent even on the value of  $\alpha$ . These are not displayed in figure 6.1 (right). The displayed spectra show the converged resonance eigenenergies extracted from computations with the four parameter sets  $(\theta = 0.20, \alpha = 0.45 \text{ and } n_{\text{base}} = 395)$ ,  $(0.20, 0.50, 395)$ ,  $(0.25, 0.45, 395)$  and  $(0.25, 0.50, 395)$ .<sup>1</sup> As criterion of convergence a coincidence, of eigenvalues computed for at least three different parameter sets, with a maximal relative deviation of  $10^{-5}$  for  $\text{Re}(E_{i,\theta})$ ,  $10^{-2}$  for  $\text{Im}(E_{i,\theta})$ ,  $10^{-2}$  for  $\langle \cos(\theta_{12}) \rangle$  and  $5 \times 10^{-2}$  for  $\langle \overline{\Psi}_{i,\theta} | R(\theta) D | \phi_E^{\text{in}} \rangle^2$ , has been used. Note, that due to the truncation of the basis, the exact thresholds cannot be reached, but only effective thresholds  $I_N^{\text{eff}}$  [113, 194]. The exact threshold energy of  $I_6$  is given by  $I_6 \approx 0.0661157024793$  a. u., which is clearly not the energy where the continuum starts in figure 6.1 (left).

The TPCS can be written as

$$\sigma(\omega) = \sigma_{\text{bg}}(\omega) + \sigma_{\text{fl}}(\omega). \quad (6.2)$$

The continuum states are responsible for the smooth background  $\sigma_{\text{bg}}(\omega)$  of the cross sections and do not affect their fluctuations. Thus, only the resonances contribute to the fluctuating part of the spectrum  $\sigma_{\text{fl}}(\omega)$ . The numerical calculation of  $\sigma_{\text{fl}}(\omega)$  has been accomplished with the help of Eq. (2.25), where only converged resonances have been taken into account.

<sup>1</sup>The size of the band structure matrices representing the eigenvalue problem for  $n_{\text{base}} = 395$  is given by  $325801 \times 16293$ .

## 6.2 Photoionization cross section for singlet helium

In this section we investigate the photoionization cross section for dipole transitions from the singlet planar helium ground state, with angular momentum  $l = 0$  and  $\Pi_x = +1$ . The energy of this state is given by

$$E_{\text{in}} = -11.8998223429530 \text{ a.u.} . \quad (6.3)$$

The dipole operator couples this state with  $|l| = 1$  singlet states of symmetry  $\Pi_x = +1$ . The resolution of the TPCS at high energies close to the double ionization threshold requires the accurate calculation of the spectrum associated to these states. The numerically obtained spectrum contains discretized continuum states rotated by  $2\theta$  in the complex plane, converged resonances (stable under moderate variations of  $\alpha$  and  $\theta$ ), and numerical artifacts and nonconverged resonances ( $\theta$ - and  $\alpha$ -dependent) due to the truncation of the basis [94]. In order to extract the converged resonances, all data points have been checked for convergence with data for other parameter sets  $(\alpha, \theta)$ . Depending on the energy regime, these parameter have to be adjusted. Finally, a given energy regime is calculated with six to twelve parameter sets  $(\alpha, \theta)$  among  $\{(0.35, 0.15), (0.35, 0.20), (0.35, 0.25), (0.35, 0.30), (0.40, 0.15), (0.40, 0.20), (0.40, 0.25), (0.40, 0.30), (0.45, 0.10), (0.45, 0.15), (0.50, 0.10), (0.50, 0.15), (0.50, 0.20), (0.50, 0.25), (0.50, 0.30), (0.55, 0.10), (0.55, 0.15)\}$  with  $n_{\text{base}} = 420$ .<sup>2</sup> As criterion of convergence for the resonances we used a coincidence for resonances of at least four different parameter sets  $(\alpha, \theta)$ , within a maximal deviation of a factor  $10^{-5}$  for  $\text{Re}(E_{i,\theta})$ ,  $10^{-2}$  for  $\text{Im}(E_{i,\theta})$ ,  $10^{-2}$  for  $\langle \cos(\theta_{12}) \rangle$  and  $5 \times 10^{-2}$  for  $\langle \overline{\psi_{i,\theta}} | R(\theta) T | \phi_E^{\text{in}} \rangle^2$ .

As the energy approaches the total break-up threshold the density of states increases dramatically. Single resonances will overlap with other resonances in the sense that the widths of individual resonances are larger than the separation from their nearest-neighbour resonances. Individual Fano profiles are thus hard or impossible to distinguish and the cross sections exhibit a strongly oscillating or fluctuating pattern around a smooth background. The fluctuating part  $\sigma_{\text{H}}(\omega)$  of the TPCS is given by Eq. (2.25), where only converged resonances are taken into account (see Sec. 6.1).

The TPCS for singlet planar helium from the ground state has been measured up to energies around the 15th single ionization threshold [65]. A direct comparison with the TPCS for planar helium is not possible, due to the different energy scales of the eigenstates of planar and three-dimensional helium. In particular, the positions of the ionization thresholds for planar helium (2.38) do not coincide with those for the three-dimensional system (2.39). This problem can be solved by rescaling the energies for planar helium according to

$$E_{2\text{D}}^{\text{scaled}} = - \frac{2}{\left( \sqrt{-\frac{2}{E_{2\text{D}}}} + \frac{1}{2} \right)^2} . \quad (6.4)$$

In figure 6.2 energy-rescaled calculated fluctuations  $\sigma_{\text{H}}$  for singlet planar helium are presented together with the experimental photoionization-yield spectra of doubly excited singlet helium from [65]. The energies are converted to eV (zero value fixed at the ground state energy) and the calculated cross section has been convoluted by a Gaussian function with 1.7 meV [full width at half maximum (FWHM)], which is consistent with the experimental resolution. Our theoretical predictions have been slightly shifted by -0.009 eV in order to match the experiment.

Planar helium is known to provide a good qualitative description [97] (see also Chapt. 5). Figure 6.2 shows moreover the quantitative power of the planar approach. Characteristic features of the cross section are well resolved within the data by the planar model. Furthermore,

---

<sup>2</sup>This results in band structure matrices of dimension  $394161 \times 18498$  for the treatment of the eigenvalue problem.

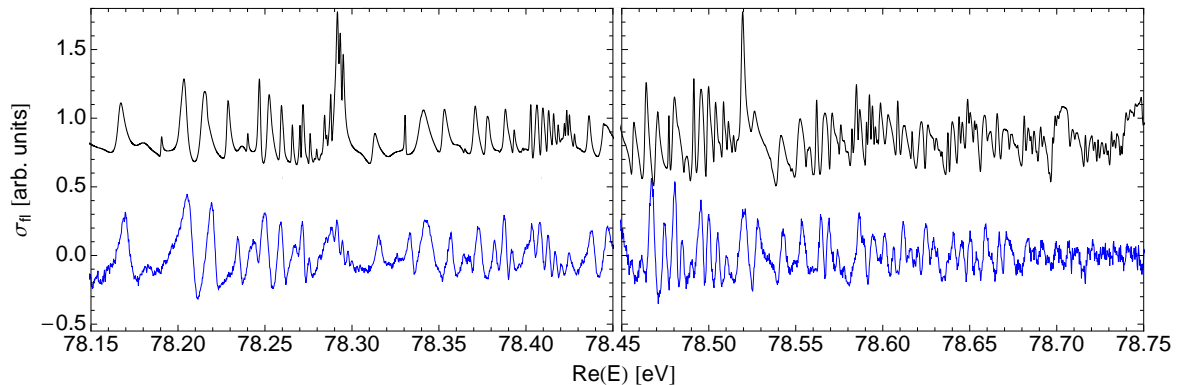


Figure 6.2: Fluctuations of photoionization cross section of doubly excited singlet helium between  $I_8$  and  $I_{15}$ : Experimental data (bottom) and theoretical results for planar helium (top). The theoretical data was scaled according to Eq. (6.4), afterwards convoluted by a Gaussian function with 1.7meV width (FWHM). The theoretical data has been displaced by  $-9$  meV in horizontal direction to match the experimental data more accurately, and one unit in vertical direction. The amplitude of the cross sections in the right panel has been enlarged by a factor of 2.5 with respect to the left panel.

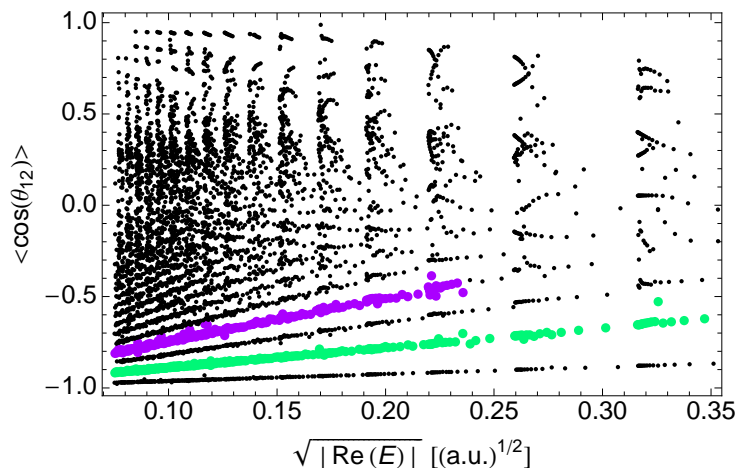


Figure 6.3: Calculated  $\langle \cos(\theta_{12}) \rangle$  values as a function of resonance energy  $E$  below the 20th threshold for singlet planar helium. Each point represents a particular singlet state resonance with  $\Pi_x = +1$  and  $|l| = 1$ . For values of  $\langle \cos(\theta_{12}) \rangle$  close to  $-1$  the resonances are organized in series along straight lines converging to  $-1$  at the double ionization threshold. These series are labeled by the approximate quantum number  $F$ . The dominant and first subdominant series are highlighted in color:  $\bullet$  ( $F = 2$ ),  $\bullet$  ( $F = 4$ ).

experimental and theoretical data show excellent agreement concerning peak positions and peak shapes. Discrepancies seem to occur near the effective ionization thresholds. These observations support once again the expectation that the planar model describes helium for the energy regime close to the double ionization threshold rather well.

The investigations by Jiang *et al.* [65, 195] show that the total cross section is dominated by the low-dimensional collinear  $eZe$  dynamics: Only very few resonances contribute significantly to the photoionization cross section in the region from  $I_9$  to  $I_{16}$  and the series of contributing resonances are associated with (small) constant values of  $F = N - K$ , where  $N$  and  $K$  are approximate quantum numbers from Herrick's algebraic classification [72–74].

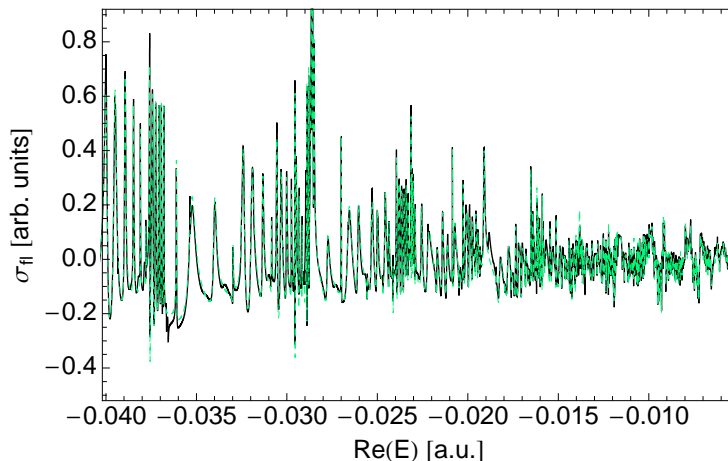


Figure 6.4: Comparison of the fluctuations of the photoionization cross sections for singlet planar helium from below  $I_8$  up to  $I_{20}$  including all resonances (solid line) and resonances with  $F = 2$  only (dashed line).

Figure 6.3 presents a plot of the calculated expectation values  $\langle \cos(\theta_{12}) \rangle$  as a function of  $\sqrt{|\text{Re}(E_\theta)|}$  for all converged resonances below  $I_4$  up to  $I_{20}$ .  $\theta_{12}$  is the angle between the two electron position vectors  $\vec{r}_1$  and  $\vec{r}_2$ . A clear decomposition into series of resonances can be identified for  $\langle \cos(\theta_{12}) \rangle \lesssim -0.5$ . From the relation

$$\langle \cos(\theta_{12}) \rangle \xrightarrow{n \rightarrow \infty} -\frac{K}{N}, \quad (6.5)$$

the  $eZe$  configuration can be identified with the maximum value of  $K = N - 1$ , i.e.,  $F = N - K = 1$ . Furthermore, the values of  $\langle \cos(\theta_{12}) \rangle$  in the low-lying series in figure 6.3 decrease smoothly with decreasing values of  $\sqrt{|\text{Re}(E_\theta)|}$ . This can be understood as a consequence of the presence of perturbers with different  $K$  values that belong to Rydberg series below the next higher thresholds, i.e., of a strong mixing of resonances with different  $N$  and  $K$ , but the same  $N - K$ . The approximate quantum number  $F = N - K$  thus allows the classification of these series of resonances, of which all members lie on straight lines. As the energy approaches the total fragmentation threshold new series associated to higher values of  $F$  appear and no mixing between series with different values of  $F$  is found. In addition, the extrapolations of the straight lines for series classified by a constant value of  $F$  cross each other at a value of  $\langle \cos(\theta_{12}) \rangle = -1$  at the double ionization threshold. In this limit these resonances correspond to the  $eZe$  configuration, which is stable under angular perturbations, but unstable under radial perturbations. Therefore, the existence of the approximate quantum number  $F$  can be understood by the regularity in the angular direction in helium, though the radial motion remains chaotic. In contrast to these resonances, series of resonances in the region where  $\langle \cos(\theta_{12}) \rangle$  is close to unity exhibit a systematic increase of  $\langle \cos(\theta_{12}) \rangle$ , though no mixing between  $N$  and  $K$  takes place. This is a consequence of the underlying regular classical dynamics of the frozen planet ( $Zee$ ) configuration.

The approximate classification of helium resonances unveiled in figure 6.3 allows us to study separately the contributions of different series to the photoionization cross sections. Indeed, only a small fraction of states contribute significantly to the cross section. For singlet helium the resonances which yield major contributions are characterized by even values of  $F$ ,

$$F = 2m, \quad m \in \mathbb{N}, \quad (6.6)$$

which is a consequence of the propensity rules for dipole transitions [52]. Series with odd  $F$  and

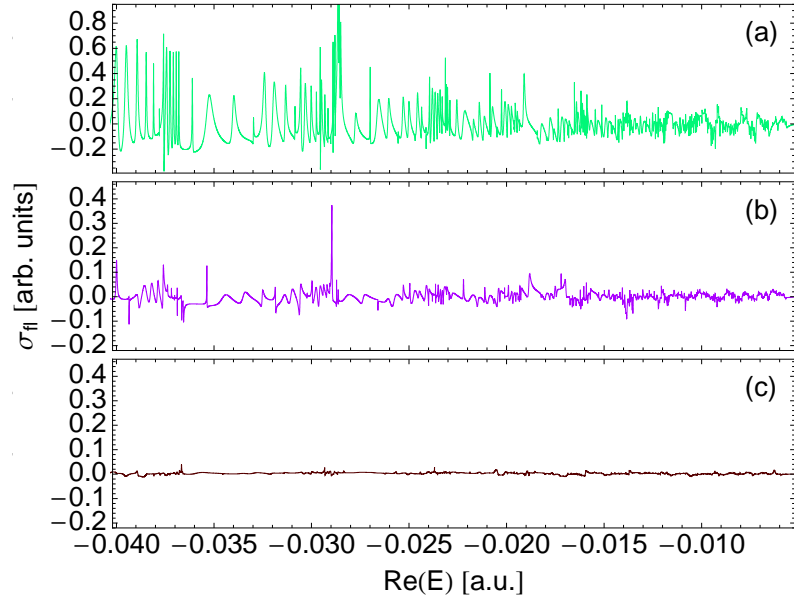


Figure 6.5: Contributions of subsets of resonances to the fluctuations of the photoionization cross section for singlet planar helium from below  $I_8$  to below  $I_{20}$ . The fluctuations due to the series  $F = 2$  and  $F = 4$  are shown in (a) and (b), respectively. The contributions from all remaining resonances are depicted in (c). The rapid decrease of the amplitudes in (a) in comparison to (b) suggests a competition between the  $F = 2$  and  $F = 4$  series and an eventual loss of the dominant role of the  $F = 2$  series.

all resonances that can not be characterized by  $F$  – e.g. those resonances close to the double ionization threshold for which  $-0.5 \lesssim \langle \cos(\theta_{12}) \rangle$  –, result in almost no contribution.

In figure 6.4, we present a comparison of the fluctuations of the photoionization cross section with the contributions of the resonances associated to  $F = 2$ . The subset of resonances with  $F = 2$  resembles the cross section quite well and, therefore, it yields the dominant contributions. However, as the energy approaches the total fragmentation threshold the influence of series with higher values of  $F$  grows. This is illustrated in figure 6.5 where we present the separate contributions of the series with  $F = 2$  and  $F = 4$ , and the contributions of the remaining resonances. A direct comparison of the plots in figure 6.5 provides a rough estimate of the amplitudes of the fluctuations. The typical magnitude of the fluctuations for the resonances series  $F = 2$  around  $I_9$  is about six times larger than the one for the  $F = 4$ , which however reduces to a factor of roughly 2.5 around  $I_{18}$ . The slower decay of the fluctuations for larger values of  $F$  might be due to the fact, that these states are still farther from being collinear than the ones with  $F = 2$  at low energies, though at the total fragmentation threshold all those series apparently converge to the collinear configuration. This might eventually lead to a breakdown of the dominant series picture which then would have to be substituted by a picture where an increasing number of series with even  $F$  will have to be taken into account with decreasing distance to the double ionization threshold. Moreover, figure 6.5 yields that basically all contributions up to the 20th threshold are due to members of the  $F = 2$  and  $F = 4$  series. Indeed, it is possible to associate a single resonance of the  $F = 2$  or  $F = 4$  series to almost every peak in the cross section. This shows that the fluctuations in the TPCS are not due to the overlap between resonances and, thus, the Ericson regime is not reached yet.<sup>3</sup>

<sup>3</sup>A more detailed analysis concerning the occurrence of Ericson fluctuations is given in section 6.4 for triplet helium.

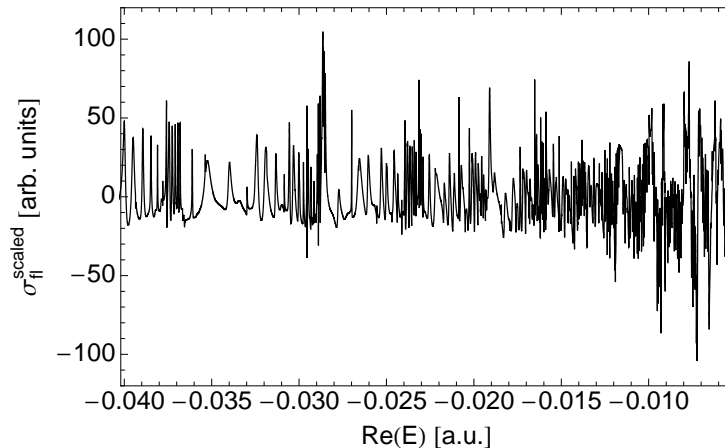


Figure 6.6: Scaled fluctuations  $\sigma_{\text{ff}}^{\text{scaled}}$  (6.7) of the cross section of singlet planar helium from below  $I_8$  up to  $I_{20}$ . The amplitude of the fluctuations remains approximately constant as a function of the energy with a slight increase close to the threshold.

An accurate analysis of the fluctuations' scaling law in planar helium requires going beyond the energy regime we can reach at present. Nevertheless, the trend of the behaviour predicted by Eq. 6.1 can already be recognized in our calculations up to  $I_{20}$ : the amplitude of the scaled fluctuations,

$$\sigma_{\text{ff}}^{\text{scaled}}(E) = |E|^{-\mu} \sigma_{\text{ff}}, \quad (6.7)$$

exhibits rather small fluctuations along the energy regime from  $I_8$  to  $I_{20}$  (see Fig. 6.6). However, a slight increase of the amplitude of the fluctuations is observed close to the total fragmentation threshold. A reason for this might be, that the scaling law (6.1) correctly reproduces the change in amplitude with decreasing distance to the total fragmentation threshold for the collinear configuration, however, the collinearity is an idealization as the expectation values of  $\cos(\theta_{12})$  for the involved resonances deviates from  $-1$ . Indeed, it seems that the magnitude of the contributions to the TPCS increases with decreasing value of  $\langle \cos(\theta_{12}) \rangle$ . Moreover, we have seen that more than one  $F$ -series of resonances contributes significantly to the cross section and that their relative weight changes with decreasing distance to the double ionization threshold, which seems also to be connected with the deviation from collinearity.

### 6.3 Photoionization cross section for singlet ionic lithium

The Wannier ridge influences the scaling law (6.1) if the charge of the nucleus  $Z > 9/4$ . A complete test of the scaling law requires the computation of photoionization cross sections for two-electron atoms other than helium. Therefore, we investigate the photoionization cross section for dipole transitions from the singlet planar lithium ion ground state, with angular momentum  $l = 0$  and  $\Pi_x = +1$ , and energy

$$E_{\text{in}} = -29.5502793111317 \text{ a.u.}, \quad (6.8)$$

coupled by the dipole operator to  $|l| = 1$  singlet states of symmetry  $\Pi_x = +1$ . For a given energy regime calculations with six to twelve parameter sets  $(\alpha, \theta)$  among  $\{(0.35, 0.10), (0.35, 0.15), (0.35, 0.20), (0.40, 0.10), (0.40, 0.15), (0.40, 0.20), (0.40, 0.25), (0.45, 0.05), (0.45, 0.10), (0.45, 0.15), (0.45, 0.20), (0.45, 0.25), (0.50, 0.05), (0.50, 0.10), (0.50, 0.15), (0.50, 0.20), (0.50, 0.25), (0.55, 0.05), (0.55, 0.10), (0.55, 0.15)\}$  with  $n_{\text{base}} = 420$  have been performed and

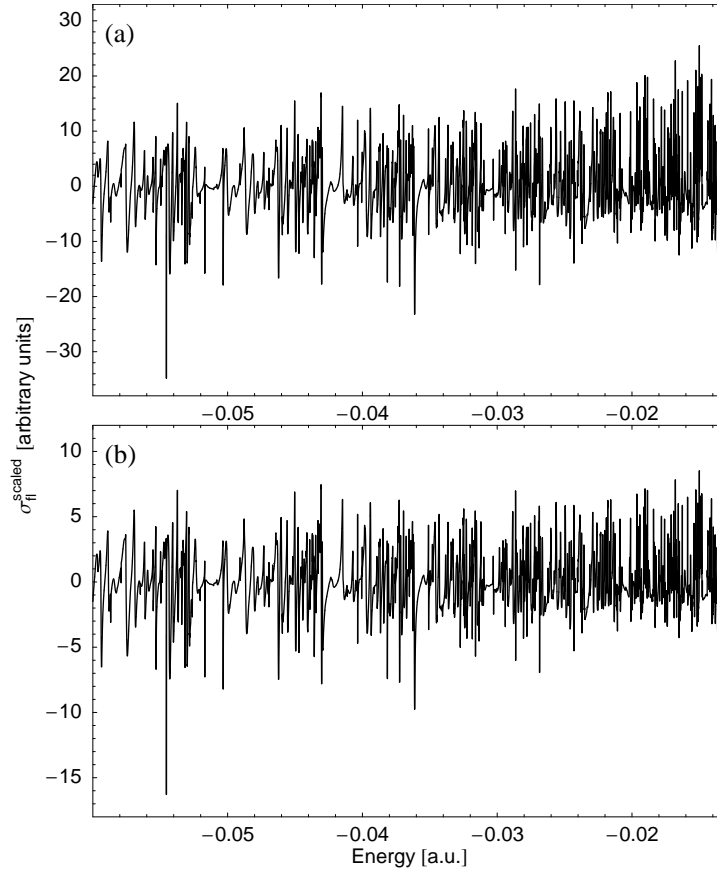


Figure 6.7: Scaled fluctuations  $\sigma_{\text{II}}^{\text{scaled}}$  of the cross section for singlet planar ionic lithium from below  $I_{10}$  up to  $I_{20}$ . (a) presents the fluctuations scaled with the exponent  $\mu = \mu_{eZ_e} + 2\mu_{WR}$ , while the fluctuations in (b) have been scaled using  $\mu = \mu_{eZ_e}$  as exponent. The amplitude of the fluctuations remains, for both cases, approximately constant as a function of energy, with a slight increase for  $\mu = \mu_{eZ_e} + 2\mu_{WR}$  close to the double ionization threshold.

converged resonances have been extracted with the same criterion as for singlet planar helium. The fluctuations in the photoionization cross sections have been computed on the basis of these resonances as described in section 6.1.

In figure 6.7 the fluctuations of the photoionization cross section scaled according to (6.7) are presented. However, to test the influence of the Wannier ridge, fluctuations scaled with two different exponents  $\mu$  are given, one as given in (6.1) with  $\mu = \mu_{eZ_e} + 2\mu_{WR}$  (Fig. 6.7(a)) and a second  $\mu = \mu_{eZ_e}$  without the contribution of the Wannier ridge (Fig. 6.7(b)). The amplitude of the fluctuations exhibit rather small variations along the energy regime from  $I_{10}$  to  $I_{20}$  for both exponents. The amplitude of the fluctuations of figure 6.7(a) shows a small increase close to double ionization threshold. On basis of these plots alone, it can not be verified that the contribution of the Wannier ridge to the exponent  $\mu$  is needed. However, considering that the amplitude of the fluctuations for singlet planar helium increases close to the double ionization threshold, too, indicates that the exponent of (6.1) reflects the general behaviour of decay of the amplitude of the fluctuations, apart from the observed differences connected with the deviations from collinearity.

Figure 6.8 presents a plot of the calculated expectation values  $\langle \cos(\theta_{12}) \rangle$  as a function of  $\sqrt{|\text{Re}(E_\theta)|}$  for all converged resonances below  $I_8$  up to  $I_{20}$ , which shows for  $\langle \cos(\theta_{12}) \rangle < -0.5$  an organization into series similar to the one for singlet planar helium. Major contributions to

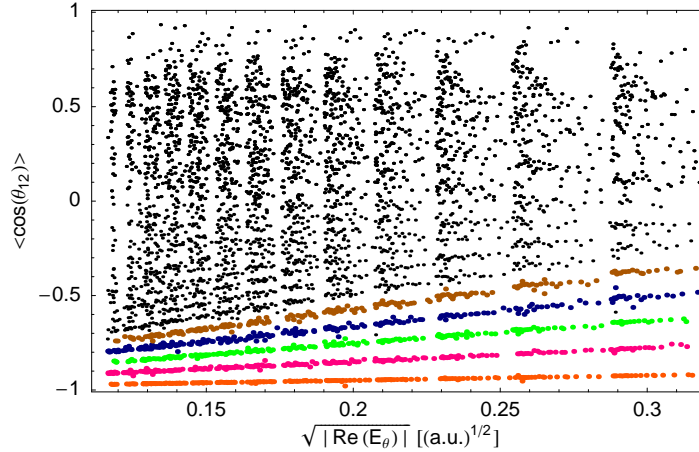


Figure 6.8: Calculated values of  $\langle \cos(\theta_{12}) \rangle$  as a function of resonance energy  $E$  below the 20th threshold for singlet planar ionic lithium. Each point represents a particular singlet state resonance with  $\Pi_x = +1$  and  $|l| = 1$ . For values of  $\langle \cos(\theta_{12}) \rangle$  close to -1 the resonances are organized in series along straight lines converging to -1 at the double ionization threshold. These series are labeled by the approximate quantum number  $F$ . The resonances are displayed in color according to their allocation to these series:  $\bullet$  ( $F = 1$ ),  $\bullet$  ( $F = 2$ ),  $\bullet$  ( $F = 3$ ),  $\bullet$  ( $F = 4$ ),  $\bullet$  ( $F = 5$ ) and  $\bullet$  for resonances not identified with any one of these series.

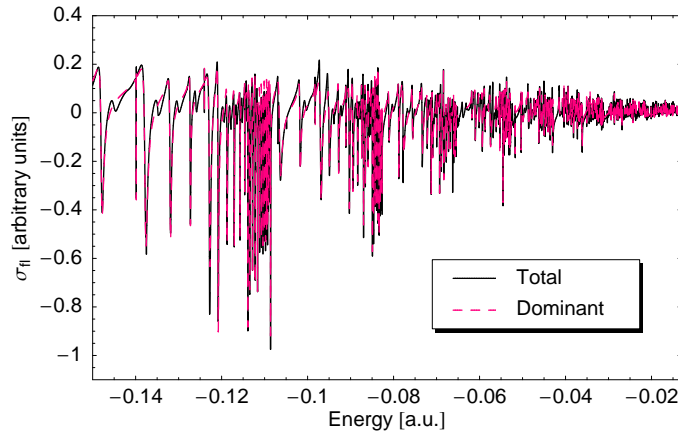


Figure 6.9: Comparison of the fluctuations of the photoionization cross sections for singlet planar ionic lithium from below  $I_7$  up to  $I_{20}$  including all resonances (solid line) and resonances with  $F = 2$  only (dashed line).

the cross sections are again given by members of series characterized by even values of  $F$ , where  $F = 2$  gives the dominant contribution which already describes the cross section rather well (see Fig. 6.9). However, with decreasing distance to the total fragmentation threshold the relative weight of the contributions of subdominant series increases. In figure 6.10 the contributions of the dominant ( $F = 2$ ), first subdominant ( $F = 4$ ) and all other resonances are given. Note, that the change in the relative weight of the series is roughly the same as for singlet planar helium, however, the weight of the contribution for the resonances not identified with  $F = 2$  and  $F = 4$  is larger than in the helium case.

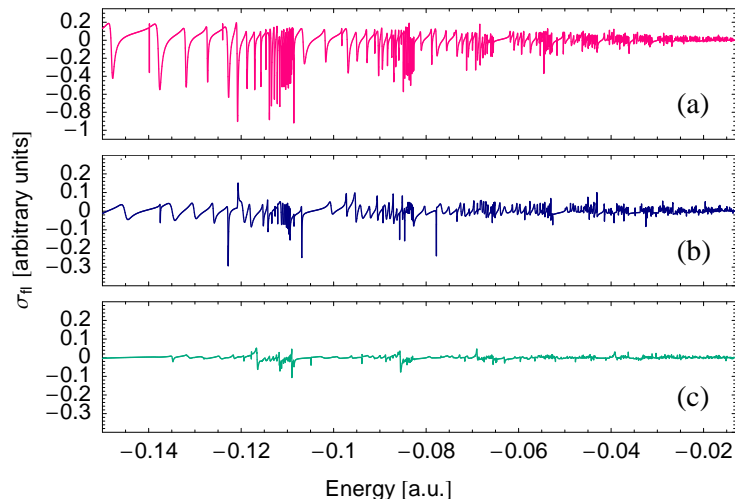


Figure 6.10: Contributions of subsets of resonances to the fluctuations of the photoionization cross section for singlet planar ionic lithium from below  $I_7$  to below  $I_{20}$ . The fluctuations due to the series  $F = 2$  and  $F = 4$  are shown in (a) and (b), respectively. The contributions from all remaining resonances are depicted in (c). The rapid decrease of the amplitudes in (a) in comparison to (b) suggests a competition between the  $F = 2$  and  $F = 4$  series and an eventual loss of the dominant role of the  $F = 2$  series.

## 6.4 Photoionization cross section for triplet helium

After analysing the fluctuations of the photoionization cross sections below  $I_{20}$  for singlet planar helium and ionic lithium, we are going to investigate the cross sections for triplet planar helium for energies up to the 25th single ionization threshold. The fluctuations of the photoionization cross section are computed for dipole transitions from the lowest lying triplet bound state, with angular momentum  $l = 0$  and  $\Pi_x = +1$ , of planar helium. The energy of this state is given by

$$E_{\text{in}} = -8.29596372809043 \text{ a.u.} \quad (6.9)$$

The dipole operator couples this state with  $|l| = 1$  triplet states of symmetry  $\Pi_x = +1$ . For a given energy regime calculations with six to twelve parameter sets  $(\alpha, \theta)$  among  $\{(0.40, 0.05), (0.40, 0.10), (0.40, 0.15), (0.40, 0.20), (0.40, 0.25), (0.45, 0.05), (0.45, 0.10), (0.45, 0.15), (0.45, 0.20), (0.45, 0.25), (0.50, 0.05), (0.50, 0.10), (0.50, 0.15), (0.50, 0.20), (0.50, 0.25), (0.55, 0.05), (0.55, 0.10), (0.55, 0.15), (0.55, 0.20), (0.60, 0.05), (0.60, 0.10), (0.60, 0.15)\}$  with  $n_{\text{base}} = 480^4$  have been performed and converged resonances have been extracted with the same criterion as for singlet planar helium, on basis of which the fluctuations of the photoionization cross section was calculated as described in 6.1.

Figure 6.11 displays the fluctuations scaled according to (6.1). Similar to the case of singlet symmetry the amplitude of the scaled fluctuations stays nearly constant as a function of energy, however, it exhibits a slight increase close to the double ionization threshold. The analysis of the contributions to the cross sections suggests again, that this is due to deviations from the collinear configuration.

In figure 6.12 the calculated expectation values  $\langle \cos(\theta_{12}) \rangle$ , as a function of  $\sqrt{|\text{Re}(E_\theta)|}$ , for all converged resonances below  $I_8$  up to  $I_{25}$  are presented. In the region  $|\langle \cos(\theta_{12}) \rangle| < 0.3$  some resonances are missing in this plot as they possess widths which are too large to be uncovered

<sup>4</sup>This results in band structure matrices of dimension  $586760 \times 24102$  for the treatment of the eigenvalue problem.

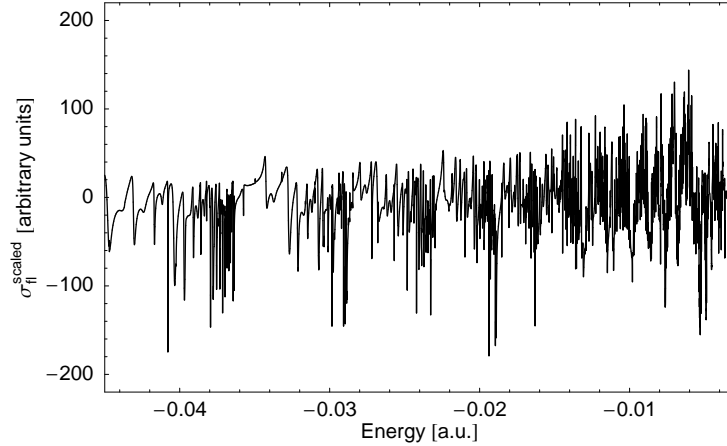


Figure 6.11: Scaled fluctuations  $\sigma_{\text{fi}}^{\text{scaled}}$  of the cross sections for triplet planar helium between  $I_8$  and  $I_{25}$ . The amplitude of the fluctuations remains approximately constant as function of the energy. A slight increase in amplitude is found close to the double ionization threshold.

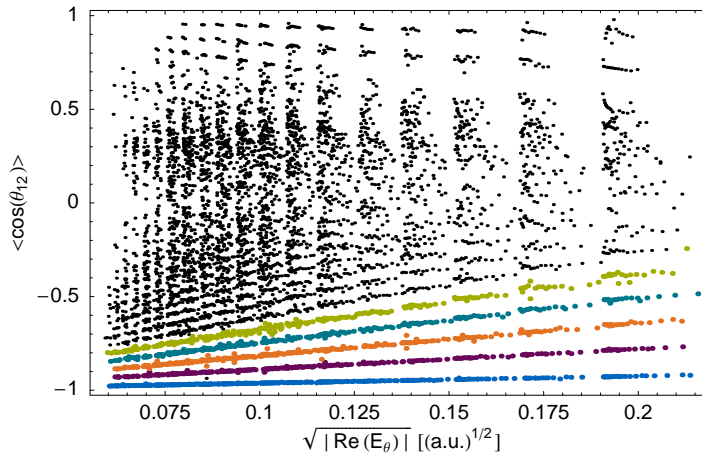


Figure 6.12: Calculated values of  $\langle \cos(\theta_{12}) \rangle$  as a function of resonance energy  $E$  below the 25th single ionization threshold for triplet planar helium. In the regions  $|\langle \cos(\theta_{12}) \rangle| < 0.3$  and  $\langle \cos(\theta_{12}) \rangle > 0.5$  some resonances are missing, details are given in the text. Each point represents a particular triplet state resonance with  $\Pi_x = +1$  and  $|l| = 1$ . The resonances are displayed in color according to their allocation to Rydberg series: ● (1st), ● (2nd), ● (3rd), ● (4th), ● (5th), and ● for resonances not identified with anyone of these series.

with some of the values used for the complex rotation angle  $\theta$ . The same is true for the region  $\langle \cos(\theta_{12}) \rangle > 0.3$ , however, in this case the widths are very small. In both cases the resonances do not meet the convergence criterion for  $\text{Im}(E)$ . A convergence analysis with a less rigid criterion for the width shows, that these resonances are resolved and that they do, as expected, not yield a significant contribution to the cross section. A clear decomposition into series of resonances can be identified for  $\langle \cos(\theta_{12}) \rangle \lesssim -0.5$ .

The approximate classification of helium resonances unveiled in Fig. 6.12 allows us to study separately the contributions of different series to the photoionization cross sections. Indeed, only a small fraction of states contribute significantly to the cross section. For triplet states the

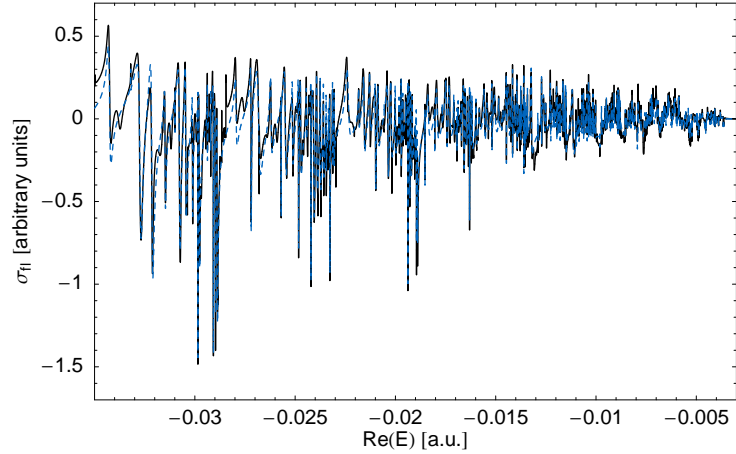


Figure 6.13: Comparison of the fluctuations of the photoionization cross sections for triplet planar helium from  $I_8$  up to  $I_{25}$  including all resonances (solid line) and resonances with  $F = 1$  only (dashed line).

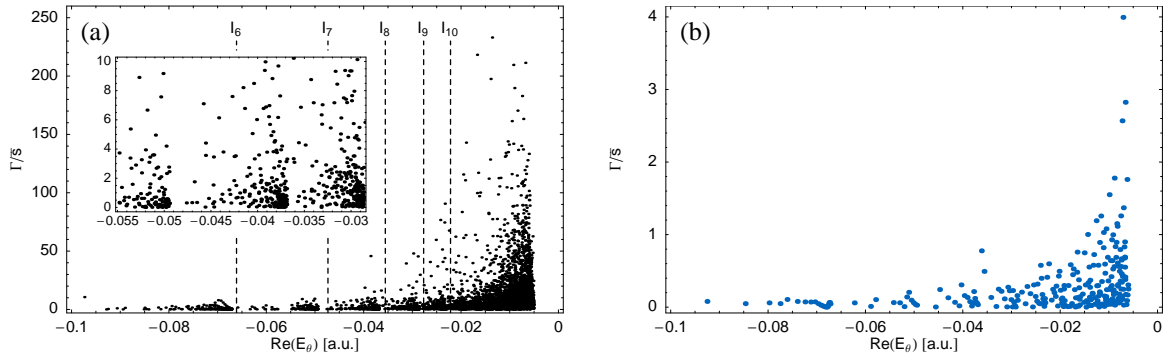


Figure 6.14: Resonance widths of triplet planar helium resonances in units of the mean level spacing  $\bar{s}$  for resonances from  $I_5$  to below  $I_{20}$ . (a) shows the widths of all resonance states found in this energy regime, with the inset giving a close-up of the regime around  $I_7$  to  $I_9$ , while (b) includes exclusively resonances characterized by  $F = 1$ . Details for the computation of  $\bar{s}$  are to be found in [94, 95].

resonances which yield major contributions are characterized by odd values of  $F$ ,

$$F = 2m + 1, \quad m \in \mathbb{N}_0, \quad (6.10)$$

while series with even  $F$  and all resonances that can not be characterized by  $F$  – e.g. those resonances close to the total fragmentation threshold for which  $-0.5 \lesssim \langle \cos(\theta_{12}) \rangle -$ , result in almost no contribution. This is a consequence of the nodal structure of the initial and final wave functions which leads to the propensity rules for dipole transitions [22, 52, 196].

The data available at present demonstrates that the size of the contributions decreases with increasing value of  $m$  in Eq. (6.10), resulting in a dominant series with  $F = 1$ . In figure 6.13, a comparison of the fluctuations of the photoionization cross section of the dominant resonance series and the one including all resonances is presented. The comparison illustrates, that the subset of resonances with  $F = 1$  reproduces the cross section quite well and therefore that this group of resonances truly yields the dominant contributions. The fact, that the  $F = 1$  series yields the dominant contribution renders triplet helium ideal for further investigations, as these states are very close to the collinear configuration (see Fig. 6.12).

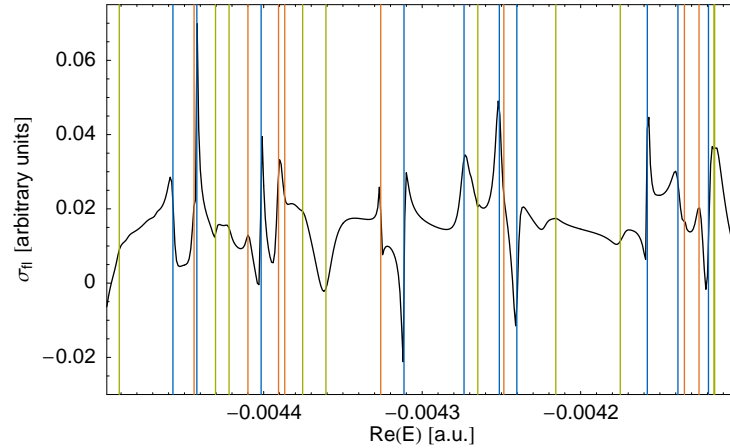


Figure 6.15: Fluctuations of the photoionization cross section for triplet planar helium around  $I_{22}$ . The vertical lines indicate the position of resonances associated with  $F = 1$  (I),  $F = 3$  (II) and  $F = 5$  (III).

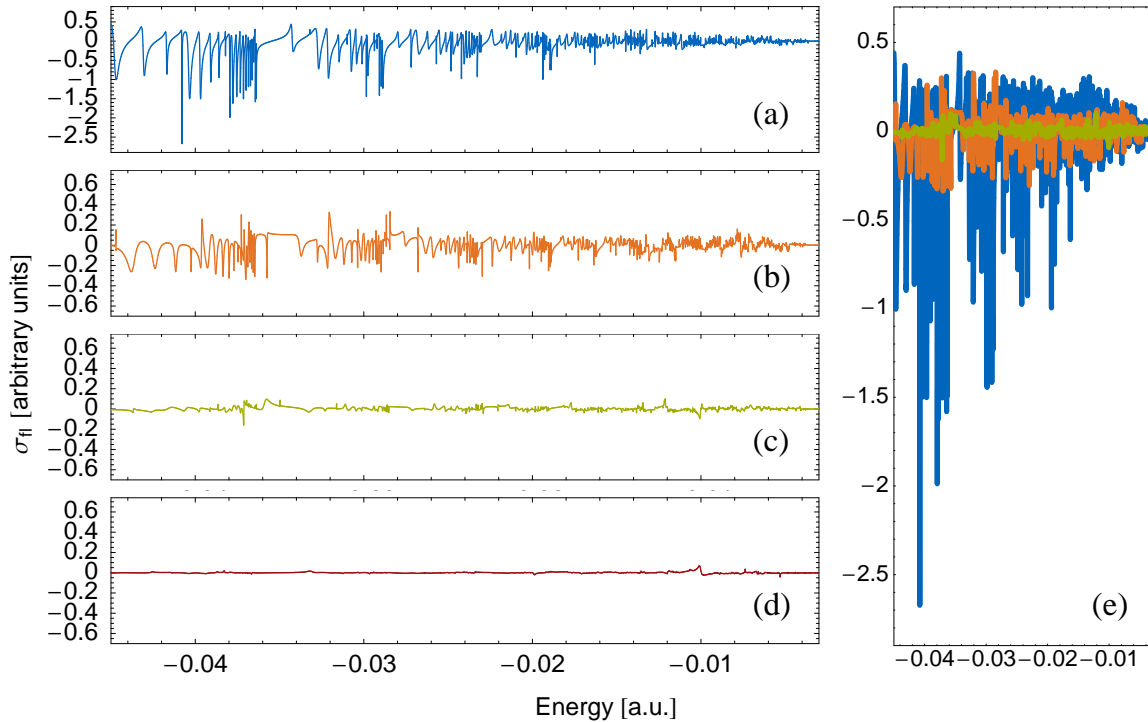


Figure 6.16: Contributions of subsets of resonances to the fluctuations of the photoionization cross section for triplet planar helium from below  $I_8$  to below  $I_{25}$ . The fluctuations due to the series  $F = 1$ ,  $F = 3$  and  $F = 5$  are shown in (a), (b) and (c), respectively. The contributions from all remaining resonances are depicted in (d). In (e) the series  $F = 1$ ,  $F = 3$  and  $F = 5$  are shown in one plot with the same color coding as in (a)-(c). The rapid decrease of the amplitudes for  $F = 1$  in comparison to  $F = 3$  suggests a competition between the  $F = 1$  and  $F = 3$  series and an eventual loss of the dominant role of the  $F = 1$  series.

The existence of a dominant subset of resonances has important consequences for the discussion of Ericson fluctuations in the cross sections. We will demonstrate this in a rather crude

way by computing a kind of local mean level spacing  $\bar{s}$  for converged resonances (see [94, 95] for details) and comparing this to the resonance widths. In figure 6.14 the resonance widths are displayed in units of the computed local mean level spacing. Figure 6.14(a) clearly illustrates, that if one considers all resonances, the condition  $\bar{\Gamma} \gg \bar{s}$  is already met around  $I_9$  and therefore the Ericson regime seems to be reached. At energies as high as  $I_{20}$  more than 90% of the resonances overlap. From this one might expect that single peaks in the cross sections observed in figure 6.13 have random character and are not the result of individual resonances. However, figure 6.14(b) indicates that the resonances of the dominant series have not reached the Ericson regime yet, since the condition  $\Gamma_i \geq \bar{s}$  is only fulfilled by a small fraction of resonances and therefore  $\bar{\Gamma} \gg \bar{s}$  is not satisfied. In figure 6.15, the fluctuations of the photoionization cross section around  $I_{22}$  and the position of resonances with  $F = 1$ ,  $F = 3$  and  $F = 5$  are presented. Note, that even in this energy regime most peaks in the cross section can be associated to a single resonance. The value of  $\cos(\theta_{12})$  expected for the resonances belonging to the  $F = 1$  series is close to  $-1$  even at low energies and approaches  $-1$  rather fast as the energy increases. Therefore, practically all of these resonances can be associated to the collinear  $eZe$  configuration. Provided the picture of a dominant series remains valid for high enough energies, Ericson fluctuations in helium are expected around  $I_{34}$  [65, 127, 183].

Note, however, that on the one hand, neither currently available studies of the full three-dimensional problem nor experimental observations [65] supply any evidence for the mixture of series with different approximative quantum numbers  $F$  or for the loss or existence of the dominant role of a single series above  $I_{17}$ . On the other hand, the decay behaviour of fluctuations from different series is not known at low energies, where the states of these series cannot be associated to collinear configurations (e.g. around  $I_{10}$ ), though it is expected to decay according to (6.7) at the break-up threshold. Therefore, it is not entirely clear whether the picture described above holds for the whole energy region up to the double ionization threshold. In particular the influence of other series characterized by  $F$  has to be understood. In order to investigate this issue we have studied the contributions to the photoionization cross section of the first five series of resonances separately. In figure 6.16(a)-(d) the contributions of the series with  $F = 1$ ,  $F = 3$  and  $F = 5$ , and the contribution of the remaining resonances are presented. In figure 6.16(e) the contributions of the series with  $F = 1$ ,  $F = 3$  and  $F = 5$  are depicted simultaneously in one plot. It indicates the change in the relative weight of the contributions with increasing energy. Note, however, that figure 6.16(e) distorts the situation slightly due to the linethickness. A direct comparison of the plots in figure 6.16 provides a rough estimate of the amplitudes of the fluctuations. The typical magnitude of the fluctuations for the resonance series  $F = 1$  around  $I_9$  is about three times larger than the one for the  $F = 3$  series and about ten times larger than the one for the  $F = 5$  series. Nevertheless, we observe that the decay of the magnitude of the fluctuations is more rapid for series with smaller  $F$ , e.g. around  $I_{18}$  the rate for the the typical magnitude of the fluctuations for the series  $F = 1$  to the one for the series  $F = 3$  decreased from three to slightly less than two and the one between  $F = 1$  and  $F = 5$  from ten to around five. This might eventually lead to a breakdown of the dominant series picture. Instead one might have to consider more and more resonance series with odd  $F$  the closer one gets to the double ionization threshold, where the fluctuations of each of these series are comparable in magnitude and which lead to an earlier onset of Ericson fluctuations than expected for the one-dimensional helium picture. The slower decay of the fluctuations for larger vales of  $F$  might be due to the fact that these states are still farther from being collinear than the ones with  $F = 1$  at low energies, though at the total fragmentation threshold all those series apparently converge to the collinear configuration.

## 6.5 Summary

The fluctuations in photoionization cross sections of two-electron atoms have been investigated for singlet planar helium and ionic lithium up to  $I_{20}$  and for triplet planar helium for energies below the 25th single ionization threshold. For singlet planar helium the cross section has been compared to experimental data, which is resembled by the planar counterpart on an almost quantitative level. Tests for a semiclassical scaling law have been performed for all three systems, which indicate that the scaling law correctly reflects the general behaviour, however, does not consider deviations from the collinear configuration. The dominance of a series of resonances associated to the  $eZe$  configuration and identified with a constant value of the approximate quantum number  $F$  has been established for all three systems. Moreover, subdominant contributions have been analysed, which indicate a breakdown of the picture of one dominant series and suggest the competition of an increasing number of series with decreasing distance to the total fragmentation threshold. In addition, we have investigated the consequences of a dominant series for the onset of the Ericson regime for the example of triplet planar helium. It turns out, that the regime of strongly overlapping resonances is not yet reached for the dominant series and that therefore Ericson fluctuations are absent.

# Conclusions and Outlook

## Summary and Conclusions

In the present thesis, we have studied bound states and resonances of helium, and photoionization cross sections of two-electron atoms. A non-standard configuration interaction approach for the treatment of two-electron atoms in three-dimensions and a planar model have been used for this purpose. Our planar approach, which is of explicitly correlated type and based on a representation of the eigenvalue problem in parabolic coordinates, has been presented together with key features of its numerical implementation in chapter 2. The spectral method used for the treatment of two-electron atoms in three dimensions and its numerical implementation have been given in chapter 3. This chapter includes the description of a newly developed, highly efficient method for the computation of matrix elements of the electron-electron interaction. The efficiency of this method provides the means to apply our configuration interaction approach to the description of highly doubly excited states, which requires the computation of large matrices.

Starting with a discussion on the slow convergence of the ground state in our approach, results for helium bound states and resonances, computed within our configuration interaction approach, have been presented in chapter 4. Our approach has then successfully been applied to the computation of  $1,3S^e$  resonances up to the tenth threshold, and they have been compared to available reference data. The computation of these doubly excited states has been achieved within a basis size not exceeding 9000, which is three to five times smaller than the basis size needed in other state-of-the-art approaches. Apart from the common natural parity states and resonances, we have applied our approach to the description of doubly excited states of unnatural parity. Results for non-autoionizing doubly excited states of helium with  $L = 1, \dots, 9$  and  $3P^e$  resonances up to the eighth single ionization threshold have been given. Our data is in perfect agreement with the few available results by Ho *et al.* [148], however, it disagrees strongly with recent results by Saha *et al.* [141], which have been obtained using a stabilization method. Note, that further spectral data has been given in appendix C.

Frozen planet states for total angular momenta  $L = 1, 2$  have been calculated for planar and three-dimensional helium and presented in chapter 5. For total angular momentum  $L = 1$ , the frozen planet states possess the largest expectation values of  $\cos(\theta_{12})$  and the smallest widths in the respective energy regime. For total angular momentum  $L = 2$ , an identification of frozen planet states in three-dimensional helium on basis of the above mentioned criterion is not possible. Indeed, in three-dimensional calculations the frozen planet states for  $L = 2$  are not the most stable states in the respective energy regime anymore. Conditional and one-electron densities allow an unambiguous identification of the frozen planet states. A comparison of frozen planet states for planar and three-dimensional treatment reveals that the planar approach provides a good description of these states, however, the outer electron is in general localized farther away from the nucleus and the states are closer to the collinear configuration than their three-dimensional counterparts.

The computation of highly doubly excited states with our three-dimensional approach, lays the foundation for a future treatment of multiphoton processes, as the description of resonances

with  $L \geq 2$  poses no additional difficulties in a configuration interaction approach. Furthermore, the relatively small dimensions of the matrices compared to those of other state-of-the-art methods – the largest matrix to diagonalize for the description of doubly excited states has been smaller than  $16000 \times 16000$  – should allow for the simultaneous treatment of several values of the total angular momentum, as needed in the description of multiphoton processes, within the presently available computational resources.

In chapter 6, the planar model has been applied to the computation of photoionization cross sections. The planar model allowed us to reach an energy regime far beyond the one accessible in three-dimensional approaches. For singlet planar helium the fluctuations in photoionization cross sections have been computed up to the 20th single ionization threshold and compared to experimental data. The planar results resemble the experimental cross section on an almost quantitative level, reproducing practically every feature of the cross section with some deviations occurring close to single ionization thresholds. This emphasizes the descriptive power of the planar approach. The data for singlet helium is used together with results for the photoionization cross section for singlet planar ionic lithium to test the semiclassical scaling law [19]. Our data indicates, that the scaling law correctly reflects the general behaviour of the decay of the fluctuations in photoionization cross sections, however, it shows deviations close to the total fragmentation threshold. These seem to be a consequence of deviations of the quantum states from the collinear configuration and of a competition of dominant and subdominant contributions with a different degree of collinearity. In addition, the fluctuations in the photoionization cross section of triplet planar helium have been studied up to the 25th single ionization threshold. The dominance of a series of resonances associated to the  $eZe$  configuration and identified with a constant value of the approximate quantum number  $F$  has been established for all three systems. Moreover, subdominant contributions have been analysed, which indicate a breakdown of the picture of one dominant series and suggest the competition of an increasing number of series with decreasing distance to the total fragmentation threshold. We have also investigated the consequences of a dominant series for the onset of the Ericson regime for the example of triplet planar helium. It turns out, that the regime of strongly overlapping resonances is, for the dominant series, not yet reached even at the 25th single ionization threshold and that therefore Ericson fluctuations are absent.

## Outlook

One of the main results of this thesis is the application of a non-standard configuration interaction approach to the description of highly doubly excited states. On the one hand, a parallelization of our code will allow us to access an energy regime even closer to the double ionization threshold. To access a higher energy regime a larger number of Coulomb-Sturmian functions and more angular configurations need to be included into the respective bases. Due to the highly efficient method for the computation of matrix elements of  $1/r_{12}$  the inclusion of additional Coulomb-Sturmian functions does not pose a problem. However, the inclusion of additional angular configurations increases the computation time tremendously, as the inner summation of Eq. (3.15) includes an increasing number of terms for increasing values of the individual angular momenta (see Eq. (B.29)) and makes a parallelization necessary. On the other hand, the computation of highly doubly excited states in our approach opens up the possibility for a treatment of multiphoton processes in a spectral method, by either implementing Floquet theory or an advanced time propagation method [197] in our code. In particular, our approach should be suitable for the investigation of a possible formation of non-dispersive two-electron wave packets through near resonant driving of frozen planet states. Frozen planet states are inaccessible through a dipole transition from the ground state and have so far not been observed in experiments. The development of a transition scheme with intermediate states on basis of

our approach might provide some clues how to access these states, which also poses the initial step for the experimental verification of the existence of non-dispersive wave packets. Note, that in the case of circularly polarized light, which might be necessary in this case, the treatment of states and resonances of unnatural parity might play an important role. Moreover, with the inclusion of relativistic corrections, i.e., radiative decay, our three-dimensional code could be used for further investigations of the unnatural parity bound state of  $H^-$  in order to assist in the experimental observation.

Our planar approach has already shown to be adapted to investigate the formation of non-dispersive two-electron wave packets, however, it is also perfectly suited for the treatment of double ionization processes induced by laser fields. Furthermore, our approach is equally appropriate for the treatment of planar quantum dots [198] or  $H_2^+$  (with and without fields).

# Appendix A

## Planar two-electron atom supplement

### A.1 Parabolic transformation

In the transformation from Cartesian  $(x_1, y_1, x_2, y_2)$  to parabolic coordinates  $(x_p, y_p, x_m, y_m)$ , as defined by Eqs. (2.2), (2.3) and (2.4), two fundamental planar transformations are involved, which are used several times: a parabolic transformation and a rotation by  $\pi/4$ .

A single generic parabolic transformation between the coordinates  $(x, y)$  and  $(\mu, \nu)$  is given by

$$\begin{aligned}x &= \frac{1}{2}(\mu^2 - \nu^2), & \mu &= \sqrt{r+x}, \\y &= \mu\nu, & \nu &= \sqrt{r-x},\end{aligned}\tag{A.1}$$

with  $r = \sqrt{x^2 + y^2} = \frac{1}{2}(\mu^2 + \nu^2)$ . The partial derivatives then read

$$\begin{aligned}\frac{\partial}{\partial x} &= \frac{1}{2r} \left( \mu \frac{\partial}{\partial \mu} - \nu \frac{\partial}{\partial \nu} \right), \\ \frac{\partial}{\partial y} &= \frac{1}{2r} \left( \nu \frac{\partial}{\partial \mu} + \mu \frac{\partial}{\partial \nu} \right),\end{aligned}\tag{A.2}$$

and the two dimensional Laplacian is given by

$$\frac{\partial^2}{\partial x^2} + \frac{\partial^2}{\partial y^2} = \frac{1}{\mu^2 + \nu^2} \left( \frac{\partial^2}{\partial \mu^2} + \frac{\partial^2}{\partial \nu^2} \right) = \frac{1}{2r} \left( \frac{\partial^2}{\partial \mu^2} + \frac{\partial^2}{\partial \nu^2} \right).\tag{A.3}$$

The coordinate transformation (2.3) involves two rotations of type

$$\begin{aligned}x &= \frac{(u+v)}{\sqrt{2}}, & u &= \frac{(x+y)}{\sqrt{2}}, \\y &= \frac{(u-v)}{\sqrt{2}}, & v &= \frac{(x-y)}{\sqrt{2}},\end{aligned}\tag{A.4}$$

the derivatives are given by

$$\begin{aligned}\frac{\partial}{\partial x} &= \frac{1}{\sqrt{2}} \left( \frac{\partial}{\partial u} + \frac{\partial}{\partial v} \right), \\ \frac{\partial}{\partial y} &= \frac{1}{\sqrt{2}} \left( \frac{\partial}{\partial u} - \frac{\partial}{\partial v} \right).\end{aligned}\tag{A.5}$$

For the full transformation between  $(x_1, y_1, x_2, y_2)$  and  $(x_p, y_p, x_m, y_m)$ , the Cartesian coordinates are given in terms of the parabolic ones by

$$\begin{aligned} x_1 &= \frac{1}{4} \left[ -(x_m y_m + x_p y_p)^2 + \frac{1}{4} (x_m^2 + x_p^2 - y_m^2 - y_p^2)^2 \right], \\ y_1 &= \frac{1}{4} (x_m y_m + x_p y_p) (x_m^2 + x_p^2 - y_m^2 - y_p^2), \\ x_2 &= \frac{1}{4} \left[ -(x_m y_m - x_p y_p)^2 + \frac{1}{4} (x_m^2 - x_p^2 - y_m^2 + y_p^2)^2 \right], \\ y_2 &= \frac{1}{4} (x_m y_m - x_p y_p) (x_m^2 - x_p^2 - y_m^2 + y_p^2). \end{aligned} \quad (\text{A.6})$$

The expressions for  $r_1 = \sqrt{x_1^2 + y_1^2}$ ,  $r_2 = \sqrt{x_2^2 + y_2^2}$  and  $r_{12} = \sqrt{(x_1 - x_2)^2 + (y_1 - y_2)^2}$  are in parabolic coordinates given by

$$\begin{aligned} r_1 &= \frac{1}{16} \left( (x_p - y_m)^2 + (x_m + y_p)^2 \right) \left( (x_p + y_m)^2 + (x_m - y_p)^2 \right), \\ r_2 &= \frac{1}{16} \left( (x_p - x_m)^2 + (y_p - y_m)^2 \right) \left( (x_p + x_m)^2 + (y_p + y_m)^2 \right), \\ r_{12} &= \frac{1}{4} (x_p^2 + y_p^2) (x_m^2 + y_m^2). \end{aligned} \quad (\text{A.7})$$

## A.2 Some integrable two-dimensional systems

### A.2.1 Eigenfunctions of the two-dimensional harmonic oscillator

The coordinate representation of the wave functions of the two-dimensional harmonic oscillator are presented here. They are used in section A.2.2, to find the representation of the tensorial product  $|n_1 n_2\rangle$  of Fock states, and through this, to calculate the wave functions of planar two-electron atoms.

The Hamiltonian of the two-dimensional harmonic oscillator is  $H = -\frac{1}{2}\nabla^2 + \frac{1}{2}\omega^2 r^2$ , where  $\nabla^2$  is the two-dimensional Laplacian. Scaling the Cartesian coordinates by  $r \rightarrow \sqrt{\omega} r$ , the scaled Hamiltonian  $H \rightarrow H/\omega$  reads

$$H = -\frac{1}{2}\nabla^2 + \frac{1}{2}r^2. \quad (\text{A.8})$$

For the purpose of solving the eigenvalue problem for this Hamiltonian polar coordinates  $(\rho, \phi)$  are chosen resulting in the Schrödinger equation to take the form

$$\left( \frac{\partial^2}{\partial \rho^2} + \frac{1}{\rho} \frac{\partial}{\partial \rho} + \frac{1}{\rho^2} \frac{\partial^2}{\partial \phi^2} - \rho^2 \right) \psi(\rho, \phi) = -2E \psi(\rho, \phi). \quad (\text{A.9})$$

This equation is separable [199] and the angular part of the solutions is given by eigenfunctions  $e^{im\phi}$  ( $m \in \mathbb{Z}$ ) of the angular momentum  $L_z = -i\partial/\partial\phi$ . Therefore, writing the radial part of  $\psi$  as  $g(\rho)/\sqrt{\rho}$ , the function  $g$  satisfies the following differential equation:

$$g''(\rho) + \left( \frac{\frac{1}{4} - m^2}{\rho^2} - \rho^2 + 2E \right) g(\rho) = 0. \quad (\text{A.10})$$

The solutions of this equation in terms of the Laguerre polynomials  $L_n^{(|m|)}(\rho^2)$  are [103]

$$\begin{cases} g(\rho) &= e^{\rho^2/2} \rho^{|m|+1/2} L_n^{(|m|)}(\rho^2), \\ E &= 2n + |m| + 1, \quad \text{with } n = 0, 1, 2, \dots \end{cases} \quad (\text{A.11})$$

Consequently, the normalized eigenfunctions of the two-dimensional harmonic oscillator of frequency  $\omega$  are given by

$$\begin{cases} \psi(\rho, \phi) = \sqrt{\frac{\omega}{\pi}} \sqrt{\frac{n!}{(n+|m|)!}} e^{im\phi} (\sqrt{\omega}\rho)^{|m|} e^{-\omega\rho^2/2} L_n^{(|m|)}(\omega\rho^2), \\ E = 2n + |m| + 1, \quad \text{with } m \in \mathbb{Z} \text{ and } n = 0, 1, 2, \dots \end{cases} \quad (\text{A.12})$$

### A.2.2 Planar hydrogenic atoms

In this part of the appendix, the most important features of two-dimensional hydrogenic atoms represented in parabolic coordinates and in particular its symmetries are discussed. The essential ideas which are outlined here are crucial for our treatment of a planar two-electron atom in chapter 2.

The Hamiltonian of a planar hydrogenic atom in atomic units reads

$$H = \frac{1}{2}(p_x^2 + p_y^2) - \frac{Z}{r}. \quad (\text{A.13})$$

In parabolic coordinates, defined in (A.1), the Laplacian and the radius take the form  $\nabla^2 = \partial_x^2 + \partial_y^2 = (\partial_\mu^2 + \partial_\nu^2)/(\mu^2 + \nu^2)$  and  $r = (\mu^2 + \nu^2)/2$ , respectively, and the Schrödinger equation  $H|\psi\rangle = E|\psi\rangle$  can be regularized by multiplication with the Jacobian  $2r$ :

$$\left( -\frac{1}{2} \left( \frac{\partial^2}{\partial\mu^2} + \frac{\partial^2}{\partial\nu^2} \right) - 2Z \right) \psi(\mu, \nu) = E(\mu^2 + \nu^2)\psi(\mu, \nu). \quad (\text{A.14})$$

This can be rewritten as

$$(H_\mu(\omega_E) + H_\nu(\omega_E))\psi(\mu, \nu) = 2Z\psi(\mu, \nu), \quad (\text{A.15})$$

where  $H_\mu(\omega_E) = \frac{1}{2}p_\mu^2 + \omega_E^2\mu^2/2$  and  $H_\nu(\omega_E) = \frac{1}{2}p_\nu^2 + \omega_E^2\nu^2/2$  are two harmonic oscillators with frequency

$$\omega_E = \sqrt{-2E}. \quad (\text{A.16})$$

An eigenfunction of (A.13) can thus be written as a product of harmonic oscillator eigenfunctions

$$\psi(\mu, \nu) = \phi_{n_\mu}(\mu)\phi_{n_\nu}(\nu), \quad (\text{A.17})$$

where  $n_\mu, n_\nu = 0, 1, 2, \dots$ , and the harmonic oscillator frequency  $\omega_E$  is determined by the eigenenergy  $E$ .

Substituting (A.17) in (A.15), and evaluating the harmonic oscillator eigenvalue equation yields  $\omega_E(n_\mu + n_\nu + 1) = 2Z$ , and this implies for the eigenvalues of (A.14), with (A.16):

$$E_{n_\mu, n_\nu} = -\frac{2Z^2}{(n_\mu + n_\nu + 1)^2}. \quad (\text{A.18})$$

However, not all of these are actually eigenvalues of (A.13) since the double representation in parabolic coordinates introduces unphysical symmetries. Each physical solution must be uniquely defined in the Cartesian plane and, therefore, must satisfy  $\psi(\mu, \nu) = \psi(-\mu, -\nu)$ . The parity of a harmonic oscillator wave function  $\phi_n(x)$  is  $(-1)^n$  (i.e.,  $\phi_n(-x) = (-1)^n\phi_n(x)$ ) [200] leading to  $\psi(-\mu, -\nu) = (-1)^{n_\mu+n_\nu}\psi(\mu, \nu)$ . It follows that for the physical solutions of (A.13)

$n_\mu + n_\nu$  is an even integer. Consequently, we can label the eigenstates of a planar hydrogenic atom by the integer number

$$N = \frac{1}{2}(n_\mu + n_\nu). \quad (\text{A.19})$$

Finally, from (A.18), the eigenvalues of the planar hydrogenic atom become

$$E_N = -\frac{Z^2}{2(N + \frac{1}{2})^2}, \quad \text{with } N = 0, 1, 2, \dots \quad (\text{A.20})$$

### Representation in creation and annihilation operators

The creation and annihilation operators of a harmonic oscillator with frequency  $\omega > 0$  are

$$\begin{aligned} a_u^\dagger(\omega) &= \frac{1}{\sqrt{2}} \left( \sqrt{\omega}u - i\frac{p_u}{\sqrt{\omega}} \right) \\ a_u(\omega) &= \frac{1}{\sqrt{2}} \left( \sqrt{\omega}u + i\frac{p_u}{\sqrt{\omega}} \right). \end{aligned} \quad (\text{A.21})$$

The number operator  $N_u(\omega) = a_u^\dagger(\omega)a_u(\omega)$  is related to the corresponding Hamiltonian  $H_u(\omega) = p_u^2/2 + \omega^2 u^2/2$  by the relation

$$H_u(\omega) = \omega \left( N_u(\omega) + \frac{1}{2} \right). \quad (\text{A.22})$$

On basis of the creation and annihilation operators  $a_\mu^\dagger$ ,  $a_\mu$ ,  $a_\nu^\dagger$  and  $a_\nu$  for  $H_\mu(\omega)$  and  $H_\nu(\omega)$  ( $\omega$  is not necessarily equal to  $\omega_E$  here) of Eq. (A.15) the circular operators

$$\begin{aligned} a_1 &= (a_\mu - ia_\nu)/\sqrt{2}, \\ a_2 &= (a_\mu + ia_\nu)/\sqrt{2}, \end{aligned} \quad (\text{A.23})$$

are defined, which satisfy the usual commutation relations for creation and annihilation operators [200]:

$$[a_i, a_j] = 0, \quad [a_i^\dagger, a_j^\dagger] = 0, \quad [a_i, a_j^\dagger] = \delta_{ij}, \quad \text{for } i = 1, 2. \quad (\text{A.24})$$

The number operators  $N_1 = a_1^\dagger a_1$  and  $N_2 = a_2^\dagger a_2$  in terms of the creation and annihilation operators  $a_\mu^\dagger$ ,  $a_\mu$ ,  $a_\nu^\dagger$  and  $a_\nu$  are given by

$$\begin{aligned} N_1 &= \frac{1}{2}(a_\mu^\dagger a_\mu + a_\nu^\dagger a_\nu) + \frac{i}{2}(a_\nu^\dagger a_\mu - a_\mu^\dagger a_\nu), \\ N_2 &= \frac{1}{2}(a_\mu^\dagger a_\mu + a_\nu^\dagger a_\nu) - \frac{i}{2}(a_\nu^\dagger a_\mu - a_\mu^\dagger a_\nu), \end{aligned} \quad (\text{A.25})$$

leading to

$$\begin{aligned} N_1 + N_2 &= N_\mu + N_\nu, \\ N_1 - N_2 &= i(a_\nu^\dagger a_\mu - a_\mu^\dagger a_\nu), \end{aligned} \quad (\text{A.26})$$

and hence, in the coordinates  $(\mu, \nu)$ ,

$$N_1 + N_2 = \frac{1}{\omega} (H_\mu(\omega) + H_\nu(\omega)) - 1, \quad (\text{A.27})$$

$$N_1 - N_2 = \mu p_\nu - \nu p_\mu. \quad (\text{A.28})$$

In particular,  $N_1 - N_2$  is independent of the frequency  $\omega$ , and

$$L_z = \frac{1}{2}(N_1 - N_2), \quad (\text{A.29})$$

where  $L_z = xp_y - yp_x$  is the angular momentum of the planar hydrogenic atom.

The eigenvalue problem (A.15) can also be written in terms of the circular operators:

$$\left(-\frac{\omega}{2}(-1 + a_1 a_2 + a_1^\dagger a_2^\dagger - a_1^\dagger a_1 - a_2^\dagger a_2) - 2Z\right) |\psi\rangle = \frac{E}{\omega}(1 + a_1 a_2 + a_1^\dagger a_2^\dagger + a_1^\dagger a_1 + a_2^\dagger a_2) |\psi\rangle, \quad (\text{A.30})$$

which reduces for the particular choice  $\omega = \omega_E$ , as expected from (A.27), to

$$\omega_E(N_1 + N_2 + 1) |\psi\rangle = 2Z |\psi\rangle. \quad (\text{A.31})$$

The eigenvectors are given by  $|\psi\rangle = |n_1 n_2\rangle^{(\omega_E)} = |n_1\rangle^{(\omega_E)} \otimes |n_2\rangle^{(\omega_E)}$ , where  $|n_i\rangle^{(\omega_E)}$  are the eigenstates of  $N_i$ ,  $i = 1, 2$ . The energy  $E$  of the planar hydrogenic atom is again given by (A.20), however, in this case  $N = (n_1 + n_2)/2$ . Thus, the eigenfunctions of the planar hydrogenic atom are  $|n_1 n_2\rangle^{(\omega_E)}$ , with  $n_1 + n_2 = 2N$ . Since there are  $2N + 1$  ordered pairs of non-negative integer numbers  $(n_1, n_2)$  such that  $n_1 + n_2 = 2N$ , the degeneracy of the eigenvalues (A.20) is  $2N + 1$ .

Alternatively, we can use the quantum numbers  $N$  and  $L$  to label the quantum eigenstates of the planar hydrogenic atom:  $H|\psi_{NL}\rangle = E_N|\psi_{NL}\rangle$  and  $L_z|\psi_{NL}\rangle = L|\psi_{NL}\rangle$ . From (A.19), (A.26) and (A.29) it follows that  $-N \leq L \leq N$  (again this leads to the degeneracy  $2N + 1$  of the energy levels).

If  $\omega$  is a positive real number,  $|\psi_{NL}\rangle$  takes the form

$$|\psi_{NL}\rangle = \sum_{n_1, n_2 \in \mathcal{B}_{NL}} c(n_1, n_2) |n_1 n_2\rangle^{(\omega)}, \quad (\text{A.32})$$

where  $\mathcal{B}_{NL} = \{n_1, n_2 | n_1 + n_2 = 2N \text{ and } n_1 - n_2 = 2L\}$ .

### Coordinate representation of tensorial products of Fock states

The coordinate representation of a product state  $|n_1 n_2\rangle^{(\omega)}$  is found by noticing that these are eigenstates of  $N_1 + N_2$  and  $L_z = \frac{1}{2}(N_1 - N_2)$ , with eigenvalues  $n_1 + n_2$  and  $(n_1 - n_2)/2$ . Since  $H_\mu(\omega) + H_\nu(\omega)$  is an isotropic two dimensional harmonic oscillator (in the space  $(\mu, \nu)$ ) in (A.27), the eigenstates and the eigenvalues of  $\omega(N_1 + N_2 + 1)$  have the form given in (A.12) (here, instead of  $(\rho, \phi)$  we use  $(R, \Phi)$ , to distinguish polar coordinates and parabolic coordinates  $(\mu, \nu)$ , i.e.,  $R = \sqrt{\mu^2 + \nu^2}$ , and  $\Phi = \arctan(\nu/\mu)$ ). The quantum number  $m$  is the eigenvalue of the operator

$$-i\partial_\Phi = -i(\mu\partial_\nu - \nu\partial_\mu) = N_1 - N_2, \quad (\text{A.33})$$

and a direct comparison with (A.12) leads to

$$\begin{cases} n_1 + n_2 = 2n + |m| + 1, \\ n_1 - n_2 = m. \end{cases} \quad (\text{A.34})$$

Hence, the coordinate representation of  $|n_1 n_2\rangle^{(\omega)}$ , i.e.,

$$\psi_{n_1 n_2}(R, \Phi) = \langle R, \Phi | n_1 n_2 \rangle^{(\omega)},$$

is given by

$$\begin{cases} \psi_{n_1 n_2}(R, \Phi) = \sqrt{\frac{\omega}{\pi}} \sqrt{\frac{n!}{(n+|m|)!}} e^{im\Phi} (\sqrt{\omega}R)^{|m|} e^{-\omega R^2/2} L_n^{(|m|)}(\omega R^2), \\ n = \min\{n_1, n_2\}, \\ m = n_1 - n_2. \end{cases} \quad (\text{A.35})$$

### Eigenfunctions of the planar hydrogenic atom

The eigenfunctions of the planar hydrogenic atom are given by (A.12), when  $\omega = \omega_E = \sqrt{-2E_{n_1 n_2}}$ , with (see Eq. (A.18))

$$E_{n_1 n_2} = -\frac{2Z^2}{(n_1 + n_2 + 1)^2}. \quad (\text{A.36})$$

Notice also that these wave functions are normalized as eigenfunctions of the two-dimensional harmonic oscillator of *fixed* frequency  $\omega$ . However, here the frequency changes, and therefore the normalization constant is not the same for distinct energies. In addition, if  $(\rho, \phi)$  are the polar coordinates of the Cartesian coordinates  $(x, y)$ , then  $\Phi = \phi/2$  and  $R = \sqrt{\mu^2 + \nu^2} = \sqrt{2\rho}$ . Finally, since the angular momentum  $L = (n_1 - n_2)/2$ , then  $L = m/2$ . Taking this into account, the expression for the normalized eigenfunctions of the planar hydrogenic atom reads

$$\begin{aligned} \psi_{NL}(r, \phi) &= \frac{Z}{N + \frac{1}{2}} \sqrt{\frac{(N - |L|)!}{\pi(N + |L|)!(N + \frac{1}{2})}} e^{iL\phi} u^{|L|} e^{-u/2} L_{N-|L|}^{(2|L|)}(u), \\ \text{where } u &= \frac{2Z}{N + \frac{1}{2}} \rho. \end{aligned} \quad (\text{A.37})$$

In particular, the ground state of the planar hydrogenic atom is given by

$$\psi_0(\rho, \phi) = \psi_{00}(\rho, \phi) = 2Z \sqrt{\frac{2}{\pi}} e^{-2Z\rho}. \quad (\text{A.38})$$

### A.2.3 Planar two-electron atom without electron-electron interaction

Removing the electron-electron interaction term  $1/r_{12}$  from the Hamiltonian of a planar two-electron atom, the resulting problem corresponds to two independent hydrogenic atoms. Thus, from (A.20), the spectrum of a planar two-electron atom without electron-electron interaction is given by

$$E_{N_1, N_2, L_1, L_2} = -\frac{Z^2}{2(N_1 - 1/2)^2} - \frac{Z^2}{2(N_2 - 1/2)^2}, \quad (\text{A.39})$$

as illustrated for  $Z = 2$  in figure A.1. Here,  $N_1$  and  $N_2$  are the principal quantum numbers of the two electrons, and  $L_1$  and  $L_2$  their angular momenta. The total angular momentum is given by  $L = L_1 + L_2$ , and the total degeneracy is  $2(2N_1 - 1)(2N_2 - 1)$ , if  $N_1 \neq N_2$ , or  $(2N_1 - 1)^2$ , if  $N_1 = N_2$ . The factor 2 in the  $N_1 \neq N_2$  case arises from the particle exchange symmetry.

The single ionization thresholds (defined by the ionization of one electron) are given by the energies of the hydrogenic quantum states of the resulting ion:

$$I_N = -\frac{Z^2}{2(N - 1/2)^2}. \quad (\text{A.40})$$

Consequently, the energy levels of a planar two-electron atom without electron-electron interaction are organized in series  $S_N$  of energies  $E_{N,n} = E_{N,n,L_1,L_2}$ , for a fixed value of the principal quantum number  $N$  of the inner electron, and variable  $n = N, N+1, \dots$ . The threshold energies  $I_N$  of the series  $S_N$  converge to the double ionization threshold  $I_\infty$ . Starting from the second series, i.e. doubly excited states, the discrete energy levels are immersed in the continuum of lower lying series.

The ground state of a planar two-electron atom with neglected electron-electron interaction is simply the tensorial product of the ground states of the two independent planar hydrogenic atoms (A.38):

$$\psi_0(r_1, r_2) = \frac{8}{\pi} Z^2 e^{-2Z(r_1+r_2)}. \quad (\text{A.41})$$

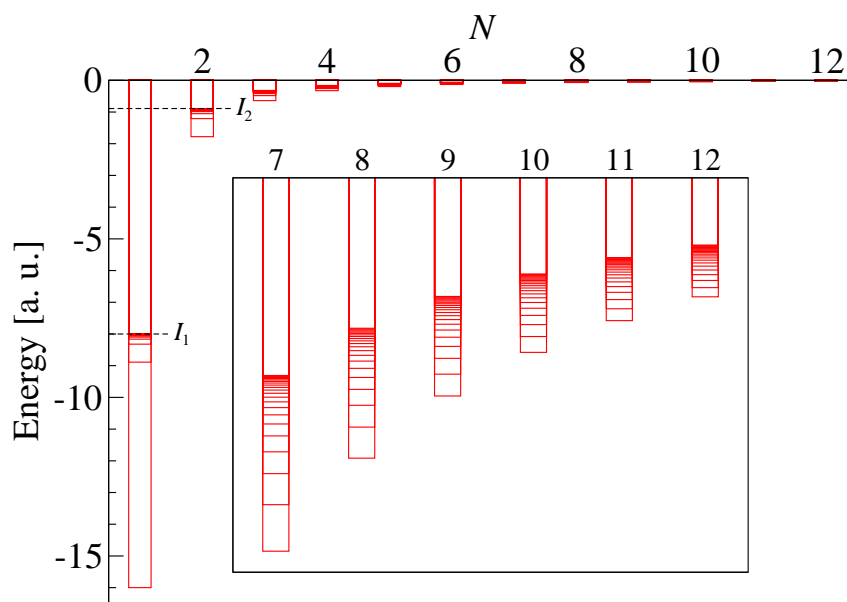


Figure A.1: Spectrum of planar helium without electron-electron interaction. The energy levels (horizontal bars) are organized in series labeled by the principal quantum number  $N$  of the inner electron. The dashed lines are the single ionization thresholds of the respective series.

## Appendix B

# Three dimensional treatment of a two-electron atom supplement

### B.1 Coulomb-Sturmian functions

The Coulomb-Sturmian functions [98, 99] are the solutions of the Sturm-Liouville eigenvalue problem

$$\left(-\frac{1}{2} \frac{d^2}{dr^2} + \frac{l(l+1)}{2r^2} - \frac{Z}{r} + \frac{k^2}{2}\right) S_{n,l}^{(k)}(r) = 0, \quad (\text{B.1})$$

with associated boundary conditions:

$$S_{n,l}^{(k)}(0) = 0, \text{ and } S_{n,l}^{(k)}(\infty) = 0. \quad (\text{B.2})$$

$n$  and  $l$  are positive integer numbers satisfying  $n \geq l + 1$ ,  $k$  a real positive (dilation) parameter and  $Z$  an eigenvalue which equals  $kn$ . Note, that Eq. (B.1) describes the radial motion of an electron with energy

$$E = -\frac{k^2}{2} = -\frac{Z^2}{2n^2}, \quad (\text{B.3})$$

in the Coulomb field of a nucleus with charge  $Z$ , and can be rewritten as

$$\left(-\frac{1}{2} \frac{d^2}{dr^2} - \frac{1}{r} \frac{d}{dr} + \frac{l(l+1)}{2r^2} - \frac{kn}{r} + \frac{k^2}{2}\right) \frac{S_{n,l}^{(k)}(r)}{r} = 0. \quad (\text{B.4})$$

Choosing the dilation parameter  $k$  as  $k = Z/n$  the functions coincide with the eigenstates of a hydrogenic atom with core charge  $Z$ . The Coulomb-Sturmian functions are square integrable and form a complete basis for the Hilbert space  $\mathcal{L}^2([0, \infty[, dr)$ .

Sturmian functions are widely used in physics, e.g., to study atoms in strong magnetic fields [201, 202], ionization processes [45, 203–207] and highly asymmetrically excited states of two-electron atoms [120]. There are various definitions for the Coulomb-Sturmian functions, however, all of them differ in their behaviour at the origin ( $r^l$  or  $r^{l+1}$ ) and the normalization.

Solving the differential equation (B.1) with the boundary conditions (B.2) yields

$$S_{n,l}^{(k)}(r) = N_{n,l}^{(k)} e^{-kr} (2kr)^{l+1} L_{n-l-1}^{(2l+1)}(2kr), \quad (\text{B.5})$$

where  $L_{n-l-1}^{(2l+1)}(2kr)$  is a Laguerre polynomial [103]. The normalization constant  $N_{n,l}^{(k)}$  given by

$$N_{n,l}^{(k)} = \sqrt{\frac{k}{n}} \left( \frac{(n-l-1)!}{(n+l)!} \right)^{1/2}, \quad (\text{B.6})$$

is chosen in order to satisfy the overlap condition

$$\int_0^{\infty} dr S_{n,l}^{(k)}(r) S_{n,l}^{(k)}(r) = 1. \quad (\text{B.7})$$

With this, the orthogonality relation for the Coulomb-Sturmian functions reads

$$\int_0^{\infty} dr S_{n,l}^{(k)}(r) \frac{1}{r} S_{n',l}^{(k)}(r) = \frac{k}{n} \delta_{nn'}. \quad (\text{B.8})$$

Note, that the above definition for the Coulomb-Sturmian functions coincides with

$$S_{n,l}^{(k)}(r) = \tilde{N}_{n,l}^{(k)} e^{-kr} (2kr)^{l+1} {}_1F_1(-(n-l-1); 2l+2; 2kr), \quad (\text{B.9})$$

with the normalization constant

$$\tilde{N}_{n,l}^{(k)} = \frac{1}{(2l+1)!} \sqrt{\frac{k}{n}} \left( \frac{(n+l)!}{(n-l-1)!} \right)^{1/2}, \quad (\text{B.10})$$

where  ${}_1F_1$  is the confluent hypergeometric or Kummer's function [103, 208].

## B.2 Matrix Formulation of the Schrödinger equation

Using the definition

$$F_{k_1,s,k_2,s,n_1,n_2}^{l_1,l_2,L,M} = \frac{S_{n_1,l_1}^{(k_1s)}(r_1) S_{n_2,l_2}^{(k_2s)}(r_2)}{r_1 r_2} \Lambda_{l_1,l_2}^{L,M}(\hat{r}_1, \hat{r}_2), \quad (\text{B.11})$$

the expansion (3.4) of the wavefunction can be rewritten as

$$\Psi(\vec{r}_1, \vec{r}_2) = \sum_{L,M} \sum_{\epsilon,\pi} \sum_{l_1,l_2}^{\pi} \sum_s \sum_{n_1,n_2} \psi_{k_1s,k_2s,n_1,n_2}^{l_1,l_2,L,M,\epsilon} \beta_{n_1,n_2}^{l_1,l_2} \mathcal{A} F_{k_1,s,k_2,s,n_1,n_2}^{l_1,l_2,L,M}(\vec{r}_1, \vec{r}_2). \quad (\text{B.12})$$

In order to obtain a matrix equation, the expansion (B.12) is substituted into the Schrödinger equation

$$(T + V + U - E) \Psi = 0, \quad (\text{B.13})$$

where the Hamiltonian has been split into the kinetic term  $T$ , nucleus-electrons interaction term  $V$ , and the electron-electron repulsion term  $U$  given through

$$T = \frac{\vec{p}_1^2}{2} + \frac{\vec{p}_2^2}{2}, \quad V = -\frac{Z}{r_1} - \frac{Z}{r_2}, \quad U = \frac{1}{r_{12}}, \quad (\text{B.14})$$

followed by a multiplication from the left by  $\beta_{\nu_1,\nu_2}^{\lambda_1,\lambda_2} \mathcal{A}' F_{\kappa_1,\sigma,\kappa_2,\sigma,\nu_1,\nu_2}^{\lambda_1,\lambda_2,L',M'}(\vec{r}_1, \vec{r}_2)$  and an integration over the whole space for spatial and angular coordinates.<sup>1</sup> This yields

$$\begin{aligned} & \sum_{L,M} \sum_{\epsilon,\pi} \sum_{l_1,l_2}^{\pi} \sum_s \sum_{n_1,n_2} \beta_{n_1,n_2}^{l_1,l_2} \beta_{\nu_1,\nu_2}^{\lambda_1,\lambda_2} \psi_{k_1s,k_2s,n_1,n_2}^{l_1,l_2,L,M,\epsilon} \left( T_{k_1,s,k_2,s,n_1,n_2,\kappa_1,\sigma,\kappa_2,\sigma,\nu_1,\nu_2}^{l_1,l_2,L,M,\lambda_1,\lambda_2,L',M'} \right. \\ & \left. + V_{k_1,s,k_2,s,n_1,n_2,\kappa_1,\sigma,\kappa_2,\sigma,\nu_1,\nu_2}^{l_1,l_2,L,M,\lambda_1,\lambda_2,L',M'} + U_{k_1,s,k_2,s,n_1,n_2,\kappa_1,\sigma,\kappa_2,\sigma,\nu_1,\nu_2}^{l_1,l_2,L,M,\lambda_1,\lambda_2,L',M'} - E S_{k_1,s,k_2,s,n_1,n_2,\kappa_1,\sigma,\kappa_2,\sigma,\nu_1,\nu_2}^{l_1,l_2,L,M,\lambda_1,\lambda_2,L',M'} \right) = 0, \end{aligned} \quad (\text{B.15})$$

<sup>1</sup>The symmetrization operator  $\mathcal{A}'$  is defined by  $\mathcal{A}' = (1 + \epsilon' P')/\sqrt{2}$  where  $P'$  exchanges simultaneously  $\lambda_1, \kappa_1, \nu_1, \mu_1$  with  $\lambda_2, \kappa_2, \nu_2, \mu_2$ .

with the integrals

$$S_{k_1,s,k_2,s,n_1,n_2,\kappa_1,\sigma,\kappa_2,\sigma,\nu_1,\nu_2}^{l_1,l_2,L,M,\lambda_1,\lambda_2,L',M'} = \int d\vec{r}_1 \int d\vec{r}_2 \mathcal{A}' F_{\kappa_1,\sigma,\kappa_2,\sigma,\nu_1,\nu_2}^{\lambda_1,\lambda_2,L',M'} * (\vec{r}_1, \vec{r}_2) \mathcal{A} F_{k_1,s,k_2,s,n_1,n_2}^{l_1,l_2,L,M} (\vec{r}_1, \vec{r}_2), \quad (\text{B.16})$$

$$T_{k_1,s,k_2,s,n_1,n_2,\kappa_1,\sigma,\kappa_2,\sigma,\nu_1,\nu_2}^{l_1,l_2,L,M,\lambda_1,\lambda_2,L',M'} = \int d\vec{r}_1 \int d\vec{r}_2 \mathcal{A}' F_{\kappa_1,\sigma,\kappa_2,\sigma,\nu_1,\nu_2}^{\lambda_1,\lambda_2,L',M'} * (\vec{r}_1, \vec{r}_2) T \mathcal{A} F_{k_1,s,k_2,s,n_1,n_2}^{l_1,l_2,L,M} (\vec{r}_1, \vec{r}_2), \quad (\text{B.17})$$

$$V_{k_1,s,k_2,s,n_1,n_2,\kappa_1,\sigma,\kappa_2,\sigma,\nu_1,\nu_2}^{l_1,l_2,L,M,\lambda_1,\lambda_2,L',M'} = \int d\vec{r}_1 \int d\vec{r}_2 \mathcal{A}' F_{\kappa_1,\sigma,\kappa_2,\sigma,\nu_1,\nu_2}^{\lambda_1,\lambda_2,L',M'} * (\vec{r}_1, \vec{r}_2) V \mathcal{A} F_{k_1,s,k_2,s,n_1,n_2}^{l_1,l_2,L,M} (\vec{r}_1, \vec{r}_2), \quad (\text{B.18})$$

$$U_{k_1,s,k_2,s,n_1,n_2,\kappa_1,\sigma,\kappa_2,\sigma,\nu_1,\nu_2}^{l_1,l_2,L,M,\lambda_1,\lambda_2,L',M'} = \int d\vec{r}_1 \int d\vec{r}_2 \mathcal{A}' F_{\kappa_1,\sigma,\kappa_2,\sigma,\nu_1,\nu_2}^{\lambda_1,\lambda_2,L',M'} * (\vec{r}_1, \vec{r}_2) U \mathcal{A} F_{k_1,s,k_2,s,n_1,n_2}^{l_1,l_2,L,M} (\vec{r}_1, \vec{r}_2), \quad (\text{B.19})$$

giving, apart from the factors due to redundancies of the basis, the matrix elements of the matrices  $\mathbf{S}$ ,  $\mathbf{T}$ ,  $\mathbf{V}$  and  $\mathbf{U}$  associated to the overlap, the kinetic term, the electron-nucleus interaction term and the electron-electron repulsion, respectively. Solving the Schrödinger equation is equivalent to solving the generalized eigenvalue problem

$$\mathbf{H}\Psi = E\mathbf{S}\Psi, \quad \mathbf{H} = \mathbf{T} + \mathbf{V} + \mathbf{U}, \quad (\text{B.20})$$

where  $\Psi$  is the vector representation of the wavefunction  $\Psi$  and  $\mathbf{H}$  the matrix associated to the Hamiltonian.

The evaluation of the integrals is straightforward and yields<sup>2</sup>

$$S_{k_1,s,k_2,s,n_1,n_2,\kappa_1,\sigma,\kappa_2,\sigma,\nu_1,\nu_2}^{l_1,l_2,L,M,\lambda_1,\lambda_2,L',M'} = \frac{1}{2} \left\{ \left[ \left\langle S_{\nu_1,\lambda_1}^{(\kappa_1,\sigma)} \middle| S_{n_1,l_1}^{(k_1,s)} \right\rangle \left\langle S_{\nu_2,\lambda_2}^{(\kappa_2,\sigma)} \middle| S_{n_2,l_2}^{(k_2,s)} \right\rangle \delta_{l_1,\lambda_1} \delta_{l_2,\lambda_2} \right. \right. \\ \left. \left. + \epsilon [(l_1, n_1, k_1,s) \rightleftharpoons (l_2, n_2, k_2,s)] \right] \\ \left. + \epsilon [(\lambda_1, \nu_1, \kappa_1,\sigma) \rightleftharpoons (\lambda_2, \nu_2, \kappa_2,\sigma)] \right\} \delta_{L,L'} \delta_{M,M'} \delta_{\pi,\pi'} \delta_{\epsilon,\epsilon'}, \quad (\text{B.21})$$

$$T_{k_1,s,k_2,s,n_1,n_2,\kappa_1,\sigma,\kappa_2,\sigma,\nu_1,\nu_2}^{l_1,l_2,L,M,\lambda_1,\lambda_2,L',M'} = \frac{1}{2} \left\{ \left[ \left( k_2,s n_2 \left\langle S_{\nu_1,\lambda_1}^{(\kappa_1,\sigma)} \middle| S_{n_1,l_1}^{(k_1,s)} \right\rangle \left\langle S_{\nu_2,\lambda_2}^{(\kappa_2,\sigma)} \middle| \frac{1}{r} S_{n_2,l_2}^{(k_2,s)} \right\rangle \right. \right. \\ \left. \left. + k_1,s n_1 \left\langle S_{\nu_1,\lambda_1}^{(\kappa_1,\sigma)} \middle| \frac{1}{r} S_{n_1,l_1}^{(k_1,s)} \right\rangle \left\langle S_{\nu_2,\lambda_2}^{(\kappa_2,\sigma)} \middle| S_{n_2,l_2}^{(k_2,s)} \right\rangle \right. \right. \\ \left. \left. - \frac{k_1,s^2 + k_2,s^2}{2} \left\langle S_{\nu_1,\lambda_1}^{(\kappa_1,\sigma)} \middle| S_{n_1,l_1}^{(k_1,s)} \right\rangle \left\langle S_{\nu_2,\lambda_2}^{(\kappa_2,\sigma)} \middle| S_{n_2,l_2}^{(k_2,s)} \right\rangle \right) \delta_{l_1,\lambda_1} \delta_{l_2,\lambda_2} \right. \\ \left. + \epsilon [(l_1, n_1, k_1,s) \rightleftharpoons (l_2, n_2, k_2,s)] \right] \\ \left. + \epsilon [(\lambda_1, \nu_1, \kappa_1,\sigma) \rightleftharpoons (\lambda_2, \nu_2, \kappa_2,\sigma)] \right\} \delta_{L,L'} \delta_{M,M'} \delta_{\pi,\pi'} \delta_{\epsilon,\epsilon'}, \quad (\text{B.22})$$

<sup>2</sup>The  $\delta_{\pi,\pi'}$  is already implicitly contained in the  $\delta_{l_1,\lambda_1} \delta_{l_2,\lambda_2}$  (or the respective term under exchange of individual angular momenta), and is put only for clarity.

$$\begin{aligned}
V_{k_{1,s},k_{2,s},n_1,n_2,\kappa_{1,s},\kappa_{2,s},\nu_1,\nu_2}^{l_1,l_2,L,M,\lambda_1,\lambda_2,L',M'} = & \frac{1}{2} \left\{ -Z \left[ \left( \left\langle S_{\nu_1,\lambda_1}^{(\kappa_{1,\sigma})} \middle| S_{n_1,l_1}^{(k_{1,s})} \right\rangle \left\langle S_{\nu_2,\lambda_2}^{(\kappa_{2,\sigma})} \middle| \frac{1}{r} \middle| S_{n_2,l_2}^{(k_{2,s})} \right\rangle \right. \right. \\
& + \left. \left. \left\langle S_{\nu_1,\lambda_1}^{(\kappa_{1,\sigma})} \middle| \frac{1}{r} \middle| S_{n_1,l_1}^{(k_{1,s})} \right\rangle \left\langle S_{\nu_2,\lambda_2}^{(\kappa_{2,\sigma})} \middle| S_{n_2,l_2}^{(k_{2,s})} \right\rangle \right) \delta_{l_1,\lambda_1} \delta_{l_2,\lambda_2} \right. \\
& + \left. \epsilon [(l_1, n_1, k_{1,s}) \rightleftharpoons (l_2, n_2, k_{2,s})] \right] \\
& + \left. \epsilon [(\lambda_1, \nu_1, \kappa_{1,\sigma}) \rightleftharpoons (\lambda_2, \nu_2, \kappa_{2,\sigma})] \right\} \delta_{L,L'} \delta_{M,M'} \delta_{\pi,\pi'} \delta_{\epsilon,\epsilon'} , \quad (\text{B.23})
\end{aligned}$$

with

$$\left\langle S_{\nu,\lambda}^{(\kappa)} \middle| S_{n,l}^{(k)} \right\rangle = \int_0^\infty dr S_{\nu,\lambda}^{(\kappa)}(r) S_{n,l}^{(k)}(r) , \quad \left\langle S_{\nu,\lambda}^{(\kappa)} \middle| \frac{1}{r} \middle| S_{n,l}^{(k)} \right\rangle = \int_0^\infty dr S_{\nu,\lambda}^{(\kappa)}(r) \frac{1}{r} S_{n,l}^{(k)}(r) . \quad (\text{B.24})$$

These radial integrals can be evaluated analytically [120], however, the Gauß-Laguerre integration method [103, 120] described in appendix B.3 is used here for their evaluation. The symbol  $[(l, n, k) \rightleftharpoons (\lambda, \nu, \kappa)]$  stands for the repetition of the original term with exchange of the quantities  $(l, n, k)$  and  $(\lambda, \nu, \kappa)$ . Substitution of the multipole expansion (3.15) of  $1/r_{12}$  in the integral (B.19) allows for a separation of radial and angular parts:

$$\begin{aligned}
U_{k_{1,s},k_{2,s},n_1,n_2,\kappa_{1,\sigma},\kappa_{2,\sigma},\nu_1,\nu_2}^{l_1,l_2,L,M,\lambda_1,\lambda_2,L',M'} = & \frac{1}{2} \sum_{q=0}^\infty \left[ \left( \mathcal{R}_{k_{1,s},k_{2,s},n_1,n_2,\kappa_{1,\sigma},\kappa_{2,\sigma},\nu_1,\nu_2}^{l_1,l_2,\lambda_1,\lambda_2,q} \mathcal{A}_{l_1,l_2,\lambda_1,\lambda_2}^{L,M,L',M',q} \right. \right. \\
& \left. \left. + \epsilon [(l_1, n_1, k_{1,s}) \rightleftharpoons (l_2, n_2, k_{2,s})] \right) + \epsilon [(\lambda_1, \nu_1, \kappa_{1,\sigma}) \rightleftharpoons (\lambda_2, \nu_2, \kappa_{2,\sigma})] \right] \delta_{\epsilon,\epsilon'} , \quad (\text{B.25})
\end{aligned}$$

with the radial part

$$\mathcal{R}_{k_{1,s},k_{2,s},n_1,n_2,\kappa_{1,\sigma},\kappa_{2,\sigma},\nu_1,\nu_2}^{l_1,l_2,\lambda_1,\lambda_2,q} = \int_0^\infty dr_1 \int_0^\infty dr_2 S_{\nu_1,\lambda_1}^{(\kappa_{1,\sigma})}(r_1) S_{\nu_2,\lambda_2}^{(\kappa_{2,\sigma})}(r_2) \frac{r_<^q}{r_>^{q+1}} S_{n_1,l_1}^{(k_{1,s})}(r_1) S_{n_2,l_2}^{(k_{2,s})}(r_2) , \quad (\text{B.26})$$

and the angular part given by

$$\mathcal{A}_{l_1,l_2,\lambda_1,\lambda_2}^{L,M,L',M',q} = \frac{4\pi}{2q+1} \sum_{p=-q}^q \int d\hat{r}_1 \int d\hat{r}_2 \Lambda_{\lambda_1,\lambda_2}^{L',M'*}(\hat{r}_1, \hat{r}_2) Y_{q,p}^*(\hat{r}_1) Y_{q,p}(\hat{r}_2) \Lambda_{l_1,l_2}^{L,M}(\hat{r}_1, \hat{r}_2) . \quad (\text{B.27})$$

Using standard angular momentum algebra results for the angular part in<sup>3</sup>

$$\begin{aligned}
\mathcal{A}_{l_1,l_2,\lambda_1,\lambda_2}^{L,M,L',M',q} = & (-1)^{l_1+\lambda_1+L} [(2l_1+1)(2l_2+1)(2\lambda_1+1)(2\lambda_2+1)]^{1/2} \\
& \times \begin{pmatrix} \lambda_1 & q & l_1 \\ 0 & 0 & 0 \end{pmatrix} \begin{pmatrix} \lambda_2 & q & l_2 \\ 0 & 0 & 0 \end{pmatrix} \begin{Bmatrix} l_1 & l_2 & L \\ \lambda_2 & \lambda_1 & q \end{Bmatrix} \delta_{L,L'} \delta_{M,M'} \delta_{\pi,\pi'} . \quad (\text{B.28})
\end{aligned}$$

Note, that the Wigner  $3jm$  symbols [82] in the last equation limit the summation index  $q$  in (B.25) for the respective term to

$$\max(|\lambda_1 - l_1|, |\lambda_2 - l_2|) \leq q \leq \min(|\lambda_1 + l_1|, |\lambda_2 + l_2|) \quad (\text{B.29})$$

<sup>3</sup>The  $\delta_{\pi,\pi'}$  is already implicitly contained in the Wigner  $3jm$  symbols, and is put only for clarity.

with  $\lambda_1 + l_1 + q$  and  $\lambda_2 + l_2 + q$  even.

As for the radial integrals (B.24) an analytic computation of  $\mathcal{R}_{k_{1,s},k_{2,s},n_1,n_2,\kappa_{1,\sigma},\kappa_{2,\sigma},\nu_1,\nu_2}^{l_1,l_2,\lambda_1,\lambda_2,q}$  is possible [120], however, apart from numerical issues the use of many Coulomb-Sturmian sets makes an implementation and computation on basis of this analytic expression cumbersome. Replacing  $r_<$  and  $r_>$  in (B.26) appropriately,  $\mathcal{R}_{k_{1,s},k_{2,s},n_1,n_2,\kappa_{1,\sigma},\kappa_{2,\sigma},\nu_1,\nu_2}^{l_1,l_2,\lambda_1,\lambda_2,q}$  can be brought to the following form:

$$\begin{aligned} \mathcal{R}_{k_{1,s},k_{2,s},n_1,n_2,\kappa_{1,\sigma},\kappa_{2,\sigma},\nu_1,\nu_2}^{l_1,l_2,\lambda_1,\lambda_2,q} &= \int_0^\infty dr_1 S_{\nu_1,\lambda_1}^{(\kappa_{1,\sigma})}(r_1) S_{n_1,l_1}^{(k_{1,s})}(r_1) r_1^q \int_{r_1}^\infty dr_2 S_{\nu_2,\lambda_2}^{(\kappa_{2,\sigma})}(r_2) S_{n_2,l_2}^{(k_{2,s})}(r_2) \frac{1}{r_2^{q+1}} \\ &+ \int_0^\infty dr_2 S_{\nu_2,\lambda_2}^{(\kappa_{2,\sigma})}(r_2) S_{n_2,l_2}^{(k_{2,s})}(r_2) r_2^q \int_{r_2}^\infty dr_1 S_{\nu_1,\lambda_1}^{(\kappa_{1,\sigma})}(r_1) S_{n_1,l_1}^{(k_{1,s})}(r_1) \frac{1}{r_1^{q+1}}. \end{aligned} \quad (\text{B.30})$$

The previous expression can be computed with the Gauß-Laguerre integration method [103, 120] as described in appendix B.3.1.

Finally, under complex rotation the generalized eigenvalue problem (B.20) and involved matrices transform to

$$\mathbf{H}_\theta \Psi_\theta = E_\theta \mathbf{S} \Psi_\theta, \quad \mathbf{H}_\theta = \mathbf{T} e^{-2i\theta} + \mathbf{V} e^{-i\theta} + \mathbf{U} e^{-i\theta}. \quad (\text{B.31})$$

### B.2.1 Matrix elements of $\cos(\theta_{12})$

Analogously to the matrix elements of  $\mathbf{S}$ ,  $\mathbf{T}$ ,  $\mathbf{V}$  and  $\mathbf{U}$  the matrix elements associated to  $C = \cos(\theta_{12})$  are given by<sup>4</sup>

$$C_{k_{1,s},k_{2,s},n_1,n_2,\kappa_{1,\sigma},\kappa_{2,\sigma},\nu_1,\nu_2}^{l_1,l_2,L,M,\lambda_1,\lambda_2,L',M'} = \int d\vec{r}_1 \int d\vec{r}_2 \mathcal{A}' F_{\kappa_{1,\sigma},\kappa_{2,\sigma},\nu_1,\nu_2}^{\lambda_1,\lambda_2,L',M'}(\vec{r}_1, \vec{r}_2) C \mathcal{A} F_{k_{1,s},k_{2,s},n_1,n_2}^{l_1,l_2,L,M}(\vec{r}_1, \vec{r}_2). \quad (\text{B.32})$$

A straight forward evaluation of this integral using (3.17) leads to

$$\begin{aligned} C_{k_{1,s},k_{2,s},n_1,n_2,\kappa_{1,\sigma},\kappa_{2,\sigma},\nu_1,\nu_2}^{l_1,l_2,L,M,\lambda_1,\lambda_2,L',M'} &= (-1)^{L+l_2+\lambda_2} \sqrt{(2l_1+1)(2\lambda_1+1)(2l_2+1)(2\lambda_2+1)} \\ &\times \left( \left[ \left\langle S_{\nu_1,\lambda_1}^{(\kappa_{1,\sigma})} \middle| S_{n_1,l_1}^{(k_{1,s})} \right\rangle \left\langle S_{\nu_2,\lambda_2}^{(\kappa_{2,\sigma})} \middle| S_{n_2,l_2}^{(k_{2,s})} \right\rangle \begin{pmatrix} l_1 & 1 & \lambda_1 \\ 0 & 0 & 0 \end{pmatrix} \begin{pmatrix} l_2 & 1 & \lambda_2 \\ 0 & 0 & 0 \end{pmatrix} \begin{Bmatrix} \lambda_1 & l_1 & 1 \\ l_2 & \lambda_2 & L \end{Bmatrix} \right. \right. \\ &\left. \left. + \epsilon[(l_1, n_1, k_{1,s}) \rightleftharpoons (l_2, n_2, k_{2,s})] \right] + \epsilon[(\lambda_1, \nu_1, \kappa_{1,\sigma}) \rightleftharpoons (\lambda_2, \nu_2, \kappa_{2,\sigma})] \delta_{L,L'} \delta_{M,M'} \delta_{\epsilon,\epsilon'} \delta_{\pi,\pi'}, \end{aligned} \quad (\text{B.33})$$

The radial integrals can be easily evaluated using Gauß-Laguerre integration.

## B.3 Gauß-Laguerre integration

The numerical Gauß-Laguerre integration is based on the formula [103, 209]

$$\int_0^\infty dx e^{-x} f(x) = \sum_{i=1}^n \omega_i f(x_i) + R_n, \quad (\text{B.34})$$

<sup>4</sup>The factors  $\beta_{n_1,n_2}^{l_1,l_2}$  and  $\beta_{\nu_1,\nu_2}^{\lambda_1,\lambda_2}$ , which account for possible redundancies in the basis, are not included and have to be treated separately in the computation of  $(\cos(\theta_{12}))$ .

with  $x_i$  being the  $i$ th zero of the Laguerre polynomial  $L_n(x) \equiv L_n^0(x)$ . The weights  $\omega_i$  and the remainder  $R_n$  are given by

$$\omega_i = \frac{(n!)^2 x_i}{(n+1)^2 [L_{n+1}(x_i)]^2}, \quad R_n = \frac{(n!)^2}{(2n)!} f^{(2n)}(\xi), \quad 0 < \xi < \infty. \quad (\text{B.35})$$

If  $f(x)$  is a polynomial the remainder  $R_n$  equals zero provided, that the number of integration points is larger than half of the degree of  $f(x)$ .

Using the Gauß-Laguerre formula (B.34) and defining the polynomial in  $r$ ,

$$T_{n,l}^{(k)}(r) = e^{kr} S_{n,l}^{(k)}(r), \quad (\text{B.36})$$

results, for an arbitrary integer  $p$ , in

$$\begin{aligned} \langle S_{\nu,\lambda}^{(\kappa)}(r) | r^p | S_{n,l}^{(k)}(r) \rangle &= \int_0^\infty dr e^{-(\kappa+k)r} T_{\nu,\lambda}^{(\kappa)}(r) r^p T_{n,l}^{(k)}(r) \\ &= \frac{1}{\kappa+k} \sum_{i=1}^N \omega_i \tilde{r}_i^p T_{\nu,\lambda}^{(\kappa)}(\tilde{r}_i) T_{n,l}^{(k)}(\tilde{r}_i), \end{aligned} \quad (\text{B.37})$$

with  $\tilde{r}_i = r_i/(\kappa+k)$ . The number of integration points  $N$  should be larger than  $(\nu+n+p)/2$  to obtain an “exact” result.

### B.3.1 Matrix elements of the electron-electron interaction

The computation of the matrix elements of the electron-electron repulsion involves the evaluation (B.25) of integrals of structure

$$\mathcal{R} = \int_0^\infty dx S_{\nu',\lambda'}^{(\kappa')}(x) S_{n',l'}^{(k')}(x) x^q \int_x^\infty dy S_{\nu,\lambda}^{(\kappa)}(y) S_{n,l}^{(k)}(y) \frac{1}{y^{q+1}}. \quad (\text{B.38})$$

Remembering the definition of the Coulomb-Sturmian functions (see appendix B.1) and that the range of  $q$  is given by Eq. (B.29) it is clear that apart from the exponentials the integrands of the subintegrals have polynomial structure and therefore an “exact” numerical integration is possible with the Gauß-Laguerre integration method. In the following coordinates with subscript  $i$  or  $j$  indicate discrete values of the respective coordinate, i.e, zeros of Laguerre polynomials.

To apply Gauss-Laguerre integration to (B.38) the coordinate of the inner integral has to be substituted by  $u = y - x$  in order to have an integration region  $[0, \infty[$ :

$$\begin{aligned} \mathcal{R} &= \int_0^\infty dx e^{-(\kappa'+k')x} x^q T_{\nu',\lambda'}^{(\kappa')}(x) T_{n',l'}^{(k')}(x) \\ &\quad \times \int_0^\infty du e^{-(\kappa'+k')(u+x)} (u+x)^{-(q+1)} T_{\nu,\lambda}^{(\kappa)}(u+x) T_{n,l}^{(k)}(u+x). \end{aligned} \quad (\text{B.39})$$

In a second transformation  $v = (\kappa+k)u$  the exponential in the inner integral is brought in the form required by (B.34)

$$\begin{aligned} \mathcal{R} &= \int_0^\infty dx e^{-\alpha x} x^q T_{\nu',\lambda'}^{(\kappa')}(x) T_{n',l'}^{(k')}(x) \\ &\quad \times \int_0^\infty \frac{dv}{\kappa+k} e^{-v} \left( \frac{v}{\kappa+k} + x \right)^{-(q+1)} T_{\nu,\lambda}^{(\kappa)} \left( \frac{v}{\kappa+k} + x \right) T_{n,l}^{(k)} \left( \frac{v}{\kappa+k} + x \right), \end{aligned} \quad (\text{B.40})$$

with  $\alpha = \kappa' + k' + \kappa + k$ . Employing Eq. (B.34) and using  $\tilde{y} = v/(\kappa + k)$  the last equation reads

$$\mathcal{R} = \int_0^\infty dx e^{-\alpha x} x^q T_{\nu', \lambda'}^{(\kappa')}(x) T_{n', l'}^{(k')}(x) \sum_{j=1}^{N_j} \frac{\omega_j}{\kappa + k} (\tilde{y}_j + x)^{-(q+1)} T_{\nu, \lambda}^{(\kappa)}(\tilde{y}_j + x) T_{n, l}^{(k)}(\tilde{y}_j + x). \quad (\text{B.41})$$

Through transformation of the remaining integral into a sum the expression

$$\begin{aligned} \mathcal{R} = & \sum_{i=1}^{N_i} \frac{\omega_i}{\alpha} \left(\frac{z_i}{\alpha}\right)^q T_{\nu', \lambda'}^{(\kappa')}\left(\frac{z_i}{\alpha}\right) T_{n', l'}^{(k')}\left(\frac{z_i}{\alpha}\right) \\ & \times \sum_{j=1}^{N_j} \frac{\omega_j}{\kappa + k} \left(\tilde{y}_j + \frac{z_i}{\alpha}\right)^{-(q+1)} T_{\nu, \lambda}^{(\kappa)}\left(\tilde{y}_j + \frac{z_i}{\alpha}\right) T_{n, l}^{(k)}\left(\tilde{y}_j + \frac{z_i}{\alpha}\right), \end{aligned} \quad (\text{B.42})$$

is obtained, with  $z = \alpha x$ . After a final coordinate transformation  $\tilde{x} = z/(\kappa' + k)$  this becomes

$$\begin{aligned} \mathcal{R} = & \sum_{i=1}^{N_i} \frac{\omega_i}{\alpha} \left(\frac{\tilde{x}_i(\kappa' + k)}{\alpha}\right)^q T_{\nu', \lambda'}^{(\kappa')}\left(\frac{\tilde{x}_i(\kappa' + k)}{\alpha}\right) T_{n', l'}^{(k')}\left(\frac{\tilde{x}_i(\kappa' + k)}{\alpha}\right) \\ & \times \sum_{j=1}^{N_j} \frac{\omega_j}{\kappa + k} \left(\tilde{y}_j + \frac{\tilde{x}_i(\kappa' + k)}{\alpha}\right)^{-(q+1)} T_{\nu, \lambda}^{(\kappa)}\left(\tilde{y}_j + \frac{\tilde{x}_i(\kappa' + k)}{\alpha}\right) T_{n, l}^{(k)}\left(\tilde{y}_j + \frac{\tilde{x}_i(\kappa' + k)}{\alpha}\right), \end{aligned} \quad (\text{B.43})$$

which can be further simplified to

$$\begin{aligned} \mathcal{R} = & \frac{1}{(\kappa' + k')(\kappa + k)} \sum_{i=1}^{N_i} \omega_i T_{\nu', \lambda'}^{(\kappa')}\left(\frac{\tilde{x}_i}{\gamma}\right) T_{n', l'}^{(k')}\left(\frac{\tilde{x}_i}{\gamma}\right) \\ & \times \sum_{j=1}^{N_j} \omega_j \frac{\tilde{x}_i^q}{(\tilde{x}_i + \gamma \tilde{y}_j)^{q+1}} T_{\nu, \lambda}^{(\kappa)}\left(\tilde{y}_j + \frac{\tilde{x}_i}{\gamma}\right) T_{n, l}^{(k)}\left(\tilde{y}_j + \frac{\tilde{x}_i}{\gamma}\right), \end{aligned} \quad (\text{B.44})$$

with  $\gamma = \alpha/(\kappa' + k')$ . To obtain numerically “exact” results the number of integration points for the outer and inner sum have to fulfill  $N_i > 1 + (\nu' + n' + \nu + n - 1)/2$  and  $N_j > 1 + (\nu + n - q - 1)/2$ , respectively.

# Appendix C

## Spectral properties of helium supplement

This appendix complements chapter 4. Further data for natural and unnatural parity states is presented.

### C.1 Natural parity

In this section, spectral data for  $^1P^o$ ,  $^3P^o$ ,  $^1D^e$  and  $^3D^e$  resonances of helium, computed with the method given in chapter 3, is presented together with available reference data. The results have been tested for convergence with respect to variation of basis size (including variation of the number of Sturmians as well as the number of angular configurations), dilation parameters and the complex rotation angle. Only converged digits are given in the tabulars. Note, that the effective matrix dimension for these calculations did not exceed  $p = 16000$ .

#### C.1.1 $^1P^o$ resonance data

$N = 2$							
This work			Rost <i>et al.</i> [52]		This work (continued)		
Re( $-E$ )	Im( $-E$ )	$\langle \cos(\theta_{12}) \rangle$	Re( $-E$ )	Im( $-E$ )	Re( $-E$ )	Im( $-E$ )	$\langle \cos(\theta_{12}) \rangle$
0.69313	0.00069	0.03312	0.693134920	0.000686625	0.504732103	0.000000035	-0.29033
0.597073801	0.000001922	-0.4168372	0.597073804	0.000001923	0.50426276	0.00000303	0.028056
0.5640830	0.0001501	0.015690	0.564085188	0.000150594	0.503950312	$< 0.6 \times 10^{-8}$	0.26241
0.54709214	$< 0.1 \times 10^{-7}$	0.13595	0.547092709	0.000000005	0.503930243	0.000000026	-0.29196
0.54649297	0.00000096	-0.21408	0.546493257	0.000001014	0.5035724	0.0000023	0.02812
0.5343622	0.0000639	0.022382	0.534363144	0.000064173	0.503331778	$< 0.4 \times 10^{-8}$	0.26395
0.52761598	$< 0.7 \times 10^{-7}$	0.19787	0.527616338	$0.7 \times 10^{-10}$	0.50331618	0.00000002	-0.29322
0.52729761	0.00000046	-0.24832	0.527297770	0.000000491	0.5030371	0.0000018	0.028165
0.5215042	0.0000327	0.025232	0.521504666	0.000032898	0.502847900	$< 0.3 \times 10^{-8}$	0.26514
0.51811805	$< 0.5 \times 10^{-7}$	0.22516	0.518118268	$0.17 \times 10^{-10}$	0.50283554	0.00000002	-0.29422
0.51793724	0.00000025	-0.26527	0.517937328	0.000000267	0.50261375	0.00000146	0.02820
0.5147337	0.0000189	0.026546	0.514733994	0.000018998	0.502462252	$< 0.3 \times 10^{-8}$	0.26609
0.51279090	$< 0.3 \times 10^{-7}$	0.23965	0.512791034	$0.47 \times 10^{-10}$	0.502452292	0.000000013	-0.29502
0.51267993	0.00000015	-0.2750	0.512679987	0.000000160	0.50227312	0.00000118	0.02822
0.51072663	0.00001188	0.027220	0.510726795	0.000011926	0.502149942	$< 0.2 \times 10^{-8}$	0.26686
0.50950837	$< 0.2 \times 10^{-7}$	0.24828	0.509508462	$0.4 \times 10^{-10}$			
0.50943582	0.00000010	-0.28113	0.509435853	0.000000107			
0.50815844	0.00000793	0.027596	0.50815854	0.00000796			
0.50734418	$< 0.2 \times 10^{-7}$	0.25386	0.507344240	$0.5 \times 10^{-10}$			
0.507294291	0.000000066	-0.28526	0.507294315	0.000000068			
0.50641378	0.00000556	0.027821	0.50641384	0.00000559			
0.50584264	$< 0.1 \times 10^{-7}$	0.25767	0.50584269				
0.505806932	0.000000047	-0.28819	0.50580696	0.00000010			
0.50517456	0.00000404	0.02796	0.505175	0.000004			
0.50475851	$< 0.1 \times 10^{-7}$	0.26039	0.5047590				

Table C.1:  $^1P^o$  resonances of helium below the  $N = 2$  threshold compared with data from [52].

$N = 3$							
Re( $-E$ )	This work		Rost <i>et al.</i> [52]		This work (continued)		
	Im( $-E$ )	$\langle \cos(\theta_{12}) \rangle$	Re( $-E$ )	Im( $-E$ )	Re( $-E$ )	Im( $-E$ )	$\langle \cos(\theta_{12}) \rangle$
0.335626	0.003514	-0.256	0.335625935	0.003511869	0.226805300	0.000000448	0.078617
0.285950742	0.000017047	-0.6042595	0.285950743	0.000017046	0.22667230	0.00000004	0.5159464
0.282826	0.000731	0.20914	0.282828970	0.000731040	0.2265819489	0.0000007056	-0.637170
0.271193	0.001449	-0.29668	0.271193403	0.001448131	0.2262389	0.0000428	-0.20828
0.26764400	0.00001134	-0.005868	0.267644001	0.00001134	0.226197614	0.000007270	0.2413
0.25743229	0.00001101	-0.618230	0.257432288	0.000011017	0.226038193	0.000000342	0.082158
0.2515776	0.0002601	0.3387	0.251578561	0.000260089	0.22593878	0.00000003	0.5144795
0.250773	0.000650	-0.3550	0.250773561	0.000650018	0.225970165	0.000000544	-0.637817
0.24822439	0.00000535	0.016591	0.248224394	0.000005362	0.22560564	0.00003309	-0.21017
0.24551751	0.00000006	0.495763	0.245517652	0.000000068	0.225572803	0.000005641	0.2440
0.244412373	0.000006559	-0.625120	0.244412373	0.000006559	0.225448946	0.000000267	0.08496
0.240949	0.000381	-0.237	0.240948845	0.000381019	0.22537262	0.00000002	0.513186
0.2408476	0.0001115	0.244	0.240848064	0.000111798	0.225319277	0.000000428	-0.638335
0.239292309	0.000002994	0.0356933	0.239292313	0.000002997	0.22511109	0.00002609	-0.2116
0.2380616	0.0000001	0.514718	0.238061744	0.000000106	0.225084606	0.000004467	0.2461
0.23743302	0.00000406	-0.629238	0.237433023	0.000004058	0.224986473	0.000000212	0.087227
0.235381	0.000246	-0.1892	0.235381267	0.000245901	0.22492654	0.00000002	0.5120633
0.23524268	0.00004793	0.2073	0.235242888	0.000048022	0.224884260	0.000000343	-0.638757
0.234331070	0.000001841	0.049910	0.234331075	0.000001844	0.22471751	0.00002093	-0.2128
0.2336632	0.0000001	0.519872	0.233663277	0.000000102	0.224695883	0.000003598	0.2477
0.233279233	0.000002642	-0.631966	0.233279233	0.000002642	0.224616816	0.000000171	0.08907
0.2319699	0.0001604	-0.1928	0.231969855	0.000160266	0.224568873	0.000000016	0.511095
0.23185540	0.00002812	0.2171	0.231855536	0.000028170	0.22453479	0.000000027	-0.639105
0.231269828	0.000001211	0.060391	0.231269832	0.000001213	0.22439919	0.00001705	-0.21377
0.2308645	0.0000001	0.520295	0.230864587	0.000000086	0.224381319	0.000002940	0.24899
0.2306146277	0.0000018016	-0.633885	0.230614628	0.000001801	0.22431668	0.00000014	0.09059
0.2297308	0.0001092	-0.1982	0.229730760	0.000109106	0.224277713	0.000000013	0.510259
0.22964226	0.00001858	0.2262	0.229642356	0.000018608	0.224249833	0.000000229	-0.639394
0.229242989	0.000000837	0.068191	0.229242993	0.000000839	0.22413809	0.00001407	-0.21455
0.22897741	0.00000005	0.5191381	0.228977474	0.000000069	0.224123176	0.000002434	0.25004
0.228806184	0.000001278	-0.63529	0.228806184	0.000001278	0.224069664	0.000000116	0.09185
0.2281826	0.0000774	-0.2025	0.22818257	0.00007734	0.224037546	0.000000011	0.509538
0.22811467	0.00001308	0.2329	0.228114738	0.000013098	0.224014450	0.000000191	-0.639639
0.227830074	0.000000603	0.074086	0.227830076	0.000000604	0.22392129	0.00001774	-0.21520
0.22764607	0.00000004	0.5175479	0.227646123	0.000000055	0.223908718	0.000002037	0.25090
0.2275237757	0.0000009364	-0.636351	0.22752358	0.00000008	0.223863917	0.000000097	0.09292
0.2270679	0.0000568	-0.2058	0.227068	0.000056	0.223837128	0.000000009	0.50891
0.22701533	0.00000960	0.2377	0.2270153	0.0000095			

Table C.2:  $^1P^0$  resonances of helium below the  $N = 3$  threshold compared with data from [52].

$N = 4$									
This work			Rost <i>et al.</i> [52]		This work (continued)			Rost <i>et al.</i> [52] (continued)	
Re( $-E$ )	Im( $-E$ )	$\langle \cos(\theta_{12}) \rangle$	Re( $-E$ )	Im( $-E$ )	Re( $-E$ )	Im( $-E$ )	$\langle \cos(\theta_{12}) \rangle$	Re( $-E$ )	Im( $-E$ )
0.194513	0.001787	-0.4126	0.194512131	0.001787174	0.1317505	0.0000296	0.41473	0.131750537	0.000029682
0.17880	0.00239	-0.0107	0.178798722	0.002386550	0.131648243	0.000001770	0.252544	0.131648243	0.000001780
0.1688609	0.0000230	-0.69745	0.168846093	0.000023060	0.131383964	0.000007480	-0.232036	0.131383962	0.000007481
0.161252	0.001084	-0.446179	0.161251205	0.0010839	0.13115996	0.00000003	0.627725	0.131139886	0.000000032
0.16068953	0.00005272	-0.21735	0.160689529	0.000052718	0.130919534	0.000002970	-0.724423	0.130919534	0.000002970
0.152734	0.001132	0.0954	0.152734009	0.001131881	0.1307456	0.0001448	0.0794	0.130745628	0.000144973
0.15183285	0.00001833	-0.7086555	0.151832846	0.000018339	0.1305225	0.0000408	-0.48297	0.130522475	0.000040842
0.150557	0.000391	0.17020	0.150557131	0.000390874	0.1304127	0.0000214	0.42384	0.130412715	0.000021493
0.14976399	0.00000756	0.15983	0.149763990	0.000007594	0.130335158	0.000001361	0.26286	0.130335158	0.000001368
0.148050	0.000603	-0.462478	0.148049432	0.000603197	0.130149303	0.000005518	-0.23176	0.130149302	0.000005519
0.14673378	0.00003534	-0.226807	0.146733780	0.000004243	0.12999768	0.00000003	0.628658	0.129997623	0.000000025
0.14299236	0.00001242	-0.71498	0.142992362	0.000012411	0.129823092	0.000002225	-0.7253167	0.12982309	0.00000223
0.142629	0.000702	0.0665	0.142629121	0.000703336	0.1296910	0.0001056	0.08042	0.129691063	0.000105707
0.1412526	0.0001175	0.3616	0.141252456	0.000117707	0.12954255	0.00002389	-0.48639	0.12954254	0.00002388
0.14096913	0.00000423	0.19160	0.140969138	0.000004243	0.12943804	0.00001604	0.42969	0.129438038	0.000016058
0.140850	0.000322	-0.47441	0.140850169	0.000332216	0.129378050	0.000001062	0.270668	0.129378050	0.000001068
0.13975447	0.00002279	-0.23005	0.139754471	0.000022789	0.129241901	0.000004179	-0.23133	0.129241900	0.000004178
0.13861396	0.00000038	0.5997586	0.138613869	0.000000412	0.12913433	0.00000003	0.628516	0.129134285	0.000000023
0.13784040	0.00000833	-0.718849	0.137840402	0.000008336	0.12900384	0.00000170	-0.725933	0.1290039	0.0000021
0.1374516	0.0004502	0.07150	0.137451388	0.000450529	0.1289020	0.0000789	0.0814	0.12890207	0.00007904
0.1365398	0.0000669	0.38888	0.136539778	0.000066974	0.12880339	0.00001322	-0.48948	0.1288034	0.0000131
0.1365291	0.0001911	-0.4717	0.136528961	0.000191047	0.12870543	0.00001229	0.4339	0.12870543	0.00001231
0.136349931	0.000003116	0.219126	0.136349933	0.000003129	0.12865819	0.00000084	0.27672	0.12865820	0.00000085
0.135701427	0.000015138	-0.23150	0.135701425	0.000015139	0.12855525	0.00000323	-0.23082		
0.13510236	0.00000012	0.616777	0.135102260	0.000000154	0.12847605	0.00000001	0.62788	0.12847602	0.00000001
0.134596793	0.000005737	-0.721400	0.134596793	0.000005757	0.12837608	0.00000133	-0.726315		
0.1342890	0.0002982	0.07551	0.134288843	0.000298427	0.1282963	0.0000603	0.08268		
0.1337467	0.0001137	-0.46675	0.133746663	0.000113664	0.12823243	0.00000663	-0.4928		
0.13366116	0.00004262	0.39658	0.133661140	0.000042682	0.12814064	0.00000963	0.43719		
0.133523368	0.000002337	0.238580	0.133523369	0.000002348	0.12810283	0.00000067	0.28149		
0.133126051	0.000010453	-0.232025	0.133126050	0.000010455	0.12802302	0.00000256	-0.2303		
0.13277430	0.00000005	0.624551	0.132774213	0.000000059	0.12796292	0.00000001	0.62705		
0.132432020	0.000004069	-0.7231672	0.132432020	0.000004069	0.12788470	0.00000106	-0.72647		
0.1322004	0.0002045	0.07794	0.132200330	0.000204658	0.1278213	0.0000469	0.0851		
0.1318592	0.0000682	-0.47798	0.131859129	0.000068171					

Table C.3:  $^1P^o$  resonances of helium below the  $N = 4$  threshold compared with data from [52].

$N = 5$									
Re( $-E$ )	This work		Rost <i>et al.</i> [52]		This work (continued)			Rost <i>et al.</i> [52] (continued)	
	Im( $-E$ )	$\langle \cos(\theta_{12}) \rangle$	Re( $-E$ )	Im( $-E$ )	Re( $-E$ )	Im( $-E$ )	$\langle \cos(\theta_{12}) \rangle$	Re( $-E$ )	Im( $-E$ )
0.11923	0.00163	-0.150	0.119233456	0.001628873	0.086107303	0.000009325	0.05887	0.086107301	0.000009328
0.1117436282	0.0000247544	-0.7542302	0.111743628	0.000024754	0.0859956	0.0001447	-0.5763	0.085995647	0.000144735
0.1090974	0.0009203	0.100	0.109097499	0.000920979	0.08578806	0.00001276	-0.37745	0.085788056	0.000012761
0.10747672	0.00005453	-0.348724	0.107476720	0.000054525	0.08557836	0.00000132	0.69933	0.085578293	0.000001323
0.107288	0.000780	-0.5404	0.107287651	0.000780776	0.08555043	0.00001181	-0.20500	0.085550431	0.000011814
0.1021502	0.0010520	-0.17796	0.102150534	0.001052069	0.0854279	0.0001073	0.25112	0.085427964	0.000107406
0.10193843	0.00006420	-0.022778	0.101938432	0.000064196	0.085325948	0.000004808	-0.7784013	0.085325948	0.000004808
0.10090954	0.00002258	-0.763013	0.100909544	0.000022579	0.08505907	0.00000737	0.35779	0.085059034	0.000007385
0.098616	0.000462	-0.55640	0.098616265	0.000462287	0.08496123	0.00003087	0.4621	0.084961197	0.000030868
0.09788768	0.00004570	-0.362504	0.097887683	0.000045698	0.084938509	0.000006755	0.05390	0.084938504	0.000006758
0.0965474	0.0004068	0.1370	0.096547358	0.000407284	0.0849190	0.0000920	-0.5820	0.084918985	0.000092098
0.0951890	0.0007001	-0.17703	0.095189318	0.000700204	0.08471871	0.00000974	-0.37034	0.084718712	0.000009738
0.09500886	0.00001402	0.257187	0.095008763	0.000014040	0.08466951	0.00001532	0.1889	0.084669506	0.000015324
0.09473690	0.00001682	-0.7686375	0.094736906	0.000016822	0.084576579	0.000000465	0.69596	0.084576520	0.000000470
0.09430037	0.00003938	-0.002098	0.094300364	0.000039374	0.0844637	0.0000796	0.2354	0.084463776	0.000079689
0.09368586	0.00013118	0.30495	0.093685604	0.000131190	0.08438984	0.00000367	-0.779431	0.084389840	0.000003674
0.0934465	0.0002279	-0.56917	0.093446374	0.000227996	0.084169175	0.000005764	0.3688	0.084169144	0.000005772
0.09262944	0.00003307	-0.369115	0.092629436	0.000033073	0.08410291	0.00002477	0.4872	0.084102891	0.000024771
0.0915235	0.0002678	0.20294	0.091523508	0.000268169	0.0840917	0.0000629	-0.5907	0.084091661	0.000062894
0.0911373	0.0004131	-0.17421	0.091137537	0.000413142	0.08407862	0.00000583	0.04880	0.084078611	0.000005837
0.09089135	0.00001208	-0.772190	0.090891352	0.000012084	0.0839668	0.0000568	-0.1633	0.083966869	0.000056842
0.09061107	0.00001549	0.029916	0.090610992	0.000015508	0.08391948	0.00000760	-0.38615	0.083919479	0.000007597
0.09025264	0.00002615	0.2234	0.090252625	0.000026141	0.083819810	0.000000317	0.70021	0.083819758	0.000000321
0.09023515	0.00005549	-0.57747	0.090235128	0.000055505	0.0837370	0.0000596	0.2254	0.083737043	0.000059688
0.09012742	0.00007250	0.41142	0.090127327	0.000072517	0.0836783	0.0000029	-0.78025	0.08367830	0.00000287
0.08939903	0.00002358	-0.372689	0.089399031	0.000023582	0.08349657	0.00000459	0.3768	0.083496539	0.000004592
0.088845297	0.000002916	0.67231	0.088845250	0.000002921	0.0834519	0.0000457	-0.592	0.083452	0.000046
0.0886327	0.0001910	0.2220	0.088632704	0.000191307	0.08344915	0.00002020	0.514	0.083449134	0.000020201
0.0885376	0.0002051	-0.14796	0.088537716	0.000205050	0.08342625	0.00000492	0.0484	0.08342624	0.00000492
0.0884920	0.0000646	-0.6075	0.088491985	0.000064588	0.083390	0.000082	0.1739	0.08338954	0.00008250
0.088348876	0.000008797	-0.776266	0.088348875	0.000008796	0.0833080	0.0000059	-0.38564	0.0833079	0.0000060
0.08800223	0.00001253	0.32419	0.088002165	0.000012546	0.083234920	0.000000220	0.70206	0.083234874	0.000000221
0.08776435	0.00001905	-0.0470	0.087764354	0.000019031	0.0831749	0.0000450	0.2194	0.08317501	0.00004498
0.0877516	0.0000482	0.5225	0.087751551	0.000048256	0.083125	0.000002	-0.7809		
0.0873003	0.0002184	-0.57180	0.087300171	0.000218446	0.082975	0.000004	0.383		
0.08726810	0.00001756	-0.37499	0.087268098	0.000017562	0.082948	0.000035	-0.5845		
0.086939118	0.000001705	0.68604	0.086939055	0.000001712	0.0829404	0.0000157	0.518		
0.08677016	0.00007996	-0.2093	0.086770197	0.000079981	0.082922	0.000089	-0.172		
0.0867486	0.0001487	0.2610	0.086748626	0.000148913	0.0829197	0.0000039	0.045		
0.08658970	0.00000642	-0.777115	0.086589702	0.000006417	0.082829	0.000005	-0.386		
0.086273970	0.000009607	0.34322	0.086273922	0.000009620	0.08277397	0.00000016	0.7029		
0.08612347	0.00003985	0.4397	0.086123429	0.000039851	0.082731	0.000034	0.216		

Table C.4:  $^1P^0$  resonances of helium below the  $N = 5$  threshold compared with data from [52].

$N = 6$				
This work			Rost <i>et al.</i> [52]	
$\text{Re}(-E)$	$\text{Im}(-E)$	$\langle \cos(\theta_{12}) \rangle$	$\text{Re}(-E)$	$\text{Im}(-E)$
0.07951576	0.00002469	-0.79276	0.079515759	0.000024694
0.07702045	0.00004964	-0.440972	0.077020444	0.000049639
0.0766486	0.0005931	-0.6060	0.076648564	0.000593082
0.0738922	0.0000742	-0.15114	0.073892177	0.000074210
0.073645	0.000829	-0.291	0.073645119	0.000829397
0.072693	0.000601	0.1695	0.072692534	0.000602213
0.072223314	0.000024771	-0.7996064	0.072223314	0.000024771
0.0707579	0.0003578	-0.62274	0.070757965	0.000357664
0.070308608	0.000047446	-0.45429	0.070308609	0.000047446
0.070200	0.000827	-0.034	0.070199995	0.000826531
0.06997533	0.00005176	0.089062	0.069975284	0.000051741
0.0686225	0.0005570	-0.30945	0.068622411	0.000556881
0.06806514	0.00006457	-0.15853	0.068065139	0.000064580
0.067779451	0.000019827	-0.804506	0.067779451	0.000019827
0.0670723	0.0001054	-0.63593	0.067072296	0.000105357
0.06635158	0.00003735	-0.46207389	0.066351579	0.000037352
0.0662321	0.0001617	0.18043	0.066231347	0.000161997
0.066203	0.000744	0.0213	0.066203931	0.000743663
0.0656576	0.0000416	0.17430	0.065657455	0.000041590
0.0655127	0.0002169	-0.31515	0.065512641	0.000216889
0.0652919	0.0000962	-0.63963	0.065291914	0.000096177
0.06517972	0.00000295	0.275631	0.065179472	0.000002907
0.06486117	0.00001500	-0.80831	0.064861167	0.000015003
0.0647505	0.0000490	-0.15967	0.064750545	0.000049026
0.0639415	0.0002572	-0.6342	0.063941556	0.000257144
0.06389763	0.00003639	0.35492	0.063897456	0.000036370
0.0637939	0.0000283	-0.46635	0.063793922	0.000028314
0.063773	0.000466	0.0320	0.063773028	0.000466195
0.0635871	0.0000058	-0.3310	0.063587132	0.000005808
0.0634749	0.0001095	0.3147	0.063474312	0.000109833
0.0631534	0.0000308	0.2280	0.063153276	0.000030859
0.0628518	0.0000112	-0.8106	0.062851836	0.000011216
0.0628342	0.0000041	0.2994	0.062833968	0.000004059
0.062633	0.000035	-0.157	0.062631764	0.000036535
0.06234	0.00017	-0.3	0.062334868	0.000174421
0.062332	0.000050	0.474	0.062332355	0.000050767
0.06233	0.00017	-0.6	0.062332268	0.000163381
0.06212	0.00018	-0.04	0.062199713	0.000185324
0.06205	0.00002	-0.47	0.062044175	0.000021189
0.06178	0.00011	0.36	0.061773868	0.000103957
0.0617345	0.0000076	0.735	0.061734162	0.000007671
0.06152	0.00002	0.26	0.061521397	0.000023124
0.061416	0.000009	-0.812	0.061416692	0.000008381
0.06130	$< 0.1 \times 10^{-4}$	0.3	0.061301429	0.000004726

Table C.5:  $^1P^o$  resonances of helium below the  $N = 6$  threshold compared with data from [52].

C.1.2  ${}^3P^0$  resonance data

$N = 2$					
Re( $-E$ )	Im( $-E$ )	$\langle \cos(\theta_{12}) \rangle$	Re( $-E$ )	Im( $-E$ )	$\langle \cos(\theta_{12}) \rangle$
0.7604922	0.0001492	-0.364874	0.504845316	$< 0.1 \times 10^{-8}$	0.4573377
0.5846722	0.0000411	-0.4143051	0.504622085	0.000000572	-0.4305061
0.57903096	0.00000094	-0.0208351	0.5044617392	0.0000000186	-0.0297116
0.54884429	$< 0.1 \times 10^{-7}$	0.3584342	0.5040162143	$< 0.6 \times 10^{-9}$	0.4585935
0.54283722	0.00001576	-0.4215271	0.503847045	0.000000435	-0.4308022
0.539558770	0.000000395	-0.023095	0.5037243968	0.0000000142	-0.0299718
0.52863838	$< 0.1 \times 10^{-7}$	0.4101493	0.5033829632	$< 0.5 \times 10^{-9}$	0.4595263
0.52571189	0.00000744	-0.424719	0.503251735	0.000000338	-0.4310369
0.523946635	0.000000204	-0.0250746	0.50315587161	0.00000001116	-0.0301797
0.518710071	$< 0.6 \times 10^{-8}$	0.4320504	0.5028884309	$< 0.4 \times 10^{-9}$	0.46023747
0.51710730	0.00000406	-0.4267008	0.502784604	0.000000267	-0.431226
0.516079739	0.000000118	-0.0265517	0.50270828176	0.00000000890	-0.0303482
0.513156015	$< 0.4 \times 10^{-8}$	0.4430261	0.5024948854	$< 0.3 \times 10^{-9}$	0.46079185
0.512191320	0.000002448	-0.42802822	0.502411338	0.000000216	-0.4313806
0.5115478001	0.0000000749	-0.02761331	0.50234959869	0.00000000721	-0.0304866
0.509747324	$< 0.1 \times 10^{-8}$	0.4492363	0.5021765989	$< 0.2 \times 10^{-9}$	0.46123215
0.509123886	0.000001587	-0.42895608	0.502108378	0.000000176	-0.4315084
0.5086964426	0.0000000492	-0.02838248	0.50205773884	0.00000000592	-0.0306016
0.507508411	$< 0.2 \times 10^{-8}$	0.4530691	0.5019155415	$< 0.2 \times 10^{-9}$	0.46158757
0.507082993	0.000001086	-0.4296268	0.5018591186	0.0000001461	-0.431615
0.5067854543	0.0000000343	-0.0289510	0.50181707450	0.00000000492	-0.030698
0.505960107	$< 0.1 \times 10^{-8}$	0.45559221	0.5016987747	$< 0.2 \times 10^{-9}$	0.4618786
0.505657168	0.000000775	-0.4301258	0.50165158	0.00000012	-0.4317
0.5054420898	0.0000000249	-0.0293804	0.50161629	$< 0.1 \times 10^{-7}$	-0.0307

Table C.6:  ${}^3P^0$  resonances of helium below the  $N = 2$  threshold.

$N = 3$					
$\text{Re}(-E)$	$\text{Im}(-E)$	$\langle \cos(\theta_{12}) \rangle$	$\text{Re}(-E)$	$\text{Im}(-E)$	$\langle \cos(\theta_{12}) \rangle$
0.3503776	0.0014933	-0.56382	0.22660203	0.00000682	0.019298
0.3093797	0.0005587	0.006019	0.22650567	0.00001459	-0.62254
0.27947758	0.00068721	-0.598199	0.226471625	0.000000243	0.289548
0.27881704	0.00003128	-0.308891	0.226342232	0.000001099	-0.334872
0.2602338	0.0001549	-0.00222	0.226014549	0.000000011	0.6392148
0.25852486	0.00000267	0.247147	0.225884160	0.000005219	0.01928
0.2551621	0.0003232	-0.61152	0.225812304	0.000011150	-0.622881
0.25355291	0.00001673	-0.317379	0.225783377	0.000000188	0.29051
0.24605967	0.00000015	0.5278342	0.225684742	0.000000853	-0.335612
0.24523493	0.00007765	0.01020	0.225432506	0.000000009	0.6414684
0.24403669	0.00000178	0.2655788	0.225329398	0.000004083	0.019228
0.2433744	0.0001671	-0.61677	0.22527434	0.00000871	-0.623150
0.242190147	0.000009820	-0.322772	0.225249950	0.000000149	0.29124
0.23851299	0.00000010	0.5755645	0.225172994	0.000000674	-0.336212
0.23775720	0.00004426	0.01524	0.224974640	0.000000007	0.6431773
0.237013541	0.000001258	0.2756880	0.224891808	0.000003254	0.01916
0.2368766	0.0000956	-0.61955	0.22484865	0.00000694	-0.62337
0.236070361	0.000006093	-0.326527	0.224828101	0.000000120	0.291818
0.23399144	0.00000006	0.6013444	0.224766879	0.000000542	-0.33670
0.23343211	0.00002749	0.01755	0.224608047	0.000000006	0.644502
0.232947683	0.000000979	0.284331	0.22454056	0.00000263	0.01909
0.23294750	0.00005916	-0.62381	0.22450609	0.00000561	-0.62354
0.232392355	0.000003996	-0.329239	0.224488716	0.000000098	0.29228
0.231100332	0.000000045	0.616369	0.224439197	0.000000442	-0.33711
0.23069633	0.00001820	0.01860	0.224310021	0.000000005	0.645548
0.23040124	0.00003912	-0.621478	0.22425435	0.00000216	0.01902
0.230365457	0.000000636	0.284693	0.22422636	0.00000461	-0.62369
0.230008407	0.000002747	-0.331249	0.224211604	0.000000081	0.29264
0.229149422	0.000000030	0.625734	0.2241709736	0.0000003655	-0.337457
0.22885408	0.00001265	0.01906	0.2240644906	0.0000000039	0.6463881
0.22866084	0.00002715	-0.62160	0.224018053	0.000001797	0.01896
0.228618954	0.000000439	0.28656	0.22399501	0.00000383	-0.62381
0.228374868	0.000001963	-0.3327711	0.223982399	0.000000067	0.292947
0.227774243	0.000000022	0.631906	0.223948645	0.000000305	-0.337748
0.22755393	0.00000914	0.019249	0.223859825	0.000000003	0.64707
0.22742031	0.00001959	-0.622105	0.22382070	0.00000151	0.0189
0.227381223	0.000000321	0.288269	0.2238015	0.0000032	-0.6239
0.227206612	0.000001449	-0.333947	0.22379066	0.00000006	0.2932
0.226769865	0.000000015	0.6361645	0.2237623	0.0000003	-0.3380

Table C.7:  ${}^3P^o$  resonances of helium below the  $N = 3$  threshold.

$N = 4$					
$\text{Re}(-E)$	$\text{Im}(-E)$	$\langle \cos(\theta_{12}) \rangle$	$\text{Re}(-E)$	$\text{Im}(-E)$	$\langle \cos(\theta_{12}) \rangle$
0.200074	0.001053	-0.66904	0.13130270	0.00000043	0.699072
0.185808	0.002536	-0.182	0.1312088	0.0001216	-0.14303
0.16547992	0.00003763	-0.4536933	0.13113207	0.00002566	0.1658
0.165140	0.000641	-0.69469	0.130991256	0.000005420	0.32816
0.1637087	0.0006819	0.14085	0.13094042	0.00000851	-0.727136
0.15623631	0.00004875	-0.02421	0.130867727	0.000004061	0.099266
0.155802	0.001212	-0.2205	0.13057116	0.00000451	-0.4854685
0.1504764	0.0003413	-0.705066	0.13010942	0.00000025	0.711219
0.14963682	0.00002794	-0.468364	0.1300375	0.0000833	-0.1469
0.1456517	0.0002015	0.2001	0.12996907	0.00001894	0.1720
0.14482654	0.00002002	0.31333	0.129920094	0.000000615	-0.730545
0.144774	0.000688	-0.23939	0.12986240	0.00000406	0.336935
0.14408438	0.00002166	0.03979	0.1297701012	0.0000030973	0.09519
0.142391	0.000182	-0.7127	0.12956004	0.00000341	-0.4860617
0.14156513	0.00001861	-0.475113	0.12922266	0.00000016	0.719743
0.1389621	0.0000723	0.218	0.12921417	0.00001658	-0.6773
0.1388839	0.0000415	0.592	0.1291618	0.0000587	-0.2012
0.1388340	0.0004182	-0.2243	0.12910813	0.00001458	0.1719
0.13843238	0.00001324	0.301567	0.129025959	0.000003109	0.34381
0.13809982	0.00001045	0.12171	0.128955334	0.000002407	0.09210
0.13754955	0.00009944	-0.71752	0.128800852	0.000002679	-0.485743
0.136885292	0.000012474	-0.479364	0.1286768	0.0000445	-0.71372
0.13533969	0.00000316	0.63989	0.12854667	0.00000011	0.72502
0.13521083	0.00027206	-0.1592	0.1285024	0.0000452	-0.1755
0.1351531	0.0000571	0.1832	0.12845375	0.00001156	0.1843
0.134870976	0.000010224	0.302571	0.128388673	0.000002429	0.34907
0.134631945	0.000007432	0.112095	0.12833350	0.00000190	0.08971
0.13445890	0.00005400	-0.721044	0.12821632	0.00000230	-0.4858
0.13393536	0.00000861	-0.482227	0.1282028	0.0000439	-0.7213
0.13295781	0.00000091	0.67929	0.12802005	0.00000009	0.729193
0.1328409	0.0001799	-0.1430	0.1279865	0.0000338	-0.1750
0.13276163	0.00003667	0.1638	0.12794417	0.00000933	0.1921
0.132568314	0.000007397	0.3164629	0.127891829	0.000001932	0.35319
0.132398583	0.000005433	0.104631	0.127847944	0.000001529	0.087832
0.13238424	0.00002651	-0.7239308	0.1277797	0.0000322	-0.7187
0.13195887	0.00000614	-0.48419	0.12775670	0.00000178	-0.4918

Table C.8:  ${}^3P^0$  resonances of helium below the  $N = 4$  threshold.

$N = 5$					
$\text{Re}(-E)$	$\text{Im}(-E)$	$\langle \cos(\theta_{12}) \rangle$	$\text{Re}(-E)$	$\text{Im}(-E)$	$\langle \cos(\theta_{12}) \rangle$
0.114347	0.001893	-0.009	0.0860681	0.0002142	0.02834
0.10991437	0.00003711	-0.5487163	0.085745706	0.000005394	0.552862
0.1093937	0.0005220	-0.75032	0.0856563	0.0000420	0.28394
0.10513161	0.00006776	-0.18436	0.08563002	0.00000728	0.47628
0.1045332	0.0010647	-0.34793	0.085442437	0.000003572	0.3980
0.1004820	0.0007824	0.1973	0.085401674	0.000013136	-0.14006
0.1000581	0.0002952	-0.761127	0.0852602	0.0001747	-0.36538
0.099578431	0.000032864	-0.561246	0.08523739	0.00004854	-0.79214
0.098966684	0.000035512	0.13474	0.08504548	0.00000700	-0.582253
0.098843	0.000880	-0.0266	0.0849593	0.0001220	0.02837
0.0967715	0.0006694	-0.36349	0.084695336	0.000003001	0.640875
0.096324167	0.000054469	-0.192245	0.08461491	0.00003310	0.3167
0.0944352	0.0001396	-0.76901	0.08460527	0.00000567	0.4088
0.093791812	0.000024190	-0.5685010	0.084458394	0.000003029	0.3841
0.0932137	0.0007772	0.04065	0.0844413	0.0001723	-0.3750
0.09275719	0.00002680	0.19443	0.08442611	0.00000991	-0.1384
0.0925968	0.0001738	0.2347	0.0843301	0.0000337	-0.7851
0.0922099	0.0003538	-0.37549	0.08417250	0.00000535	-0.58339
0.09186876	0.00000126	0.409470	0.0841285	0.0000621	0.02127
0.09157690	0.00003836	-0.191066	0.083909992	0.000001818	0.68944
0.091043816	0.000010939	-0.7753067	0.08384044	0.00002764	0.3446
0.09021419	0.00001735	-0.572512	0.08383403	0.00000416	0.3737
0.0897984	0.0005477	0.04186	0.0837606	0.0001306	-0.3767
0.0896707	0.0001323	-0.76961	0.08371975	0.00000252	0.374
0.08935433	0.00001621	0.29294	0.08369412	0.00000757	-0.136
0.08931317	0.00014899	-0.36064	0.0836365	0.0000242	-0.7840
0.08922198	0.00009377	0.24407	0.0835070	0.0000042	-0.5844
0.088990798	0.000001976	0.560563	0.0834928	0.0000266	0.0108
0.088725745	0.000003952	0.473744	0.0833060	0.0000012	0.717
0.088666730	0.000024899	-0.158722	0.0832472	0.00002376	0.3644
0.0880458	0.0001257	-0.773088	0.0832408	0.0000034	0.3585
0.08785465	0.00001262	-0.576722	0.083206	0.000096	-0.37670
0.0876004	0.0003527	0.04514	0.0831510	0.0000021	0.367
0.087452676	0.000011922	-0.38722	0.0831305	0.0000059	-0.134
0.08720727	0.00000966	0.42006	0.083095	0.000018	-0.784
0.087106	0.000060	0.2774	0.082996	0.000008	0.001
0.087026825	0.000005476	0.54106	0.0829882	0.0000033	-0.585
0.086794744	0.000004014	0.42179	0.0828312	0.0000009	0.7352
0.086743689	0.000017695	-0.14620	0.082782	0.000021	0.379
0.0864399	0.0000697	-0.7785	0.0827750	0.0000029	0.351
0.08624638	0.00006659	-0.36828	0.08275	0.00007	-0.377
0.08622062	0.00000991	-0.58355			

Table C.9:  ${}^3P^o$  resonances of helium below the  $N = 5$  threshold.

$N = 6$					
$\text{Re}(-E)$	$\text{Im}(-E)$	$\langle \cos(\theta_{12}) \rangle$	$\text{Re}(-E)$	$\text{Im}(-E)$	$\langle \cos(\theta_{12}) \rangle$
0.07841777	0.00003500	-0.61464	0.0645515	0.0001567	-0.80794
0.0779064	0.0000426	-0.7886	0.06442655	0.00002262	0.25763
0.07663	0.00085	0.08	0.06437313	0.00002168	-0.62457
0.0756571	0.0000628	-0.29414	0.06434955	0.00002887	-0.48719
0.075103	0.000782	-0.4364	0.06396010	0.00004310	-0.0130
0.0722062	0.0000753	-0.0300	0.0639209	0.0001353	0.3233
0.071862	0.000896	-0.147	0.06340250	0.00000017	0.49922
0.0716673	0.0002457	-0.798593	0.0632613	0.0000341	-0.3144
0.07136541	0.00003456	-0.625088	0.063109	0.000328	-0.466
0.0696575	0.0004968	-0.45359	0.0627852	0.0003114	0.1673
0.06930412	0.00005804	-0.3060	0.062780	0.000060	-0.1746
0.068486	0.000528	0.1312	0.0627228	0.0000865	-0.8124
0.0679586	0.0000526	0.18066	0.062479	0.000015	-0.6418
0.06774595	0.00006287	-0.8066239	0.0623589	0.0000176	0.30898
0.067374	0.000637	-0.1569	0.06208	0.00003	0.023
0.0671311608	0.0000274852	-0.6320185	0.0620507	0.0000883	0.355
0.06711413	0.00036332	0.22511	0.06183	0.00025	-0.47
0.0669161	0.0000574	-0.016435	0.061680	0.000001	0.606
0.0662603	0.0001647	-0.4410	0.06158	0.00004	-0.2
0.06617487	0.00011827	-0.8310	0.06139	0.00020	0.16
0.06562381	0.00004524	-0.311970	0.061352	0.000050	-0.813
0.0648583	0.0004040	0.1527	0.06112	0.00002	-0.64
0.0646205	0.0003173	-0.15621	0.06097	0.00002	0.35

Table C.10:  $^3P^o$  resonances of helium below the  $N = 6$  threshold.C.1.3  $^1D^e$  resonance data

$N = 2$					
$\text{Re}(-E)$	$\text{Im}(-E)$	$\langle \cos(\theta_{12}) \rangle$	$\text{Re}(-E)$	$\text{Im}(-E)$	$\langle \cos(\theta_{12}) \rangle$
0.70193	0.00118	-0.23441	0.5043784	0.0000051	-0.40037
0.569216	0.000277	-0.33449	0.504141722	0.000000332	0.13605
0.5564290	0.0000097	0.0526063	0.504038246	$< 0.2 \times 10^{-8}$	0.263273
0.5367246	0.0001157	-0.363283	0.5036612	0.0000039	-0.40141
0.5315119	0.0000054	0.091932	0.50347949	0.00000026	0.13711
0.52929296	$< 0.1 \times 10^{-7}$	0.2485407	0.503399784	$< 0.2 \times 10^{-8}$	0.263494
0.5227417	0.0000580	-0.377664	0.50310683	0.00000303	-0.4022
0.52011736	0.00000310	0.110313	0.502964278	0.000000203	0.13793
0.51900127	$< 0.1 \times 10^{-7}$	0.25577263	0.502901572	$< 0.2 \times 10^{-8}$	0.263659
0.5154540	0.0000329	-0.385990	0.5026694	0.0000024	-0.4029
0.51395263	0.00000189	0.12027	0.50255557	0.00000016	0.13859
0.51331135	$< 0.1 \times 10^{-7}$	0.2590787	0.502505352	$< 0.1 \times 10^{-8}$	0.26378
0.5111802	0.0000204	-0.391239	0.50231830	0.00000195	-0.4034
0.51024285	0.00000122	0.12625	0.502225911	0.000000133	0.1391
0.509840312	$< 0.7 \times 10^{-8}$	0.260838	0.5021850734	$< 0.7 \times 10^{-9}$	0.263882
0.5084616	0.0000135	-0.394756	0.50203214	0.00000160	-0.40384
0.50783793	0.00000084	0.130120	0.501956158	0.000000110	0.1395
0.507568669	$< 0.5 \times 10^{-8}$	0.261873	0.5019225013	$< 0.7 \times 10^{-9}$	0.263960
0.50662613	0.00000939	-0.397225	0.50179588	0.00000133	-0.4042
0.5061904	0.0000006	0.132766	0.501732629	0.000000092	0.13990
0.506001475	$< 0.5 \times 10^{-8}$	0.262528	0.5017045619	$< 0.5 \times 10^{-9}$	0.264023
0.5053289	0.0000068	-0.39902	0.50159854	0.00000112	-0.4045
0.50501272	0.00000044	0.13465	0.50154533	0.00000008	0.1402
0.504874989	$< 0.3 \times 10^{-8}$	0.262967	0.50152168	$< 0.1 \times 10^{-7}$	0.2641

Table C.11:  $^1D^e$  resonances of helium below the  $N = 2$  threshold.

$N = 3$					
$\text{Re}(-E)$	$\text{Im}(-E)$	$\langle \cos(\theta_{12}) \rangle$	$\text{Re}(-E)$	$\text{Im}(-E)$	$\langle \cos(\theta_{12}) \rangle$
0.343173	0.002581	-0.4939	0.2264039	0.0000254	-0.587617
0.315532	0.002147	-0.0492	0.2263718	0.0000085	0.04967
0.290091	0.000628	0.06174	0.226239914	0.000001050	-0.26288
0.275865	0.001132	-0.5473	0.22616746	0.00000053	0.48897
0.27471041	0.00001328	-0.2357	0.226096237	0.000000014	0.30910
0.2623501	0.0007371	-0.04123	0.22594909	0.00002477	-0.006512
0.254625	0.000166	0.054376	0.2257338	0.0000195	-0.58835
0.253338	0.000539	-0.56491	0.2257077	0.0000065	0.04915
0.251656539	0.000010017	-0.25085	0.225605629	0.000000824	-0.263123
0.2496374	0.0000034	0.24937	0.225550254	0.000000425	0.49327
0.2462602	0.0003760	-0.025962	0.225494994	0.000000012	0.30798
0.242556	0.000086	0.05591	0.22538010	0.00001934	-0.006123
0.2423690	0.0002825	-0.57446	0.2252126	0.0000153	-0.58895
0.241175647	0.000007165	-0.25635	0.22519113	0.00000514	0.04874
0.2402470	0.0000030	0.36134	0.225110575	0.000000657	-0.2633
0.23956077	0.00000002	0.34225	0.225067278	0.000000341	0.49655
0.2383285	0.0002140	-0.017738	0.225023546	0.000000011	0.30712
0.236274	0.000163	-0.58264	0.224932149	0.000015391	-0.00583
0.236257	0.000051	0.05836	0.22479921	0.00001217	-0.58944
0.23546832	0.00000494	-0.25906	0.2247815	0.0000041	0.04840
0.2349659	0.0000023	0.41529	0.224716772	0.000000533	-0.26345
0.23455766	0.00000003	0.32799	0.224682263	0.000000277	0.49910
0.2337822	0.0001324	-0.013208	0.224647064	0.000000009	0.306444
0.2325610	0.0001015	-0.58368	0.22457318	0.00001244	-0.005610
0.2325054	0.0000325	0.05509	0.22446589	0.00000986	-0.58986
0.23200708	0.00000345	-0.26058	0.2244511	0.0000034	0.04812
0.23170416	0.00000165	0.44510	0.22439837	0.00000044	-0.26357
0.23144134	0.00000003	0.32029	0.224370410	0.000000229	0.50112
0.23092612	0.00008732	-0.010545	0.224341662	0.000000007	0.30590
0.2301396	0.0000674	-0.58452	0.224281108	0.000010204	-0.005436
0.2300837	0.0000218	0.05263	0.22419325	0.00000810	-0.5902
0.229747419	0.000002466	-0.26152	0.22418084	0.00000276	0.04788
0.22955034	0.00000121	0.46323	0.224137270	0.000000363	-0.26367
0.22937122	0.00000002	0.3157	0.224114296	0.000000191	0.50275
0.22901293	0.00006050	-0.008883	0.224090514	0.000000006	0.30545
0.2284760	0.0000470	-0.58567	0.224040268	0.000008470	-0.005298
0.2284280	0.0000154	0.05126	0.22396741	0.00000674	-0.59050
0.22819008	0.00000181	-0.26214	0.22395690	0.00000231	0.04768
0.22805445	0.00000091	0.47504	0.22392050	0.00000030	-0.263753
0.22792693	0.00000002	0.31267	0.223901389	0.000000160	0.5041
0.22766827	0.00004360	-0.007791	0.223881492	0.000000005	0.30508
0.2272851	0.0000340	-0.586729	0.22383934	0.00000711	-0.00518
0.2272456	0.0000113	0.050342	0.2237783	0.00000056	-0.5908
0.227071076	0.000001364	-0.26257	0.2237693	0.0000020	0.048
0.22697361	0.00000069	0.48315	0.2237385	0.0000003	-0.264
0.226879652	0.000000017	0.31060	0.2237225	0.0000001	0.505
0.22668705	0.00003244	-0.007042			

Table C.12:  $^1D^e$  resonances of helium below the  $N = 3$  threshold.

$N = 4$					
Re( $-E$ )	Im( $-E$ )	$\langle \cos(\theta_{12}) \rangle$	Re( $-E$ )	Im( $-E$ )	$\langle \cos(\theta_{12}) \rangle$
0.198231	0.001395	-0.62616	0.1325974	0.0002032	-0.18585
0.187333	0.002245	-0.20426	0.1322506	0.0000204	0.2940
0.182784	0.002725	-0.1415	0.1322465	0.0000398	-0.6995
0.167612	0.001791	0.07529	0.13217276	0.00001358	-0.00778
0.164203375	0.000044749	-0.41084	0.131819823	0.000006923	-0.41707
0.163944	0.000850	-0.66391	0.131803657	0.000001457	0.58224
0.156706	0.001203	-0.22666	0.131625024	0.000000110	0.372770
0.1557091	0.0003587	0.15813	0.1313623	0.0001397	0.198
0.154193	0.001308	-0.18950	0.13129160	0.00008820	-0.2196
0.15382088	0.00001715	0.03265	0.1310359	0.0001382	-0.18696
0.1497709	0.0004598	-0.67349	0.13082721	0.00001733	-0.70032
0.14889002	0.00003138	-0.435427	0.1307707	0.0000149	0.2955
0.146956	0.000620	0.1568	0.13070926	0.00000947	-0.00549
0.145287	0.000678	-0.24892	0.130470234	0.000004861	-0.3606
0.143902	0.000795	-0.18132	0.130463699	0.000001438	0.5434
0.1431727	0.0000948	0.27257	0.130330340	0.000000101	0.370386
0.1430536	0.0000378	-0.0356	0.1301404	0.0001033	0.1738
0.141960	0.000247	-0.682447	0.13009377	0.00005924	-0.190
0.14110958	0.00002091	-0.445305	0.1299097	0.0000967	-0.18723
0.140755520	0.000001401	0.36413	0.12980324	0.00000378	-0.704630
0.139685	0.000390	0.2049	0.1297032	0.0000112	0.2983
0.1391260	0.0003901	-0.2645	0.12965450	0.00000688	-0.00320
0.1382812	0.0004887	-0.18266	0.12948479	0.00000311	-0.239
0.1376726	0.0000434	0.2743	0.1294820664	0.0000017309	0.4340
0.1375548	0.0000326	-0.0142	0.129380810	0.000000088	0.369227
0.1372724	0.0001362	-0.688605	0.1292400	0.0000774	0.1626
0.136592115	0.000014107	-0.448594	0.1292077	0.0000418	-0.1754
0.136481737	0.000001676	0.528905	0.1290706	0.0000683	-0.17858
0.136162775	0.000000095	0.394402	0.12905231	0.00000215	-0.71756
0.135633	0.000267	0.2373	0.12890741	0.00000867	0.29999
0.13539671	0.00022973	-0.2781	0.12886835	0.00000516	-0.00105
0.1348515	0.0003094	-0.18439	0.128743885	0.000001608	0.525
0.1343915	0.0000287	0.2843	0.12874170	0.00000220	-0.321
0.1342933	0.0000205	-0.0099	0.128663897	0.000000076	0.368617
0.1342702	0.0000756	-0.69332	0.1285569	0.0000588	0.1599
0.133737436	0.000009780	-0.44254	0.12853403	0.00003076	-0.1701
0.133696493	0.000001607	0.578572	0.1284928	0.0000154	-0.6798
0.133454834	0.000000114	0.378325	0.1284265	0.0000510	-0.2201
0.1330835	0.0001911	0.23186	0.12829800	0.00000683	0.3011
0.1329646	0.0001390	-0.26103			

Table C.13:  $^1D^e$  resonances of helium below the  $N = 4$  threshold.

$N = 5$					
$\text{Re}(-E)$	$\text{Im}(-E)$	$\langle \cos(\theta_{12}) \rangle$	$\text{Re}(-E)$	$\text{Im}(-E)$	$\langle \cos(\theta_{12}) \rangle$
0.1149119	0.0014100	-0.02250	0.0868242	0.0000091	0.238
0.112375	0.001508	0.0158	0.086639	0.000033	0.3297
0.10939910	0.00004188	-0.520825	0.0865991	0.0000200	-0.1726
0.1088995	0.0006245	-0.72931	0.0863531	0.0000919	-0.7544
0.1048460	0.0009461	-0.35228	0.0863382	0.0000824	-0.3848
0.10427751	0.00007048	-0.153887	0.086242	0.000003	0.6682
0.10311	0.00115	0.139	0.086168	0.000139	0.054
0.099738	0.000358	-0.73951	0.08614012	0.00001090	-0.54929
0.0994207	0.0007914	-0.0266	0.086069	0.000001	0.4535
0.099233943	0.000036576	-0.539055	0.0860579	0.0000302	-0.3699
0.099233943	0.000036576	-0.539055	0.085920	0.000123	0.272
0.098168	0.000832	0.0071	0.0858540	0.0001849	0.002
0.098168	0.000832	0.0071	0.08545058	0.00000750	0.257
0.0975072	0.0000097	0.12322	0.0853609	0.0001800	-0.3874
0.096976	0.000588	-0.37046	0.085330	0.000023	0.3305
0.096363	0.000683	-0.34077	0.08529724	0.00001574	-0.1680
0.096343	0.000198	0.249	0.0851756	0.0000595	-0.759773
0.09581349	0.00005360	-0.16713	0.0851061	0.0001351	-0.3538
0.0942259	0.0001704	-0.748328	0.085070	0.000003	0.69267
0.0942259	0.0001704	-0.748328	0.085025	0.000078	0.038
0.093793	0.000502	0.172	0.084983069	0.000008117	-0.56977
0.093560995	0.000026753	-0.548027	0.0849286	0.0000001	0.45446
0.093256	0.000422	0.071	0.084821	0.000094	0.31
0.0925918	0.0006047	0.0093	0.084800	0.000121	-0.001
0.0923370	0.0003064	-0.38030	0.0845130	0.0001542	-0.390208
0.0919446	0.0003728	-0.34826	0.08445866	0.00000615	0.2707
0.0919248	0.0000120	0.1823	0.084377	0.000017	0.332
0.091364	0.000081	0.31182	0.08434841	0.00001199	-0.1688
0.0912561	0.0000380	-0.1735	0.0843216	0.0001655	-0.3493
0.09087340	0.00001889	-0.755368	0.0842836	0.0000428	-0.77032
0.090091	0.000368	0.1056	0.0841949	0.0000022	0.70810
0.090055471	0.000019209	-0.55203	0.084178	0.000038	0.015
0.090049	0.000006	0.4514	0.08412477	0.00000610	-0.56985
0.089705	0.000246	0.1887	0.0840814	0.0000001	0.4562
0.0894046	0.0001360	-0.7462	0.084006	0.000086	0.21
0.0893941	0.0001191	-0.3890	0.084005	0.000064	0.14
0.089391	0.000423	0.0110	0.0838058	0.0001106	-0.39233
0.0891182	0.0001651	-0.3649	0.08371714	0.00000506	0.2817
0.0888178	0.0000107	0.2147	0.0836794	0.0001397	-0.3541
0.088511	0.000050	0.326	0.083660	0.000012	0.333
0.0884566	0.0000272	-0.1764	0.0836347	0.0000092	-0.16974
0.0879054	0.0001619	-0.75392	0.0836004	0.0000308	-0.7677
0.087852	0.000004	0.6258	0.0835338	0.0000141	-0.002
0.087768	0.000235	0.0872	0.0835260	0.0000020	0.7199
0.087741750	0.000014214	-0.557577	0.08346964	0.00000476	-0.5707
0.0876566	0.0000001	0.4578	0.0834350	0.0000002	0.458
0.08752437	0.00000722	-0.399556	0.0833910	0.0000390	0.05
0.087454	0.000168	0.239	0.083382	0.000067	0.32
0.087308	0.000282	0.017	0.0832366	0.0000799	-0.3932
0.08727169	0.00002587	-0.36936	0.083150	0.000106	-0.357

Table C.14:  $^1D^e$  resonances of helium below the  $N = 5$  threshold.

C.1.4  ${}^3D^e$  resonance data

$N = 2$					
Re( $-E$ )	Im( $-E$ )	$\langle \cos(\theta_{12}) \rangle$	Re( $-E$ )	Im( $-E$ )	$\langle \cos(\theta_{12}) \rangle$
0.583784235	$< 0.6 \times 10^{-8}$	-0.29371700	0.504878014	$< 0.1 \times 10^{-8}$	0.3210616
0.56068624	0.00000371	0.01970972	0.5045542797	$< 0.2 \times 10^{-9}$	-0.3664303
0.541678994	$< 0.4 \times 10^{-8}$	-0.3296968	0.504236710	0.000000100	0.0429082
0.53346309	0.00000189	0.03657626	0.5040405715	$< 0.7 \times 10^{-9}$	0.3225828
0.529312233	$< 0.6 \times 10^{-8}$	0.27281196	0.5037951085	$< 0.1 \times 10^{-9}$	-0.3673325
0.525018616	$< 0.3 \times 10^{-8}$	-0.3450135	0.503552583	0.000000077	0.0428792
0.521131108	0.000001022	0.0408525	0.5034016067	$< 0.5 \times 10^{-9}$	0.3237324
0.519016815	$< 0.5 \times 10^{-8}$	0.2937825	0.5032111026	$< 0.1 \times 10^{-9}$	-0.3680360
0.516688517	$< 0.2 \times 10^{-8}$	-0.3532344	0.503021708	0.000000061	0.0428487
0.514540919	0.000000604	0.0422198	0.5029030252	$< 0.4 \times 10^{-9}$	0.3246220
0.513322284	$< 0.4 \times 10^{-8}$	0.305055	0.50275223380	$< 0.9 \times 10^{-10}$	-0.3685951
0.5119245284	$< 0.8 \times 10^{-9}$	-0.3581963	0.502601511	0.000000048	0.0428192
0.510613226	0.000000384	0.0427071	0.5025065283	$< 0.3 \times 10^{-9}$	0.3253245
0.509847973	$< 0.3 \times 10^{-8}$	0.3117649	0.50238514134	$< 0.8 \times 10^{-10}$	-0.3690468
0.5089450531	$< 0.5 \times 10^{-9}$	-0.3614279	0.502263235	0.000000039	0.0427919
0.508085781	0.000000259	0.0428806	0.5021860385	$< 0.3 \times 10^{-9}$	0.3258887
0.507574151	$< 0.2 \times 10^{-8}$	0.3160692	0.50208688517	$< 0.8 \times 10^{-10}$	-0.3694169
0.5069578476	$< 0.4 \times 10^{-9}$	-0.3636513	0.501986891	0.000000032	0.0427670
0.506364305	0.000000182	0.0429305	0.5019233024	$< 0.2 \times 10^{-9}$	0.3263488
0.506005498	$< 0.2 \times 10^{-8}$	0.3189903	0.50184127013	$< 0.5 \times 10^{-10}$	-0.3697239
0.5055664091	$< 0.3 \times 10^{-9}$	-0.3652467	0.5017582346	0.0000000270	0.042745
0.505139297	0.000000133	0.0429297	0.5017052339	$< 0.2 \times 10^{-9}$	0.326729

Table C.15:  ${}^3D^e$  resonances of helium below the  $N = 2$  threshold.

$N = 3$					
Re( $-E$ )	Im( $-E$ )	$\langle \cos(\theta_{12}) \rangle$	Re( $-E$ )	Im( $-E$ )	$\langle \cos(\theta_{12}) \rangle$
0.3253309	0.0003620	-0.168459	0.226605766	0.000000044	0.0363283
0.2830465	0.0000244	-0.5395038	0.2264960502	0.0000009619	-0.600851
0.26976025	0.00001867	-0.0622195	0.22626003	0.00000055	0.378844
0.2673176	0.0001228	-0.211858	0.22612669	0.00000404	-0.275838
0.2616026	0.0000008	0.048003	0.226108952	0.000000011	0.459192
0.255929717	0.000015247	-0.5656638	0.226081036	0.000000228	-0.006720
0.2508406	0.0000047	0.248321	0.225886171	0.000000034	0.0358771
0.24913455	0.00003321	-0.14514	0.225803941	0.000000743	-0.602033
0.2488169	0.0000387	-0.12713	0.22562210	0.00000043	0.380399
0.24560284	0.00000042	0.0445346	0.225518657	0.000003130	-0.276057
0.24357401	0.00000897	-0.5784778	0.225505097	0.000000009	0.462638
0.2410448	0.0000038	0.319531	0.2254822223	0.0000001829	-0.0078204
0.23987874	0.00003665	-0.26303	0.225330456	0.000000027	0.0355171
0.23970847	0.00000309	0.04161	0.225267177	0.000000585	-0.602980
0.23958965	0.00000030	0.346111	0.225124132	0.000000340	0.38155
0.23789051	0.00000025	0.0418743	0.22504230	0.00000247	-0.27625
0.236927333	0.000005525	-0.5861615	0.225031690	0.000000007	0.465242
0.23547335	0.00000267	0.347471	0.2250128294	0.0000001483	-0.008607
0.23473577	0.00002324	-0.273406	0.224892326	0.000000021	0.0352253
0.234614364	0.000000268	0.31442	0.224842551	0.000000469	-0.60375
0.23456279	0.00000076	0.10268	0.224728011	0.000000275	0.382437
0.23348866	0.00000016	0.0399958	0.224662182	0.000001988	-0.276418
0.232953822	0.000003592	-0.5912416	0.224653715	0.000000006	0.467266
0.23203924	0.00000184	0.361154	0.2246380458	0.0000001217	-0.009197
0.23155407	0.00001505	-0.274610	0.224540770	0.000000017	0.034986
0.231479329	0.00000050	0.41189	0.224500890	0.000000381	-0.60438
0.231425177	0.000000630	0.01882	0.224407760	0.000000225	0.383126
0.23072284	0.00000011	0.0386450	0.224354026	0.000001622	-0.2765643
0.230394035	0.000002449	-0.594800	0.224347158	0.000000005	0.468874
0.22978121	0.00000131	0.368838	0.2243340347	0.0000001010	-0.0096541
0.22944767	0.00001024	-0.275014	0.224254379	0.000000015	0.034787
0.229399214	0.000000026	0.43607	0.224221917	0.000000314	-0.604911
0.229349936	0.000000492	0.003230	0.22414518	0.000000019	0.38367
0.22886737	0.00000008	0.0376515	0.22410075	0.000000134	-0.276692
0.2286502291	0.0000017383	-0.597396	0.224095104	0.000000004	0.47018
0.22821963	0.00000095	0.373570	0.2240840255	0.0000000846	-0.01002
0.22798132	0.00000727	-0.2753174	0.224017976	0.000000012	0.0346193
0.227948073	0.000000019	0.447483	0.223991191	0.000000262	-0.60535
0.227906513	0.000000371	-0.002307	0.223927214	0.000000156	0.38411
0.22756089	0.00000006	0.0369036	0.223890068	0.000001119	-0.27680
0.227409667	0.000001275	-0.599347	0.2238853634	0.0000000035	0.471244
0.22709562	0.00000071	0.376686	0.223875940	0.000000072	-0.01032
0.22691976	0.00000534	-0.275591	0.22382057	0.000000001	0.0345
0.226895907	0.000000014	0.454442	0.22379820	0.000000022	-0.6057
0.226861748	0.000000289	-0.005068	0.22374430	0.000000014	0.3845

Table C.16:  ${}^3D^e$  resonances of helium below the  $N = 3$  threshold.

$N = 4$					
Re( $-E$ )	Im( $-E$ )	$\langle \cos(\theta_{12}) \rangle$	Re( $-E$ )	Im( $-E$ )	$\langle \cos(\theta_{12}) \rangle$
0.1916071	0.0019040	-0.3646	0.132874092	0.000008125	-0.16487
0.171527	0.000665	0.05028	0.132311226	0.000004924	-0.6978766
0.16787558	0.00002821	-0.658463	0.13198639	0.00000274	0.51297
0.16129752	0.00004489	-0.239823	0.13178424	0.00002068	0.11115
0.1595683	0.0009917	-0.40672	0.13170975	0.00001220	0.2480
0.15897907	0.00005955	-0.181968	0.13168782	0.00007697	-0.36917
0.15122995	0.00002217	-0.676280	0.13165783	0.00000335	0.3603
0.1509878	0.0000255	0.12472	0.131449082	0.000007167	-0.253479
0.1491307	0.0002025	0.04649	0.13128304	0.00000308	0.16613
0.14708577	0.00003249	-0.245385	0.131204959	0.000005604	-0.15961
0.147079	0.000561	-0.42129	0.130831298	0.000003601	-0.699673
0.1466933	0.0000042	0.194360	0.130596612	0.000002033	0.532814
0.14579356	0.00003551	-0.1953176	0.130439255	0.000016586	0.0828
0.142611814	0.000014965	-0.685781	0.13039618	0.00004975	-0.3654
0.1416865	0.0000181	0.218096	0.13039210	0.00000621	0.31320
0.1409989	0.0000632	0.1307	0.13035346	0.00000357	0.32479
0.1408729	0.0000540	0.2430	0.130196821	0.000005290	-0.254531
0.1402696	0.0003206	-0.42932	0.13007401	0.00000240	0.16318
0.139967367	0.000021535	-0.248487	0.130017813	0.000004040	-0.15639
0.13951882	0.00000526	0.19106	0.129756885	0.000002702	-0.700926
0.139184920	0.000020556	-0.18606	0.129581894	0.000001561	0.544451
0.137590623	0.000010056	-0.6915335	0.129459138	0.000012509	0.0262
0.1368997	0.0000075	0.38351	0.12944590	0.00003268	-0.3708
0.13656470	0.00002925	0.19597	0.12942783	0.00000373	0.401905
0.1363861	0.0000481	0.16735	0.12939666	0.00000326	0.30300
0.13620744	0.00000128	0.43960	0.129277588	0.000004007	-0.255379
0.1361613	0.0001916	-0.42682	0.12918451	0.00000188	0.16141
0.135838135	0.000014440	-0.250504	0.129142594	0.000003014	-0.15431
0.13551250	0.00000485	0.17936	0.128953002	0.000002075	-0.701775
0.135332083	0.000012480	-0.17352	0.128819086	0.000001223	0.551901
0.134426182	0.000006931	-0.6953003	0.12872483	0.00002256	-0.2577
0.13395946	0.00000399	0.47424	0.12872431	0.00000863	-0.128
0.13370209	0.00002509	0.144098	0.12870043	0.00000243	0.46125
0.13358288	0.00002519	0.20266	0.12867479	0.00000271	0.28883
0.1335028	0.0001197	-0.4042	0.128582713	0.000003103	-0.256069
0.13349784	0.00000251	0.4075	0.12851062	0.00000149	0.16033
0.133218438	0.000010005	-0.25216	0.128478480	0.000002311	-0.1529
0.13298814	0.00000394	0.17111	0.12833625	0.000000162	-0.70231

Table C.17:  ${}^3D^e$  resonances of helium below the  $N = 4$  threshold.

$N = 5$					
$\text{Re}(-E)$	$\text{Im}(-E)$	$\langle \cos(\theta_{12}) \rangle$	$\text{Re}(-E)$	$\text{Im}(-E)$	$\langle \cos(\theta_{12}) \rangle$
0.11781	0.00209	-0.121	0.08651649	0.00000729	-0.760871
0.11133207	0.00002817	-0.7282413	0.086483	0.000011	0.4223
0.10771238	0.00005019	-0.361777	0.086279	0.000012	0.457
0.10682968	0.00006004	-0.322851	0.0862169	0.0000672	0.152
0.1066188	0.0008790	-0.52031	0.086187	0.000007	0.2079
0.1047144	0.0008116	0.15723	0.0861004	0.0000027	0.479
0.1023324	0.0000566	-0.0395	0.0860066	0.0000148	0.09710
0.1011565	0.0012677	-0.1617	0.0858575	0.0001719	-0.55661
0.1008623	0.0000590	0.0025	0.08582465	0.00001164	-0.404
0.10062339	0.00002557	-0.74112715	0.085824	0.000003	0.242
0.0981944	0.0005270	-0.53657	0.085695398	0.000014015	-0.36190
0.09804390	0.00004259	-0.3735134	0.0853884	0.0000399	-0.1770
0.09747798	0.00004906	-0.342663	0.085270825	0.000005466	-0.762333
0.095741	0.000024	0.2263	0.085223	0.000007	0.4838
0.0946127	0.0009644	-0.12599	0.085090	0.000012	0.464
0.094573	0.000212	0.1306	0.0850259	0.0000567	0.193
0.0945612	0.0000342	-0.0030	0.085002	0.000006	0.198
0.094539896	0.000019031	-0.748717	0.0849534	0.0000030	0.444
0.0938286	0.0000417	0.0405	0.08486616	0.00001114	0.1102
0.093187	0.000006	0.2545	0.0848290	0.0001121	-0.55852
0.0931803	0.0002611	-0.54897	0.084745785	0.000008892	-0.3890
0.09273307	0.00003096	-0.380230	0.0847347	0.0000026	0.2223
0.09236295	0.00003524	-0.35125	0.08464933	0.00001040	-0.35731
0.091019	0.000021	0.2978	0.08451448	0.00000072	-0.19145
0.0907624	0.0006273	-0.11352	0.08434745	0.00000418	-0.76363
0.090753250	0.000013674	-0.7532561	0.084302	0.000005	0.5306
0.0904340	0.0000220	0.0285	0.084204	0.000011	0.4487
0.0904114	0.0001107	0.12982	0.0841488	0.0000465	0.212
0.090909	0.000033	0.3110	0.084131	0.000005	0.249
0.09004682	0.00007123	-0.55842	0.0840993	0.0000035	0.380
0.089997	0.000029	0.069	0.0840261	0.0000770	-0.56164
0.089595	0.000004	0.245	0.0840250	0.0000088	0.1209
0.08946976	0.00002212	-0.38390	0.08394106	0.00000694	-0.39007
0.08921878	0.00002511	-0.35497	0.0839272	0.0000024	0.2230
0.0882813	0.0003444	-0.13145	0.08386847	0.00000876	-0.32506
0.088280	0.000015	0.3516	0.0838322	0.0000141	-0.2308
0.08825826	0.00002327	-0.5271	0.0836451	0.0000032	-0.76469
0.08824544	0.00001567	-0.78478	0.0836047	0.0000039	0.5635
0.087930	0.000012	0.253	0.083529	0.000010	0.4322
0.0878993	0.0000824	0.1191	0.0834840	0.0000370	0.223
0.087845	0.000009	0.39	0.083471	0.000004	0.32
0.087691	0.000002	0.492	0.0834467	0.0000036	0.310
0.0876127	0.0000201	0.0843	0.0834014	0.0000553	-0.5670
0.087350	0.000003	0.2326	0.0833859	0.0000073	0.1296
0.087318165	0.000016028	-0.3853	0.08332479	0.00000568	-0.3931
0.08714169	0.00001969	-0.35459	0.0833106	0.0000027	0.225
0.0870580	0.0002137	-0.56216	0.0832784	0.0000351	-0.161
0.08658917	0.00015559	-0.1561	0.0832653	0.0000077	-0.399

Table C.18:  $^3D^e$  resonances of helium below the  $N = 5$  threshold.

## C.2 Unnatural parity

### C.2.1 $^1P^e$ resonance data

The data for the 3rd up to the 5th threshold of  $^1P^e$  resonances (Tab. C.19, C.20 and C.21) is compared to existing data [148]. Table C.21 presents our results for  $^1P^e$  resonances below the sixth, seventh and eighth single ionization threshold, which have been calculated by us for the first time. The tables are limited to at most 50 entries even if more converged resonances have been identified.

$N = 3$					
This work		Ho <i>et al.</i> [148]		This work (continued)	
$-\text{Re}(E_{i,\theta})$	$-\text{Im}(E_{i,\theta})$	$-\text{Re}(E_{i,\theta})$	$-\text{Im}(E_{i,\theta})$	$-\text{Re}(E_{i,\theta})$	$-\text{Im}(E_{i,\theta})$
0.2789925	0.0000221	0.2789925	0.00002215	0.225688553	0.000000658
0.259352043	0.00000628	0.259352	0.000006295	0.2252751151	0.000000350
0.25363872	0.00001320	0.2536387	0.0000131915	0.225176001	0.000000520
0.244513616	0.00000435	0.2445136	0.000004375	0.2248481993	0.000000282
0.24223748	0.00000769	0.242237	0.000008	0.224769293	0.000000418
0.237282423	0.00000290			0.2245050215	0.000000230
0.23609888	0.00000475			0.2244411635	0.0000003413
0.2331144072	0.0000001971			0.2242250134	0.0000000191
0.232410753	0.000003104			0.2241725969	0.0000002819
0.2304760586	0.0000001383			0.22399356071	0.0000001593
0.230020923	0.000002129			0.2239500007	0.0000002356
0.2286960596	0.0000001001			0.22380004645	0.00000001345
0.228383750	0.000001520			0.2237634503	0.0000001988
0.2274371191	0.0000000745			0.22363660629	0.00000001145
0.227213135	0.000001121			0.2236055623	0.0000001693
0.2265134362	0.0000000568			0.2234973139	0.0000000098
0.226347159	0.000000849			0.223470751	0.000000145
0.2258154670	0.0000000442				

Table C.19:  $^1P^e$  resonances of helium below the  $N = 3$  SIT: our results are compared with data from [148]. Only converged digits are displayed for our results. The results of [148] have been converted from Ry to a. u..

$N = 4$					
This work		Ho <i>et al.</i> [148]		This work (continued)	
$-\text{Re}(E_{i,\theta})$	$-\text{Im}(E_{i,\theta})$	$-\text{Re}(E_{i,\theta})$	$-\text{Im}(E_{i,\theta})$	$-\text{Re}(E_{i,\theta})$	$-\text{Im}(E_{i,\theta})$
0.16551928	0.00003481	0.1655193	0.0000363	0.1283507197	0.0000021733
0.15640849	0.00004201	0.1564085	0.0000420	0.128217530	0.000001931
0.14966102	0.00002641	0.149660985	0.0000264	0.1279219917	0.0000005669
0.145222196	0.000005624	0.14522225	0.0000056	0.1278615011	0.0000017338
0.14423254	0.00002289	0.1442325	0.000022885	0.1277578228	0.0000015431
0.14157953	0.00001758	0.141578	0.0000175	0.1275211156	0.0000004561
0.138778490	0.000004604			0.1274723209	0.0000014046
0.13823181	0.00001404			0.127389968	0.000001252
0.136894328	0.000011765			0.1271975118	0.0000003722
0.1350694494	0.0000032298			0.12715759075	0.00000115318
0.134717582	0.000009398			0.1270910482	0.0000010293
0.133941318	0.000008109			0.12693249839	0.00000030768
0.1326980414	0.0000022709			0.1268994292	0.0000009581
0.1324563572	0.0000066066			0.1268448661	0.0000008562
0.131962967	0.000005774			0.12671272436	0.00000025719
0.1310817499	0.0000016378			0.12668502849	0.00000080439
0.1309084038	0.0000048136			0.1266397143	0.0000007197
0.130574062	0.000004235			0.126528440305	0.000000217152
0.1299283144	0.0000012139			0.12650501667	0.00000068175
0.1297997937	0.0000036095			0.1264669606	0.0000006106
0.129562145	0.000003190			0.12637239094	0.00000018499
0.1290755425	0.0000009224			0.12635240606	0.00000058274
0.1289776666	0.0000027724			0.1263201282	0.0000005224
0.128802370	0.000002457			0.126239086	0.000000159
0.1284269401	0.0000007163			0.126221900	0.000000502

$N = 5$					
This work		Ho <i>et al.</i> [148]		This work (continued)	
$-\text{Re}(E_{i,\theta})$	$-\text{Im}(E_{i,\theta})$	$-\text{Re}(E_{i,\theta})$	$-\text{Im}(E_{i,\theta})$	$-\text{Re}(E_{i,\theta})$	$-\text{Im}(E_{i,\theta})$
0.10992709	0.00003633	0.10992705	0.00003633	0.084173628	0.000005213
0.10517908	0.00006412	0.10517915	0.0000641	0.083877652	0.000004761
0.09958738	0.00003220	0.099588	0.000032	0.083775500	0.000002276
0.09913181	0.00004030	0.0991315	0.0000405	0.083699897	0.000008022
0.09635344	0.00005097	0.096355	0.00010	0.083507802	0.000004074
0.09379757	0.00002374			0.083272693	0.000003656
0.09284200	0.00002789			0.083193307	0.000001933
0.092085843	0.000001652			0.083135007	0.000006331
0.09159661	0.00003609			0.082988895	0.000003237
0.09021782	0.00001700			0.0827995497	0.0000028689
0.08939833	0.00001844			0.082736551	0.000001637
0.088983560	0.000002856			0.08269061	0.00000508
0.08868311	0.00002552			0.082576812	0.000002611
0.097857284	0.000012278			0.082422356	0.000002293
0.087220161	0.000012482			0.082371490	0.000001388
0.086954588	0.000003169			0.082334626	0.000004136
0.08675613	0.00001843			0.082244211	0.000002134
0.08622304	0.00000904			0.0821167302	0.0000018627
0.085734152	0.000008757			0.082075055	0.000001182
0.0855495554	0.0000029960			0.082045009	0.000003409
0.085411125	0.000013654			0.0819719449	0.0000017655
0.085047016	0.000006795			0.0818655993	0.0000015339
0.084669095	0.000006360			0.0818310193	0.0000010112
0.084534149	0.000002639			0.081806201	0.000002842
0.084433498	0.000010356			0.0817462876	0.0000014761

Table C.20:  $1P^e$  resonances of helium below the  $N = 4$  and  $N = 5$  SIT: our results are compared with data from [148]. Only converged digits are displayed for our results. The results of [148] have been converted from Ry to a. u..

$N = 6$		$N = 7$		$N = 8$	
$-\text{Re}(E_{i,\theta})$	$-\text{Im}(E_{i,\theta})$	$-\text{Re}(E_{i,\theta})$	$-\text{Im}(E_{i,\theta})$	$-\text{Re}(E_{i,\theta})$	$-\text{Im}(E_{i,\theta})$
0.07842283	0.00003470	0.05498563	0.00007429	0.0411149	0.0000530
0.07567410	0.00006156	0.05379687	0.00003440	0.04002452	0.00006960
0.07224947	0.00007379	0.05244029	0.00006347	0.03965467	0.00004567
0.07136929	0.00003424	0.05242598	0.00005634	0.03964537	0.00002974
0.06931597	0.00005675	0.05085099	0.00007015	0.038878998	0.000046634
0.06804670	0.00002951	0.05062700	0.00002905	0.03879548	0.00007029
0.06713378	0.00002726	0.04956944	0.00004669	0.03802800	0.00006044
0.06694910	0.00005892	0.04943868	0.00002863	0.037941778	0.000023810
0.06563172	0.00004420	0.04904712	0.00004163	0.037565069	0.000039814
0.06448432	0.00002421	0.048472274	0.000022801	0.037331038	0.000037500
0.06437363	0.00002059	0.048398038	0.000057117	0.0372827848	0.0000119970
0.06398306	0.00004317	0.04765760	0.00003662	0.037098091	0.000056651
0.063509277	0.000000322	0.04733800	0.00002919	0.0367510629	0.0000088988
0.06326638	0.00003322	0.047106953	0.000028058	0.03666614	0.00004901
0.06248020	0.00001541	0.04694618	0.00001716	0.0365475035	0.0000109742
0.06239599	0.00001880	0.04677744	0.00004475	0.036235803	0.000033929
0.06209055	0.00003172	0.0463982183	0.0000001004	0.036226863	0.000025302
0.061854177	0.000000995	0.04631248	0.00002800	0.0360251077	0.0000163801
0.06165078	0.00002498	0.046001749	0.000024303	0.035950619	0.000040618
0.061129523	0.000011573	0.04588046	0.00000563	0.0357978779	0.0000028588
0.06099789	0.00001439	0.04583700	0.00002176	0.0357415165	0.0000164475
0.060789409	0.000023612	0.045681944	0.000008656	0.03569077	0.00003726
0.060650304	0.000001608	0.045639315	0.000034766	0.03537667402	0.00000004761
0.06049658	0.00001899	0.0454287476	0.0000003049	0.03533276	0.00002654
0.060135459	0.000008693	0.04533424	0.00002042	0.03532486	0.00002804
0.060000138	0.000011071	0.04505874	0.00001950	0.035172746	0.000019904
0.059849171	0.000017862	0.044961036	0.000011745	0.035127772	0.000026941
0.059757586	0.000001966	0.044936141	0.000017547	0.035028755	0.000012623
0.05964286	0.00001462	0.04480626	0.00002681	0.035018480	0.000013207
0.059387022	0.000006243	0.044681170	0.000002718	0.03479384	0.00001410
0.05925830	0.00000862	0.0446750807	0.0000005270	0.0347548968	0.0000001409
0.059144754	0.000013756	0.044857747	0.000014471	0.034703614	0.000020698
0.059079707	0.000002080	0.044359353	0.000015631	0.034656412	0.000023140
0.05899369	0.00001135	0.044315742	0.000009102	0.03454630	0.00002049
0.0588677275	0.0000005169	0.04426580	0.00001433	0.034510834	0.000017374
0.05872764	0.00000572	0.044175595	0.000020766	0.034470248	0.000009508
0.058689952	0.000006813	0.0440854658	0.0000006741	0.034354198	0.000027905
0.058602152	0.000010788	0.043987367	0.000015535	0.03425506932	0.00000024764
0.058553488	0.000002031	0.043823270	0.000012646	0.034203523	0.000016100
0.058487751	0.000009006	0.043806797	0.000007182	0.034146526	0.000019309
0.058323987	0.000005157	0.043750863	0.000011800	0.034076654	0.000018621
0.058244147	0.000005463	0.043692093	0.000014920	0.034038254	0.000007958
0.058174779	0.000008607	0.0436185919	0.0000007461	0.034035005	0.000005440
0.058137002	0.000001892	0.03543029	0.00001224	0.033923963	0.000022555
0.058086914	0.000007123	0.043402328	0.000010416	0.03384991526	0.00000032044
0.057959583	0.000004030	0.043399909	0.000005738	0.033829442	0.000002015
0.057887672	0.000004441	0.043354373	0.000006963	0.033803874	0.000012300
0.057831903	0.000006976	0.043333045	0.000006771	0.0337975841	0.0000013586
0.057801762	0.000001715	0.04324394218	0.00000072520	0.033742379	0.000014370
0.057763951	0.000005597	0.043183398	0.000009805	0.0336681989	0.0000059655

Table C.21:  $^1P^e$  resonances of helium below the sixth ( $N = 6$ ), seventh ( $N = 7$ ) and eighth ( $N = 8$ ) SIT, only converged digits are displayed.

# Bibliography

- [1] H. Poincaré, *Les méthodes nouvelles de la mécanique céleste* (Gauthier-Villars, Paris, 1899).
- [2] M. C. Gutzwiller, *Rev. Mod. Phys.* **70**, 589 (1998).
- [3] G. Tanner, K. Richter, and J.-M. Rost, *Rev. Mod. Phys.* **72**, 497 (2000).
- [4] A. Einstein, *Verh. Dtsch. Phys. Ges.* **19**, 82 (1917).
- [5] M. C. Gutzwiller, *J. Math. Phys.* **8**, 1979 (1967).
- [6] M. C. Gutzwiller, *Journal of Mathematical Physics* **12**, 343 (1971).
- [7] G. S. Ezra, K. Richter, G. Tanner, and D. Wintgen, *J. Phys. B* **24**, L413 (1991).
- [8] D. Wintgen, K. Richter, and G. Tanner, *Chaos* **2**, 19 (1992).
- [9] N. Bohr, *Philos. Mag.* **26**, 476 (1913).
- [10] W. Heisenberg, *Z. Phys.* **33**, 879 (1925).
- [11] E. Schrödinger, *Ann. d. Phys.* **384**, 489 (1926).
- [12] C. L. Pekeris, *Phys. Rev.* **112**, 1649 (1958).
- [13] C. L. Pekeris, *Phys. Rev.* **115**, 1216 (1959).
- [14] G. W. F. Drake, *Phys. Rev. Lett.* **65**, 2769 (1990).
- [15] G. W. F. Drake and Z.-C. Yan, *Phys. Rev. A* **46**, 2378 (1992).
- [16] R. P. Madden and K. Codling, *Phys. Rev. Lett.* **10**, 516 (1963).
- [17] T. Ericson, *Phys. Rev. Lett.* **5**, 430 (1960).
- [18] T. Ericson, *Ann. Phys.* **23**, 390 (1963).
- [19] C. W. Byun, N. N. Choi, M.-H. Lee, and G. Tanner, *Phys. Rev. Lett.* **98**, 113001 (2007).
- [20] R. Blümel, *Phys. Rev. A* **54**, 5420 (1996).
- [21] K. Richter and D. Wintgen, *Phys. Rev. Lett.* **65**, 1965 (1990).
- [22] K. Richter, J. S. Briggs, D. Wintgen, and E. A. Solov'ev, *J. Phys. B* **25**, 3929 (1992).
- [23] P. Schlagheck, Dissertation, Technische Universität München, 1999.
- [24] P. Schlagheck and A. Buchleitner, *Eur. Phys. J. D* **22**, 401 (2003).

- 
- [25] G. J. Madroñero Pabón, Dissertation, Ludwig-Maximilians-Universität München, 2004.
- [26] J. Madroñero and A. Buchleitner, Phys. Rev. A **77**, 053402 (2008).
- [27] A. Buchleitner, D. Delande, and J. Zakrzewski, Phys. Rep. **368**, 409 (2002).
- [28] D. N. Fittinghoff, P. R. Bolton, B. Chang, and K. C. Kulander, Phys. Rev. Lett. **69**, 2642 (1992).
- [29] B. Walker *et al.*, Phys. Rev. Lett. **73**, 1227 (1994).
- [30] K. J. Schafer, B. Yang, L. F. DiMauro, and K. C. Kulander, Phys. Rev. Lett. **70**, 1599 (1993).
- [31] B. Yang *et al.*, Phys. Rev. Lett. **71**, 3770 (1993).
- [32] T. Weber *et al.*, Nature **405**, 658 (2000).
- [33] R. Moshhammer *et al.*, Phys. Rev. A **65**, 035401 (2002).
- [34] V. L. B. de Jesus *et al.*, J. Phys. B **37**, L161 (2004).
- [35] J. S. Parker *et al.*, Phys. Rev. Lett. **96**, 133001 (2006).
- [36] T. Nubbemeyer *et al.*, Phys. Rev. Lett. **101**, 233001 (2008).
- [37] J. S. Parker, K. J. Meharg, G. A. McKenna, and K. T. Taylor, J. Phys. B **40**, 1729 (2007).
- [38] L. A. A. Nikolopoulos and P. Lambropoulos, J. Phys. B **34**, 545 (2001).
- [39] L. Feng and H. W. van der Hart, Phys. Rev. A **66**, 031402(R) (2002).
- [40] L. Feng and H. W. van der Hart, J. Phys. B **36**, L1 (2003).
- [41] B. Piraux, J. Bauer, S. Laulan, and H. Bachau, Eur. Phys. J. D **26**, 7 (2003).
- [42] S. X. Hu, J. Colgan, and L. A. Collins, J. Phys. B **38**, L35 (2005).
- [43] I. A. Ivanov and A. S. Kheifets, Phys. Rev. A **71**, 043405 (2005).
- [44] A. S. Kheifets and I. A. Ivanov, J. Phys. B **39**, 1731 (2006).
- [45] E. Fomouo, G. Lagmago Kamta, G. Edah, and B. Piraux, Phys. Rev. A **74**, 063409 (2006).
- [46] E. Fomouo *et al.*, J. Phys. B **41**, 051001 (2008).
- [47] A. K. Bhatia and A. Temkin, Rev. Mod. Phys. **36**, 1050 (1964).
- [48] B. Schiff, H. Lifson, C. L. Pekeris, and P. Rabinowitz, Phys. Rev. **140**, A1104 (1965).
- [49] Y. Accad, C. L. Pekeris, and B. Schiff, Phys. Rev. A **4**, 516 (1971).
- [50] A. Kono and S. Hattori, Phys. Rev. A **29**, 2981 (1984).
- [51] A. Bürgers, D. Wintgen, and J.-M. Rost, J. Phys. B **28**, 3163 (1995).
- [52] J. M. Rost, K. Schulz, M. Domke, and G. Kaindl, J. Phys. B **30**, 4663 (1997).
- [53] B. Grémaud and D. Delande, Europhys. Lett. **40**, 363 (1997).

- 
- [54] B. Grémaud, Thèse de doctorat, Université Pierre et Marie Curie (Paris 6), 1997.
- [55] A. Scrinzi and B. Piraux, Phys. Rev. A **56**, R13 (1997).
- [56] A. Scrinzi and B. Piraux, Phys. Rev. A **58**, 1310 (1998).
- [57] A. W. Weiss, Phys. Rev. **122**, 1826 (1961).
- [58] H. L. Davis, J. Chem. Phys. **39**, 1183 (1963).
- [59] D. P. Carroll, H. J. Silverstone, and R. M. Metzger, J. Chem. Phys. **71**, 4142 (1979).
- [60] B. F. Davis and K. T. Chung, Phys. Rev. A **25**, 1328 (1982).
- [61] S. P. Goldman, Phys. Rev. Lett. **73**, 2547 (1994).
- [62] S. P. Goldman, Phys. Rev. A **52**, 3718 (1995).
- [63] J. Rao, Y. Li, H. Qiao, and B. Li, Phys. Rev. A **55**, 2439 (1997).
- [64] H. Bachau *et al.*, Rep. Prog. Phys. **64**, 1815 (2001).
- [65] Y. H. Jiang *et al.*, Phys. Rev. A **78**, 021401(R) (2008).
- [66] T. Kato, Comm. Pure Appl. Math. **10**, 151 (1957).
- [67] C. C. J. Roothaan and A. W. Weiss, Rev. Mod. Phys. **32**, 194 (1960).
- [68] G. Lagmago Kamta, B. Piraux, and A. Scrinzi, Phys. Rev. A **63**, 040502(R) (2001).
- [69] C. W. McCurdy, D. A. Horner, T. N. Rescigno, and F. Martín, Phys. Rev. A **69**, 032707 (2004).
- [70] S. Laulan and H. Bachau, Phys. Rev. A **69**, 033408 (2004).
- [71] P. Antoine *et al.*, Phys. Rev. A **78**, 023415 (2008).
- [72] O. Sinanoğlu and D. R. Herrick, J. Chem. Phys. **62**, 886 (1975).
- [73] D. R. Herrick and O. Sinanoğlu, Phys. Rev. A **11**, 97 (1975).
- [74] D. R. Herrick, Adv. Chem. Phys. **52**, 1 (1983).
- [75] M. Bylicki and E. Bednarz, Phys. Rev. A **67**, 022503 (2003).
- [76] J. W. Cooper, U. Fano, and F. Prats, Phys. Rev. Lett. **10**, 518 (1963).
- [77] C. D. Lin, Phys. Rev. Lett. **51**, 1348 (1983).
- [78] C. D. Lin, Phys. Rev. A **29**, 1019 (1984).
- [79] C. Lin, Adv. At. Mol. Phys. **22**, 77 (1986).
- [80] J. M. Feagin and J. S. Briggs, Phys. Rev. A **37**, 4599 (1988).
- [81] S. I. Themelis, Y. Komninos, and C. A. Nicolaidis, Eur. Phys. J. D **18**, 277 (2002).
- [82] D. A. Varschalovich, A. N. Moskalev, and V. K. Khersonskii, *Quantum Theory of Angular Momentum* (World Scientific, Singapore, 2008).
- [83] J. Aguilar and J. M. Combes, Comm. Math. Phys. **22**, 269 (1971).

- 
- [84] E. Balslev and J. M. Combes, *Comm. Math. Phys.* **22**, 280 (1971).
- [85] B. Simon, *Ann. Math.* **97**, 247 (1973).
- [86] W. P. Reinhardt, *Annu. Rev. Phys. Chem.* **33**, 223 (1982).
- [87] Y. Ho, *Phys. Rep.* **99**, 1 (1983).
- [88] S. Graffi, V. Grecchi, and H. J. Silverstone, *Ann. Inst. Henri Poincaré, Sect. A* **42**, 215 (1985).
- [89] M. Pont and R. Shakeshaft, *Phys. Rev. A* **43**, 3764 (1991).
- [90] M. Reed and B. Simon, *Methods of modern mathematical physics* (Academic Press, New York, 1978), Vol. IV. Analysis of operators.
- [91] A. Buchleitner, B. Grémaud, and D. Delande, *J. Phys. B* **27**, 2663 (1994).
- [92] B. R. Johnson and W. P. Reinhardt, *Phys. Rev. A* **28**, 1930 (1983).
- [93] L. Hilico *et al.*, *Phys. Rev. A* **66**, 022101 (2002).
- [94] J. Eiglsperger and J. Madroñero, *Phys. Rev. A* **80**, 022512 (2009).
- [95] J. Eiglsperger and J. Madroñero, *Phys. Rev. A* **80**, 039902(E) (2009).
- [96] I. C. Percival, *Proc. R. Soc. London, Sect. A* **353**, 289 (1977).
- [97] J. Madroñero *et al.*, *Europhys. Lett.* **70**, 183 (2005).
- [98] M. Rotenberg, *Adv. At. Mol. Phys.* **6**, 233 (1970).
- [99] E. Huens, B. Piraux, A. Bugacov, and M. Gajda, *Phys. Rev. A* **55**, 2132 (1997).
- [100] L. D. Landau and E. M. Lifschitz, *Lehrbuch der Theoretischen Physik: III. Quantenmechanik* (Akademie-Verlag, Berlin, 1979).
- [101] H. Friedrich, *Theoretical Atomic Physics*, 3rd ed. (Springer, Berlin, 2005).
- [102] A. Buchleitner, Thèse de doctorat, Université Pierre et Marie Curie (Paris 6), 1993.
- [103] M. Abramowitz and I. Stegun, *Handbook of mathematical functions* (Dover Publications, New York, 1972).
- [104] V. Fock, *Z. Phys.* **47**, 446 (1928).
- [105] C. G. Darwin, *Math. Proc. Cambridge Philos. Soc.* **27**, 86 (1931).
- [106] D. Delande, Thèse d'état, Université Pierre et Marie Curie (Paris 6), 1988.
- [107] A. George and J. W. Liu, *SIAM Rev.* **31**, 1 (1989).
- [108] J. R. Gilbert, C. Moler, and R. Schreiber, *SIAM J. Matrix Anal. Appl.* **13**, 333 (1992).
- [109] G. Karypis and V. Kumar, *J. Parallel Distrib. Comput.* **48**, 96 (1998).
- [110] C. Lanczos, *J. Res. Natl. Bur. Stand.* **45**, 255 (1950).
- [111] B. N. Parlett and D. S. Scott, *Math. Comput.* **33**, 217 (1979).

- [112] T. Ericsson and A. Ruhe, *Math. Comput.* **35**, 1251 (1980).
- [113] A. Krug, Dissertation, Ludwig-Maximilians-Universität München, 2001.
- [114] G. H. Golub and C. F. van Loan, *Matrix Computations, Johns Hopkins Series in the Mathematical Sciences*, 3rd ed. (The Johns Hopkins University Press, Baltimore, 1996).
- [115] Message Passing Interface Forum, *MPI: A Message-Passing Interface Standard, Version 2.1* (High-Performance Computing Center Stuttgart, Stuttgart, 2008).
- [116] <http://www.mpi-forum.org/docs/docs.html>.
- [117] <http://openmp.org/wp>.
- [118] <http://www.lrz-muenchen.de/services/compute/linux-cluster>.
- [119] <http://www.lrz-muenchen.de/services/compute/hlrb>.
- [120] G. Lagmago Kamta, Ph.D. thesis, Université Nationale du Bénin, 1999.
- [121] E. Fomouo, Dissertation doctorale, Université catholique de Louvain, 2008.
- [122] J. Eiglsperger, B. Piraux, and J. Madroñero, *Phys. Rev. A* **80**, 022511 (2009).
- [123] B. Eckhardt, J. S. Prauzner-Bechcicki, K. Sacha, and J. Zakrzewski, *Phys. Rev. A* **77**, 015402 (2008).
- [124] J. Zamastil *et al.*, *J. Math. Phys.* **45**, 2674 (2004).
- [125] J. Zamastil, F. Vinette, and M. Šimánek, *Phys. Rev. A* **75**, 022506 (2007).
- [126] M. H. Halley, Ph.D. thesis, University of London, 1993.
- [127] R. Püttner *et al.*, *Phys. Rev. Lett.* **86**, 3747 (2001).
- [128] A. Czasch *et al.*, *Phys. Rev. Lett.* **95**, 243003 (2005).
- [129] G. Tanner *et al.*, *J. Phys. B* **40**, F157 (2007).
- [130] K. T. Compton and J. C. Boyce, *J. Frank. Inst* **205**, 497 (1928).
- [131] P. G. Kruger, *Phys. Rev.* **36**, 855 (1930).
- [132] R. Whiddington and H. Priestley, *Proc. R. Soc. London, Sect. A* **145**, 462 (1934).
- [133] T.-Y. Wu, *Phys. Rev.* **66**, 291 (1944).
- [134] G. A. Doschek *et al.*, *Astrophys. J.* **164**, 165 (1971).
- [135] A. B. C. Walker and H. R. Rugge, *Astrophys. J.* **164**, 181 (1971).
- [136] N. J. Peacock, R. J. Speer, and M. G. Hobby, *J. Phys. B* **2**, 798 (1969).
- [137] A. Gabriel and C. Jordon, *Nature* **221**, 947 (1969).
- [138] T. Fujimoto and T. Kato, *Astrophys. J.* **246**, 994 (1981).
- [139] S. Kar and Y. Ho, *Int. J. Quantum Chem.* **106**, 814 (2006).
- [140] A. Sil, S. Bhattacharyya, and P. Mukherjee, *Int. J. Quantum Chem.* **107**, 2708 (2007).

- [141] J. K. Saha and T. K. Mukherjee, Phys. Rev. A **80**, 022513 (2009).
- [142] S. Kar and Y. K. Ho, Phys. Rev. A **79**, 062508 (2009).
- [143] R. Hilger, H.-P. Merckens, and H. Kleindienst, Chem. Phys. Lett. **262**, 400 (1996).
- [144] T. K. Mukherjee and P. K. Mukherjee, Phys. Rev. A **69**, 064501 (2004).
- [145] S. Bhattacharyya, T. K. Mukherjee, J. K. Saha, and P. K. Mukherjee, Phys. Rev. A **78**, 032505 (2008).
- [146] A. Mihelič, Doktorska disertacija, Univerza v Ljubljani, 2006.
- [147] R. El-Wazni and G. W. F. Drake, Phys. Rev. A **80**, 064501 (2009).
- [148] Y. K. Ho and A. K. Bhatia, Phys. Rev. A **47**, 2628 (1993).
- [149] P. Schlagheck and A. Buchleitner, Europhys. Lett. **46**, 24 (1999).
- [150] A. Assion *et al.*, Science **282**, 919 (1998).
- [151] T. C. Weinacht, J. Ahn, and P. H. Bucksbaum, Nature **397**, 233 (1999).
- [152] D. G. Arbó, C. O. Reinhold, and J. Burgdörfer, Phys. Rev. A **69**, 023409 (2004).
- [153] L. G. Hanson and P. Lambropoulos, Phys. Rev. Lett. **74**, 5009 (1995).
- [154] I. Bialynicki-Birula, M. Kaliński, and J. H. Eberly, Phys. Rev. Lett. **73**, 1777 (1994).
- [155] A. F. Brunello, T. Uzer, and D. Farrelly, Phys. Rev. Lett. **76**, 2874 (1996).
- [156] D. Delande and A. Buchleitner, Adv. At. Mol. Opt. Phys. **34**, 85 (1994).
- [157] H. Maeda and T. F. Gallagher, Phys. Rev. Lett. **92**, 133004 (2004).
- [158] H. Maeda, D. V. L. Norum, and T. F. Gallagher, Science **307**, 1757 (2005).
- [159] H. Maeda and T. F. Gallagher, Phys. Rev. A **75**, 033410 (2007).
- [160] K. Richter, Dissertation, Albert-Ludwigs-Universität Freiburg, 1991.
- [161] A. Lichtenberg and M. A. Leiberman, *Regular and Chaotic Dynamics* (Springer-Verlag, New York, 1992).
- [162] V. N. Ostrovsky and N. V. Prudov, J. Phys. B **28**, 4435 (1995).
- [163] P. Camus *et al.*, Phys. Rev. Lett. **62**, 2365 (1989).
- [164] U. Eichmann, V. Lange, and W. Sandner, Phys. Rev. Lett. **64**, 274 (1990).
- [165] K.-D. Heber *et al.*, Phys. Rev. A **56**, 1255 (1997).
- [166] J. G. Leopold and I. C. Percival, J. Phys. B **13**, 1037 (1980).
- [167] J. Müller, J. Burgdörfer, and D. Noid, Phys. Rev. A **45**, 1471 (1992).
- [168] J. Müller and J. Burgdörfer, Phys. Rev. Lett. **70**, 2375 (1993).
- [169] J. Müller, X. Yang, and J. Burgdörfer, Phys. Rev. A **49**, 2470 (1994).
- [170] Y. Qiu, J. Müller, and J. Burgdörfer, Phys. Rev. A **54**, 1922 (1996).

- [171] K. Richter, G. Tanner, and D. Wintgen, *Phys. Rev. A* **48**, 4182 (1993).
- [172] O. Bohigas, M. J. Giannoni, and C. Schmit, *Phys. Rev. Lett.* **52**, 1 (1984).
- [173] G. H. Wannier, *Phys. Rev.* **90**, 817 (1953).
- [174] H. Kossmann, V. Schmidt, and T. Andersen, *Phys. Rev. Lett.* **60**, 1266 (1988).
- [175] P. V. Brentano *et al.*, *Phys. Lett.* **9**, 48 (1964).
- [176] A. S. Sachrajda *et al.*, *Phys. Rev. Lett.* **80**, 1948 (1998).
- [177] H. Schanze, E. R. P. Alves, C. H. Lewenkopf, and H.-J. Stöckmann, *Phys. Rev. E* **64**, 065201(R) (2001).
- [178] C. Dembowski *et al.*, *Phys. Rev. E* **71**, 046202 (2005).
- [179] R. Blümel and U. Smilansky, *Phys. Rev. Lett.* **60**, 477 (1988).
- [180] G. Stania and H. Walther, *Phys. Rev. Lett.* **95**, 194101 (2005).
- [181] J. Madroñero and A. Buchleitner, *Phys. Rev. Lett.* **95**, 263601 (2005).
- [182] G. Stania, Doktorarbeit, Ludwig-Maximilians-Universität München, 2005.
- [183] R. Blümel and W. P. Reinhardt, *Chaos in Atomic Physics* (Cambridge University Press, Cambridge, 1997).
- [184] J. Xu, A.-T. Le, T. Morishita, and C. D. Lin, *Phys. Rev. A* **78**, 012701 (2008).
- [185] J.-L. Pichard, N. Zanon, Y. Imry, and A. Douglas Stone, *J. Phys. France* **51**, 587 (1990).
- [186] F. Borgonovi and I. Guarneri, *J. Phys. A* **25**, 3239 (1992).
- [187] T. Dittrich *et al.*, *Quantum Transport and Dissipation* (Wiley-VCH, Weinheim, 1998).
- [188] A. R. Kolovsky and A. Buchleitner, *Phys. Rev. E* **68**, 056213 (2003).
- [189] M. Domke *et al.*, *Phys. Rev. A* **53**, 1424 (1996).
- [190] G. Handke, M. Draeger, and H. Friedrich, *Physica A* **197**, 113 (1993).
- [191] G. Handke, M. Draeger, W. Ihra, and H. Friedrich, *Phys. Rev. A* **48**, 3699 (1993).
- [192] M. Draeger, G. Handke, W. Ihra, and H. Friedrich, *Phys. Rev. A* **50**, 3793 (1994).
- [193] W. Ihra, M. Draeger, G. Handke, and H. Friedrich, *Phys. Rev. A* **52**, 3752 (1995).
- [194] A. Buchleitner, D. Delande, and J.-C. Gay, *J. Opt. Soc. Am. B* **12**, 505 (1995).
- [195] Y. Jiang, Dissertation, Freie Universität Berlin, 2006.
- [196] J. M. Rost and J. S. Briggs, *J. Phys. B* **23**, L339 (1990).
- [197] J. Madroñero and B. Piraux, *Phys. Rev. A* **80**, 033409 (2009).
- [198] R. G. Nazmitdinov, N. S. Simonović, and J. M. Rost, *Phys. Rev. B* **65**, 155307 (2002).
- [199] P. M. Morse and H. Feshbach, *Methods of theoretical physics 1* (McGraw-Hill, New York, 1953).

- 
- [200] C. Cohen-Tannoudji, B. Diu, and F. Laloë, *Quantenmechanik 1*, 2nd ed. (de Gruyter, Berlin, 1999).
- [201] C. W. Clark and K. T. Taylor, *J. Phys. B* **13**, L737 (1980).
- [202] D. Delande and J. C. Gay, *J. Phys. B* **19**, L173 (1986).
- [203] J. T. Broad, *Phys. Rev. A* **31**, 1494 (1985).
- [204] M. Pont and R. Shakeshaft, *Phys. Rev. A* **44**, R4110 (1991).
- [205] M. Pont and R. Shakeshaft, *J. Phys. B* **28**, L571 (1995).
- [206] M. Pont, R. Shakeshaft, F. Maulbetsch, and J. S. Briggs, *Phys. Rev. A* **53**, 3671 (1996).
- [207] M. Pont and R. Shakeshaft, *Phys. Rev. A* **54**, 1448 (1996).
- [208] I. S. Gradshteyn and I. M. Ryzhik, *Tables of Integrals, Series and Products*, 6th ed. (Academic Press, San Diego, 2000).
- [209] W. H. Press, B. P. Flannery, S. A. Teukolsky, and W. T. Vetterling, *Numerical Recipes: The Art of Scientific Computing*, 3rd ed. (Cambridge University Press, Cambridge, 2007).

# Publications

Parts of this work have been published in scientific Journals or are in the process of publication. These are:

- J. Eiglsperger, B. Piraux and J. Madroñero, *Spectral representation of the three-body Coulomb problem: Perspectives for highly doubly excited states of helium*, Physical Review A **80**, 022511 (2009).
- J. Eiglsperger and J. Madroñero, *Highly doubly excited states of planar helium: Fluctuations in photoionization cross sections*, Physical Review A **80**, 022512 (2009).
- J. Eiglsperger and J. Madroñero, *Publisher's Note: Highly doubly excited states of planar helium: Fluctuations in photoionization cross sections [Phys. Rev. A **80**, 022512 (2009)]*, Physical Review A **80**, 033902(E) (2009).
- J. Eiglsperger, B. Piraux and J. Madroñero, *Spectral representation of the three-body Coulomb problem: I. Nonautoionizing doubly-excited states of high angular momentum in helium*, Physical Review A **81**, 042527 (2010).
- J. Eiglsperger, B. Piraux and J. Madroñero, *Spectral representation of the three-body Coulomb problem: II. Autoionizing doubly-excited states of unnatural parity in helium*, Physical Review A **81**, 042528 (2010).
- J. Eiglsperger and J. Madroñero, *Fluctuations in photoionization cross sections of highly doubly excited two-electron atoms*, accepted for publication in "High Performance Computing in Science and Engineering, Garching 2009".
- J. Eiglsperger and J. Madroñero, *Fluctuations in photoionization cross sections of singlet planar helium*, submitted.

Further publications:

- J. Eiglsperger, M. Fink, H. Friedrich and J. Madroñero, *Comment on "Nonuniqueness of the Phase Shift in Central Scattering due to Monodromy"*, Physical Review Letters **102**, 188901 (2009).
- M. Fink, J. Eiglsperger, H. Friedrich and J. Madroñero, *Smoothness properties of the quantum-mechanical and WKB phase shifts for two-dimensional scattering*, Physical Review A **80**, 024701 (2009).
- M. Fink, A. Naranjo, F. Arnecke, J. Eiglsperger, H. Friedrich, J. Madroñero, P. Raab and A. Wirzba, *s-wave scattering of a polarizable atom by an absorbing nanowire*, accepted for publication in Physical Review A.

# Acknowledgements

First and foremost I would like to thank Prof. Dr. Harald Fiedrich for the opportunity to do this work, as well as for all the discussions and advice. The pleasant atmosphere in his group and his unrestrictive manner made it easy to work even in hard times.

I am very grateful to Dr. Javier Madroñero, who more than the supervisor of this thesis, has been a friend. His enthusiasm, advice and insight, his numerous ideas, critical questions and helpful comments have contributed substantially to the progress and success of this project.

I thank Prof. Dr. Bernard Piraux for the possibility to stay some months in Louvain-la-Neuve and for the illuminating discussions about many aspects of this thesis. I would like to thank Prof. Dr. Dominique Delande, Dr. Yuhai Jiang and Dr. Ralph Püttner for sharing their data with me, Prof. Dr. Yuri Popov and Prof. Dr. Gregor Tanner for many vivid discussions. I would also like to thank the main characters of two further collaborations, who are Prof. Andreas Buchleitner and Dr. Celsus Bouri, and Dr. Tobias Kramer, respectively.

Access to the computing facilities of the “Leibniz-Rechenzentrum der Bayerischen Akademie der Wissenschaft” and of the “Calcul Intensif et Stockage de Masse” through the “Université catholique de Louvain” as well as financial support by the “Deutsche Forschungsgemeinschaft” under Contract No. FR 591/16-1 are gratefully acknowledged.

I am also indebted to my co-workers Dr. Florian Arnecke, Dr. Patrick Raab, Dipl. Phys. Tim-Oliver Müller, Dipl. Phys. Sebastian Schröter, Martin Fink and Moritz Schönwetter for discussions, helpful comments and distractions from physics.

Last but not least I want to thank my family, and especially Tina, who “has to” live together with a physicist,<sup>1</sup> for her love and understanding.

---

<sup>1</sup>I hear that physicists are like babies with less goo but more gibberish.